Georg C. Ganzenmüller (Editor)

Dynamic Behaviour of Additively Manufactured Structures & Materials

DYMAT 2022,
26th Technical Meeting
Conference Proceedings

DYMAT

Dynamic Behaviour of Additively Manufactured Structures & Materials

Dynamic Behaviour of Additively Manufactured Structures & Materials

DYMAT 2022,
26th Technical Meeting
Conference Proceedings

11 – 14. Steptember 2022
Freiburg, Germany

DYMAT
connects, supports, researches.

DYMAT

is a European research association in the field of dynamic behaviour of materials and its applications.

Founded in 1983, the association connects researchers, supports young scientists, and fosters scientific progress.

dymat.org

Scientific Comittee of the 26th Technical Meeting

Prof. N. Bahlouli
University of Strasbourg, France

Dr. E. Buzaud
CEA, Bordeaux, France

Prof. E. Cadoni
University of Applied Sciences
and Arts of Southern Switzerland,
Switzerland

Dr. A. Cosculluela
CEA, Bordeaux, France

Dr. HDR H. Couque
Nexter Munitions, Bourges, France

Prof. P. Forquin
Université Grenoble Alpes, France

Prof. F. Galvez
Universidad Politecnica de Madrid,
Spain

Dr. G. C. Ganzenmüller
University of Freiburg / INATECH,
Germany

Prof. M. Hokka
Tampere University of Technology,
Finland

Prof. M. Langseth
Norwegian University of Science and
Technology, Norway

Dr. Yaël Demarty
French German research Institute of
Saint-Louis, France

Prof. D. Mohr
ETH Zürich, Switzerland

Prof. L. Peroni
Politecnico di Torino, Torino, Italy

Prof. P. Verleysen
Ghent University, Belgium

Prof. P. Viot
Arts et Métiers ParisTech – École Na-
tionale Supérieure d'Arts et Métiers,
France

Dr. S. M. Walley
University of Cambridge, United
Kingdom

Organizing Comittee

Dr. Georg C. Ganzenmüller

Gips Schüle Chair for Sustainable
Systems Engineering, University of
Freiburg / INATECH

**Prof. Dr.-Ing. habil.
Stefan Hiermaier**

Professor at the Gips Schüle Chair
for Sustainable Systems Engineering,
University of Freiburg / INATECH

Director Fraunhofer Institute for
High-Speed Dynamics, Ernst-Mach-
Institut, Germany

Dr. Kilian Kreb

Gips Schüle Chair for Sustainable
Systems Engineering, University of
Freiburg / INATECH

Fraunhofer Institute for High-Speed
Dynamics, Ernst-Mach-Institut,
Germany

Preface

New materials, new opportunities

by **Dr. Georg C. Ganzenmüller**

In recent years, additive manufacturing has leapt forward at an extraordinary pace. Today, the technology enables us to realise the most complex structures, which are not obtainable by conventional machining.

As a result, new functional materials with their engineered mesoscale structures have become a central pillar in today's materials research. The term "materials", however, requires attention. Is the matter that is produced by additive manufacturing a material or a structure? The answer depends of course on the length scale used to characterise the matter.

To avoid contradiction, the term mechanical metamaterial is used to describe a structured material, whose properties are very different from the intrinsic behaviour of the constituting base material used for manufacturing. The mechanical properties of a metamaterial are governed by its geometrical structure on a length scale smaller than the overall dimensions of the manufactured object, i.e., its external dimensions, but larger than the microscopic length scales, i.e., its atomistic structure.

Metamaterials allow us to design mechanical behaviour with properties that are dramatically enhanced compared to, or inexistent in natural materials. Examples include negative elastic moduli, negative compressibility, and negative thermal expansion.

The understanding of these effects is limited at the moment. Considerable research effort has been devoted to investigate the phenomena under quasi-static, or steady-state conditions. However, investigation into the dynamic properties of mechanical metamaterials is still in its infancy. The research is complex, as the term metamaterials implies that both the constituting base material as well as geometrical choice for the mesoscale are significant.
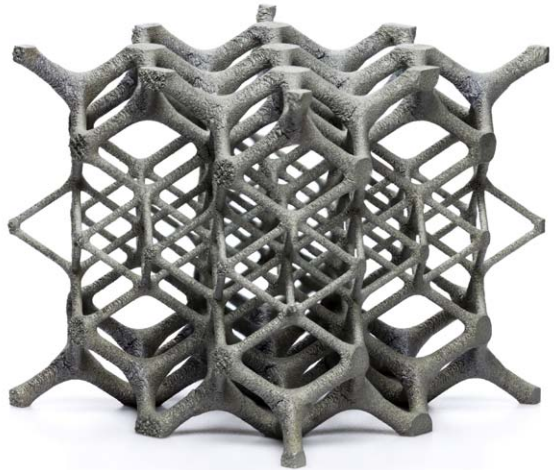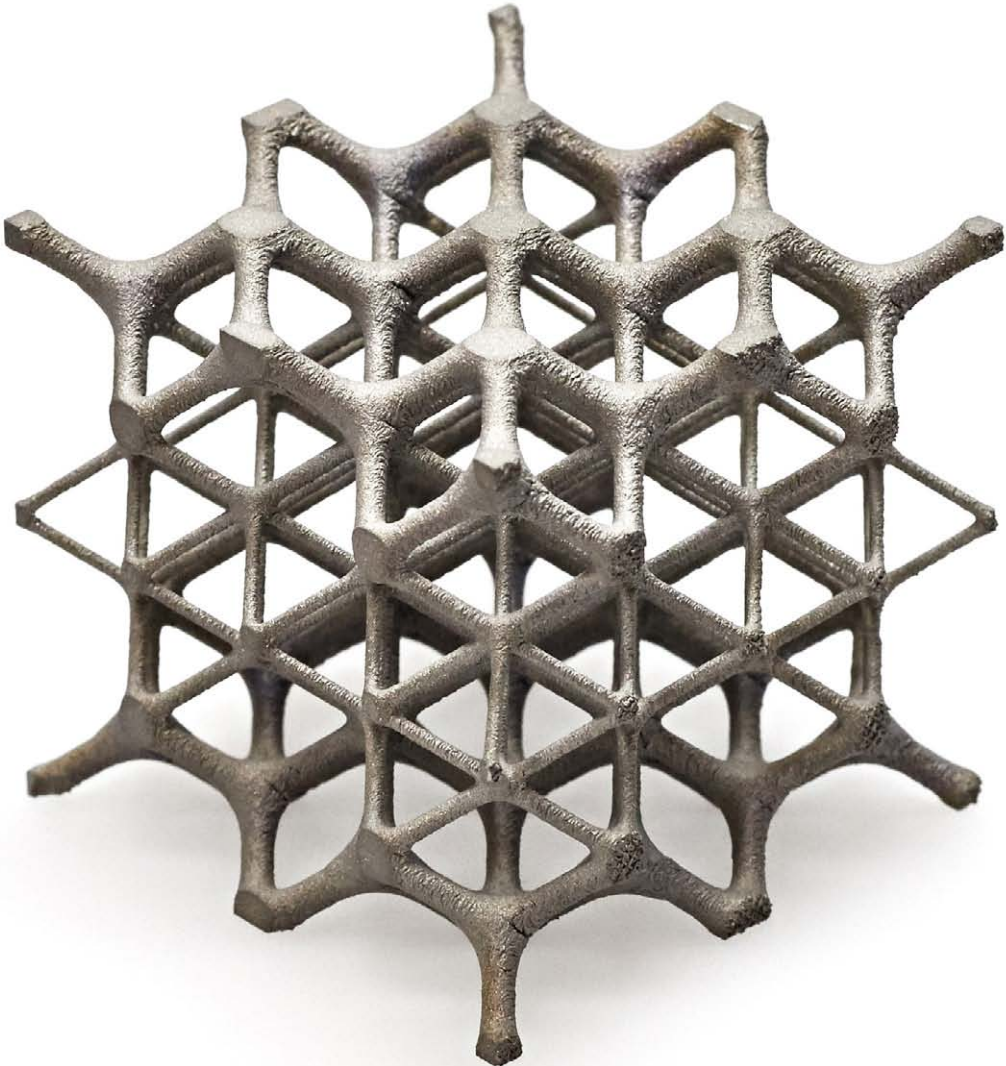
At the same time, the possibilities of new material behaviour that can be achieved by suitable geometrical design choices are fascinating: anisotropic gradients in wave propagation, surface localization of vibration and deformation energy, acoustic and mechanical rectifiers as well as by-passers are within reach.

At this threshold, the 26th Technical Meeting of the DYMAT Association takes place. More than 30 presentations are presented along the four topics:

1. Metallic base materials
2. Metallic structures
3. Simulation
4. Polymers

The conference proceedings thus offer a comprehensive view of current research in the field of »Dynamic Behavior of Additively Manufactured Structures & Materials«.

Contents

Sessions:

03 Session 03: Simulation

PAGE 184

04 Session 04: Polymers

PAGE 230

01

Metallic base materials

$\bigcirc$ 01

Substructure Evolution in a Shock Loaded [100] Aluminum Single Crystal

G.T. (Rusty) Gray III[1][*], V. Anghel[1], C. Lear[1], C.P. Trujillo[1], G. Euser[1]

[1]Los Alamos National Laboratory, Los Alamos, NM, USA

Correspondence
[*]George T. Gray III, Los Alamos National Laboratory, MailStop G755, DP01U, Los Alamos, NM 87545, USA
Email: rusty@lanl.gov

Interest in the shock-loading response of aluminum(Al) dates to the early seminal study of John S. Rinehart in 1955. In this study, a [100] high purity Al single crystal was shock loaded in a target assembly comprised of three machined pieces, the sample a [100] Al single crystal and two surrounding concentric tantalum rings. A 3.94mm thick tantalum(Ta) flyer plate was accelerated and impacted target assembly at 455 m/s at -165° C. Due to this configuration, the stress path in the [100] Al crystal starts at 5.7 GPa in the Al but transitions to the peak stress state given by the Ta impactor hitting the Ta ring around the Al crystal at the impact velocity which is ~ 14 GPa. The central Al crystal thereafter rings up via lateral Mach waves such that the Al crystal sees a complex biaxial strain field across the Al and higher shear stresses. In this paper, the substructure evolution in the (100) Al crystal is presented and discussed in relation to previous data on the shocked polycrystalline Al.

1   INTRODUCTION

Deformation twinning is an important mode of plastic deformation, particularly in lower symmetry metals and alloys, and is also known to occur in a variety of face-centered-cubic(fcc) metals and alloys[1, 2]. While deformation twinning is commonly seen in many fcc metals and alloys, its occurrence in fcc metals and alloys with higher stacking fault energies, like Cu, Ni, and Al, is less commonly observed[1]. Unlike many other face-centered-cubic pure metals and alloys, such as Ag and brass, these studies have documented the absence of shock-induced twinning in polycrystalline Al even when Al is shock loaded to high peak shock stresses and at low temperature[3]. This is especially

*Equally contributing authors

true in single- and polycrystalline Al alloys which do not twin under normal deformation conditions but were seen in a shock-loaded Al-4.8Mg alloy[4] and emanating from a crack in a foil of pure aluminum[5]. Twinning in most fcc, body-centered-cubic(bcc), hexagonal-close-packed(hcp), and intermetallic compounds is known to significantly increase in importance as the temperature is lowered or the strain rate is increased, particularly under impact and/or shock-wave loading[1, 6-8].

Research interest in the shock-loading response of copper(Cu) and aluminum(Al), including the activation of deformation twins during shock loading, dates to the early seminal study of John S. Rinehart in 1955[9] on Al and shock studies of C.S. Smith on Cu in 1958[10]. While C.S. Smith[10] found that shock loading activated extensive twinning in shock prestrained polycrystalline Cu, Rinehart did not observe deformation twin formation but rather complex dislocation slip behavior in an explosively loaded Al single crystals[9]. Ogisevskii and Bushnev also studied the deformation structure development in Al and Cu single crystals subjected to shock loading up to 50 and 100 GPa, respectively[11]. No evidence of deformation twinning was found in that study on [110] and [113] oriented Al-single crystals shocked to 20-50 GPa[11]. Since that time, numerous researchers have probed the substructure evolution in shock-loaded single and polycrystalline Al[3, 4, 12] but none of these studies have documented deformation twin formation. More recent research on a Cu [100]/ [01$\bar{1}$] bicrystal[13] has demonstrated the strong influence of crystal orientation on the peak shock stress required to initiate deformation twinning in high-purity Cu single crystals. In this study, transmission-electron microscopic(TEM) revealed well-defined dislocation cell structures in both crystal orientations shocked to 10 GPa but also found deformation twins to be dominant within the [100] grain and absent in the [01$\bar{1}$] grain. This twin activation was analyzed by examining the energetically favorable dissociations of slip dislocations into Shockley partials coupled with the stress-orientation effect on the width of the partial dislocation[13]. In this analysis, it was shown that the core separation in the [100] crystal shocked to 10 GPa was enough to cause twinning but not in the [01$\bar{1}$] Cu crystal case[13].

The focus of the current study was to investigate if deformation twinning can be activated in a 99.999 purity [100] Al single crystal when the shock-loading conditions have been manipulated to suppress dislocation slip. Based upon the previous study of Cao et al.[13], a [100] single crystal was chosen as one means to bias the stress and orientation conditions conducive to dissociate dislocations into glissle twinning dislocations. Secondly, the experiment was designed to be conducted at a cryogenic temperature to favor twinning by suppressing overall thermally-activated slip processes consistent with previous literature findings on temperature effects on twin activation[1, 2, 4]. Finally, given that twins constitute homogeneously sheared regions, choosing a shock-loading loading path that can increase the magnitude of the shears applied during the shock was designed into the experiment. In this regard, research by Brown et. al.[14, 15] has demonstrated a technique by which converging shocks in a bi-material concentric shock assembly can be utilized to develop a Mach conical converging shockwave leading to higher shock stresses. Utilizing this technique conically converging shocks are generated at the interface in the bi-metallic shock assembly which upon convergence lead to irregular reflections and a high pressure state due to the formation of a Mach disk[14, 15]. As the Mach reflections grow to steady state in the central sample, a multidimensional state of longitudinal and shear stresses and strains ahead of the shock develops [14, 15]. This technique was chosen as a means to subject the [100] Al single crystal is a higher level of longitudinal stress and shear stresses than could be achieved via a 1-dimensional plane shock impact.

2   EXPERIMENTAL PROCEDURE

Aluminum (Al) single crystals of orientation [100] and 99.9999 purity were purchased from Princeton Scientific Corporation[16]. Plate-impact experiments were performed on an 80 mm bore single-stage light gas-gun. The target assembly was mounted to the front of a steel "stripper-can," designed to arrest the projectile and the material surrounding the samples, while allowing the sample to be ejected into a soft-capture media. This experimental technique has been described in detail by Gray[17]. The target assembly was comprised of three machined pieces, the sample (a disc) Al single crystal [100] and two surrounding concentric tantalum(Ta) rings. The target assembly was precision machined so that all the pieces where lightly pressed together to form an assembly 69.85mm in diameter and 7.85mm thick (Figure 1). 6.35mm soft copper tubing was soldered to the outer perimeter of the outer Ta momentum trapping ring to allow liquid nitrogen to flow and cool entire target assembly. The primary diagnostics used was Photonic Doppler Velocimetry (PDV)[18] and sample recovery with post –mortem metallurgical analysis. Sample assembly was impacted using an 80mm smooth bore gas launcher and soft recovery technique were deployed stripping sample from assembly and decelerating the Al single crystal sample into low-density materials. Seven single-point PDV probes were placed behind of sample assembly to measure free surface velocity (FSV), two on the inner Ta target ring, two on the tapered interface between the [100] Al crystal sample and Ta inner ring, and three on the [100] Al sample itself. The 80mm launcher target chamber pressure was bought to 300 millitorr and liquid nitrogen was run through the copper tubing cooling sample assembly to -165° C for 8 minutes before impact.
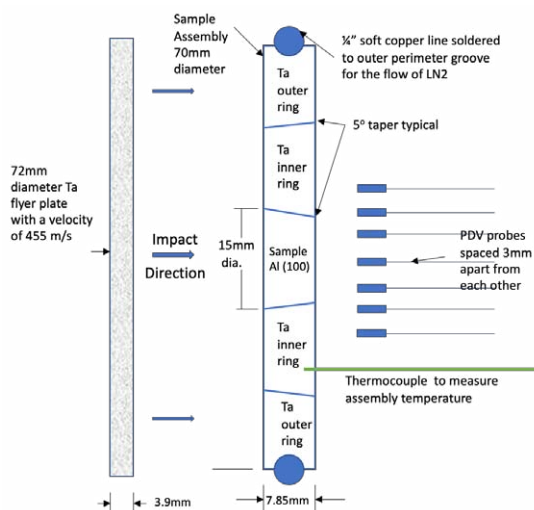
FIGURE 1   Schematic of the shock-loading assembly. The assembly was surrounded by a copper tube soldered to the assembly to allow cooling of the assembly to cryogenic temperature while multiple PDV probes track the particle velocity in the [100] Al single crystal and the surrounding Ta momentum trapping rings.

The shock-recovered [100] Al crystal was cross sectioned and prepared according to standard metallographic techniques. Sample preparation consisted of grinding on SiC paper with increasingly finer grit under very light pressure, followed by mechanical polishing with 0.3 μm alpha alumina slurry, and then a mixture of 5:1 by volume of 0.04 μm colloidal silica and hydrogen peroxide. The as-polished sample surfaces were lightly etched with a solution containing 6g of sodium hydroxide and 50 ml water. A Zeiss Axio Imager M2m optical microscope was used to interrogate the etched surface and to identify regions of interest for electron microscopy. Electron Backscatter Diffraction (EBSD) was employed to investigate the cross sections of the samples on a Thermo Scientific™ AP-REO 2 SEM, using the Oxford AZtec Data Collection software. EBSD data was acquired with a step size of 0.2μm to obtain detailed information on the microstructure. Boundaries with more than 50°

misorientation and having <111> as the disorientation axis were identified and highlighted. Amongst these boundaries, several boundary segments were highlighted as Σ3 boundaries when a 10° deviation was imposed for the identification algorithm.

Parallel to the experiment, computer simulations of the experiment were also conducted. Simulations were performed using FLAG, an Arbitrary Lagrangian-Eulerian (ALE), explicit, finite-volume hydrodynamics code using arbitrary polyhedral computational zones developed at Los Alamos National Laboratory. Two-dimensional axi-symmetry was assumed in all simulations. The utilized quadrilateral structured mesh consisted of an average cell size of 9E-3 cm. The tantalum impactor and outer rings were modeled using a Maxwell-constructed version of a multiphase Ta EOS (SESAME 93524)[19], while SESAME 3720 EOS was utilized for aluminum[20]. A Steinberg-Cochran-Guinan derived strength model was used for both materials, with model parameters obtained from[21]. Strength model parameters corresponding to pure tantalum and aluminum 6061-T6 were assumed[21]. Within the simulations, the tantalum flyer was initially moving at the impact velocity and impacted the target assembly at t_o. Thus, the simulation data has been shifted in time to coincide with the experimental results in order to facilitate comparison. Rear surface velocities coinciding with experimental photon doppler velocimetry (PDV) probe locations were monitored utilizing virtual PDV diagnostics within FLAG.

3   RESULTS AND DISCUSSION

Figure 2 presents a comparison of the measured free-surface velocity measured with the PDV probes on the [100] Al crystal versus the Flag simulation; the PDV data is offset by ~ 0.2 microseconds to allow the PDV data to be clearly visualized versus the simulation). Excellent agreement is seen between the experimental FSV data and the Flag simulation. Conversion of the FSV to shock stress reveals the impact stress in the [100] Al starts at nominally 5.7 GPa but then "rings up" to the state in the Ta rings from the Ta impactor of ~ 14 GPa. The central [100] Al therefor "rings up" via the lateral Mach waves bringing the Al crystal up to the higher peak shock stress aka Brown et al [14, 15]. The Flag simulation shows that the peak shear stress in the [100] Al crystal reaches ~ 320 MPa near the center of the Al crystal due to the complex stress state imposed within the crystal by the Mach oblique reflections.
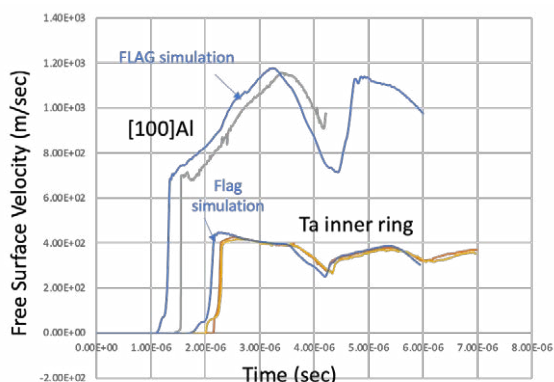
FIGURE 2   Comparison of the free-surface velocity (FSV) measured with the PDV probes as a function of time for the [100] Al crystal and the inner Ta ring surrounding the Al crystal between the experimental data and the FLAG simulation. The FSV and simulation is offset by 0.2 microseconds to allow better comparison.

The substructure evolution in the recovered [100] Al crystal is seen to be comprised of a high density of slip activity as well as long lenticular features as seen in Figure 3. Analysis of the {111} pole figure in

the regions displaying the lenticular features following the Mach disk loading of the [100] Al crystal shows a nominal ~60 degrees rotation around the $(1\bar{1}1)$ plane between the matrix and the lenticular features. The boundary character is seen to vary along the lenticular / matrix interface between 54 and nearly 58 degrees. This orientation relationship and the 60 degree rotation suggests the lenticular features are deformation twins that were formed and then subsequently severely plastically deformed during the complex stress path in the [100] Al crystal during the Mach wave "ring up". Previous research by Niewczas, Engler, and Embury[22] similarly used {111} pole figure analysis to identify deformation twins in severely deformed Cu single crystals. According to the model of Mahajan and Chin[23], the twin formation in fcc metals and alloys requires fine slip over coarse slip. In this theory[23], coplanar ½ <110> dislocations of different Burgers vectors that interact repulsively combine to form three-layer twin nuclei according to the following reaction: ½[$1\bar{1}0$] (111) + ½[$0\bar{1}1$] (111) -> 3x1/6 [$1\bar{2}1$] (111). Upon further stressing, the three-layer nuclei located at different levels within a microslip band grow into each other to form a defective twin. It is postulated that the complex loading path in this experiment, i.e., an initial nominal 1-D plane shock into the [100] Al crystal followed by the oblique reflecting shocks leading to a Mach disk within the crystal, produces the complex slip activity leading to deformation twin formation. Thereafter, the multiaxial stress state impinging on the [100] Al crystal upon rarefaction release from the shocked state produces the severe plastic deformation distorting the twins from their pristine linear orientation relationship along {111} habit plane. On-going detailed EBSD and transmission electron (TEM) analysis is underway to validate conclusively that the lenticular features in the 99.999 [100] Al single crystal are deformation twins.
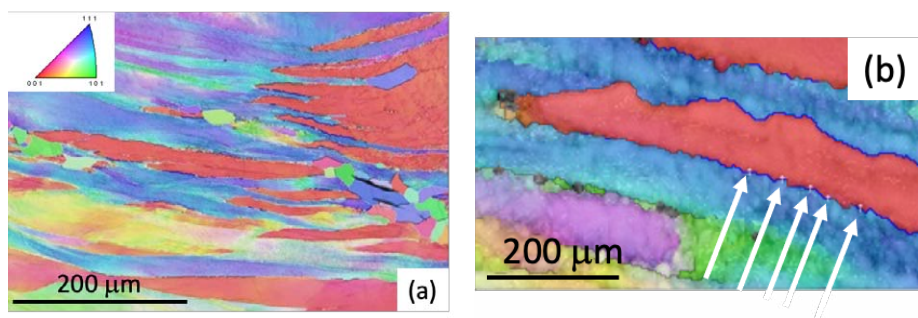
FIGURE 3 Substructure developed in shocked [100] Al crystal: a) Electron backscatter diffraction (EBSD) image of lenticular twin-like features, and b) misorientation measurements across the Al-Al features in (a) are denoted by the arrows in the figure.

4   REFERENCES

1.   Christian, J.W. and S. Mahajan, *Deformation Twinning.* Prog. Matls. Sci., 1995. **39**(1/2): p. 1-158.

Metallic base materials

2.   Mahajan, S. and D.F. Williams, *Deformation Twinning in Metals and Alloys.* Int. Metall. Reviews, 1973. **18**: p. 43-61.

3.   Gray III, G.T. and J.C. Huang, *Influence of repeated shock loading on the substructure evolution of 99.99 wt% aluminum.* Mater. Sci. Engng A, 1991. **145**: p. 21-35.

4.   Gray III, G.T., *Deformation Twinning in Aluminum-4.8 wt.% Mg.* Acta Metallurgica, 1988. **36**: p. 1745-1754.

5.   Pond, R.C. and L.M.F. Garcia-Garcia. *Deformation Twinning in Aluminum.* in *Electron Microscopy and Analysis 1981.* 1982. Cambridge, U.K.: Inst. Phys. Conf. Ser 61.

6.   Mahajan, S., *Metallurgical effects of planar shock waves in metals and alloys.* Phys. Stat. Sol. A, 1970. **2**: p. 187-201.

7.   Gray III, G.T., *Deformation Twinning: Influence of Strain Rate*, in *Twinning in Advanced Materials*, M.H. Yoo and M. Wuttig, Editors. 1994, The Minerals, Metals, and Materials Society. p. 337-349.

8.   Claisse, F. *Twinning in Shock-Induced Metals and Alloys.* in *High Energy Rate Working of Metals.* 1964. Oslo, Norway: NATO Advanced Study Institute.

9.   Rinehart, J.S., *Deformation of an explosively loaded aluminum single crystal.* J. Appl. Phys., 1955. **26**: p. 1315-1317.

10.   Smith, C.S., *Metallographic studies of metals after explosive shock.* Trans. Metall. Soc. AIME, 1958. **212**: p. 574-589.

11.   Mogilevsky, M.A. and L.S. Bushnev, *Deformation structure development in Al and Cu single crystals under 50 and 100 GPa loadings.* Inst. Phys. Conf. Ser., 1989. **102**: p. 307-315.

12.   Rose, M.F. and T.L. Berger, *Shock deformation of polycrystalline aluminium.* Philos. Mag., 1968. **17**: p. 1121-1133.

13.   Cao, F., et al., *Orientation dependence of shock-induced twinning and substructures in a copper bicrystal.* Acta mater., 2010. **58**: p. 549-559.

14.   Brown, J.L. and G. Ravichandran, *High pressure Hugoniot measurements using converging shocks*, in *Dynamic Behavior of Materials. Vol. 1: Proc. 2010 Ann. Conf. on Experimental and Applied Mechanics*, T. Proulx, Editor. 2011, Springer: Berlin. p. 403-410.

15.   Brown, J.L., et al., *High pressure Hugoniot measurements using converging shocks.* J. Appl. Phys., 2011. **109**: p. 093520.

16.   *Princeton Scientific Corporation*, in *3201 Highfield Dr, Bethleham, PA 18020*, P.S. Corporation, Editor.

17.   Gray III, G.T., *Shock wave testing of ductile materials*, in *ASM Handbook. Vol. 8: Mechanical Testing and Evaluation*, H. Kuhn and D. Medlin, Editors. 2000, ASM International: Materials Park, Ohio. p. 530-538.

18.   Strand, O.T., et al., *Compact system for high-speed velocimetry using heterodyne techniques.* Rev. Sci. Instrum., 2006. **77**: p. 083108.

19.   Greeff, C.W., et al. *Limited Range Sesame EOS for Ta.* 2017.

20.   Sjostrom, T., S. Crockett, and S. Rudin, *Multiphase Aluminum Equations of State via Density Functional Theory.* Physical Review, 2016. **94**: p. 144101-1 to 144101-10.

21.   Steinberg, D.J., *Equation of state and strength properties of selected materials.* 1991, Lawrence Livermore National Laboratory: Livermore, California.

22.   Niewczas, M., O. Engler, and J.D. Embury, *The Recrystallization of Copper Single Crystals Deformed at 4.2 K.* Acta Materialia, 2004. **52**: p. 539-552.

23.   Mahajan, S. and G.Y. Chin, *Formation of Deformation Twins in F.C.C. Crystals.* Acta Metallurgica, 1973. **21**: p. 1353-1363.

02

Experimental and numerical investigation of the rate-dependent material properties of binder jetted 316L stainless steel

C.C. Roth | T. Tancogne-Dejean | D. Mohr

Department of Mechanical and Process Engineering, ETH Zurich, Switzerland

Correspondence
C.C. Roth, Department of Mechanical and Process Engineering, ETH Zurich, Switzerland
Email: ccroth@ethz.ch

Binder jetting is an emerging process that comes with significant efficiency advantages over other additive manufacturing techniques such as selective laser melting (SLM) or shaped metal deposition (SMD). It makes use of a binder bonding process to form the initial part from metal powder, which is followed by sintering and powder removal to obtain the final part. In the present work the plasticity and fracture properties of binder jetting manufactured stainless steel 316L are characterized for stress states ranging from shear to (equi-) biaxial tension and low (0.002/s), intermediate (2/s) and high strain rates (>100/s). High speed optical photography is used for full field digital image correlation. In addition, high-speed infrared imaging is used to assess the conversion of plastic work into heat at intermediate strain rates. A microstructural analysis is carried out by means of Electron Back-Scattered Diffraction and micro computed tomography. The material is successfully modeled as an anisotropic elasto-plastic material with isotropic hardening and a Johnson-Cook type of strain rate and temperature dependence and a stress state dependent Hosford-Coulomb fracture initiation model. Finally, all results are compared to wrought and SLM made stainless steel 316L.

*Equally contributing authors
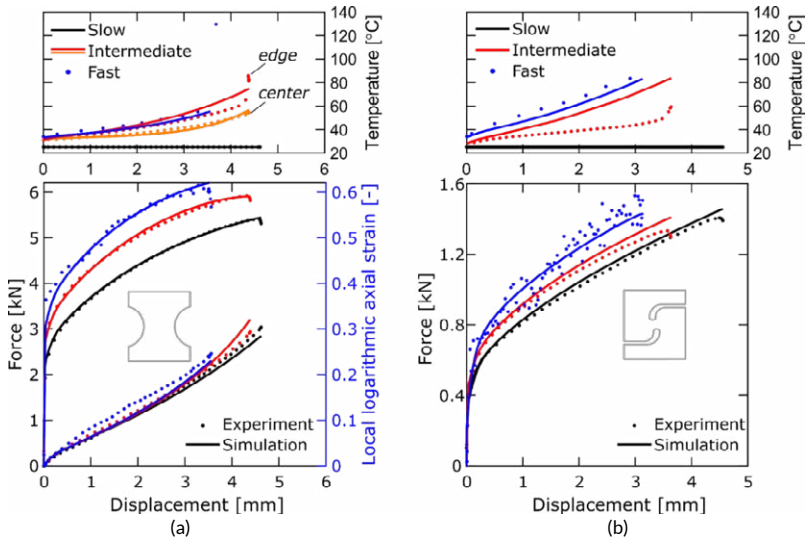
FIGURE 1   Overview of the experimental and Finite Element Analysis results for the binder jetted 316L. Comparison of the force, local strain and temperature evolution at different strain rates for the (a) NT6 and (b) SH geometries.

REFERENCES

[1]   T. Tancogne-Dejean, C.C. Roth, D. Mohr, Rate-dependent strength and ductility of binder jetting 3D-printed stainless steel 316L: Experiments and modeling, Int. J. Mech. Sci. 207 (2021) 106647. https://doi.org/10.1016/j.ijmecsci.2021.106647.

03

Equation of State measurements in AM and wrought 304L Stainless Steel

Sarah A. Thomas[,1], M. Cameron Hawkins[1], Robert S. Hixson[2], George T. Gray III[2], D. J. Luscher[2], and <u>Saryu J. Fensin[2*]</u>

[1]Nevada National Security Site, New Mexico Operations, Los Alamos, NM, USA
[2]Los Alamos National Laboratory, Los Alamos, NM, USA

Correspondence
[*]Saryu Fensin, Los Alamos National Laboratory, MailStop G755, DP01U, Los Alamos, NM 87545, USA
Email: saryuj@lanl.gov

The purpose of this work was to measure the equation of state in additively manufactured (AM) and wrought 304L stainless steel in velocity regimes where microstructure still matters or in other words the material retains a two-wave structure. The results showed that there was a measurable difference in the shock velocity between the AM and wrought 304L. Specifically, the shock velocity for the AM 304L was found to be ~3% slower than that for wrought 304L at a similar particle velocity. To understand these differences, properties such as densities, sound speeds, and texture were measured and compared between the two materials. However, no measurable difference was found in these properties. Eventually, the difference in the equation of state was attributed to differing elastic wave amplitudes which have been shown to have an effect on the shock velocity.

1   INTRODUCTION

Additive manufacturing (AM) is a process for manufacturing metals in an efficient and rapid manner which shows great promise for real-world applications. The use of AM materials is becoming more prevalent in various fields because they offer some advantages over conventionally manufactured materials. For example, AM parts can be printed to near net shape in a relatively short time with minimal machining, which can accelerate the process of producing prototypes. It is also relatively easy to make changes to part designs on the fly using AM. However, there are new challenges

---

*Equally contributing authors

associated with AM especially related to determining the suitability of the materials generated in this process to actual applications. While there has been a plethora of research to characterize the microstructure and mechanical properties of AM materials as a function of strain rate [1-3], there have only been a handful of studies investigating the dynamic properties such as spall strength and equation of state [4-8] of AM materials. These complex loading regimes that subject AM materials to extreme mechanical loads are of potential interest to various applications. The goal of this work is to systematically measure the shock velocity of additively manufactured 304L stainless steel (SS). While many studies exist to understand the specific microstructure and the resulting properties at low strain rates, there are only a handful of studies on the dynamic behavior of AM materials [4-7, 9]. Gray et al. [7] performed spall experiments on AM 316 L SS and found that while the spall strength of these materials was higher than their wrought counterpart, there was also a change in the damage morphology between the two materials. This work also investigated the effect of annealing on the dynamic response of AM materials and showed that post-processing of materials can drastically alter mechanical properties. Jones et al. [5] investigated the spall strength of AM Ti-6Al-4V and found the spall strength to be dependent on the sample orientation with respect to the build layer thickness. Specifically, the spall strength was much higher when samples were loaded parallel versus normal to the AM build layer interfaces. Fadida et al. [10] studied Ti-6Al-4V and examined the effects of initial porosity on dynamic strength, finding that denser samples displayed greater strength, while ductility remained comparable whether the samples were dense or porous. Jones et al. [11] also investigated the spall strength of AM tantalum and found that while the AM materials had a higher Hugoniot elastic limit their spall strength was lower than wrought tantalum (Ta). This was attributed to the change in the microstructure of the AM Ta that led to the creation of a higher amount of void nucleation sites. As shown above, the majority of the published work has focused on investigating failure in AM materials. To our knowledge the only previously published study to investigate the equation of state of AM metal under dynamic loading is that of Wise et al. [8] which investigated the equation of state of AM 304L and found no measurable differences in the shock stress of AM vs. wrought 304L. However, Wise et al. did not report directly measured or calculated shock velocity in the stainless samples. This scarcity in experiments investigating the equation of state of AM materials is possibly related to the fact that prior research has shown that equation of state is fairly insensitive to changes in grain size [12], texture and orientation [9, 10, 12, 13].

The goal of this work is to fill this gap in knowledge by performing systematic experiments on AM 304L SS. The rest of the paper is organized as follows. Section 2 presents the experimental methods used in this work. The results are presented in Section 3 followed by a discussion of results in Section 4. Finally, a summary of the results is presented in Section 5.

2   EXPERIMENTAL PROCEDURE

The top-hat method was used to accurately determine the shock velocity in these experiments. This top-hat method uses z-cut quartz below its Hugoniot elastic limit as the "brim" so that a single wave travels through the quartz and breaks out at the free surface creating a sharp timing fiducial. Because the metal studied was manufactured with a directional printing technique, this design also allowed for dependence of the equation of state on the orientation of the samples w.r.t the build direction. To achieve this goal, samples were obtained from a manufactured plate in multiple directions as will be discussed later. This section describes the manufacturing process in more detail and elaborates on the experimental techniques used to carefully measure shock and particle velocities.

2.1 Material and AM processing

A single lot of pedigreed micro-melt 304L SS powder (termed ADET powder) manufactured by Carpenter Powder Products in Sweden was used for manufacturing the AM material. A detailed chemistry analysis of this powder is shown in Table 1.

Element	wt%	Element	wt%
C	0.015	N	0.05
Si	0.53	O	0.019
Mn	1.5	Cr	18.4
P	0.012	Ni	9.8
S	0.003	Fe	Balance

Table 1. The measured chemical composition of the 304L SS powder.

The plates fabricated on the GmbH Electro Optical Systems (EOS) M 280 were built on a 50.5 mm thick AISI 304L baseplate in the vertical and horizontal directions as shown in Figure 1. The processing parameters used were the EOS-developed PH1 20 μm settings. This license from EOS was developed specifically for SS and uses rotational rectilinear hatching with 20 μm layer heights. However, due to the proprietary nature of the fabrication method, the only detail that was known during the fabrication was the layer height. The plate from which samples for the current work were obtained was manufactured by the Sigma Division at Los Alamos National Laboratory (LANL), with raster directions set at 0, 90, and 45 degrees. Figure 1 (right) depicts plate 2 and shows the locations from which samples were obtained. These included two large samples in the z-direction and many smaller samples at various orientations. The specific samples studied here are Z1a, X1, XY1(+45), and XY2(+45).
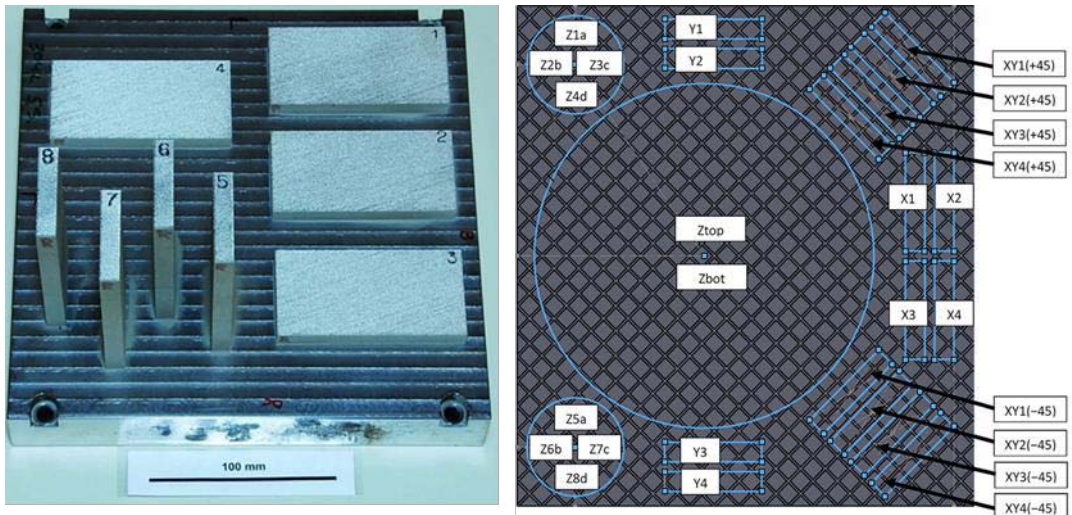
Figure 1. (left) Optical photograph of EOS builds on 304L SS baseplate. (right) Schematic of plate 2 and locations from which samples were obtained for dynamic experiments.

2.2 Equation of State measurements

A pulse-echo technique was used to measure the longitudinal and shear sound speeds. Density was characterized using immersion techniques. Sound speeds are estimated to be accurate within 0.5%, while immersion densities are estimated to be good to better than 0.5%. Sample thicknesses were measured after the samples were lapped flat and parallel to within 5 to 10 μm. These values are shown in Table 2.

Table 2. Measured thicknesses, densities, and longitudinal and shear sound speeds of the samples.

Experiment	Material	Thickness (mm)	Density (g/cm^3)	Sound speed (km/s)	
				Longitudinal	Shear
172	Wrought	2.010 ±0.010	7.86 ±0.03	5.78 ±0.08	3.15 ±0.06
173	AM-XY1	1.997 ±0.010	7.87 ±0.03	5.77 ±0.08	3.10 ±0.06
174	AM-Z1a	1.999 ±0.010	7.87 ±0.03	5.72 ±0.08	3.20 ±0.06
176	AM-XY2	2.001 ±0.010	7.90 ±0.03	5.80 ±0.08	3.12 ±0.06
177	AM-X1	1.996 ±0.010	7.83 ±0.03	5.80 ±0.08	3.16 ±0.06

Shock velocities were measured using a top-hat design with a z-quartz baseplate and stainless sample, with z-, xy-, and x-directions of the AM 304L SS material as shown in Figure 1. For these experiments, the impactor was a z-quartz disc backed by syntactic foam bonded directly to the projectile nose. The target was a quartz baseplate with the same dimensions (35 mm diameter by 2 mm thick) as the impactor, and with the sample material (304L) with the same nominal thickness (2 mm) and a smaller diameter (10 mm), bonded to the quartz baseplate using a thin glue bond. Finally, a sapphire window (10 mm diameter by 12 mm thick) was glued to the back of the target to reduce elastic-plastic wave interactions due to reflectance from the free surface. A schematic of this experimental design is shown in Figure 2. These target dimensions were carefully chosen to ensure edge releases (lateral releases) did not affect the velocimetry measurements at the sample/window interface during the desired measurement timescale. This is particularly important because of the use of a sapphire window, a material that is well known to have high wave speeds.
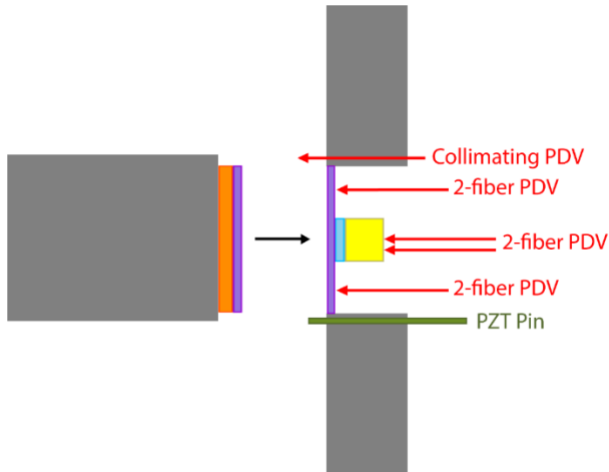
Figure 2: Quartz top-hat experimental design. The projectile and target plates are shown in gray. Affixed to the front of the projectile is the syntactic foam backing (orange) and the quartz impactor (purple). The target is centered on the target plate and is comprised of a quartz baseplate (purple), the 304L sample (blue), and a sapphire window (yellow). A single collimating probe measures the projectile velocity. There are two 2-fiber probes in the center, one slightly offset from the center of the target, and four additional 2-fiber probes that circle the quartz baseplate at a fixed radius (11.25 mm). The design also includes a single piezoelectric pin (green) that serves as a diagnostics trigger.

The projectiles were launched at a nominal velocity of 400 m/s. Four 2-fiber photonic Doppler velocimetry (PDV) probes [14] were placed at opposite sides around the brim of the quartz baseplate. These four probes not only acted as accurate timing fiducials for the arrival of the shock wave at the back surface of the 304L sample, but also provided cross-timing information. Because quartz remains elastic in the stress regime of this study, only a single wave propagates into the stainless sample. It is important to note that this technique is limited to stress states below which quartz stays elastic; for *z*-cut quartz, this is ~8.5 GPa. Timing information from these four 'brim' probes is used to calculate the time of shock wave entrance into the center of the stainless sample. Two additional 2-fiber probes illuminated the center of the sample through the sapphire window to provide information regarding the timing of the elastic and plastic waves exiting the sample, one in the center, and one offset by 2.5 mm. The difference between the entrance and exit times of the shock wave provides the transit time for the shock to travel though the sample. This information, coupled with the thickness of the samples, provides measurements for the shock velocity with an accuracy of about one percent (1%).

3   RESULTS AND DISCUSSION

The measured shock velocity for the wrought and AM 304L SS samples is shown in Table 3. Due to anisotropy in the microstructure of the AM 304L SS, measurements were performed in samples that were orientated along the various directions w.r.t the build direction as shown in Figure 1.

Table 3. Impactor velocity (U_D), particle velocity (u_p), and shock velocity (U_S) measurements from the quartz top-hat experiments.

Experiment number	Material	Velocity (km/s)		
		Impactor, U_D	Particle, u_p	Shock, U_s
172	Wrought	0.399 ±0.003	0.128 ±0.002	4.77 ±0.05
173	AM-XY1	0.400 ±0.003	0.131 ±0.002	4.68 ±0.05
174	AM-Z1a	0.400 ±0.003	0.132 ±0.002	4.64 ±0.05
176	AM-XY2	0.400 ±0.003	0.132 ±0.002	4.66 ±0.05
177	AM-X1	0.395 ±0.003	0.130 ±0.002	4.59 ±0.05

Figure 3 shows velocity-time plots extracted from all experiments, and from experiments 172 (wrought 304L) and 177 (AM 304L, X1). The velocimetry curves are plotted such that the elastic waves are aligned in time. This figure shows that the plastic wave arrives earlier in the wrought sample because of the higher shock velocity, U_s
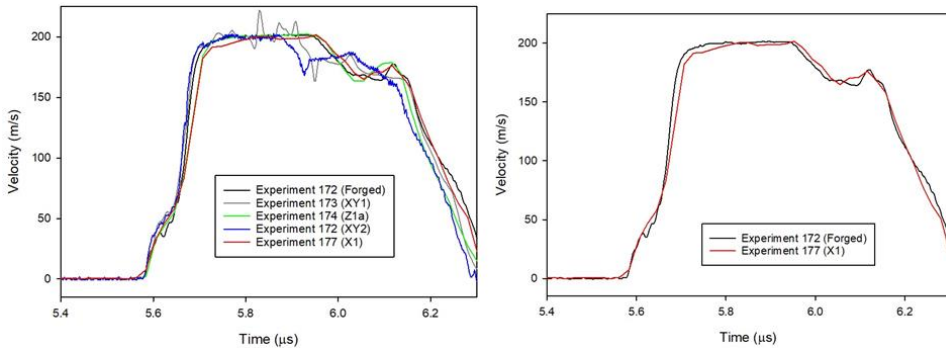
Figure 3: Velocity-time plot from (left) experiments 172 (wrought 304L) and 173 (AM XY1), 174 (Z1a), 172 (XY2) and 177 (AM X1) with aligned elastic waves. (right) Velocity-time plot for experiments 172 (wrought) and 177 (AM X1) highlighting differences between wrought and AM 304L SS.

The particle and shock velocities presented in Table 3 are plotted along with the extrapolated shock Hugoniot for 304L SS from work performed at Los Alamos Scientific Laboratory (LASL) [15] and shown in Figure 4. The shock velocities in this work were calculated by using the average of the exit times from the quartz baseplate collected by the four PDV probes and subtracting that time from the plastic wave arrivals at the back of the target, then dividing it into the thickness of the target, as shown by

$$U_S = \frac{x_{\text{target}}}{t_{\text{steel}} - t_{\text{quartz}}}, \qquad (2)$$

where U_S is the shock velocity, x_{target} is the thickness of the target, and t_{steel} and t_{quartz} are the times the plastic wave exits the steel target and quartz baseplate, respectively. Particle velocity was calculated using the measured shock speed in the target and the known Hugoniot for quartz to impedance match between the quartz and the steel target [16]. Uncertainties associated with the calculations are estimated to be between 1.0% and 1.5%.
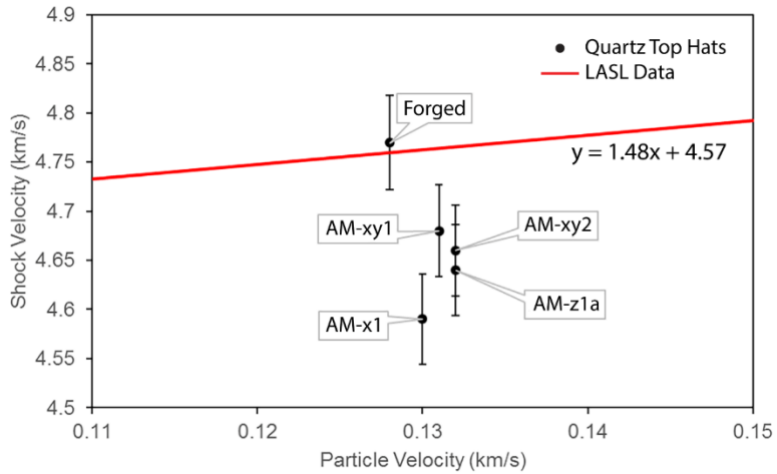
Figure 4: Shock velocity as a function of particle velocity also known as the Hugoniot equation of state from quartz top-hat experiments with 1% error bars plotted over the extrapolated shock Hugoniot for 304L SS from the LASL Shock Hugoniot Data [15].

4   DISCUSSION

The differences in the EOS measured in this work could be attributed to a few reasons: 1) porosity in the AM material, 2) grain morphology and 3) dislocation density. Each of these reasons was systematically investigated to determine if this was the cause of the varying EOS.   In fact, the effect of even relatively small amounts of porosity on shock velocity is known to cause it to be slower than for full density samples. This is due to the mechanics of the dynamic void collapse process, and the resulting increase in thermal energy. In fact, it has been shown by previous research on porous materials that even a 1% drop in density for certain metals can lead to drop in shock velocity of more than 2% [17, 18]. This highlights the importance of initial density measurements. As observed in Table 1, the initial densities for samples used in these experiments show no clear trends that are aligned with the differences in measured shock velocities. Based on this data, we conclude that porosity cannot be clearly identified as the factor leading to the measured differences in the shock velocity.

Another hypothesis is that the grain size and morphology differences between the AM and the forged samples could be causing a 3% decrease in the shock velocity. However, previous work by Yang et al. [12] on aluminum to investigate the effect of grain size on measured shock velocities has clearly shown that grain size does not alter the shock velocity. Work by Choi et al. [19] on Nickel also shows no measurable differences in the equation of state of single crystal Nickle measured through molecular dynamics and the experimental equation of state from polycrystalline Nickle. However, these studies were performed at particle velocities where the plastic wave was over-driven and as such the material microstructure did not matter. In contrast, the regime of the current experiments is much lower where the measurements exhibit two-wave structure. Systematic experiments where only the grain size is varied in a metal, in the elastic-plastic regime (<600 m/s), would be required to conclusively prove this hypothesis.

Another contributing factor to the observed differences in shock velocity could be the varying dislocation densities in the AM vs. wrought material. Systematic neutron diffraction experiments by Pokharel et al. [20] measured an increased dislocation density in the same AM 304L SS used in this study. This change in dislocation density could alter the equation of state in a measurable manner as shown by

Hahn et al. [21] in their molecular dynamics simulations. An increase in dislocation density would also lead to an increase in the Hugoniot Elastic Limit of the AM 304L SS. This is corroborated by Figure 3. In addition, a change in the Hugoniot elastic limit may have the effect of changing the shock velocity. However, additional experiments are required to test this hypothesis.

5   CONCLUSIONS

Equation of state was measured for additively manufactured 304L and compared with its wrought counterpart. The results showed that in the velocity regime where microstructure matters, the shock velocity for the AM 304L was 3% lower than that of the wrought material. Initially, this difference was attribute to porosity and hence perhaps a lower density in the AM material. However, density measured using different techniques like immersion and pycnometer did not show a systematic variation in the porosity to justify the difference measured in the EOS. Due to the fact that other parameters like grain size, morphology and dislocation density were changed in the AM 304, it was difficult to determine with high confidence the reason for the lower shock velocity. However, it was hypothesized that higher dislocation density can affect the HEL, which in turn reduced the shock velocity. Additional work is in progress to investigate the reasons behind the current observations.

6   ACKNOWLEDGEMENTS

7   REFERENCES

1. Lewandowski, J.J. and M. Seifi, *Metal Additive Manufacturing: A Review of Mechanical Properties.* Annual Review of Materials Research, Vol 46, 2016. **46**: p. 151-186.

2. Gorsse, S., et al., *Additive manufacturing of metals: a brief review of the characteristic microstructures and properties of steels, Ti-6Al-4V and high-entropy alloys.* Science and Technology of Advanced Materials, 2017. **18**(1): p. 584-610.

3. Bajaj, P., et al., *Steels in additive manufacturing: A review of their microstructure and properties.* Materials Science and Engineering a-Structural Materials Properties Microstructure and Processing, 2020. **772**.

4. Laurencon, M., et al., *Effects of additive manufacturing on the dynamic response of AlSi10Mg to laser shock loading.* Materials Science and Engineering a-Structural Materials Properties Microstructure and Processing, 2019. **748**: p. 407-417.

5. Jones, D.R., et al., *Spall fracture in additive manufactured Ti-6Al-4V.* Journal of Applied Physics, 2016. **120**(13).

6. Jones, D.R., et al., *Effect of peak stress and tensile strain-rate on spall in tantalum.* Journal of Applied Physics, 2018. **124**(8): p. 03021.

7. Gray, G.T., et al., *Structure/property (constitutive and spallation response) of additively manufactured 316L stainless steel.* Acta Materialia, 2017. **138**: p. 140-149.

8. Wise, J.L., et al., *Comparative Shock Response of Additively Manufactured Versus Conventionally Wrought 304L Stainless Steel.* Shock Compression of Condensed Matter - 2015, 2017. **1793**.

9. Thomas, S.A., et al., *Wave speeds in single-crystal and polycrystalline copper.* International Journal of Impact Engineering, 2020. **139**.

10. Fadida, R., D. Rittel, and A. Shirizly, *Dynamic Mechanical Behavior of Additively Manufactured Ti6Al4V With Controlled Voids.* Journal of Applied Mechanics-Transactions of the Asme, 2015. **82**(4).

11. Jones, D.R., et al., *Spall fracture in additive manufactured tantalum.* Journal of Applied Physics, 2018. **124**(22).

12. Yang, X., et al., *Molecular dynamics modeling of the Hugoniot states of aluminum.* Aip Advances, 2018. **8**(10).

13. Chau, R., et al., *Shock Hugoniot of single crystal copper.* Journal of Applied Physics, 2010. **107**(2).

14. Strand, O.T. and T.L. Whitworth, *Using the heterodyne method to measure velocities on shock physics experiments*, in *Shock Compression of Condensed Matter - 2007*, M. Elert, et al., Editors. 2007, American Institute of Physics: Melville, NY. p. 1143-1146.

15. Marsh, S.P., *LASL Shock Hugoniot Data*. 1980, Berkeley, California: University of California Press.

16. Forbes, J.W., *Shock Wave Compression of Condensed Matter: A Primer*. 2012, Berlin: Springer.

17. McQueen, R.G., et al., *The equation of state of solids from shock wave studies*, in *High Velocity Impact Phenomena*, R. Kinslow, Editor. 1970, Academic Press: New York. p. 293-417, 515-568.

18. Trunin, R.F., et al., *Shock compression of highly porous samples of copper, iron, nickel and their equation of state*, in *Shock Compression of Condensed Matter - 1997*, S.C. Schmidt, D.P. Dandekar, and J.W. Forbes, Editors. 1998, American Institute of Physics: Woodbury, New York. p. 83-86.

19. Choi, J., et al., *Molecular dynamics study of Hugoniot relation in shocked nickel single crystal.* Journal of Mechanical Science and Technology, 2018. **32**(7): p. 3273-3281.

20. Pokharel, R., et al., *An analysis of phase stresses in additively manufactured 304L stainless steel using neutron diffraction measurements and crystal plasticity finite element simulations.* International Journal of Plasticity, 2019. **121**: p. 201-217.

21. Hahn, E.N. and S.J. Fensin, *Influence of defects on the shock Hugoniot of tantalum.* Journal of Applied Physics, 2019. **125**(21).

04

The anisotropic behavior of Laser powder bed fusion AlSi10Mg under the various dynamic loading

Ben Amir[1]| Shmuel Samuha[2]| and Oren Sadot[1]

[1]Department of Mechanical Engineering, Ben-Gurion University of the Negev, Beer-Sheva 84105, Israel
[2]Department of Materials Engineering, NRCN, PO Box 9001, Beer-Sheva 84190, Israel

Correspondence

Ben Amir, Department of Mechanical Engineering, Ben-Gurion University of the Negev, Beer-Sheva 84105 Email: benu@post.bgu.ac.il

This study focus on the dynamic properties of additive manufacturing (AM) laser powder bed fusion (LPBF) of AlSi10Mg. Using various experimental systems such as split Hopkinson pressure bar (SHPB), newly designed dynamic punch, and highly accurate split Hopkinson tension bar (SHTB), we characterize the LPBF AlSi10Mg alloy under pure compression, shear, and tension loading. Using an SLM solutions machine, we manufacture two types of samples, parallel and perpendicular to the building direction, designated as Z and XY specimens, respectively. Surprisingly, Z samples exhibit higher dynamic stress until failure than that measured in the XY specimens. This variance at maximum dynamic stress in all mentioned dynamic loading is significant and ranges from 12% to 16%. On the other hand, the elongation until failure is higher at XY specimens, and the difference between the orientation can get up to 25%. The anisotropic dynamic property is related to the fish scale morphology and the crystallographic orientation of the LPBF AlSi10Mg.

1 INTRODUCTION

The worldwide volume of additive manufacturing (AM) was over 2 billion USD in 2017 and increasing in the past few years [1]. Specifically, the laser powder bed fusion (LPBF) of AlSi10Mg is being excessively utilized by the aerospace and automotive sectors. Therefore, the need to characterize the alloy under dynamic loading has increased. Researchers study the quasi-static properties of this alloy in various manufacturing conditions [2]. It is established convincingly that the yield point at tensile loading is virtually independent of manufacturing orientation[3]. No difference was found under compression or shear loading at quasi-static conditions regarding manufacturing orientation[4], [5]. The results present in this study suggest otherwise, where the LPBF of AlSi10Mg is loaded dynamically.

2   METHODS

The cylinder samples, 600 mm in height and 12 mm in diameter, were manufactured using the M280 model of SLM solutions by the recommended default parameters. The cylinder samples were manufactured in two different orientations, horizontally and vertically, to examine the anisotropic properties concerning the building direction. In the SLM M280 model, the center of the sample and the circumference does not manufacture by the same set of process parameters. Since this study focuses on the main bulk properties, the specimen's circumference was machined to extract the core of the specimen and make a suitable sample for each system.

The compressive dynamic loading was performed by the SHPB system located at the dynamic mechanical properties Laboratory at the Ben Gurion University of the Negev. The sample was extracted into circular discs of 7 mm diameter and 3.5 mm height. More details on the sample preparation and the SHPB system can be found in [6]–[8].

The dynamic shear tests were performed with the same SHPB system equipped with a dynamic punch assembly that assured zero triaxiality factor (pure shear) at the LPBF AlSi10Mg samples. 8.5mm in diameter and 2mm thick discs samples were machined from each differently oriented cylinder to fit into the punch assembly. The dynamic shear and the punch assembly are elaborately explained in ref. [9].

The dynamic tension loading characterization was possible due to the highly accurate split Hopkinson tension bar, built recently in the dynamic mechanical properties Laboratory. Figure 1(a) illustrates the SHTB Built vertically with the necessary adjustment to prevent undesired friction and oscillations. The result processing is supported by a high-speed camera together with strain gauges. The sample shown in Figure 1(b) is attached to the bars by a carefully prepared thread. More details on the system and the validation of its results can be found in [10].
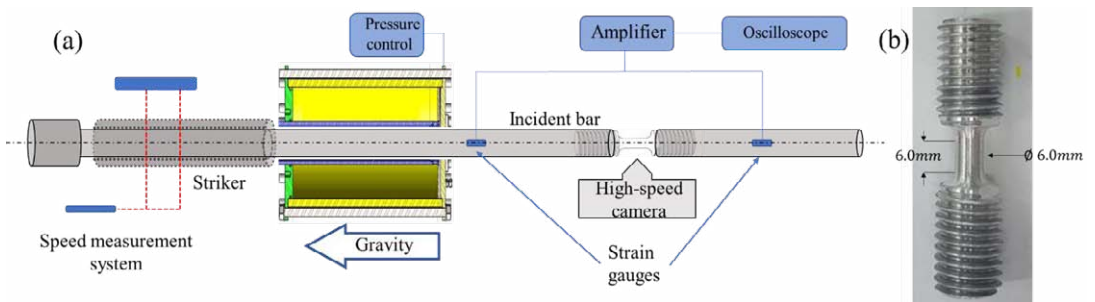
Figure 1: schematic of the split Hopkins on tension bar and tension sample

3   RESULTS AND DISCUSSION

The relative density was measured prior to the dynamic tests using Archimede's method; there was a negligible difference between the two orientations, 99.4% ± 0.05% and 99.5% ± 0.06% for Z and XY specimens, respectively. Figure 2 shows the dynamic results for XY (blue) and Z (red dash) specimens, respectively. Each curve represents the average of 3 experiments, and a representative standard deviation (STD) is placed at the point of maximum dynamic stress achieved. All the experiments were conducted at room temperature and with a strain rate of approximately 4000s^{-1}. An evaluation of the dynamic compressive results in Figure 2(a) revealed a 16% increase in dynamic stress at the Z specimen

compared to the XY specimens; the nominal values are 606±8 and 522±10 MPa for Z and XY, respectively. However, the elongation, which is the ε until the point of trend transitioning at the plastic evolution, is higher at the XY than at the Z specimen, ε≈0.9 and ε≈0.75, respectively. The dynamic shear characteristic is presented in Figure 2 (b) as the shear stress (τ) - normalized displacement (u). All the experiments achieved a normalized displacement rate ($\dot{u}$) of 4000s^{-1} before complete failure at puer shear mode. The dynamic shear strength of Z specimens is 274±4 MPa and u≈ 0.11, and for XY specimens τ= 240 ± 3.3 MPa u≈ 0.14, there is a 12.5% difference between the orientations. Figure 2 (c) presents the dynamic tension results for Z and XY specimens and their STD. The dynamic tension characteristics indicate higher dynamic strength for Z specimens and higher elongation for XY specimens. σ=608± 4 MPa and ε≈0.1 for Z and σ=562± 5 MPa and ε≈0.13 for XY specimens, concluding with a 12% higher dynamic strength and 20% elongation difference. The anisotropic dynamic behavior is characterized by three load conditions: compressive, shear, and tension. The trend in the obtained results is clear: Z specimens reach a higher dynamic strength, and XY specimen has more compliance to deformation.
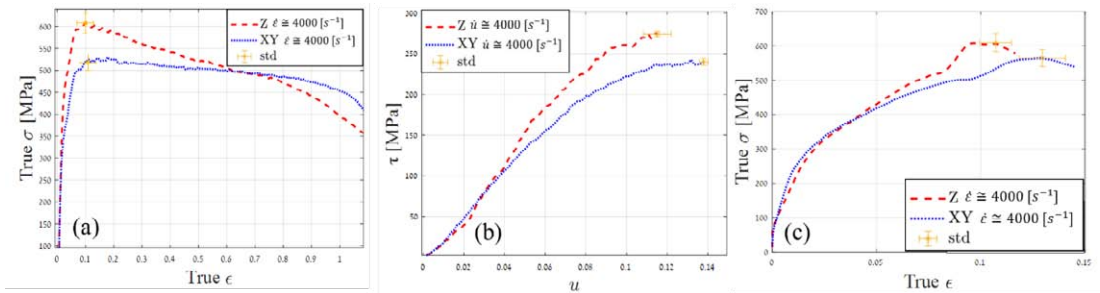
Figure 2: Dynamic characterization under (a) compressive, (b) shear and (c) tension loading.

A scanning electron microscope (SEM) combined with electron backscattered diffraction (EBSD) was used for microstructural and microtexture characterization. Figure 3 (a) presents a color-coded inverse pole figure (IPF) map with a legend triangle indicating the crystallographic orientation. In this map, the crystallographic orientation of <001> is parallel to the building direction (BD). In the center of the melt-pool, most of the grains are elongated, and the <001> orientation is parallel to the building direction. At the melt pools boundaries (MPBs), the grains are refined, equiaxed, and whit of random orientations. The layer-by-layer manufacturing process creates an overlapping of the MPBs; the overlapping between two nearby tracks along the XY plane usually are called track–track MPBs, and in between two successive layers are called layer-layer MPBs, as described in Figure 3 (b).
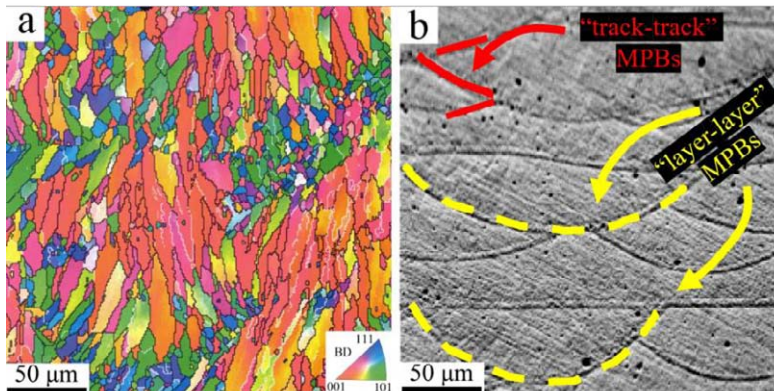
Figure 3 : (a) IPF maps of the melt pool. (b) SEM image together with the description of layer-layer in track-track MPBs

Following fracture surface analysis, the micro-crack formation follows the MPBs. It is possible to assume that crack passes at grain boundaries and nat intergrain. It can be seen in Figure 4 that under all the dynamic loading conditions, the crack pass is along the layer-layer at XY specimens and in between the tracks for the Z specimens. Since the crack path at the track-track MPBs needs more deflections to propagate, it can be assumed that higher energy is required to deform the specimens. Those results agree with the higher dynamic strength depicted in the Z specimens.
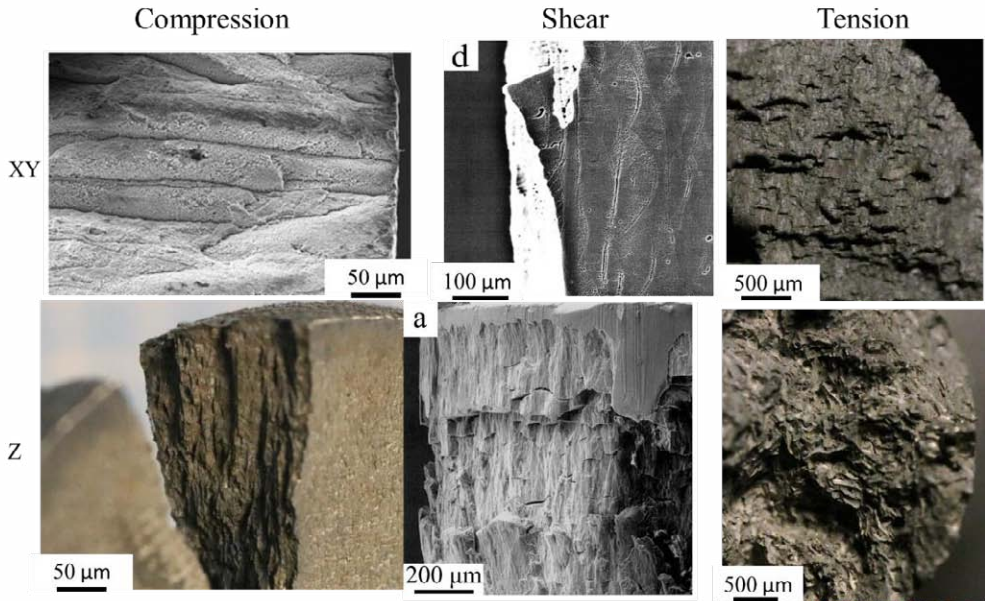
Figure 4 : Fractography images of the samples after impact loading

4   CONCLUSIONS

The LPBF AlSi10Mg alloy is characterized by anisotropic dynamic behavior under three loading conditions, compression, shear, and tension. Z-oriented specimens reached dynamic strength higher by 12-16% than XY-oriented specimens. However, the elongation in the XY samples is higher than in the Z specimens. The crack propagation is by layer-layer MPBs at XY and following track-track MPBs at Z specimens. The inherent anisotropic microstructure is responsible for the difference in dynamic behavior in samples manufactured in different orientations.

5   REFERENCES

[1]   AM Power, "Quality in Additive Manufacturing," *AM Power Insights*, vol. 4, 2018.

[2]   T. DebRoy *et al.*, "Additive manufacturing of metallic components – Process, structure and properties," *Prog. Mater. Sci.*, vol. 92, no. 6, pp. 112–224, Mar. 2018, doi: 10.1016/j.pmatsci.2017.10.001.

[3]   I. Rosenthal, A. Stern, and N. Frage, "Strain rate sensitivity and fracture mechanism of AlSi10Mg parts produced by Selective Laser Melting," *Materials Science and Engineering A,*

vol. 682. pp. 509–517, 2017, doi: 10.1016/j.msea.2016.11.070.

[4]   L. Hitzler, N. Schoch, B. Heine, M. Merkel, W. Hall, and A. Öchsner, "Compressive behaviour of additively manufactured AlSi10Mg," *Materwiss. Werksttech.*, vol. 49, no. 5, pp. 683–688, May 2018, doi: 10.1002/mawe.201700239.

[5]   L. Denti, "Additive manufactured A357.0 samples using the laser powder bed fusion technique: Shear and tensile performance," *Metals (Basel).*, vol. 8, no. 9, 2018, doi: 10.3390/met8090670.

[6]   B. Nurel, M. Nahmany, N. Frage, A. Stern, and O. Sadot, "Split Hopkinson pressure bar tests for investigating dynamic properties of additively manufactured AlSi10Mg alloy by selective laser melting," *Addit. Manuf.*, vol. 22, no. April, pp. 823–833, Aug. 2018, doi: 10.1016/j.addma.2018.06.001.

[7]   B. Amir, S. Samuha, and O. Sadot, "Influence of Selective Laser Melting Machine Source on the Dynamic Properties of AlSi10Mg Alloy," *Materials (Basel).*, vol. 12, no. 7, p. 1143, Apr. 2019, doi: 10.3390/ma12071143.

[8]   B. Amir, E. Grinberg, Y. Gale, O. Sadot, and S. Samuha, "Influences of platform heating and post-processing stress relief treatment on the mechanical properties and microstructure of selective-laser-melted AlSi10Mg alloys," *Mater. Sci. Eng. A*, vol. 822, no. January, p. 141612, 2021, doi: 10.1016/j.msea.2021.141612.

[9]   B. Amir, E. Kochavi, S. Gruntman, Y. Gale, S. Samuha, and O. Sadot, "Experimental investigation on shear strength of laser powder bed fusion AlSi10Mg under quasi-static and dynamic loads," *Additive Manufacturing*, vol. 46. 2021, doi: 10.1016/j.addma.2021.102150.

[10]   B. Amir, A. Lomnitz, E. Kochavi, S. Gruntman, and O. Sadot, "An Experimental Study of the Thread's Size Influence on Split-Hopkinson Tensile Bars Capabilities." To be published.

05

Dynamic behavior of a shock-loaded Ni-based superalloy manufactured by Laser Metal Deposition

E. Barraud[1*] | T. de Rességuier[1] | S. Hemery[1] | J. Cormier[1]

[1] Institut Pprime, CNRS-ENSMA-Univ. Poitiers, 1 ave. Clément Ader, 86961 Futuroscope, France

Correspondence
*Etienne Barraud
Email:
etienne.barraud@ensma.fr

Although Nickel-based superalloys are widely used in the industry, their response to shock loading is still rarely investigated. Here, shock experiments are used to study the high strain rate behavior of additively manufactured (AM) Waspaloy. Loading direction is either parallel or normal to the build direction. Time-resolved velocity measurements provide the Hugoniot elastic limit and the spall strength. Post-recovery analyses give detailed insight into dynamic failure, with a combination of transgranular ductile fracture and intergranular cracks dependent on sample orientation. Finally, the porosity inherited from AM is shown to inhibit spall fracture locally.

1   INTRODUCTION

The remarkable combination of excellent mechanical properties in a corrosive environment and at very high temperatures allows a wide use of nickel-based superalloys in many applications, such as aeronautical engines, gas turbines or turbochargers in motorsports. The important and rapid development of additive manufacturing (AM) processes is appealing to industry, including the aforementioned sectors. The literature on the challenge of AM is extensive [1], in particular for aerospace and more specifically regarding superalloys [2], [3]. However, few papers can be found yet on the effects of AM on the high strain rate behavior of materials thus produced [4]–[6].

Our study focuses on Waspaloy, a Ni-based superalloy (nickel with 19.3 wt.% chromium, 12.9 wt.% cobalt, 4.2 wt.% molybdenum, 2.8 wt.% titanium, 1.5 wt.% aluminium) rich in refractory elements. Historically developed by Pratt & Whitney on air-cooled radial piston engines, it is still used in the latest generations of jet engines. In this paper, Waspaloy was produced by an AM process, namely Laser Metal Deposition (LMD) [7], where the material is projected in powder and melted with a laser: at each pass a new bead is welded on top of the previous one, the building direction being referred as Z. Our objective is to explore the potential effects of this LMD process on the dynamic response to shock loading, generated by high-velocity impacts or laser irradiation. Free surface velocity measurements provide the Hugoniot yield strength and spall strength for different directions of shock application vs. building direction. In addition, post-recovery analyses involving a variety of complementary techniques give insights into the processes governing dynamic fracture and their dependence on the initial microstructure.

2   EXPERIMENTAL TECHNIQUES

The initial microstructure was characterized with a Scanning Electron Microscope (SEM) operated at 20 kV in the Back Scattered Electron (BSE) mode. It shows an anisotropic texture and a large population of vertical grains, parallel to Z, with a length of about 250 to 450 µm (Fig. 1). This columnar texture results from the vertical thermal gradient generated by LMD [8]. The presence of spherical porosities following a macroscopically random distribution can be observed, with about 2/3 of small pores, on the order of 5 µm, and 1/3 of larger pores about 50 µm. Rods were extracted along the Z manufacturing direction and in the normal direction, called XY. Thin targets were cut from these bars and then polished with 500 grit silicon carbide paper. The average thickness of the specimens is 388 µm within a of 16 µm scatter (close to 4 %). Material density ρ_0 was determined to be 8209 kg/m^3 by mass and volume measurements, fully consistent with the value of 8200 kg/m^3 reported by metallurgists (e.g. Haynes or ATI). Longitudinal (C_l) and transverse (C_t) elastic wave propagation velocities could not be measured in our samples. Instead, we used data from the literature [9] : C_l = 6010 m/s and C_l = 3216 m/s. The bulk sound velocity $C_b = \sqrt{C_l^2 - \frac{4}{3} C_t^2}$ is then 4725 m/s.
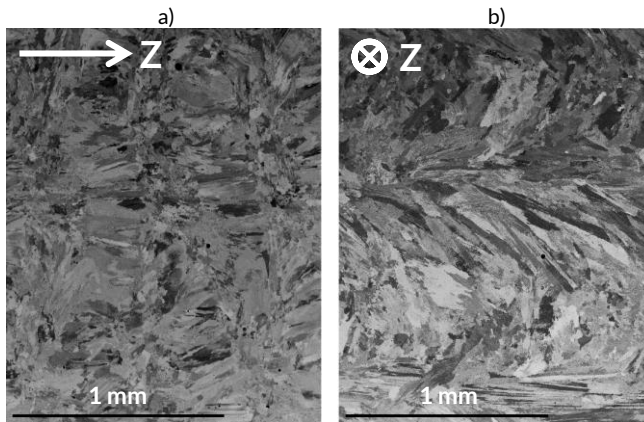
FIGURE 1 Backscatter electron microscopy of the AM Waspaloy microstructure, showing a majority of long grains roughly parallel to the building direction Z in the successive melted layers and epitaxial grains between them (a), and elongated grains of periodic orientations in the laser scan plane XY (b).

Shock loading was induced either by the impact of thin Al foils at Institut Pprime or by direct laser irradiation in vacuum at the Laboratoire pour l'Utilisation des Lasers Intenses (LULI, Ecole Polytechnique). In both facilities, time-resolved velocity measurements are performed with a Velocity Interferometer System for Any Reflector (VISAR) [10] system in a push-pull configuration. The free surface of the target, opposite the impacted surface, is illuminated with a continuous laser of wavelength 532 nm. The reflected light is sent to the VISAR where interference patterns due to the Doppler effect are recorded by photomultipliers. The time resolution is about 1 ns and the fringe factor is set to 843 m/s to ensure that no fringe could be lost upon velocity jumps. A polycarbonate shield is placed a few cm behind the free surface to protect the VISAR lens.

In the impact experiments, a laser pulse of 1053 nm wavelength, about 20 J energy and about 35 ns half-height duration is focused on a 3.5 mm diameter spot on the surface of a 150 µm thick aluminum foil. The resulting intensity is about 5 GW/cm². A thin (µm-order) Al layer is ablated into a plasma, whose expansion toward the laser source propels the foil in the opposite direction. To increase the amplitude and duration of the compression induced by the plasma, a drop of water (a few mm thick, transparent to the laser light) is deposited on the surface of the flyer before the shot. It confines the expansion of the plasma, so that the pressure load applied on this surface is higher and

longer than during a direct laser-matter interaction in vacuum [11]. After flying across a 250 μm gap, the Al foil impacts the alloy target. The diameter of the laser spot is much larger than the thickness of the complete assembly (foil + gap + target), so that one can expect one-dimensional shock loading upon planar impact (assuming a uniform energy distribution over the irradiated spot). According to preliminary shots with VISAR measurements on the Al flyer alone (without target), the average impact velocity is 680 m/s. More details on the setup can be found in [12]. The shock pressure at impact is evaluated as about 8 GPa, from a classical analysis of impedance mismatch based on the Hugoniot data of Al and Ni [13], which is the main component of Waspaloy.

In complement, direct laser shocks were performed using a Nd: YAG laser pulse of 1.053 μm-wavelength, about 200 J-maximum energy and 15.7 ns-duration focused on a 1 mm-diameter spot. Secondary vacuum prevents air ionization at high intensity. The laser energy is varied between 80, 150 and 200 J via absorbing filters in the optical path. For each shot, the pulse duration and energy are measured. The resulting intensity is between 0.5 and 1.5 TW/cm². Subsequent loading pressures are inferred from peak free surface velocities recorded by the VISAR, using the same hydrodynamic analysis as above. They are about 6 GPa (80 J), 11 GPa (150 J) and 13 GPa (200 J).

3   RESULTS AND DISCUSSION

A record of the free surface velocity in a target impacted by an Al foil is shown in Figure 3a. The first wave to emerge is the elastic precursor. It propagates at the speed of sound C_l and produces an elastic compression up to the Hugoniot elastic limit (HEL), associated with a first jump to a free surface velocity of 100 m/s in the record, equal to twice the particle velocity U_{HEL}, which provides the dynamic yield stress $\sigma_{HEL} = \rho_0\, C_l\, U_{HEL}$ (Eq. 1). A plastic compression wave follows, accelerating the free surface to a maximum velocity of 405 m/s, fully consistent with the hydrodynamic analysis mentioned earlier. Next, the arrival of the unloading wave on the free surface leads to a deceleration called velocity pullback. The interaction of this release wave with the rarefaction wave resulting from the reflection of the shock front creates local tensile stresses. If they exceed the dynamic tensile strength (or spall strength) of the material, they cause spall damage [15]. The stress relaxation created by crack opening interrupts the deceleration at about 770 ns. The end of the velocity signal shows oscillations related to wave reverberation within the spalled layer: considering the bulk sound velocity C_b of about 4700 m/s, the ~45 ns period of these oscillations indicates a spall thickness of about 100 μm. Fig. 3b shows similar records in the laser shock-loaded samples, which exhibit the same features. The 25 ns period of the final oscillations indicate a thinner spalled layer of about 60 μm. In the lower pressure shot (80 J), the surface deceleration is not interrupted by a spall signal, which shows that tensile stresses remained below the spall strength in that case. Therefore, successive reloading waves reverberate throughout the whole thickness of the intact sample, with a period of about 150 ns matching their expected transit time. Accounting for wave dynamics in an elastic plastic material [14], the spall strength can be evaluated as $\sigma_{sp} = \rho_0\, C_b\, \frac{1}{1+C_b/C_l}\,\Delta U_{FS}$ (Eq. 2). An estimate of the strain rate is given by $\dot{\varepsilon} = \frac{1}{2C_b}\frac{\Delta U_{FS}}{\Delta t}$ (Eq. 3), where Δt is the duration of the free surface deceleration in the record (see Fig. 2a). The measured values of Hugoniot yield strength σ_{HEL} (Eq. 1) and spall strength σ_{sp} (Eq. 2) are shown in Table 1. For both plate impact and direct irradiation experiments, the strain rate deduced from Eq. 3 is about 10^6 s^{-1}. The error bars, corresponding to the standard deviation around the mean value, reflect the scatter between the shots. This important scatter will be discussed further. Within these error bars, no significant difference can be stated between both orientations. The very high spall strength of AM Waspaloy, about 8 GPa, can be compared to that of high strength metals such as Ti alloys (between 3.7 and 5 GPa) or Ta (about 4.5 GPa) [14].
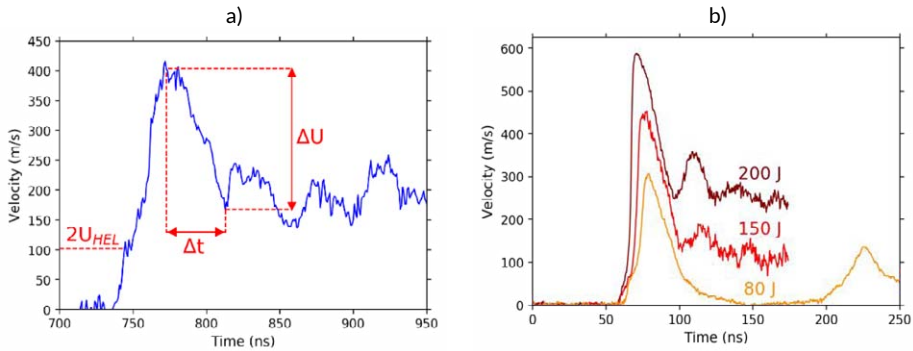
FIGURE 2 Typical velocity profiles recorded at the free surface of Waspaloy samples (a) impacted by a laser-launched Al flyer and (b) shocked by direct laser irradiation.

TABLE 1 Measured values of the yield strength (Hugoniot elastic limit) and the spall strength under shock loading along or normal to the building direction Z.

	σ_{HEL} (MPa)	σ_{SP} (MPa)
Waspaloy Z	2137 ± 446	7865 ± 1165
Waspaloy XY	2144 ± 285	7768 ± 1150

Both shock loading techniques allow for easy and systematic recovery of the samples. Several stages of damage were observed, depending on shock pressure, from incipient spall (nucleation of a few voids) to full separation of the spalled layer. Some samples were examined by X-ray micro-tomography (Fig. 3), with a spatial resolution of 5 µm/voxel. They show extensive damage near a spall plane roughly parallel to the free surface, confirming the correct planarity of impact loading. The 100 µm thickness of the spalled layer is consistent with that deduced from oscillations in the VISAR record. The fracture pattern differs from one orientation to another. In the Z-loaded sample (Fig. 3a and 3b), the macroscopic crack is fairly straight. Higher magnification views show that it results from ductile fracture, i.e. nucleation, growth and coalescence of spherical voids leading to numerous dimples. Electron backscatter diffraction (EBSD) maps suggest that void nucleation and crack propagation are predominantly transgranular for this loading direction (Fig. 4a). This is consistent with the majority of long grains normal to the direction of maximum tension in this case (Fig. 1a). In the XY-samples, where the loading direction was normal to the Z axis, some straight cracks, about 100 µm-long, are found at about 45° to the spall plane (Fig. 3c and 3d). They are very likely related to the initial microstructure observed in this XY plane (Fig. 1b). The corresponding EBSD map in Fig. 4b shows crack nucleation and growth, both intragranular (upper part) and intergranular (lower part). It suggests that grain boundaries provide preferred sites for damage initiation and propagation, which accounts for the cracks at 45° extending around the plane of maximum tension. Finally, this dependence of damage on the initial, highly heterogeneous microstructure probably explains the large scatter on the spall strength measurements (Table 1), because for both orientations, the probability that the spall plane (where release waves interact) coincides with grain boundaries is largely random.

Post-recovery observations also shed light on the role of the initial porosity on the dynamic behavior. In Fig. 3, the green arrows point to pre-existing pores of about 25 to 50 µm diameters, which have inhibited spall fracture in their vicinity. Indeed, in the left sections (Fig. 3a and 3c), cracks are seen along the spall plane but not near these pores, In the right sections (Fig. 3b and 3d), further deep inside the loaded zone (see schematic disks in the figure), away from these pores, cracks form a wide,

roughly continuous spall plane. Such inhibition of spall fracture is likely due to local stress relaxation around the pores (free surfaces), which breaks up both the incident compressive pulse and the subsequent tensile wave. Fig. 5 is a detail around a pore in a shock-recovered sample, about 75 µm beneath the free surface. Housed at a grain boundary, this pore, inherited from the LMD process, was initially spherical with a diameter of about 50 µm. The shock propagated from left to right, inducing strong deformation of the left side (set into motion by the compression front) while the right surface remained hemispherical. Strong disorientations and severe plastic strains are observed beneath the left surface of the pore, due to early tension upon wave interactions near this surface. Near very large pores, such early tension may even produce additional, local spall fracture. Such case is evidenced in Fig. 3d (red arrow), where cracks are seen beneath the left surface of a large pore.
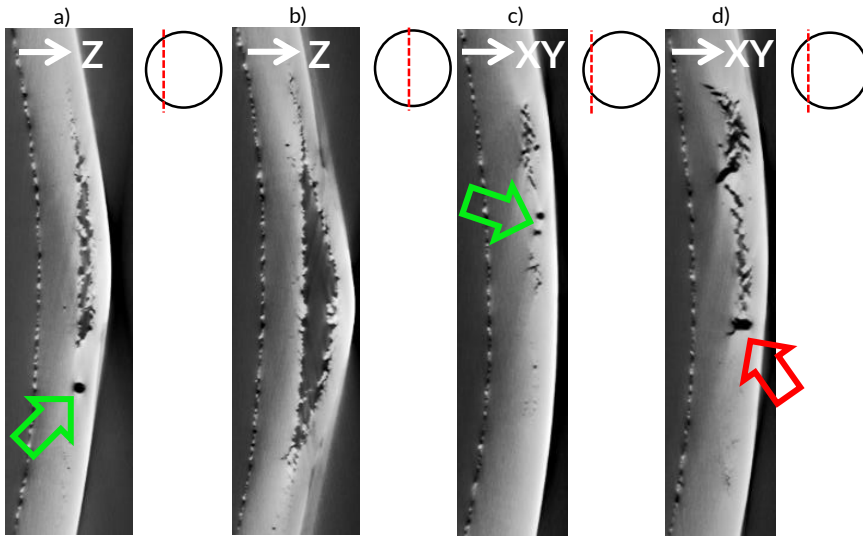
FIGURE 3 Sections extracted from 3D reconstructions by X-ray microtomography of Waspaloy samples recovered after impact. Sample thickness is about 400 µm. The fracture surface of the Z-target (a and b) shows ductile dimples along a well-defined spall plane while the XY-target (c and d) illustrates the presence of straight facets at 45°. In both orientation, the first sections (a and c) show that pre-existing pores (arrows) prevent fracture in their vicinity and the second ones (b and d) show extensive spall damage beyond these pores.
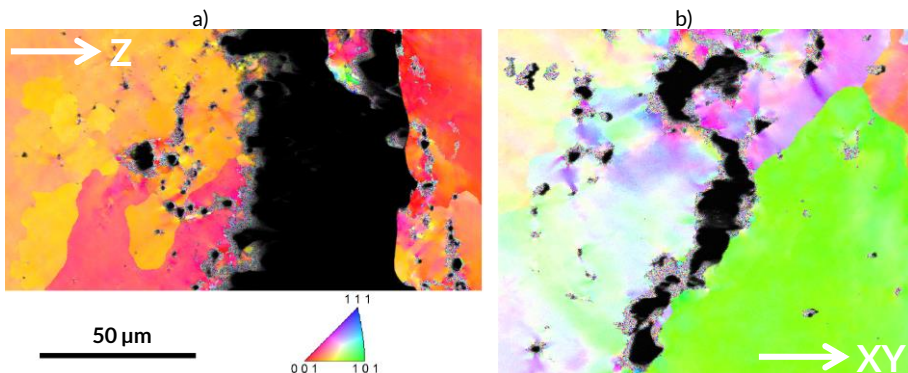
FIGURE 4 Inverse pole figure map showing the crystallographic orientations of shock recovered Z-oriented (a) and XY-oriented (b) Waspaloy target. Orientations are given along the loading direction.
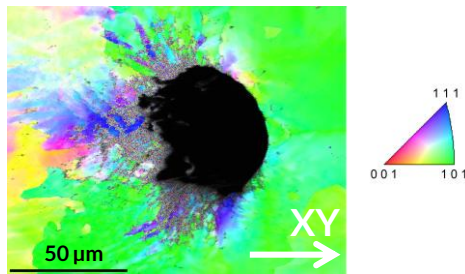
FIGURE 5 IPF map showing the crystallographic orientations in the vicinity of a pore in the shocked zone on an XY oriented target recovered by impact. Orientations are given along the loading direction.

4   CONCLUSION

High power laser pulses were used to perform shock experiment, either by Al-flyer impact or direct laser ablation, on AM targets of Waspaloy Ni-based superalloy. Shock compression ranging from 6 to 13 GPa was applied either along or normally to the Z-build direction. The Hugoniot elastic limit and spall strength were determined at very high strain rates on the order of 10^6 s^{-1}: Both values seem almost insensitive to orientation, within the experimental uncertainties. Post-recovery X-ray tomography and EBSD revealed a dynamic fracture process mainly governed by ductile damage, which is observed, unlike the strength values, to depend on the microstructure. Indeed, while Z specimens show a predominantly intragranular fracture behaviour following void nucleation at grain boundaries, XY-specimens exhibit intergranular cracks at about 45° of the spall plane. Initial porosity causes a breakup of the wavefronts, which inhibits spall fracture locally, while pore collapse is found to generate grain disorientation, severe plastic deformation, and sometimes secondary spall damage.

5   ACKNOWLEDGMENTS

6   REFERENCES

[1]   W. E. Frazier, *J. of Materi Eng and Perform*, **23** (6), pp. 1917–1928, 2014.
[2]   S. Sanchez *et al.*, *Int. J. Mach. Tools Manuf.*, **165**, p. 103729, 2021.
[3]   A. Wessman *et al.*, *Superalloys 2020*, pp. 961–971, 2020.
[4]   M. Laurençon *et al.*, *Mater. Sci. Eng. : A*, **748**, pp. 407–417, 2019.
[5]   G. Asala *et al.*, *Mater. Sci. Eng. : A*, **738**, pp. 111–124, 2018.
[6]   G. Asala *et al.*, *Int J Adv Manuf Technol*, **103**, (1–4), pp. 1419–1431, 2019.
[7]   J. Kittel *et al.*, *Procedia CIRP*, **94**, pp. 324–329, 2020.
[8]   R. J. Moat *et al.*, *Acta Mater.*, **57**, p. 1220-1229, 2009.
[9]   F. Margetan *et al.*, Final Report DOT/FAA/AR-05/17, 2005.
[10]   L. M. Barker and R. E. Hollenbach, *J. Appl. Phys.*, **43** (11), pp. 4669–4675, 1972.
[11]   L. Berthe *et al.*, *J. Appl. Phys.*, **82** (6), pp. 2826–2832, 1997.
[12]   E. Barraud *et al.*, *J. Appl. Phys.*, to be published.
[13]   LASL Shock Hugoniot Data, Stanley P. Marsh (University of California Press, 1980).
[14]   T. Antoun, *Spall fracture*, Springer, 2003.

Metallic base materials

06

Dependence of the dynamic mechanical properties of AlSi10Mg on the manufacturing parameters.

Sadot O. PhD[1] **Amir B.[1], Kochavi E. PhD[1],., Gruntman S.[1], Gale Y.[2], and Samuha S. PhD[3,4]**

[1]Department of Mechanical Engineering, Ben-Gurion University of the Negev, Beer-Sheva 8410510, Israel
[2]Additive Manufacturing Center of Excellence, Technologies Division, Israeli Aerospace Industries
[3]Department of Materials Engineering, NRCN, PO Box 9001, Beer-Sheva 84190, Israel
[4]Nuclear Engineering Department, University of California, Berkeley, 4153 Etcheverry Hall Berkeley, CA, United States

Correspondence
Sadot O. PhD, Department of Mechanical Engineering, Ben-Gurion University of the Negev, Beer-Sheva 8410510, Israel

Email: sorens@bgu.ac.il

Funding information

Additive manufacturing has become one of the most promising technology for manufacturing prototypes. One of the techniques in which the process is done is laser powder bed fusion. With this procedure, prototypes made of ALSi10Mg alloy can be manufactured. This paper investigates the effect of variation of five different manufacturing parameters on the dynamic mechanical properties using a split Hopkinson pressure bar. The investigation revealed what the dominant parameters are. The analysis was based on Taguchi's design of experiments that reduce the number of experiments with minimal loss of information.

1   INTRODUCTION

In recent years the use of additive manufacturing (AM) has become a preferred technology for prototype manufacturing. Among these ever-increasing technology, laser powder bed fusion (LPBF) is one of the popular techniques used due to significant improvements in lasers power. One of the materials needed for aircraft and automobile applications is aluminum alloys. A good candidate is an AlSi10Mg alloy. This alloy was found to be suitable for the LPBF due to its low eutectic point temperature. In order to achieve good mechanical static and dynamic properties, several studies were conducted in the effort to relate them to the micro-structure. [1],[2]–[4]. Those studies and others suggest that the most important manufacturing parameters are: laser power (P), scanning speed (V), hatching distance (H_d), the thickness of the powder layer (t), and the building orientation (Or). The energy density incorporates some of those parameters:

*Equally contributing authors

$$E_d = \frac{P}{VH_d t} \tag{1}$$

Energy density optimization is complicated since this parameter controls many mechanical properties such as hardness, density, and porosity[3], [5]–[7]. So far, there is no direct correlation between energy density and mechanical properties. Therefore, an attempt was made to improve mechanical properties by the design of experiment (DOE) methods. The methods used, among others, are the Taguchi and the linear techniques [8], [9].

Recently, an effort has been made to relate the dynamic mechanical properties of AlSi10Mg to the manufacturing parameters using a split Hopkinson pressure bar system [10]–[13]. Variations in the manufacturing parameter cause some variations in the dynamic mechanical properties, while in the quasi-static tests, no significant variation in the mechanical properties was found. However, It was found that the measured dynamic yield stress under dynamic compression loads has a dependency on the relative printing to loading directions [10], [14].

In the present study, we made an effort to correlate the dynamic mechanical behavior with different manufacturing parameters using the Taguchi DOE method. We chose the dominant fabrication parameters and investigated their effect on yield stress and fracture.

2   DESIGN OF EXPERIMENTS METHODOLOGY

Based on the Taguchi methodology [8], we select five parameters, and in each, we have three different variations neer the optimal value suggested by the printing machine manufacturer (SLM model 280). **TABLE 1** present each parameter and its variation value

TABLE 1 Selected parameters for the Taguchi DOE and their values

Parameter	Nominal value	levels
1 P [W]	350	330, 250, 370
2 Hd[mm]	0.125	0.11, 0.12, 0.13
3 V[mm/s]	1650	1500, 1600, 1700
4 Or.	-	XY, 45, Z (see figure 2)
5 SP	BNF	BNF, CB, FCB (see figure 1)

2.1   Sample preparation

According to the Taguchi method, a set of 27 parameter combinations was manufactured for five parameters and three levels. The laser power, hatching distance, and scanning velocity were changed according to the three levels presented in **TABLE 1**.

Three scanning patterns were chosen; the bi-direction pattern (BNF) in it, each layer was scanned linearly (back and forth) but with 67° rotation between each successive layer. In chessboard (CB), each layer's chessboard pattern was divided into small squares (5 x 5 mm), where the scanning in each square was linear. Two neighboring squares were scanned in tangential directions, and (FCB) the fine chessboard scan is the same as the CB scan but with smaller squares (2 x 2 mm). **FIGURE 1** deposits those patterns.
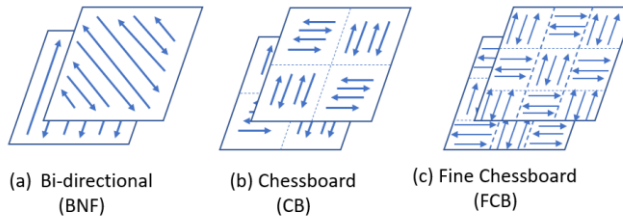
FIGURE 1   Scanning pattern schematics: a) Bi-directional (BNF). b) coarse chessboard (CB) and c) Fine chess-
board (FCB)

Orientation loads were defined as follows: three different rods were manufactured, and the SHPB samples were machined from each rod. The rods were manufactured from the building platform up (all three-rod types). The load direction for the (Z) samples is parallel to the building direction. The (XY) sample load direction is tangential to the building orientation. The load direction to the (45) samples is 45° relative to the building orientation. In **FIGURE 2**, a schematic illustration of the load direction and building direction is present.
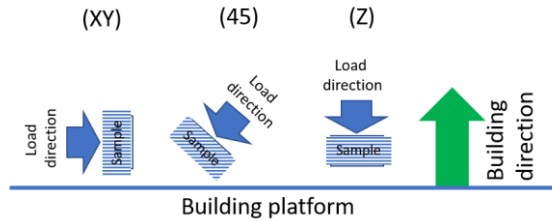
FIGURE 2   Illustration of the sample's building directions in relative to the load direction

The variations in the other three parameters (laser power, hatching distance, and scanning velocity as presented in **TABLE 1** were set in the manufacturing machine (SLM 280)

2.2   Split Hopkinson pressure bar system

The dynamic mechanical properties were found using a standard split Hopkinson pressure bar. The system operates in the laboratory of dynamic properties at Ben Gurion University. True stress and strain were extracted from the two sets of strain gages positioned on each bar. The sample size was 7 mm in diameter and 5 mm in height. Each sample was machined from the relevant rod, and the shall layer was removed. An impactor was accelerated towards the bars using a gas gun to generate the pressure load. The impactor velocity at impact was 20±0.5 m/s. This velocity permits reaching the ultimate yield stress and maximum elongation until fracture. The strain histories were captured by Lecroy HD-4054 digital oscilloscope. A standard analysis based on equilibrium conditions was used to extract the stress-strain curves. More details on the system can be found in ref's. [10], [14], [15]

3   RESULTS AND DEDICATION

According to the Taguchi method, for five parameters and three levels each, 27 different combinations were needed. Five samples were manufactured for each combination; therefore, 135 experiments were done. In each experiment, the strain–stress curve was measured, and from it, one points

was extracted: the maximum dynamic stress (MDS). The effect of the variation in the manufacturing parameters on those two measured parameters was tested.
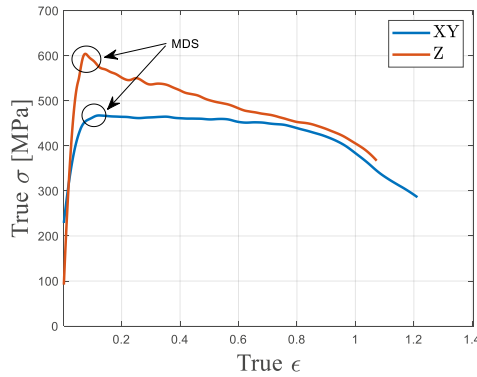
FIGURE 3 True stress-strain curves measured from samples having two different sets of parameters

FIGURE 3 depicts the true stress-strain curves measured with two samples having different parameters. The figure identifies the point of interest; MDS. This measured value was used to compare and evaluate the effect of varying manufacturing parameters. As an example, in **TABLE 2**. The MDS is significantly different in those two experiment sets.

TABLE 2 Selected two combinations from the 27 sets

Set	Scanning Pattern	Hatching distance	Scanning velocity	Laser power	Orientation	MDS
9	CB	0.13	1500	350	45	496±2
11	CB	0.12	1700	350	90 (Z)	563±2

In the next analysis stage, we implement the NOVA analysis to the obtained results. In principle, this analysis is based on estimating the mean signal to noise (S/N) response for the tested parameter. In our case, the MDS.

In **FIGURE 4**, the mean-S/N response for the MDS dependency on P, V, Hd, SP, and Or. As seen in the figure, the must influence parameter is the orientation. The other parameters have less influence on the dynamic response; however, there is clear dependence on the other parameters.

As seen in **FIGURE 4**, the second affecting parameter is the laser power. This can be related to the heat generated during the melting process. An increase in the scanning speed (v) reduces the energy transferring to the powder per unit length, reducing the effective heating temperature. Similar effects appear when varying the Hd; an increase in the Hd reduces the effective temperature. It is clear that increasing the temperature decreases the MDS. Therefore, the resulting MDS will decrease when changing a parameter that causes temperature increas.
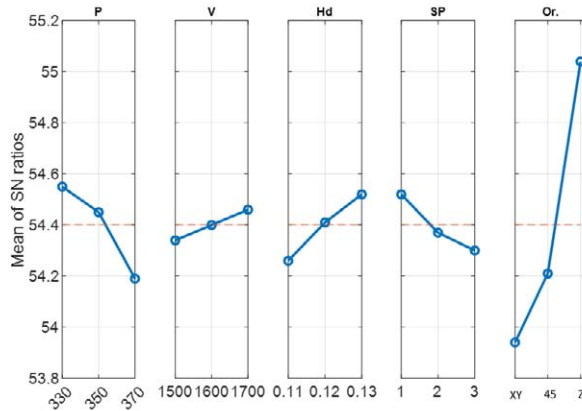
FIGURE 4 Means Signal to noise response for the five parameters : P, V, Hd, SP, and Or.

4   SUMMARY AND CONCLUSIONS

In the present study, we investigate the effect of building parameters on the dynamic strength and elongation of fracture for the printed AlSi10Mr alloy. The design of experiments based on the Taguchi methods was used to limit the number of experiments. The effect of five manufacturing parameters was tested. It was found that the dominant parameter affecting the MDS is the relative orientation of the load to building directions. This result agrees with our previous studies; Moreover, the effect of the other parameters was found to be statistically significant. We can distinguish between the relative load to building directions and the powder's temperature during printing. Those two processes initiate different mechanisms during dynamic load. Due to the high temperature during the process, the material softened, similar to the aging process, while the orientation dependency could be related to the material's microstructure. More details can be found in ref. [16]

5   REFERENCES

[1]   L. Hitzler *et al.*, "Direction and location dependency of selective laser melted AlSi10Mg specimens," *Journal of Materials Processing Technology*, vol. 243, pp. 48–61, 2017, doi: 10.1016/j.jmatprotec.2016.11.029.

[2]   U. K. uz Zaman, E. Boesch, A. Siadat, M. Rivette, and A. A. Baqai, "Impact of fused deposition modeling (FDM) process parameters on strength of built parts using Taguchi's design of experiments," *International Journal of Advanced Manufacturing Technology*, vol. 101, no. 5–8. pp. 1215–1226, 2019. doi: 10.1007/s00170-018-3014-6.

[3]   A. Majeed, Y. Zhang, J. Lv, T. Peng, Z. Atta, and A. Ahmed, "Investigation of T4 and T6 heat treatment influences on relative density and porosity of AlSi10Mg alloy components manufactured by SLM," *Computers and Industrial Engineering*, vol. 139. 2020. doi: 10.1016/j.cie.2019.106194.

[4]   A. Maamoun, Y. Xue, M. Elbestawi, and S. Veldhuis, "The Effect of Selective Laser Melting Process Parameters on the Microstructure and Mechanical Properties of Al6061 and AlSi10Mg Alloys," *Materials*, vol. 12, no. 1, p. 12, Dec. 2018, doi: 10.3390/ma12010012.

[5]   H. Meier and C. Haberland, "Experimentelle Untersuchungen zum Laserstrahlgenerieren Metallischer Bauteile," *Materialwissenschaft und Werkstofftechnik*, vol. 39, no. 9. pp. 665–670, 2008. doi: 10.1002/mawe.200800327.

[6]   C. Márquez, J. D. López, L. Cabrera, L. González, and J. Botana, "Study of the influence of laser energy density on the surface roughness of Scalmalloy ® samples manufactured by

DMLS technology," *IOP Conference Series: Materials Science and Engineering*, vol. 1193, no. 1, p. 012036, Oct. 2021, doi: 10.1088/1757-899X/1193/1/012036.

[7]   N. T. Aboulkhair, M. Simonelli, L. Parry, I. Ashcroft, C. Tuck, and R. Hague, "3D printing of Aluminium alloys: Additive Manufacturing of Aluminium alloys using selective laser melting," *Progress in Materials Science*, vol. 106, no. July, p. 100578, Dec. 2019, doi: 10.1016/j.pmatsci.2019.100578.

[8]   G. Taguchi, *System of experimental design; engineering methods to optimize quality and minimize costs*, No. 04. New York UNIPUB/Kaus International1982 v, 1987.

[9]   G. Dellino, J. P. C. Kleijnen, and C. Meloni, "Robust Optimization in Simulation: Taguchi and Krige Combined," *INFORMS Journal on Computing*, vol. 24, no. 3, pp. 471–484, Aug. 2012, doi: 10.1287/ijoc.1110.0465.

[10]   B. Nurel, M. Nahmany, N. Frage, A. Stern, and O. Sadot, "Split Hopkinson pressure bar tests for investigating dynamic properties of additively manufactured AlSi10Mg alloy by selective laser melting," *Additive Manufacturing*, vol. 22, no. April, pp. 823–833, Aug. 2018, doi: 10.1016/j.addma.2018.06.001.

[11]   T. Maconachie *et al.*, "Effect of build orientation on the quasi-static and dynamic response of SLM AlSi10Mg," *Materials Science and Engineering: A*, vol. 788, p. 139445, Jun. 2020, doi: 10.1016/j.msea.2020.139445.

[12]   P. Ponnusamy *et al.*, "Dynamic compressive behaviour of selective laser melted AlSi12 alloy: Effect of elevated temperature and heat treatment," *Additive Manufacturing*, p. 101614, 2020, doi: 10.1016/j.addma.2020.101614.

[13]   E. Zaretsky, A. Stern, and N. Frage, "Dynamic response of AlSi10Mg alloy fabricated by selective laser melting," *Materials Science and Engineering: A*, vol. 688, no. December 2016, pp. 364–370, Mar. 2017, doi: 10.1016/j.msea.2017.02.004.

[14]   B. Amir, S. Samuha, and O. Sadot, "Influence of Selective Laser Melting Machine Source on the Dynamic Properties of AlSi10Mg Alloy," *Materials*, vol. 12, no. 7, p. 1143, Apr. 2019, doi: 10.3390/ma12071143.

[15]   B. Amir, E. Grinberg, Y. Gale, O. Sadot, and S. Samuha, "Influences of platform heating and post-processing stress relief treatment on the mechanical properties and microstructure of selective-laser-melted AlSi10Mg alloys," *Materials Science and Engineering: A*, vol. 822, no. January, p. 141612, 2021, doi: 10.1016/j.msea.2021.141612.

[16]   B. Amir, Y. Gale, A. Sadot, S. Samuha, and O. Sadot "Study on the effects of manufacturing parameters on the dynamic properties of AlSi10Mg under dynamic loads using Taguchi procedure", submitted to publication in *Additive manufacturing*. 2022

07

Dynamic Tensile Behaviour and Adiabatic Heating of Wrought and Additively Manufactured Ti6Al4V

G. C. Soares[1],* | K. Kakko[2] | M. Hokka[1]

[1]Impact – Multiscale Mechanics Research Group, Engineering Materials Science
Materials Science and Environmental Engineering, Tampere University
POB 589, FI-33014, Tampere, Finland

[2]EOS Electro Optical Systems Finland Oy, FI-20520, Finland

Correspondence
*G. C. Soares PhD, Impact – Multiscale Mechanics Research Group, Engineering Materials Science, Materials Science and Environmental Engineering, Tampere University, POB 589, FI-33014, Finland
Email: guilherme.correasoares@tuni.fi

This work presents a comparison of the dynamic tensile behaviour of additively manufactured and wrought Ti6Al4V. Additively manufactured blocks were produced with different printing and post processing parameters. The tension specimens were wire cut from these blocks and from a hot rolled thin sheet. Tension tests were carried out at room temperature with a universal testing machine and a Tensile Split Hopkinson Bar (TSHB), at strain rates ranging from $1.25{\times}10^{-4}$ to 850 s^{-1}. Adiabatic heating of the specimens was measured with a high speed infrared camera. The mechanical behaviour, strain hardening parameters, and heat release during deformation of the materials were compared. The mechanical behaviour of the investigated materials was similar at both low strain and high strain rates, and all materials showed similar positive strain rate sensitivity in the investigated conditions. The strength of the additively manufactured specimens was in general higher than that of the wrought specimens, whereas the strain hardening rate of all specimens decreased with increasing strain rate. The ductility was similar for all investigated materials and marginally decreased with strain rate. These results show that additively manufactured materials have been developed to a point where their dynamic behaviour is similar to that of wrought materials.

1   INTRODUCTION

Titanium alloys are versatile materials which are essential in a variety of aerospace, sports, automobile, power generation and biomedical applications [1–3]. They usually have balanced properties such as high strength, low density and good corrosion resistance [1,4]. Depending on the alloying elements and heat treatments, titanium alloys can be single phase alpha or beta, or a combination of the two different

phases. The dual phase Ti6Al4V is the most used titanium alloy in industrial applications [3], and it is also of great interest for additive manufacturing of complex components.

Additive manufacturing (AM) is a term that groups manufacturing techniques which work by joining several layers to create a three dimensional part .The most common additive manufacturing technique for metallic materials is the Laser Powder Bed Fusion (LPBF) [5], also known as selective laser melting (SLM). The 3D object is built by selectively melting metallic powder on a flat surface with a focused laser beam according to according to a computer model, and then covering the surface again with metallic powder before repeating the melting sequence to build the subsequent slices [6]. The properties of the additively manufactured parts are affected by many factors related to the powder metal characteristics, laser properties, layer thickness, and post processing treatments. The printing process can lead to considerable variation in mechanical strength, ductility and microstructural features [7]. Understanding the dynamic behaviour of these materials and the effects of manufacturing parameters on their thermomechanical behaviour is essential for widespread utilization in the aerospace and automotive sectors.

The plastic deformation and failure of titanium alloys is significantly affected by strain rate and temperature [3]. Fast deformation such as that experienced by a material in machining or various impacts, can lead to fast strain localizations and failure due to the formation of adiabatic shear bands in both wrought and additively manufactured titanium [8,9]. The heat release and consequent thermal softening during high rate deformation has been related to possible changes in deformation mechanisms in additively manufactured Ti6Al4V [10].

The thermomechanical behaviour of additively manufactured titanium alloys has mostly been studied at low strain rates, so the effect of strain rate on the strain hardening and heat release of additively manufactured titanium alloys still requires further investigation. The novelty of this work is in the description of the thermomechanical behaviour under tension of wrought and additively manufactured Ti6Al4V at a wide range of strain rates.

2   MATERIALS AND METHODS

The materials investigated in this work were wrought Ti6Al4V and additively manufactured Ti6Al4V with different manufacturing and post-processing parameters. The different materials, parameters, and strain rates in which they were tested are shown in Table 1. The additively manufactured (35 x 45 x 78 mm^3) test samples were built on an EOS M 290 using 60 µm and 80 µm processes. The purpose of using multiple layer thicknesses was to study the effects of the increase in the build rate on the properties of the material. A batch of additively manufactured material was heat treated at a temperature of 800 °C for 2 hours. Other batches with the two different layer thicknesses were Hot Isostatic Pressed (HIP) with standard (920 °C, 100 MPa, 2 h) and optimized HIP parameters (820 °C, 140 MPa, 2 h). Industrial standard HIP-parameters were originally developed for Ti6Al4V castings and therefore the AM microstructure optimized HIP-parameters proposed by Kosonen et al. [11] were also used.

Dog-bone tensile specimens were machined with electrical discharge machining from a 2 mm thin plate of wrought and annealed alloy, and from the additively manufactured blocks. The wrought specimens were cut so that the rolling direction was parallel to the loading (tension) axis, and the additively manufactured specimens were cut so that the loading direction was parallel to the building direction. The low rate (1.25×10^{-4}–0.5 s^{-1}) tension tests were carried out with a servohydraulic testing machine and the high strain rate (850 s^{-1}) tests were carried out with a tensile Split Hopkinson Pressure Bar

system. The engineering strain in the tests was measured using an optical extensometer based on Digital Image Correlation (DIC). A detailed description of the specimen geometry and the testing setup is found in references [12,13].

TABLE 1 Test material conditions, additive manufacturing parameters and tensile test strain rate.

Material	Condition	Layer thickness (μm)	Strain rate (s^{-1})
Wrought Ti6Al4V	Annealed	-	$1.25×10^{-4}$–850
Additively manufactured Ti6Al4V	Heat treated	60	$1.25×10^{-4}$–850
	HIP	60 80	$1.25×10^{-4}$–0.5
	HIP optimized	60 80	$1.25×10^{-4}$–850 $1.25×10^{-4}$–0.5

The temperature of the specimens was monitored during testing with a Telops FAST M2k high speed infrared camera. The radiometric temperature measurements of the infrared camera were converted to surface temperature measurements using calibration curves constructed by monitoring the cooling down of the specimens with both a thermocouple and the camera. A more detailed description of this temperature calibration process can be found at reference [12]. The tension tests were also monitored with two M-lite 16 MPix CMOS cameras for the low strain rate tests and Photron Fastcam SA-X2 high-speed cameras for the high strain rate tests. DIC was used to follow the deformation of the specimens and a virtual extensometer was used to measure the global engineering strain throughout the tests.

3 RESULTS AND DISCUSSION

Figures 1 and 2 show the engineering stress-strain and the strain hardening rate curves of the materials in tension at strain rates from $1.25×10^{-4}\,s^{-1}$ to $850\,s^{-1}$. Both the wrought and the additively manufactured Ti6Al4V alloys had a positive strain rate sensitivity in the investigated strain rate range. The heat treated specimens had the highest yield and the highest ultimate tensile strengths (UTS). The optimized HIPped specimens were the second strongest followed by the wrought material and the standard HIPped specimens. This trend was observed at strain rates from $1.25×10^{-4}\,s^{-1}$ to $0.5\,s^{-1}$. The tensile strength of the material with a 60 μm layer thickness was marginally higher than those with a 80 μm layer thickness, although further testing is required to investigate the significance of this difference in their mechanical behaviour. The UTS of the all investigated materials increased from 1050–1150 MPa at $10^{-4}\,s^{-1}$ to 1200 MPa at the strain rate of $850\,s^{-1}$. The fracture strain of the investigated materials decreased with strain rate but remained approximately constant at strain rates of $0.5\,s^{-1}$ and $850\,s^{-1}$. The wrought and additively manufactured materials had a remarkably similar mechanical behavior at high strain rates. Fadida et al. [14] observed a similar dynamic behavior in tension for both additively manufactured and wrought Ti6Al4V. The authors also reported a lower yield strength and a higher fracture strain in a wrought Ti6Al4V in comparison to an AM counterpart. Rodriguez at al. [10] reported strain softening at higher strain rates. In the current work, strain softening was also observed throughout plastic deformation at the strain rates of $0.5\,s^{-1}$ and $850\,s^{-1}$.
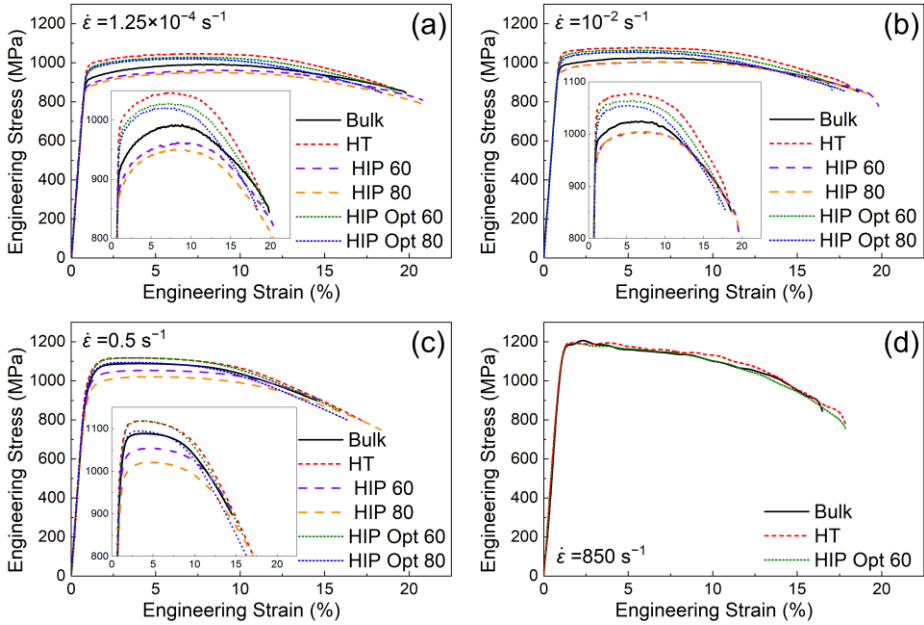
FIGURE 1 Engineering stress-strain plots of the Ti6Al4V at strain rates from 1.25×10^{-4} s^{-1} to 850 s^{-1}. The close ups show the difference in the stress-strain curves in more detail.
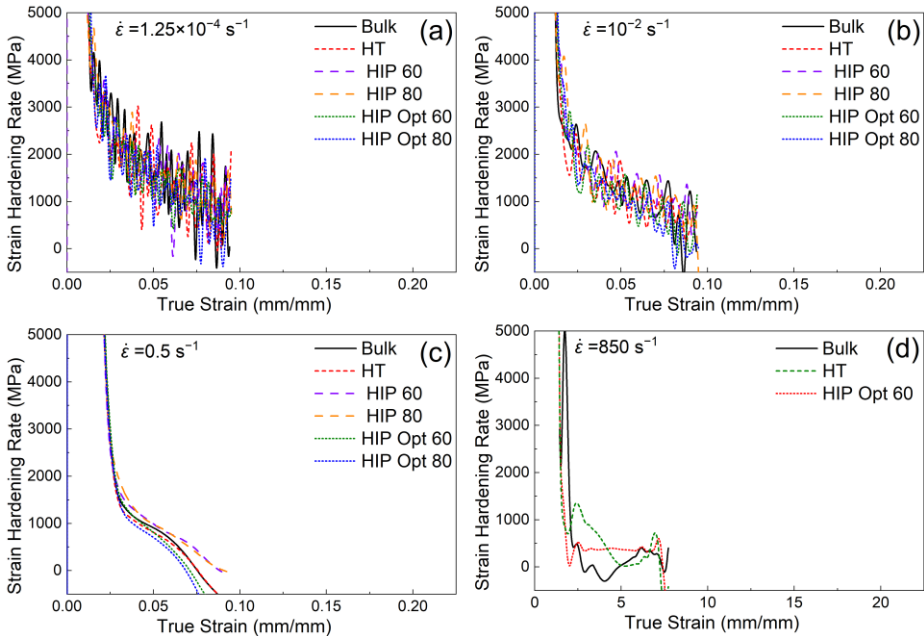
FIGURE 2 Strain hardening rate as a function of true strain for the Ti6Al4V specimens at strain rates from 1.25×10^{-4} s^{-1} to 850 s^{-1}.

The strain hardening rate of both wrought and additively manufactured Ti6Al4V were similar for each investigated strain rate. In general, the strain hardening rate after yielding at all strain rates decreased at the constant rate. A positive strain hardening rate was observed at strain rates of 1.25×10^{-4} s^{-1}, $10^{-2}\,s^{-1}$ and $0.5\,s^{-1}$ but the strain hardening rate was roughly zero at $850\,s^{-1}$.

Figure 3 shows average temperature increase (ΔT) of the gage section of the specimens as a function of true strain. The onset of necking was determined using waterfall plots based on the DIC data. The spatial average of the temperature increase is reported only until necking as the temperature change in that area is essentially constant during uniform deformation, but the heating is strongly localized in the neck region after the onset of necking. The adiabatic heating for all materials increased with strain rate. The heat generated by the material is mostly transferred to its surroundings in the lowest strain rate tests, but there is less time for the heat transfer at strain rates of 10^{-2}–$850\,s^{-1}$ and a considerable temperature increase is observed. The tests at a strain rate of $10^{-4}\,s^{-1}$ were essentially isothermal and the small observed temperature increase was caused by the heat conducted from the test machine grips to the specimen. A notable temperature increase was observed already at the strain rate of $10^{-2}\,s^{-1}$ due to the low thermal conductivity of titanium. No considerable heat transfer was observed from the specimen gauge section to the shoulder areas at strain rates of $0.5\,s^{-1}$ and $850\,s^{-1}$, so these tests can be considered to have been adiabatic. At all investigated strain rates, the adiabatic heating was the highest in wrought Ti6Al4V, followed by the heat treated, and the HIPped specimens. The reason for the lower ΔT for additively manufactured Ti6Al4V requires further investigation. It is possible that the observed differences in the behaviour are caused by the different microstructures produced by AM, the slightly lower density of the AM specimens, or also differences in the efficiency at which these materials convert plastic work into heat.
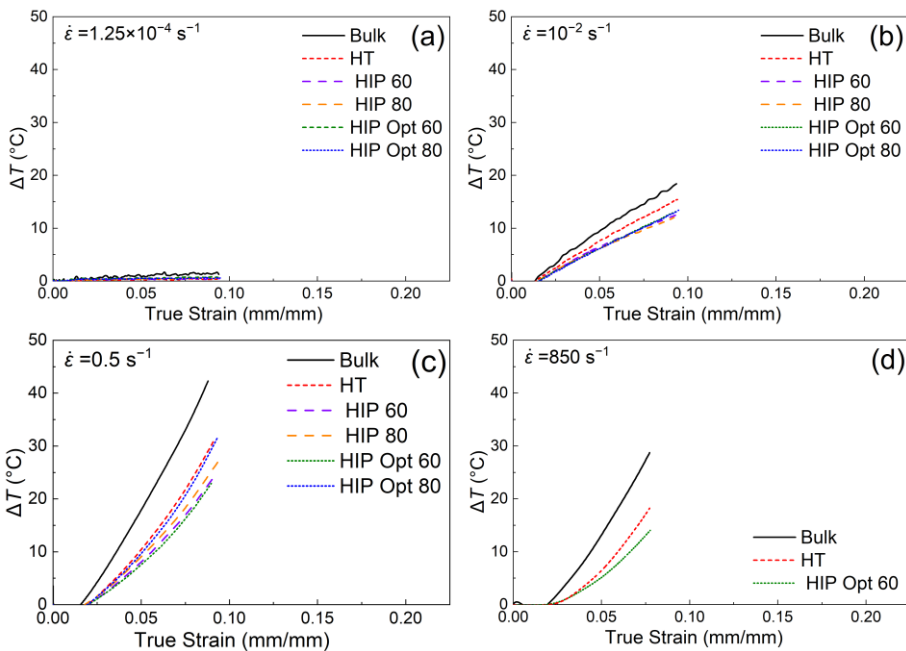
FIGURE 3 Temperature increase of the Ti6Al4V specimens at strain rates from $1.25\times10^{-4}\,s^{-1}$ to $850\,s^{-1}$.

4   SUMMARY

This work presented the mechanical behaviour and adiabatic heating of wrought Ti6Al4V and additively manufactured Ti6Al4V with different manufacturing and post processing parameters. Tensile tests were carried out at 1.25×10^{-4}–850 s^{-1} using a servohydraulic materials testing machine and a Split Hopkinson Pressure Bar. Temperature of the specimens was monitored with a high speed infrared camera. Each investigated material had a positive strain rate sensitivity in the studied strain rate range. At each strain rate, the mechanical behaviour of the wrought specimens was similar to the additively manufactured specimens. The temperature increase of the materials increased with strain rate, and the wrought material had a higher temperature increase than the additively manufactured materials. The use of a smaller layer thickness led to a small increase in the strength of the material, and the optimization of the post processing HIP procedure led to a greater increase in the mechanical strength. The heat treated material had a higher tensile strength at both low and high strain rates. However, applications which undergo cyclic loading usually employ HIP treated materials due to their much higher fatigue resistance. Additively manufacturing techniques have reached a state where they are able to produce materials with similar properties to wrought alloys, not only under quasi-static conditions but also under dynamic loading. Further studies are suggested to investigate the difference in the deformation mechanisms and failure of additively manufactured titanium alloys.

5   REFERENCES

[1]   N. Milošević, I. Aleksić, Thermophysical properties of solid phase Ti-6Al-4V alloy over a wide temperature range, Int. J. Mater. Res. 103 (2012) 707–714. https://doi.org/10.3139/146.110678.

[2]   S. Wu, K. Fan, P. Jiang, S. Chen, Grain refinement of pure Ti during plastic deformation, Mater. Sci. Eng. A. 527 (2010) 6917–6921. https://doi.org/10.1016/j.msea.2010.06.085.

[3]   P. Verleysen, J. Peirs, Quasi-static and high strain rate fracture behaviour of Ti6Al4V, Int. J. Impact Eng. 108 (2017) 370–388. https://doi.org/10.1016/j.ijimpeng.2017.03.001.

[4]   C. Bunte, G. Porta, Thermomechanical Processing of Alloys. Case of Study Ti Gr. 4, Procedia Mater. Sci. 8 (2015) 311–318. https://doi.org/10.1016/j.mspro.2015.04.078.

[5]   W.M.I. Makhetha, T.H. Becker, N. Sacks, Post-Processing Framework for As-Built LPBF Ti-6Al-4V Parts Towards Meeting Industry Functional Requirements, JOM. 74 (2022) 764–776. https://doi.org/10.1007/s11837-021-05078-y.

[6]   S. Liu, Y.C. Shin, Additive manufacturing of Ti6Al4V alloy: A review, Mater. Des. 164 (2019) 107552. https://doi.org/10.1016/j.matdes.2018.107552.

[7]   J. Yao, T. Suo, S. Zhang, F. Zhao, H. Wang, J. Liu, Y. Chen, Y. Li, Influence of heat-treatment on the dynamic behavior of 3D laser-deposited Ti–6Al–4V alloy, Mater. Sci. Eng. A. 677 (2016) 153–162. https://doi.org/10.1016/j.msea.2016.09.036.

[8]   J. Peirs, W. Tirry, B. Amin-Ahmadi, F. Coghe, P. Verleysen, L. Rabet, D. Schryvers, J. Degrieck, Microstructure of adiabatic shear bands in Ti6Al4V, Mater. Charact. 75 (2013) 79–92. https://doi.org/10.1016/j.matchar.2012.10.009.

[9]   N. Biswas, J.L. Ding, V.K. Balla, D.P. Field, A. Bandyopadhyay, Deformation and fracture behavior of laser processed dense and porous Ti6Al4V alloy under static and dynamic loading, Mater. Sci. Eng. A. 549 (2012) 213–221. https://doi.org/10.1016/j.msea.2012.04.036.

[10]   O.L. Rodriguez, P.G. Allison, W.R. Whittington, D.K. Francis, O.G. Rivera, K. Chou, X. Gong, T.M. Butler, J.F. Burroughs, Dynamic tensile behavior of electron beam additive

manufactured Ti6Al4V, Mater. Sci. Eng. A. 641 (2015) 323–327. https://doi.org/10.1016/j.msea.2015.06.069.

[11]   T. Kosonen, K. Kakko, K. Kupi, Evaluation of HIP-parameter effects on AM Titanium Ti-6Al-4V, in: Conf. Proc. AeroMat19, Reno, Nevada, USA, 2019.

[12]   G.C. Soares, N.I. Vázquez-Fernández, M. Hokka, Thermomechanical Behavior of Steels in Tension Studied with Synchronized Full-Field Deformation and Temperature Measurements, Exp. Tech. 45 (2021) 627–643. https://doi.org/10.1007/s40799-020-00436-y.

[13]   G.C. Soares, M. Hokka, Synchronized Full-Field Strain and Temperature Measurements of Commercially Pure Titanium under Tension at Elevated Temperatures and High Strain Rates, Metals (Basel). 12 (2022) 25. https://doi.org/10.3390/met12010025.

[14]   R. Fadida, A. Shirizly, D. Rittel, Dynamic tensile response of additively manufactured Ti6Al4V with embedded spherical pores, J. Appl. Mech. Trans. ASME. 85 (2018) 1–10. https://doi.org/10.1115/1.4039048.

[15]   R. Molaei, A. Fatemi, N. Phan, Significance of hot isostatic pressing (HIP) on multiaxial deformation and fatigue behaviors of additive manufactured Ti-6Al-4V including build orientation and surface roughness effects, Int. J. Fatigue. 117 (2018) 352–370. https://doi.org/10.1016/j.ijfatigue.2018.07.035.

08

Comparison of Dynamic Properties of AM and Wrought Titanium Ti 6Al 4V

P Church[1][*] | J Perry[2][†]   H Price[3]

[1]QinetiQ, Fort Halstead, Sevenoaks, Kent, TN14 7BP, UK

[2]Surface, Microstructure & Fracture Group Cavendish Laboratory, JJ Thomson Ave, Cambridge, CB3 0HE, UK

[3]BAE Systems, Warton Aerodrome, Warton, PR4 1AX, Preston, UK

Correspondence
Philip Church, QinetiQ, Fort Halstead, Sevenoaks, Kent TN14 7BP, UK
Email: pdchurch@qinetiq.com

Additively Manufactured (AM) materials have great potential for producing graded materials, embedded structures and near net complex shapes. One major issue with AM materials is the lack of dynamic material property data at high strain rates. This paper describes a comparison between the dynamic and some static properties of AM and wrought Ti 6Al 4V. Several tests were performed including the Split Hopkinson Pressure Bar (SHPB) and some microstructural analysis was also carried out. This showed some evidence of different deformation mechanisms between the materials where the wrought material deformed by dislocation mechanics and the AM material by general slip or shear banding, although further work is required.

1   INTRODUCTION & BACKGROUND

There is extensive interest in Additive Manufacture (AM) of metals as AM technology is developing very rapidly, particularly in the aerospace area. The development of AM opens the door to new and novel materials and more flexible manufacturing processes. Whilst there have been previous studies on the properties of AM metals, most have focussed on microstructure and static properties (Kempen,

*J Perry, H Price

2011; Jaga, 2016). The purpose of this paper was to compare the properties of wrought and AM titanium alloy (i.e. Ti 6Al 4V) over a range of strain rates to obtain a greater understanding of their behaviour. This consisted of Quasi-Static (QS) interrupted tensile tests, elastic property measurements and high rate tests on a Compression Split Hopkinson Pressure Bar (CSHPB). The wrought material data was based on work some years ago.

1.1   Material and sample Description

The AM Ti 6Al 4V material specimens were produced using Laser Powder Bed Fusion (L-PBF) on a Renishaw RenAM 500Q under full quality control processes for the material and powder. The wrought material was obtained from a standard supplier of Ti 6Al 4V alloy. The tensile specimens were made using AM techniques and then finished machined for the screw threads. The cylindrical compression specimens were AM manufactured. Some samples were made in the different x, y and z directions to check isotropy.

2   MATERIAL TEST RESULTS

The QS interrupted tests were performed in QinetiQ and used the process described in (Butler, 1994) so that isothermal stress/strain curves are produced. The elastic wave measurements and CSHPB tests were performed at Cambridge University.

2.1   Elastic Wave Measurements

The method employed for these measurements used ultrasonic waves to measure all the relevant sounds speeds as shown in **Figure 1**. The crux of the method is to measure the sound speed very accurately (i.e. ±1%). From these simple elastic relations were used to derive the elastic moduli. The density was also measured using a buoyancy method.
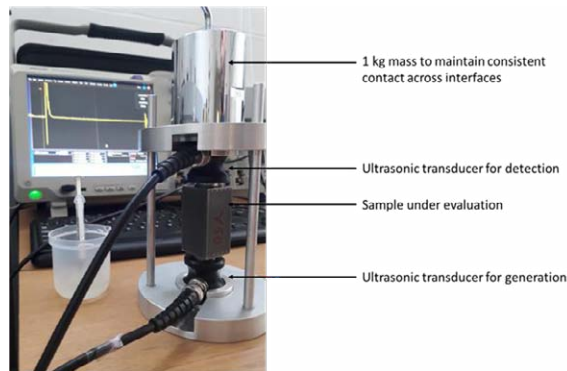
Figure 1 - - Photograph of setup of pair of transducers to independently generate and detect the ultrasound pulses

The measured properties are shown in Table 1. As can be seen there is no evidence of anisotropy in the AM material and the values are similar to the wrought material.

Table 1 – Summary of Elastic Properties

Property	X-Section	Y-section	Z-section
Longitudinal sound speed /m·s^{-1}	6190 ± 2	6189 ± 2	6165 ± 2

Shear sound speed /m·s⁻¹	3198	± 3	3199	± 2	3194	± 3
3D pressure wave speed /m·s⁻¹	4969	± 3	4966	± 3	4940	± 3
1D pressure wave speed /m·s⁻¹	5192	± 4	5193	± 3	5183	± 4
Poisson's ratio	0.3180 0.005	±	0.3178 0.004	±	0.3166 0.005	±
Longitudinal modulus /GPa	168.7	± 0.2	168.6	± 0.2	167.3	± 0.2
Shear modulus /GPa	45.0	± 0.1	45.0	± 0.1	44.9	± 0.1
Bulk modulus /GPa	108.7	± 0.2	108.6	± 0.2	107.5	± 0.2
Young's modulus /GPa	118.7	± 0.2	118.7	± 0.2	118.3	± 0.2
Density	4405	± 5	4404	± 3	4398	± 5
Combined density values used for above moduli calculations					4403	± 5

2.2   QS Interrupted Tensile Tests

Three tests were perfromed and the data was very reproducible. The comparison with the wrought material is shown in **Figure 2**
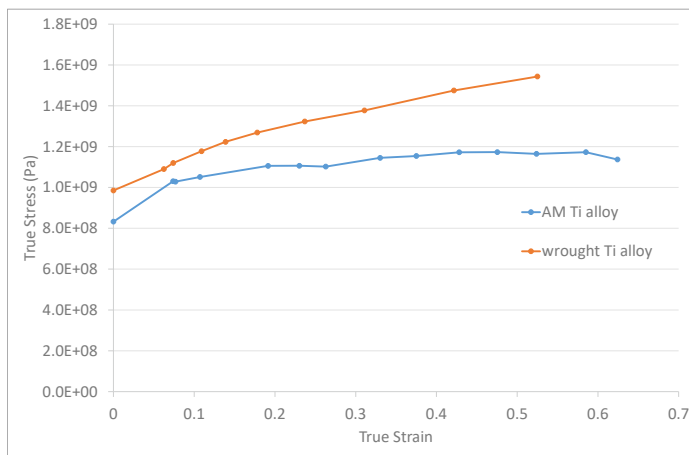
Figure 2 - Comparison of AM material with previously tested conventional material for Ti alloy

There are clearly significant differences in the stress v strain response for both materials. The AM material is seen to have much lower strain hardening response and yet a more severe localisation behaviour when compared to the conventional material indicating that there may be more general slip or shear banding involved in its deformation rather than homogeneous dislocation motion. It was noted in the interrupted tests that there was a slight rotation (i.e. 2°) just as the material was yielding, which may indicate a shear banding effect.

2.3   High Rate Data

A total of six tests were performed on the CSHPB and again the results were reproducible and there was no evidence of anisotropy in the AM materials. The comparison with the wrought material is shown in **Figure 3**.
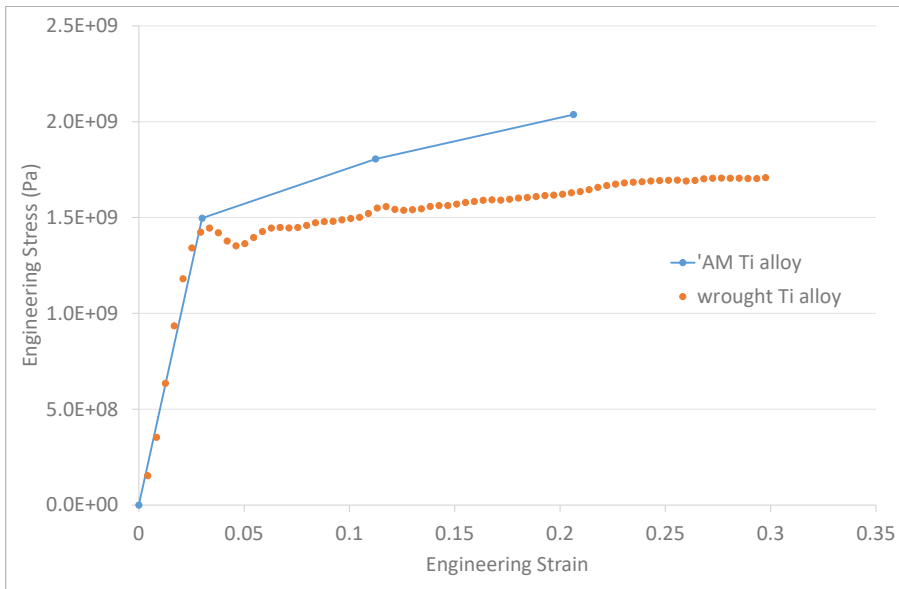
Figure 3 - Comparison of high rate CSHPB data for wrought and AM Ti alloy

A comparison of the high rate data shows the opposite effect to the QS data in that there appears to be more strain hardening at higher rates in the AM material. This may still be consistent with the proposed mechanism difference, but this requires further investigation. The response of the AM material in the Hopkinson bar exhibits more strain hardening than the conventional material. It may be, however, that it is less affected by thermal softening.

2.4   Microscopy Analysis

The fracture of the tensile specimens was examined using Scanning Electron Microscopy (SEM). The fracture surfaces consisted of two distinct regions, with the centre of the sample showing ductile micro-void coalescence and the edges mainly showing shear failure. A low magnification overview of one of the fracture surfaces is shown in **Figure 4** . SEM images often remove some of the topography of the image so an optical microscope image of the same fracture surface is given in **Figure 4** to show the shape of the shear lips formed. The shear region is quite large in respect to the overall diameter of the specimen.

Some possible defects were observed on the fracture surface. These appeared to be un-melted/partially melted powder particles. It is also possible that they are inclusions of different composition. These features were disparate and did not appear obviously in the cross-sectioned material. Whilst these particles are present on the fracture surface, they don't seem to dominate the failure mode

Figure 4 - Overview of fracture surface for AM Ti alloy (left), Optical overview of a fracture surface to show 3D nature of shear regions (right).

2.5   Conclusions

Elastic constants were measured and are within 1% uncertainty in all three directions. Tensile testing showed consistent properties in three orientations. There is a significant difference in stress v strain response between previous wrought and AM material. The AM material has a lower QS stress v strain curve than equivalent wrought material. AM material has lower QS strain hardening response and more prone to localisation based on the interrupted tests which produce isothermal stress v strain curves under adiabatic deformation conditions. At high strain rate the effect is reversed (i.e. AM material is stronger). This could be indication of different deformation mechanisms, e.g. slip/shear banding rather than dislocations. The AM material could be less resistant to thermal softening.

3   REFERENCES

1.   A, B. (1994). A Wide ranging Constitutive Model for bcc Steels. *Jnl de physique, C8*, 471.
2.   Jaga. (2016). *JOM Vol68 (3)*.
3.   Kempen. (2011). *Phys Proc 12*, 255-263.

3.1   Acknowledgements

09

Additively manufactured Ni-based Inconel 718 alloy behaviour under combined conditions of high strain-rate and temperature

Daniele Forni PhD[1]* | **Federico Mazzucato PhD[2]***
| **Anna Valente PhD[2]*** | **Ezio Cadoni PhD[1]***

[1]DynaMat SUPSI Laboratory, University of Applied Sciences and Arts of Southern Switzerland, 6850 Mendrisio, Switzerland

[2]Automation Robotics and Machines Laboratory, University of Applied Sciences and Art of Southern Switzerland, 6962 Viganello, Switzerland

Correspondence
Daniele Forni PhD, DynaMat SUPSI Laboratory.
Email: daniele.forni@supsi.ch

This paper presents the dynamic behaviour in a wide range of temperatures of additively manufactured and commercial Ni-based Inconel 718 alloys. The results highlight similar mechanical behaviour between *as-built* manufactured samples produced with a power laser of 400 W and *as-cast* samples. Samples produced at 400 W show a higher presence of inclusions than those produced at 300 W, leading to higher mechanical strength at room temperature. In contrast, at elevated temperatures, the difference was drastically reduced (e.g. the variance between the UTS values is about 6%). The calibration of the Johnson-Cook strength model highlighted the necessity of using specific thermal softening values (m) in particular ranges of strain rate and temperature.

---

* Equally contributing authors.

Metallic base materials

1 | INTRODUCTION

Inconel 718 is a Ni-based Superalloy that finds an extensive application in the Aerospace industry for the fabrication of structural components specifically designed to endure harsh environmental conditions in terms of extreme working temperatures and high strain rates [1]. Excellent toughness, good corrosion and high creep-rupture resistance at elevated temperatures are technological advantages that encourage Inconel 718 as a reference choice for the fabrication of industrial gas turbines, jet engine components, and critical rotating parts. Nevertheless, due to its superior mechanical properties, the machining of Inconel 718 components remains challenging. The manufacturing of high-functional shapes or repairing damaged surfaces is not yet cost-effective. Recently, Direct Energy Deposition (DED) has been recognised as an Additive Manufacturing (AM) technique capable of overcoming these limitations, enabling the fabrication and refurbishing of hard-to-cut metal components. To optimise process conditions [2] and the performance of the realised components, it is essential to investigate the influence of the main process parameters [3] (e.g. laser power) on the structural quality of Inconel 718 parts produced by Laser Metal Deposition (LMD) and characterise the mechanical properties of the *as-built* material undergoing the coupled effect of strain-rate, and temperature [4].

The objectives of the research investigation tried to fill these gaps, specifically by studying the mechanical behaviour of Inconel 718 parts produced by Laser Metal Deposition under a wide range of strain rates (from 0.001 to 800 s^{-1}) and temperatures (from 20°C to 550°C). The main mechanical properties and a comparison between results obtained under the same conditions on an *as-cast* Inconel 718 material have been reported. The main parameters of the Johnson-Cook strength material model have been reported as well.

2 | DESIGN OF EXPERIMENTS

The design of a comprehensive testing campaign that includes several process recipes (e.g. laser power, carrier-powder mix and axes feed) running on the same manufacturing infrastructure is necessary to satisfy specific product quality (e.g. absence of cracks, superficial roughness, porosity percentage, and dimensional fitting). The Design of Experiments (DoE) involved the combination of six levels of axis power, six levels of axis speed, two levels of hatching distances and a constant powder feed ratio. These combinations allowed the production of single track samples (Figure 1(a)), single layer samples (Figure 1(b)) and finally, 3d bulk cylinders (Figure 1(c)). From the latter, and after a careful inspection, two optimal combinations of parameters were chosen for the production (electrical discharge machining and turning) of cylindrical samples ready for mechanical characterisation. The two combinations of process parameters adopted for the manufacturing have been reported in Table 1. A detailed description of the steps for the sample preparation is reported in [3, 4].

The mechanical characterisation in tension at high strain rates and elevated temperatures has been performed using a Split Hopkinson Tensile Bar equipped with an Ambrell compact EASY-HEAT induction water-cooled heating system, whose details are reported in [5]. For the sake of comparison with *as-built* materials (Table 1), a commercial Inconel 718 was used as raw material for the preparation of *as-cast* samples.

TABLE 1   Process parameter adopted for the manufacturing. From [3].

Material name	Laser power [W]	Axis speed [mm/min]	Hatching distance [mm]	Feed rate [g/s]	Layer thickness [mm]
As-built P300W Inconel 718	300	750	0.384	0.032	0.151
As-built P400W Inconel 718	400	750	0.414	0.032	0.208
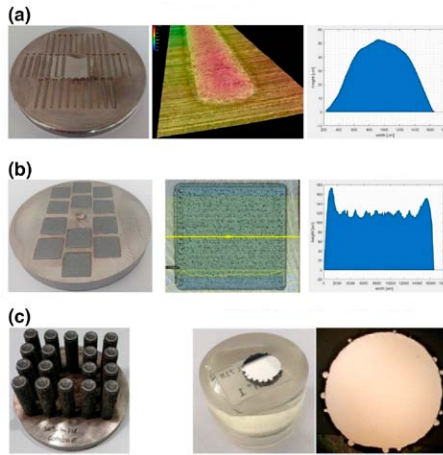
FIGURE 1   Single track (a), single layer (b) and 3d bulk cylinders (s): preparation and analyses.

3 | RESULTS

At room temperature, *as-built* specimens exhibit better repeatability and are slightly more ductile than *as-cast* specimens in terms of total elongation. In contrast, due to different sizes and the distribution of inclusions [3], the *as-built* P300W material highlighted lower mechanical strength than its counterpart produced with a 400W laser power. Despite this, the *as-built* material realised with a 400W laser power has been found to exhibit similar mechanical behaviour to the *as-cast* material in terms of uniform strain and ultimate tensile strength. Moreover, a modest strain-rate sensitivity was revealed for both the *as-cast* and *as-built* materials.

Elevated testing temperatures lead to higher repeatability of flow stresses. From Figure 3(a) it is possible to observe that the differences in mechanical properties between *as-built* materials were considerably reduced. In particular, high strain-rate tests at elevated temperature (550°C) revealed a very similar mechanical behaviour in flow stress between *as-cast* and *as-built* materials. Furthermore, the results obtained from tests at elevated temperatures highlighted the thermal softening effect. From Figure 3(b) a linear trend decrease of the ultimate tensile strength is observed for increasing temperatures.

Performing reliable numerical simulations requires the proper selection of the constitutive rela-
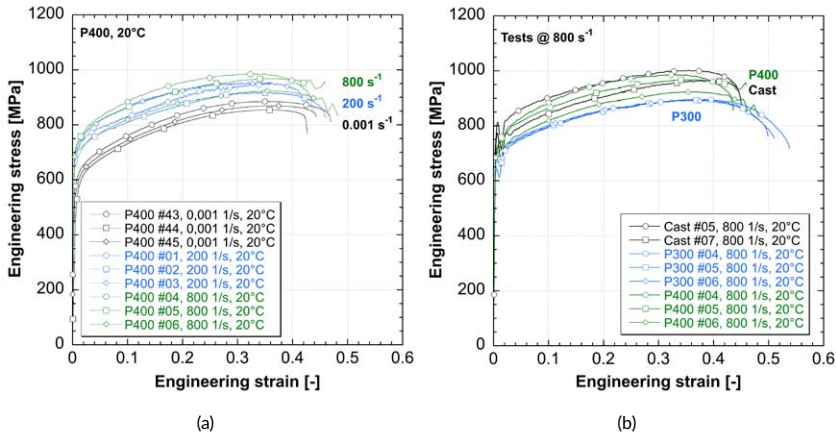
FIGURE 2 Mechanical behaviour at room temperature of (a) *as-built* P400W material, and (b) comparison of *as-builts* and *as-cast* materials at 800 s^{-1}. Images modified from [3].

TABLE 2 Constitutive parameters of Johnson-Cook at 20°C.

Material	A	B	n	c
	[MPa]	[MPa]	[-]	[-]
As-built P300W Inconel 718	532	1276	0.6309	0.01218
As-built P400W Inconel 718	519	1397	0.6314	0.02006
As-cast Inconel 718	567	1121	0.4721	0.01535

tion for the strength of the material. The present research work focuses on this issue, with consideration of the Johnson-Cook model [6] which is a plasticity model based on five constitutive parameters and suitable for the modelling of the strain hardening (*A*, *B*, and *n*), the strain-rate sensibility (*c*), and the thermal softening (*m*).

The five constitutive parameters are calibrated through the experimental mechanical results. They suggest that in dynamic conditions at room temperature (Table 2), the *as-built* materials could have a more ductile behaviour reaching higher elongations before necking starts than the *as-cast* material. In addition, a higher strain-rate sensitivity for the *as-built* samples realised with a laser power of 400 W is observed (Table 2). Moreover, lower strain-rate sensitivity parameters have been observed for samples realised with a laser power of 300 W, meaning lower mechanical strength for increasing strain-rates. Finally, it is worth noting that comparable parameters were obtained by [7, 8].

On the other hand, the thermal softening parameter (*m*), evaluated for a specific set of data in terms of effective strain-rates and temperatures, highlighted a noticeable variation. The minimum obtained value is 0.967, while the maximum is 1.447 (Figure 4(a)). Therefore, averaged *m* values could cause substantial numerical errors [4]. As a consequence, numerical simulations require specific thermal softening values (*m*) in particular ranges of strain-rate and temperature.

(a)   (b)
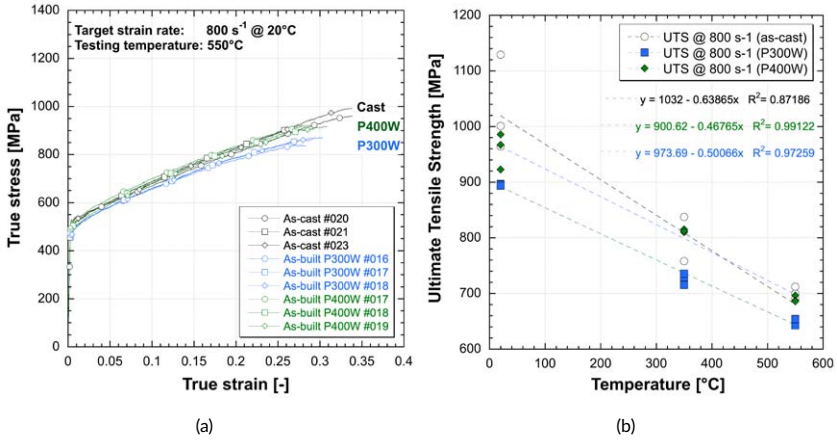
FIGURE 3   Comparison between *as-cast* and *as-built* materials of true stress vs true strain at 550° and 800 s^{-1}(a), and ultimate tensile strength decrease (b).

(a)   (b)
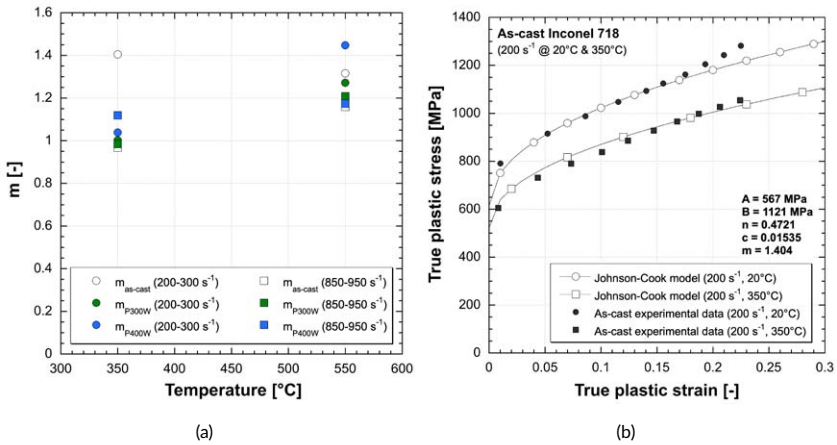
FIGURE 4   Comparison between the thermal softening parameter (a), and Johnson-Cook model comparison with experimental flow data (b).

Metallic base materials

4 | CONCLUSIONS

Two as built Inconel 718 materials and a raw Inconel 718 material were studied in this paper to compare their mechanical properties under severe combined conditions of temperature and strain rates. The experimental results led to the following conclusions:

- The *as-built* materials highlighted a modest strain-rate sensitivity keeping their strain hardening capacities under combined conditions.
- Results at room temperature highlighted that the mechanical behaviour of the *as-built* Inconel 718 manufactured with a laser power of 400 W was similar to the mechanical behaviour of the *as-cast* material.
- At elevated temperatures, the flow stress was more repeatable within materials, and the *as-cast* and the *as-built* materials showed comparable results.

Acknowledgements

References

[1] Johansson J, Persson C, Testa G, Ruggiero A, Bonora N, Hörnqvist Colliander M. Effect of microstructure on dynamic shear localisation in Alloy 718. Mechanics of Materials 2017;109:88–100. `https://www.sciencedirect.com/science/article/pii/S0167663616303854`.

[2] Mazzucato F, Aversa A, Doglione R, Biamino S, Valente A, Lombardi M. Influence of Process Parameters and Deposition Strategy on Laser Metal Deposition of 316L Powder. Metals 2019 oct;9(11):1160. `https://www.mdpi.com/2075-4701/9/11/1160`.

[3] Mazzucato F, Forni D, Valente A, Cadoni E. Laser Metal Deposition of Inconel 718 alloy and as-built mechanical properties compared to casting. Materials 2020;.

[4] Forni D, Mazzucato F, Valente A, Cadoni E. High strain-rate behaviour of as-cast and as-build Inconel 718 alloys at elevated temperatures. Mechanics of Materials 2021;159:103859. `https://www.sciencedirect.com/science/article/pii/S0167663621001101`.

[5] Cadoni E, Forni D. Mechanical behaviour of a very-high strength steel (S960QL) under extreme conditions of high strain rates and elevated temperatures. Fire Safety Journal 2019;p. 102869.

[6] Johnson G, Cook W. A constitutive model and data for metals subjected to large strains, high strain rates and high temperatures. In: Proceedings of the 7th International Symposium on Ballistics; 1983. p. 541–547.

[7] Pereira JM, Lerch BA. Effects of heat treatment on the ballistic impact properties of Inconel 718 for jet engine fan containment applications. International Journal of Impact Engineering 2001;25(8).

[8] Iturbe A, Giraud E, Hormaetxe E, Garay A, Germain G, Ostolaza K, et al. Mechanical characterization and modelling of Inconel 718 material behavior for machining process assessment. Materials Science and Engineering A 2017;682(November 2016):441–453. `http://dx.doi.org/10.1016/j.msea.2016.11.054`.

10

High strain rate of conventional and laser melting maraging

Nozères F.[1*], Bailly P.[2], Limido J. [3], Couque H.[2]

[1] Nexter Munitions, Bourges, France
[2] INSA Centre Val de Loire, Bourges, France
[3] IMPETUS Afea, Toulouse, France

Correspondence

Nozères F., Direction Technique, Nexter Munitions, 7 route de Guerry, 18023 Bourges, France

Email: f.nozeres@nexter-group.fr

High strain rate mechanical properties of maraging steels elaborated through a conventional root elaborated using a cast melting approach and through a laser melting root via an additive manufacturing approach are reported.

Compression tests were conducted from 10^{-4} to 10^4 s^{-1}. High strain rates Mode II shear tests were conducted with a direct impact Hopkinson pressure bar technique using a conventional hat specimen and a hydrodynamic hat specimen to vary the pressure from 0.5 to 1.5 GPa. The numerical simulation of the shear tests were conducted using Johnson-Cook type constitutive model and the Dolinski, Merzer, and Rittel Mode II failure criterion. The results reveal comparable compression properties between the two processing roots. For both roots, Mode II failure was found to be initiated through adiabatic shear banding.

1 INTRODUCTION

To provide high strength steels, the maraging steels with carbon percent less than 0.03% in mass have been developed providing ultimate tensile strength greater than 2060 MPa (Maraging 300 ksi). Intensive research has been conducted to generate such class of steels through laser melting process. The current study reports the high strain rate mechanical properties of maraging steels elaborated through a conventional root elaborated using a cast melting approach and through a selective laser

melting root via an additive manufacturing approach. The maragings were composed of iron along with in weight percent of 0,03% carbon, 18% nickel, 9% cobalt and 5% molybdenum.

The conventional maraging steel was provided by Aubert et Duval and identify MY19 [1]. Ingot of the conventional maraging elaborated through vacuum induction melting were forged in bars 70 mm in diameter. After aging, the material provides a tensile yield stress of 2070 MPa and tensile ductility of 12%.

The selective laser melting maraging was provided by EOS starting from pre-alloyed 40 µm powders elaborated in the vertical axis and identified M300SLM [2]. After aging, the material provides a tensile yield stress of 2030 MPa and tensile ductility of about 5 %.

High strain rate characteristics were investigated through an experimental numerical investigation. Experimental characteristics consist in compression properties as a function of strain rate and Mode II failure properties at high strain rate. For both maragings, dynamic Mode II failure was initiated through adiabatic shear banding. Numerical investigations of the Mode II failure process was investigated with two softwares. A finite element software AUTODYN [3] was used to investigate the strengthening effect in the viscous regime using a modified Johnson-Cook Model [4],[5]. A particle element software IMPETUS [6] was used to investigate the adiabatic shear failure process using the Dolinski M., Merzer M. and Rittel approach [7].

2   COMPRESSION RESULTS AND CONSTITUTIVE MODELS

Compression tests were performed with specimens of 9 mm diameter and 5 mm in height. Quasi-static and intermediate conditions tests were conducted at strain rates of 0.0006 and 2,4 s-1 with a conventional testing machine. Stress-strain curves were deduced from load displacement data obtained from a load cell and a displacement device. High strain rate tests were conducted at strain rates ranging from 5 to 8 x10^3 s^{-1} with a direct impact Hopkinson pressure bar technique [8]. High strain rate stress-strain curves were deduced from the striker impact velocity and from the Hopkinson pressure bar strain history.

Figure 1 shows the stress strain curve of the two maragings. In one hand, under quasi-static loading conditions, both maraging exhibit similar hardening. In another hand, responses at strain rate starting from 2,4 s-1, reveal a similar softening behaviour for both maragings. Adiabatic shear banding occurs at high strain rates, with an average strain onset of 0.08 at a strain rate of about 8 x 10^3 s^{-1}, for both maragings.

(a)
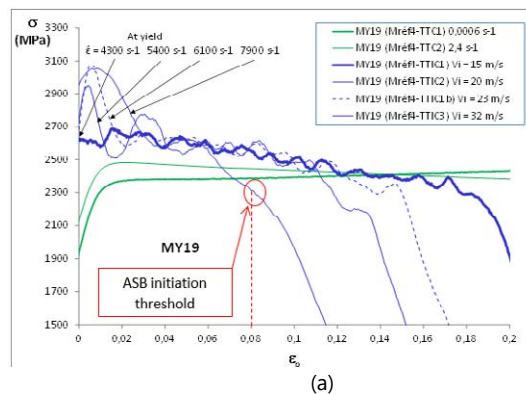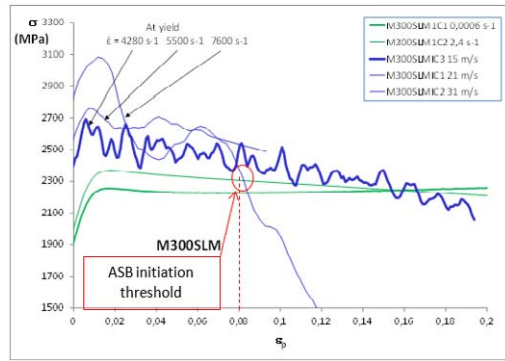
(b)

FIGURE 1 Compression stress-strain responses: (a) MY19 maraging steel, (b) M300SLM maraging steel. The impact velocities and strain rate at yield of the direct impact Hopkinson pressure bar are indicated.

Considering yield stress data, thermally activated and viscous regimes were identified, see FIGURE 2. The two maragings exhibit a transition from the thermally activated regime to the viscous regime of about 10^3 s-1.

a) MY19 maraging steel

b) M300SLM maraging steel
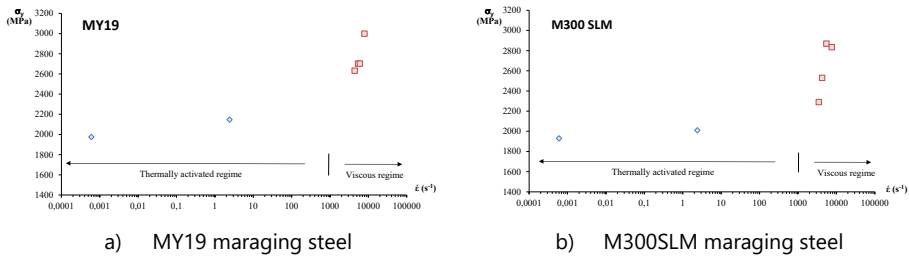
FIGURE 2 Yied stress versus strain rate of the conventional maraging MY19 and laser melting maraging M300SLM.

These data were used to calibrate Johnson-Cook constitutive type models [4], [5]incorporated in both sofwares, AUTODYN [3] and IMPETUS [6]. A standard Johnson-Cook model (JC) along with a Modified Johnson-Cook model (MJC) allowing to reproduce the viscous regime were used. These models define the flow stress as (1):

$$\sigma = (A + B \, \varepsilon_p^{n}) \, (1 + C \, ln \, (\dot{\varepsilon} / \dot{\varepsilon}_o) + D(\dot{\varepsilon} / \dot{\varepsilon}_1)^{k}) \, (1 - [(T - T_r) / (T_m - T_r)]^{m}) \qquad (1)$$

where σ is the Von Mises flow stress, ε_p is the equivalent plastic strain, $\dot{\varepsilon}$ is the equivalent plastic strain rate, $\dot{\varepsilon}_o$ is the normalized strain rate corresponding to the threshold for adiabatic conditions taken to be 1 s^{-1}, $\dot{\varepsilon}_1$ is the normalized strain rate characterizing the transition from the thermally activated regime to the viscous regime taken to be 10^3 s^{-1}, T is the normalized temperature, A is the initial yield strength, B is the hardening parameter, n is the hardening exponent, C is the strain rate parameter of the standard Johnson-Cook model Describing the thermally activated regime, D and k two strain rate parameters of the modified Johnson-Cook model characterizing the viscous regime, and m is the thermal softening exponent.

Parameters of the two Johnson Cook models for both maraging steels are provided in TABLE 1.

TABLE 1 Parameters of the standard and modified Johnson-Cook models.

Maraging	A (MPa)	B (MPa)	C	D	n	m	k
MY19	2380	150	0.007	0.01	0.17	1.11	1.1
M300SLM	2100	260	0.0075	0.0265	0.01	0.97	0.6

3   MODE II SHEAR FRACTURE INVESTIGATION

3.1   Experimental procedure

The test set-up is depicted in FIGURE 3.

(a)   (b)

(c)
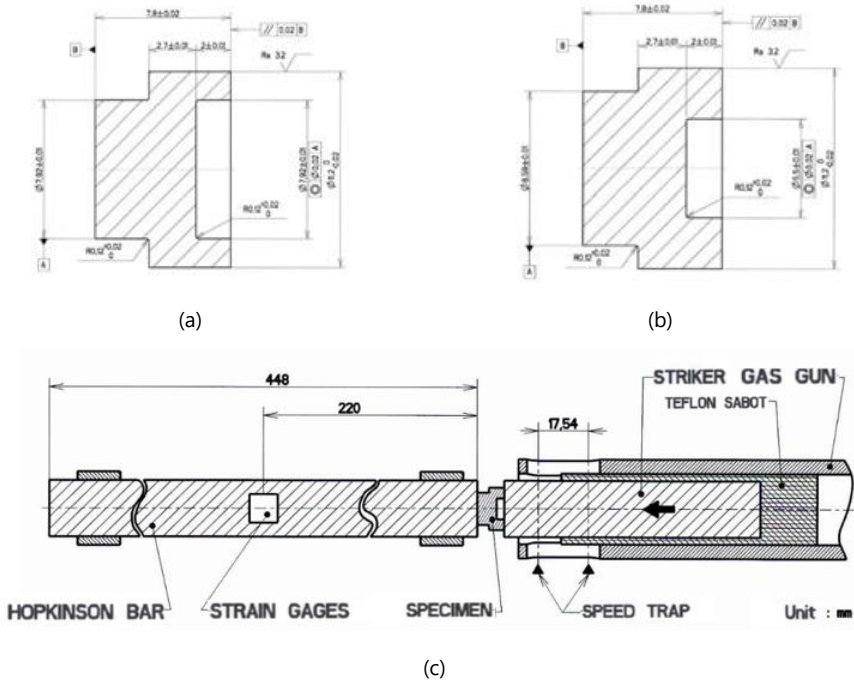
FIGURE 3   Hat-test experimental set-up: (a) conventional hat specimen, (b) hydrodynamic hat specimen, (c) direct impact Hopkinson pressure bar technique

A conventional hat specimen has been used to study adiabatic shear banding (ASB) characteristics in titanium alloys and copper, see FIGURE 3a [9]. The specimen generates ASB within a gage section submit to shear loading under low pressure. To generate high pressure in the gage section ranging from 1.2 to 1.5 GPa, another hat specimen has been introduced, called the hydrodynamic hat specimen, see FIGURE 3b [10]. A constant pressure is obtained by tilting the gage section of 32.6° with regard to the loading axis.

The loading procedure of both hat specimens consists in the direct impact with a striker bar of the specimen placed against a Hopkinson pressure bar, see FIGURE 3c [8],[11]. The striker 20 mm in diameter is sent by a gas gun. The striker velocity, V_i, is measured 9 mm prior impact with an 18 mm two-laser beams device positioned 13.5 mm prior impact. The impact velocity ranges from 20 to 50 m.s^{-1} ensuring elastically loading of the striker and Hopkinson pressure bars. Loading durations and strain rates in the 10^4 s^{-1} regime can be monitored through the use of different impact velocity and striker length, respectively. The pressure bar is 20 mm in diameter and 448 mm in length. Strains gages located on the Hopkinson pressure bar provide the specimen load and specimen / bar interface displacement history [12]. The striker and Hopkinson pressure bar are made of a tungsten alloy 1500 MPa in yield stress, 17.65 g.cm^{-3} in density and 370 GPa in Young modulus.

In addition, the crushing of the hat specimen can be limited by the use of an adaptable stop ring positioned at the top of a dedicated strut stuck onto the Hopkinson bar as depicted in FIGURE 4.
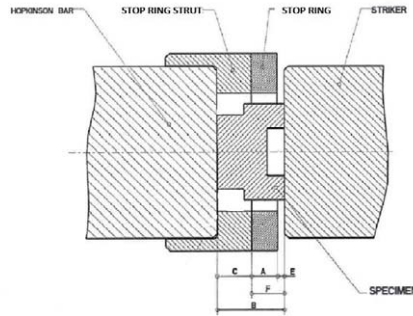
FIGURE 4   Hat-test assembly with the sample crushing limitation device

3.2   Experimental results

For both maragings, several striker velocities combined with various stop ring thicknesses have been tested in order to determine precise impact conditions leading to the initiation of ASB and the breakup of the sample, respectively. The reaching of these particular conditions is validated by post-mortem microscopic observations performed on truncated crushed samples as depicted in FIGURE 5.
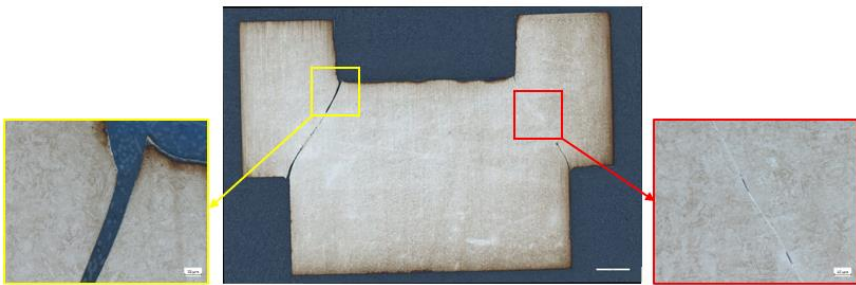
FIGURE 5   Microscopic observations performed on a maraging MY19 hat sample impacted at 20.7 m.s^{-1} with a 3.76 mm thick stop ring allowing for a controlled axial crush of 40 μm.

The huge amount of plastic work provoked by the initiation of ASB generates a dramatic increase of the local temperature, this temperature exceeding the austenitization threshold. The ensuing fast cooldown then induces a localized martensitic transformation resulting to a characteristic white shear band as depicted in the right corner of the FIGURE 5. The identified thresholds for ASB initiation and total breakup are summed up, for both maragings, in TABLE 2. It can be noticed that the associated impact conditions for these thresholds are quite similar for both materials despite their differentiated tensile ductilities (see 1)

TABLE 2   Identified impact conditions resulting to ASB initiation and sample breakup for studied materials

Maraging	ASB initiation threshold			Sample breakup threshold		
	Striker velocity (m.s^{-1})	Imposed dynamic crushing (μm)	Residual sample crushing (μm)	Striker velocity (m.s^{-1})	Imposed dynamic crushing (μm)	Residual sample crushing (μm)
MY19	20.7	40	70	16.8	700	330
M300SLM	21	40	100	13.60	700	280

4 NUMERICAL RESULTS

A numerical investigation has been undertaken to interpret these experimental data for both studied maraging steels. This investigation has been split in two successive steps, with a first step addressing the influence of the constitutive model on the elasto-plastic response prior to damage initiation, and a second step dealing with the ASB failure mechanism. As expressed above, two different softwares have been used to conduct this two-step numerical approach: AUTODYN [3] and IMPETUS [6], the former relying upon classical Finite Element Methods (FEM) whereas the latter makers use of an advanced meshless Smooth-Particle Hydrodynamics (Gamma-SPH, [13]) method.

More precisely, in the first step, the influence of the material model on its dynamic response has been exclusively carried out with AUTODYN [3], this FEM-based numerical code being fitted with both Johnson-Cook and Modified Johnson-Cook models, the latter allowing for a better apprehension of the viscous regime.

On the other hand, IMPETUS [6], despite not embedding the Modified Johnson-Cook plasticity model [5], is best suited to deal with high levels of plastic strains encountered with ASB fracture mechanisms thanks to the combination of the meshless Gamma-SPH method with the ASB-dedicated Dolinski-Merzer-Rittel [7] damage model, the associated technical details being discussed in point 4.2

4.1 Numerical simulations with non-failure criterion

Numerical simulations of the shear fracture test of an impact velocity of 20 m.s^{-1} have been conducted with the AUTODYN [3] software to investigate the importance of taking in account the viscous regime using a FEM mesh size of 200 μm. Numerical data were generated using a target positioned in the middle of the gage section where shear strain concentration occurred for both the conventional hat specimen and hydrodynamic hat specimen, see FIGURE 6.

FIGURE 6 Position of the selected target for the numerical outputs of the hat specimens.

As expected high pressure is generated with the hydrodynamic hat specimen which is about 1200 MPa for both maragings, see FIGURE 7. Low pressures less than 400 MPa are generated with the conventional hat specimen confirming the unconfined state of stress for this configuration.
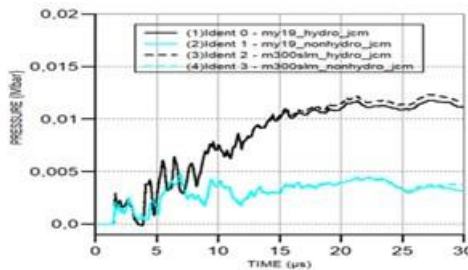
FIGURE 7 Pressure histories in Mbar for the conventional (nonhydro) and hydrodynamic hat specimens.

The effective plastic strain and effective plastic strain rate histories are provided in FIGURE 8 for the hydrodynamic hat configuration. As shown in FIGURE 8b, the deformation occurred in the viscous regime since the effective plastic strain rate is above 5000 s^{-1} for both maragings, disregarding the Johnson-Cook model used. Consequently, numerical simulations with the Modified Johnson-Cook Model provide reduced plastic strain because of the strengthening occurring in the viscous regime. This amount of plastic strain is reduced by a factor of two for the hydrodynamic hat specimen, see FIGURE 8a. Similar results were obtained with the conventional hat specimens indicating that no major differences in terms of effective plastic strain concentrations were observed between the two maragings

a) Effective plastic strain histories

MY19   M300SLM

b) Effective plastic strain rate histories

MY19   M300SLM
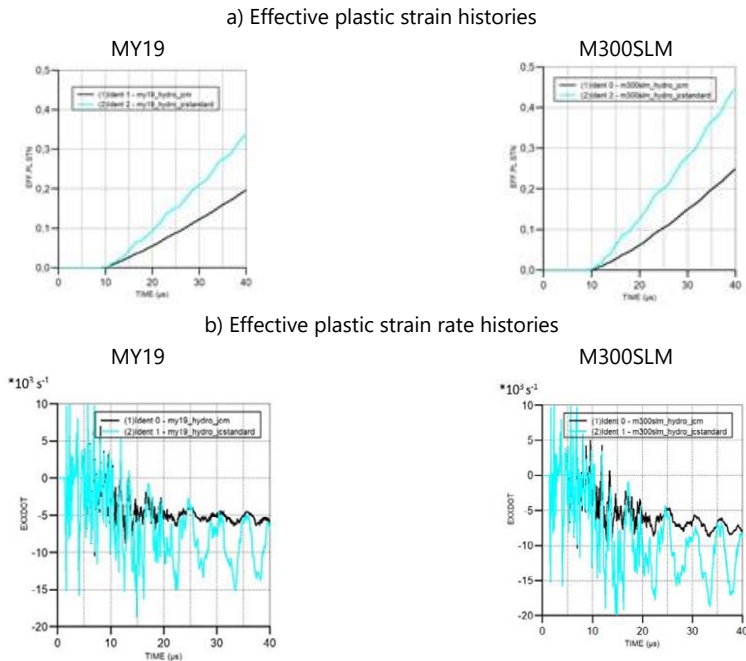
FIGURE 8   Effective plastic strain histories (a) and effective plastic strain rate histories (b) for the hydrodynamic hat specimens using the Standard Johnson-Cook model (jcstandard) and Modified Johnson-Cook Model (jcm).

4.2   Numerical simulations with a failure criterion

4.2.1 General considerations about computation techniques involved

As explained in the introduction of this paragraph hereabove, the IMPETUS [6] calculations were conducted by using mesh-free Gamma SPH [13] models combined with the Dolinski-Merzer-Rittel [7] damage criterion. This Gamma SPH [13] method is an evolution of the so-called SPH [14] approach which is, basically, a Lagrangian particle technique used to solve partial differential equations (PDE). The main advantage of this technique, regarding to FEM, is to discretize the calculation domain by a set of particles freely interacting between themselves rather than relying on a fixed-connectivity numerical grid. Indeed, SPH [14] uses a kernel approximation to rule these interactions and makes no assumptions about which particles are neighbours to calculate spatial derivatives. As such, SPH-based calculations are no longer disturbed by excessive mesh distortions as encountered in the modelling of ASB. This is the reason why SPH [14] approaches are the most suitable to deal with the high plastic strains involved in the hat-specimen tests. The Gamma-SPH [13] method embedded in IMPETUS [6] software is an evolution of this original technique which addresses its tensile-instability limitation.

4.2.2 IMPETUS hat-test model

The generic computing ¼ model used for all IMPETUS-based calculations is illustrated in **FIGURE 9**.
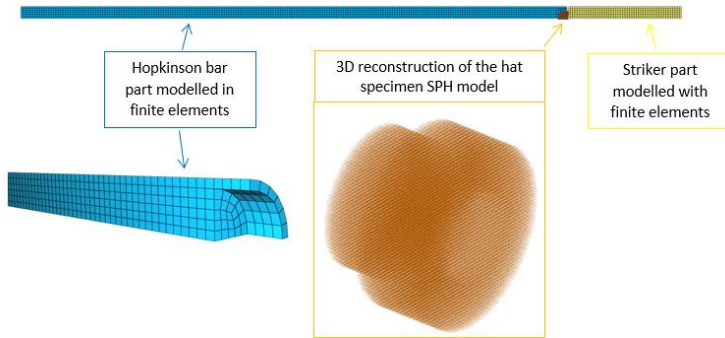
FIGURE 9   Generic computing model used for all IMPETUS [6] simulations

As depicted in **FIGURE 9** above, the striker and the Hopkinson bar are modelled with fully integrated hexahedral elements finite elements (total number of finite elements ≈ 7600) whereas the computation of the hat specimen relies on Gamma-SPH [13] particles (total number of particles ≈ 144000). It should be noticed that the design of the Hopkinson transmission bar has been modified (see FIGURE 4) so that it might embed the Hopkinson bar itself, the stop ring and its strut within the same frame. Such a simplification of the mounting, keeping in mind that all these devices are made of tungsten, allows for a better treatment of the contact between finite elements and particles from the hat-specimen in this complex interface. Respective sizes of the FEM and Gamma-SPH [13] parts are identical for all calculations, namely 2 mm for finite elements and 0.1 mm for particles. The selection of such a diameter for Gamma-SPH [13] particles has been dictated on the lower end by the need to model physical phenomena as thin as a few microns (average ASB thickness) and on the upper end by an acceptable resulting calculation time. In this context, this size of 0.1 mm for particles has emerged as a good compromise, each calculation being performed in a few hours. The proper evaluation of the crushing of the hat-specimen requires calculation duration long enough to characterize completely the elastic return of the sample structure. In that perspective, modellings of the hydrodynamic hat configuration have been performed for 480 µs after impact of the striker.

4.2.3 Material models and crack propagation

In IMPETUS calculations, the material constitutive model is based on a Johnson-Cook plasticity flow tress law, which parameters are identical to the ones presented in TABLE 1, coupled with a damage parameter (D) according to the Dolinski-Merzer-Rittel ASB criterion [7]. This criterion induces a progressive loss of material properties once a given amount of plastic energy is achieved (see (3) and (4)), this plastic energy being calculated as expressed in (2). The crack opening then occurs when this plastic energy at failure is attained, according to (5).

$$W = \int_0^{\epsilon_{eff}^p} \max(0, \sigma_1)\, d\epsilon_{eff}^p \tag{2}$$

$$D = \begin{cases} 0 & W \le W_{cr} \\ \dfrac{W - W_{cr}}{W_f - W_{cr}} & W > W_{cr} \end{cases} \tag{3}$$

$$\sigma_{eq} = \sigma_{eq}^* \cdot \left(1 - D^b\right) \tag{4}$$

$$D_d = \frac{1}{W_c} \int_0^{\epsilon_{eff}^p} \max(0, \sigma_1)\, d\epsilon_{eff}^p \tag{5}$$

where (D) is the Dolinski-Merzer-Rittel damage parameter [7], (D_d) is the ductile Cockcroft-Latham damage parameter [15], (W_{cr}) is the critical threshold energy standing for the ASB initiation, (W_f) is the plastic energy at failure, (σ_1) is the maximum principal stress and ε_{eff}^p is the effective plastic strain.

4.2.4 Numerical fracture results

Fitted Dolinski-Merzer-Rittel damage parameters for hydrodynamic hat configurations are summed up in TABLE 3, they are identical for both materials.

TABLE 3   Fitted Dolinski-Merzer-Rittel damage parameters for studied maragings

b	W_c (MPa)	W_f (MPa)
10	13.33	40

The computed hydrodynamic hat sample residual crushings are exhibited in TABLE 4 (shown in red) allowing for a direct comparison with experimental data (shown in black).

TABLE 4   Experimental and computed hydrodynamic hat-test crushings for the threshold impact conditions

Maraging	ASB initiation threshold			Sample breakup threshold		
	Striker velocity (m.s^{-1})	Imposed crushing (µm)	Residual crushing (µm)	Striker velocity (m.s-1)	Imposed crushing (µm)	Residual crushing (µm)
MY19	20.7	40	70 (exp) **66 (calc)**	16.8	700	330 (exp) **254 (calc)**
M300SLM	21	40	100 (exp) **60 (calc)**	13.60	700	280 (exp) **250 (calc)**

As presented in TABLE 4, calculations are quite in accordance with experimental results even if they tend to underestimate the ASB-induced collapse: the particles size (0,1 mm) might be too important to properly capture the very high strain gradient involved in ASB phenomena.

In order to further investigate these results, temperature and damage fringes obtained with the different numerical configurations have been compared with the post-mortem optical observations. An example of such a comparison is given, for the MY19 maraging for ASB initiation threshold, in FIGURE 10a. The calculated damage parameter equals 1, e.g, the fracture is attained in zones where breakups have been characterized, see FIGURE 10c. Average computed temperature levels, around 350°C, is however less inferior to the austenitization temperature, see FIGURE 10b .

Preliminary experimental and numerical results reveal that the impact velocity threshold for ASB initiation is lower for conventional hat specimen when compared to the hydrodynamic one. The corresponding strain threshold was found to dramatically increase accordingly to the pressure within the gage section, as previously reported with tungsten alloys and high-strength steels [16], [17].

(a)

(b)

(c)
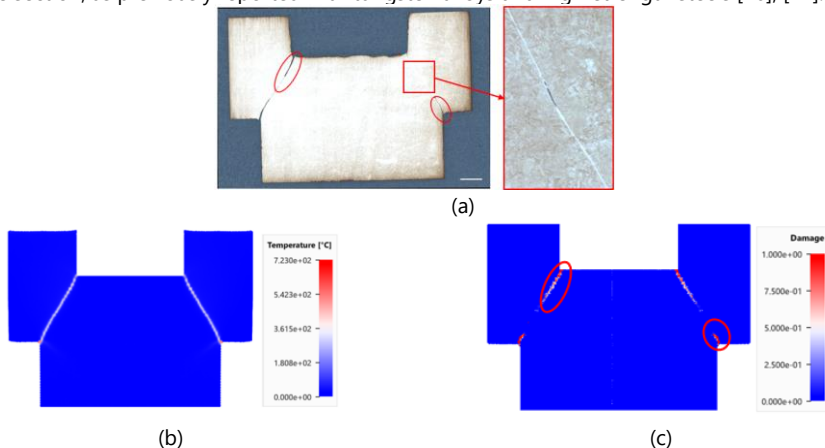
FIGURE 10   Comparison of optical observation of the MY19 sample cut section (a) with temperature (b) and damage (c) fringes of the associated numerical configuration in the impact conditions associated with ASB initiation (striker velocity = 20.7 m.s^{-1}, imposed dynamic crushing = 700 µm)

5   CONCLUSIONS

In the scope of high-performance materials, maraging steels provide superior strength, greater than 2060 MPa (Maraging 300 ksi), while keeping a certain ductility. These characteristics result from precipitation of intermetallic compounds within a low-carbon matrix, this precipitation being triggered by a dedicated aging treatment.

With the emergence of additive manufacturing processes, intensive research has been conducted to generate such class of steels through laser melting process. In order to determine the influence of this new process on the material dynamic performances, the present research work compared characteristics at high strain rates of two maraging 300 grades, a conventional vacuum melting maraging and a Selective Laser Manufacturing processed maraging. This comparison was conducted through experimental and numerical investigations.

Compression properties, acquired from 9 mm-diameter and 5 mm-length samples submitted to solicitations ranging from quasi-static conditions to strain rates up to 8×10^3 s^{-1}, outlined a similar behaviour for the two maragings. If both exhibited a quite comparable hardening in quasi-static loadings, the pair was prone to an equivalent softening at high strain rates. These experimental data were used to calibrate a standard Johnson-Cook constitutive model along a modified one designed to reproduce the viscous regime above 10^3 s^{-1} strain rates. Consecutive numerical simulations with FEM AUTODYN software revealed that the strengthening associated with the modified Johnson-Cook model induces lower effective plastic strains in the gage section.

Mode II failure mechanisms were then investigated, in dynamic conditions, through the use of conventional and hydrodynamic hat samples placed against a Hopkinson pressure bar and crushed by a direct impact from a striker. Both maragings for the hydrodynamic hat specimen were shown to be quite sensitive to ASB phenomenon, the associated thresholds for ASB initiation and final breakup being quite similar in both cases. These observations were numerically addressed on the IMPETUS software by using Gamma-SPH modelling, the material damage being monitored by a tailored Dolinski-Merzer-Rittel damage criterion. The set of parameters was found to be identical for the two maraging grades.

Preliminary experimental and numerical results reveal that the impact velocity threshold for ASB initiation is lower for conventional hat specimen when compared to the hydrodynamic one. Ongoing work is currently in progress to quantify these differences.

6   ACKNOWLEDGEMENTS

7   REFERENCES

[1]   Aubert & Duval, France.

[2]   Electro Optical Systems GmbH, Germany.

[3]   ANSYS Inc, ANSYS AUTODYN, 2017.

[4]   Johnson G. R. and Cook W. H. A constitutive model and data for metals subjected to large strains, high strain rates and high temperatures. 7th International Symposium of Ballistics, 1983, 541-547.

[5]   Couque H., Boulanger R. and Bornet F. A Modified Johnson-Cook Model for Strain Rates ranging from 10-3 to 104 s-1. Conference DYMAT 2006, Journal de Physique IV, 2006, 134: 87-93.

[6]   IMPETUS Afea AS., IMPETUS AFEA SOLVER, 2021.

[7]   Dolinski M., Merzer M. and Rittel D. Analytical formulation of a criterion for adiabatic shear failure. International Journal of Impact Engineering, 2015, 85: 20-26.

[8]   Couque H. The Use of the Direct Impact Hopkinson Pressure Bar Technique to Describe thermally Activated and Viscous Regimes of Metallic Materials. Philosophical Transactions of the Royal Society A, 2014, 372: 1-10.

[9]   Hartmann K. H., Kunze H. D. and Meyer L. W. Metallurgical effects on impact loaded materials. Conference EXPLOMET 1980, Plenum press, 1981, 325-337.

[10] Couque H. A Hydrodynamic Hat Specimen to Investigate Pressure and Strain Rate Dependence on Adiabatic Shear Band Formation. Conference DYMAT 2003, Journal Physique IV, 2003, 423-428.

[11] Dharan, C. K. H. and Hauser, F. E., Determination of stress-strain characteristics at very high strain rates, Experimental Mechanics, 1970, 10: 370-377.

[12] Couque H., Boulanger R. and Bornet F. A Modified Johnson-Cook Model for Strain Rates ranging from 10-3 to 104 s-1. Conference DYMAT 2006, Journal de Physique IV, 2006, 134: 87-93.

[13] Collé A. Limido J., Vila J-P, An accurate multi-regime SPH scheme for barotropic flows, Journal Of Computational Physics, 2019, 388: 561-600.

[14] Limido J, Espinosa C, Salaün M. and Lacome J-L, A new approach of high speed cutting modelling: SPH method, 8th International Conference on Mechanical and Physical Behaviour of Materials under Dynamic Loading, 2006, 1195-1200.

[15] Cockcroft M. G. and Latham D. J. Ductility and the workability of metals. Journal of the Institute of Metal, 1968, 96: 33-39.

[16] Hanina E., Rittel D. and Rosenberg Z. Pressure sensitivity of adiabatic shear bang in metals. Applied Physics Letters, 2007, 90-021915: 1-3.

[17] Dynamic Compression Failure of Two Metals at 0.5 GPa and 1.5 GPa, H. Couque Conference Computational Balistics II 2005, Pub. WIT Press, Ed. V. Sanchez-Galvez, C. A. Brebbia, A. A. Motta, C. E. Anderson, 2005, 239-248.

11

Defect analysis of 3D printed Al-Mg-Sc alloy using ultra high-speed X-ray phase contrast imaging

Puneeth Jakkula [1] | **Amitay Cohen**[2] |
Bratislav Lukić[3] | **David Levi-Hevroni**[2] |
Alexander Rack[3] | **Georg Ganzenmüller**[1,4] |
Stefan Hiermaier[1,4]

[1] Albert-Ludwigs-Universität Freiburg, Sustainable Systems Engineering, INATECH, Emmy-Noether Str. 2, 79110 Freiburg, Germany

[2] Department of Physics, NRCN, PO Box 9001, Be'er Sheva, 8419001, Israel

[3] European Synchrotron Radiation Facility - ESRF, CS40220, 38043 Grenoble Cedex 9, France

[4] Fraunhofer Institute for High-Speed Dynamics, Ernst-Mach-Institut, EMI, Ernst-Zermelo Str. 4, 79104 Freiburg, Germany

Correspondence
Puneeth Jakkula M.Sc.,
Albert-Ludwigs-Universität Freiburg, Sustainable Systems Engineering, INATECH, Emmy-Noether Str. 2, 79110 Freiburg, Germany
Email:
puneeth.jakkula@inatech.uni-freiburg.de

Ultra High speed X-ray phase contrast imaging (XPCI) synchronised with a custom built Split Hopkinson Tension Bar (SHTB) and a Universal Testing Machine (UTM) was utilised to investigate the defect growth behaviour of Al-Mg-Sc alloy (*a.k.a* Scalmalloy) in quasi-static to dynamic strain rate regime. These systems provide a unique opportunity for real-time *in-situ* X-ray imaging, allowing to visualise microstructural changes (*e.g.*, defect / pore formation and propagation) in the bulk of the specimen undergoing dynamic or quasi-static deformation. Scalmalloy specimens are 3D printed at 90° to the printing bed and tested under tension. Initial analysis of the experimental radiographs provides a qualitative comparison of the defect growth rate from quasi-static to dynamic rates of loading.

1 | INTRODUCTION

Design of light-weight, high-strength and sustainable materials in the fields of aerospace and auto-motive industries require material response data from crash and impact loading conditions [1, 2, 3]. In kolsky bar experiments the dynamic evolution of full-field strain on the surface of specimen is recorded by high speed cameras, and analysed by Digital Image Correlation (DIC) [4]. Similarly high speed cameras are also used to study the damage history inside the specimen for transparent mate-rials [5, 6]. However, when the transparency is destroyed during the deformation, or when the spec-imens are optically opaque to begin with, the detailed subsurface damage information is no longer visible. To study the internal damage mechanisms in such specimens, X-rays become a natural choice to image through the thickness of the specimen.

This work presents early experimental results of a custom-made dynamic and quasi-static trac-tion setups tailored to the capabilities of *operando* ultra high speed phase-contrast X-ray radiography at Beamline ID19 of the European Synchrotron Radiation Facility (ESRF), Grenoble, France. Propa-gation based X-ray phase contrast imaging (XPCI) is applied in real-time, that results in an increased contrast of material edges, while on the other hand, preserves the material geometrical representa-tion. This works incorporates both - a Split-Hopkinson Tension bar (SHTB) for high rates of strain ($500 - 5000$ s^{-1}) and a Universal Testing Machine (UTM) for low strain rate ($10^{-3} - 1$ s^{-1}) to test additively manufactured (AM) 3D printed Al-Mg-Sc alloy (*a.k.a* Scalmalloy) specimens.

2 | MATERIALS AND METHODS

2.1 | Specimens

This work investigates the Scandium modified Aluminium-magnesium alloy AA5028, sold under the trade name Scalmalloy by APworks GmbH, Germany. Previous works on Scalmalloy is detailed in [7, 8]. The raw stock blanks with dimensions of $100 \times 23 \times 3$ mm^3 ($l \times b \times t$) were produced by a commercial Laser Beam Melting system (EOS M 400). The specimens were printed in a 90° orientation to the build plate. The final specimen geometry, according to Fig. 1 was then obtained by CNC machining. This geometry of the specimen was chosen to work well with the constrains of our Split Hopkinson Tension bar and thickness at parallel gauge region are definitive of the fracture location.
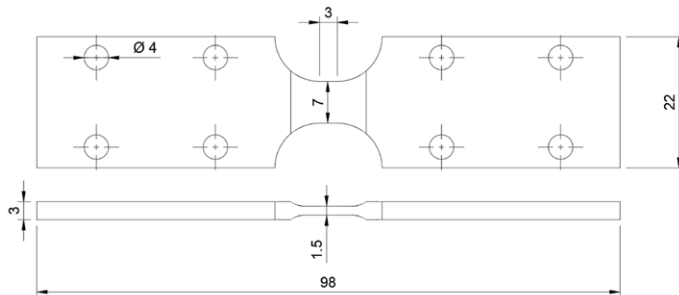
FIGURE 1   Geometry of the specimen with parallel gauge region of $7 \times 3 \times 1.5$ mm^3. All dimensions are in mm.

2.2 | Experiments

A custom-built Universal Testing Machine (UTM) is utilised in this work. A planetary gear stepper motor drives a spindle shaft in linear motion allowing to perform both compression and tension experiments. A maximum force of 10 kN can be achieved under loading of the setup. The machine works at velocities $\approx$ 10 mm/s, corresponding to slow and quasi-static strain rates ($10^{-3} - 1$ s^{-1}).

During slow tensile experiments, a 500 µm single crystal scintillator LuAG:Ce is used to convert X-rays to visible light registered by the detector. A high speed camera Photron SAZ captures image sequences of the transmitted X-ray radiographs of deforming sample. At 1$\times$ optical magnification of lens, a pixel pitch of 20 µm/px is achieved. The camera records the deformation images with a resolution of 1024 $\times$ 1024 px at a frame rate of 10 kHz for $\approx$ 20 sec. The camera frame is adjusted to capture only the parallel gauge region of the specimen. The loading onset is synchronised with the XPCI system to capture the deformation process.

The Split-Hopkinson Tension Bar (SHTB) employed in this work is sketched in Fig. 2. This setup is designed to achieve well defined loading rates and to give accurate force measurements at short time scales. The striker tube is a hollow polyoxymethylene (POM) shaft of 286 mm long with a wave propagation speed c_0 = 1400 m/s, given the length of the striker, the effective pulse duration T = (2 $\times$ striker length) / c_0 which approximates to 0.41 ms. A pressure range of 0.3 bar to 2 bar produces a velocity range of 2 - 15 m/s. At these controlled velocities, it is possible to perform high strain rate experiments in the order of 500 - 5000 s^{-1}. Forces are measured via the strain gauges mounted on both bars, which are connected diagonally to a Wheatstone bridge circuit to eliminate bending information.
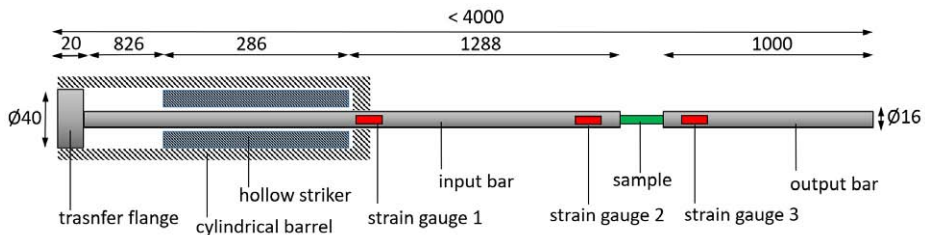
FIGURE 2 Sketch of the SHTB setup employed in this work. All dimensions in mm. Input and output bars are 16 mm diameter aluminium rods. The striker is a hollow POM tube of 40 mm outer diameter.

During the dynamic experiments, a 500 µm single crystal scintillator LYSO:Ce is used to convert transmitted X-ray spectrum into visible light registered by the detector. An ultra high speed camera, Shimadzu HPV-X2 with 1$\times$ optical magnification records the projected luminescence images of a deforming sample in an indirect fashion *via* a mirror. The detector pitch size of 32 µm/px results in a large field-of-view (FOV) of 12.8 $\times$ 8 mm^2 with a pixel count of 400 $\times$ 250 px per recorded frame. The detector continuously records 128 frames within the on-board memory. The camera can record at frame rates up-to 2 MHz. In this work, 530 ns of inter-frame temporal sampling is used at 200 ns exposure time. More information on XPCI and synchronised X-ray pulses is discussed in [9, 10, 11].

3 | RESULTS

The high strain rate dynamic experiments and slow quasi-static strain rate experiments were carried out in SHTB and UTM respectively. The crack propagation in Scalmalloy induced by tension load are shown in Fig. 3. A clear depiction of the crack was achieved by XPCI: The image contains information from both attenuation (material thickness or density) and interference effects stemming from abrupt attenuation changes at interfaces. Thus, the overall image is an attenuation image with enhanced edge contrast. Defects, such as pores provide local contrast, which we can observe in XPCI. The quasi-static radiographs (Fig. 3A) are of remarkably high quality in terms of sharpness and contrast. Dynamic experiments (Fig. 3B) has higher frame rate while compromising the image resolution (higher signal to noise ratio). In all experiments, the crack initiated from centre to orthogonal edges of the specimen with ± 45° fracture of the cross-sectional area in the parallel gauge region.
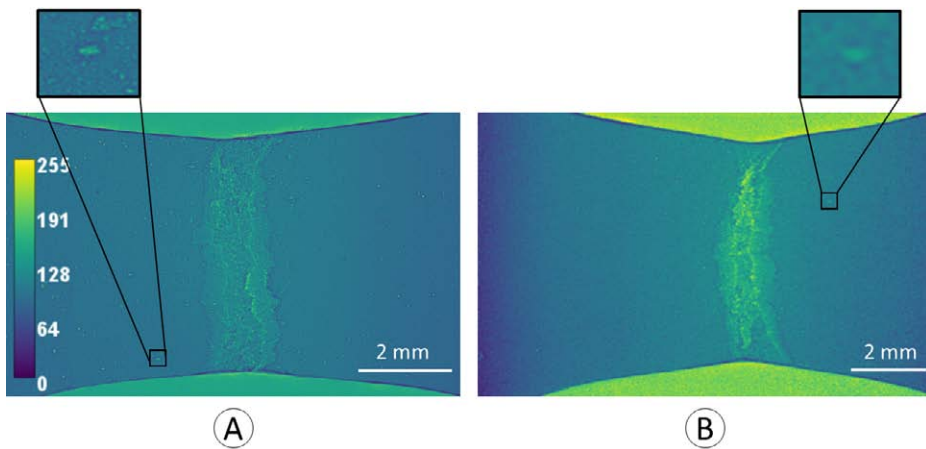
FIGURE 3 Pseudo-coloured grey values on the crack coalescence radiographs. Scalmalloy at facture in, **A** quasi-static tension test, **B** dynamic tension test

These radiographs have been utilised to study the pore (void) evolution by counting the number of defects and their size. To this end, we use a simple segmentation / particle analysis algorithm from ImageJ. The resulting graph in Fig. 4 indicates defect concentration (dimensionless) as a function of time for quasi-static and dynamic testing conditions. The data shows exponential defect growth. This is in agreement with the theoretical understanding from Tvergaard and Needleman's modification of Gurson's model [12, 13, 14]. This theory states that strong increase in local plastic strain is accompanied by exponential void growth at the location of failure: Following void growth, individual voids coalesce into a larger defect which grows into a macroscopic crack. The void growth and coalescence model is established for ductile failure. However, the material under consideration here, Scalmalloy, does certainly not exhibit typical ductile behaviour, as it fails at plastic strains of only $\approx 10\%$ [7]. Nevertheless, a cohesive zone model by Needleman also suggests exponential damage evolution in a brittle bulk material [15]. The cracks are constrained to propagate with these cohesive zones, while the surrounding material is undamaged post to fracture.
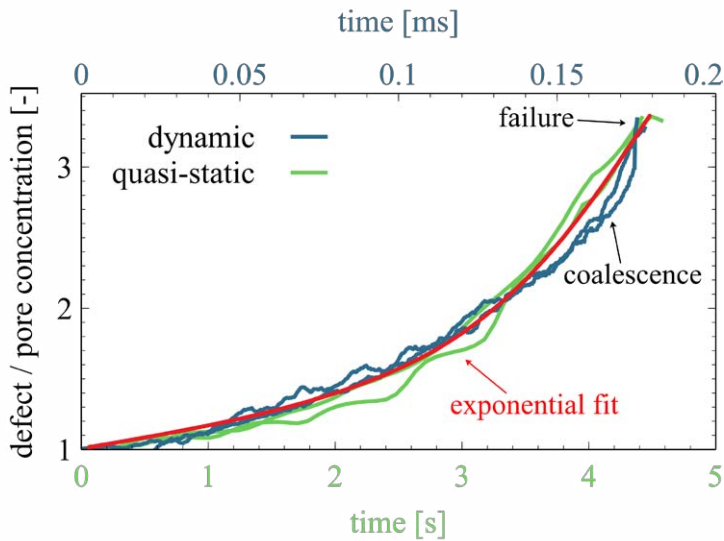
FIGURE 4 Comparison of defect concentration of dynamic with quasi-static. The vertical axis denotes defect concentration in dimensionless units (the values have been normalised with the first value so that the data set starts from unity).

We note that our defect analysis algorithm using ImageJ is sensitive enough to measure variations in brightness to approximately $\pm$ 5 %. This allows us to qualitatively compare the growth rate of defects in the material. An absolute measurement could be obtained by normalizing the defect count from our algorithm with respect to a reference defect count. The latter can be obtained from CT scans of the specimens prior to destructive tension, however, this was not done here.

4 | SUMMARY AND CONCLUSION

This work investigates the defect growth rate of Al-Mg-Sc alloy Scalmalloy, which is specifically used for additive manufacturing purposes. Here, the bulk tensile specimens were 3D printed and machined to final dimensions. Using a combination of Universal Testing machine and Split Hopkinson Tension bar methods, Scalmalloy tension tests ranging from 10^{-3} to 10^3 /s of strain rates were performed. Scalmalloy fails to show any strain rate sensitivity and we note that the observations made here only apply to strain rates of 1000 /s and below. The defect/void growth rate is observed to be exponential in both quasi-static and dynamic tension experiments. Further detailed analysis is required to understand the influence of stress triaxiality and strain hardening on void nucleation and coalescence with ductile specimens in consideration. Ultra high speed *in-situ* XPCI with combination of the mentioned setups provides a possibility to study the material micro-structure, void nucleation and collapse, fracture, delamination, and hot spot formation with high temporal and spatial resolution.

Acknowledgements

Metallic base materials

References

[1] Z. Ozdemir, E. Hernandez-Nava, A. Tyas, J. A. Warren, S. D. Fay, R. Goodall, I. Todd, and H. Askes, "Energy absorption in lattice structures in dynamics: Experiments," *Journal of Impact Engineering*, vol. 89, pp. 49–61, Dec. 2016.

[2] A. Tsouknidas, M. Pantazopoulos, I. Katsoulis, D. Fasnakis, S. Maropoulos, and N. Michailidis, "Impact absorption capacity of 3d-printed components fabricated by fused deposition modelling," *Materials and Design*, vol. 102, pp. 41–44, Apr. 2016.

[3] S. Li, S. Zhao, W. Hou, C. Teng, Y. Hao, Y. Li, R. Yang, and R. D. K. Misra, "Functionally graded ti-6al-4v meshes with high strength and energy absorption," *Advanced Engineering Materials*, vol. 18, pp. 34–38, May 2016.

[4] A. Gilat, T. E. Schmidt, and A. L. Walker, "Full field strain measurement in compression and tensile split hopkinson bar experiments," *Experimental Mechanics*, vol. 49, pp. 291–302, Aug. 2009.

[5] W. W. Chen, A. M. Rajendran, B. Song, and X. Nie, "Dynamic fracture of ceramics in armor applications," *Journal of The American Ceramic Society*, vol. 90, pp. 1005–1018, Apr. 2007.

[6] B. Paliwal, K. T. Ramesh, J. W. McCauley, and M. Chen, "Dynamic compressive failure of alon under controlled planar confinement," *Journal of The American Ceramic Society*, vol. 91, pp. 3619–3629, Nov. 2008.

[7] P. Jakkula, G. Ganzenmüller, F. Gutmann, A. Pfaff, J. Mermagen, and S. Hiermaier, "Strain rate sensitivity of the additive manufacturing material scalmalloy," *Journal of Dynamic Behavior of Materials*, vol. 7, pp. 518–525, Apr. 2021.

[8] M. Vorel, S. Hinsch, M. Konopka, and M. Scheerer, "Almgsc alloy 5028 status of maturation," *7th European Conference for Aeronautics and Space Sciences (EUCASS)*, vol. 633, p. 4, July 2017.

[9] A. Rack, M. Scheel, L. Hardy, C. Curfs, A. Bonnin, and H. Reichert, "Exploiting coherence for real-time studies by single-bunch imaging," *Journal of Synchrotron Radiation*, vol. 21, pp. 815–818, May 2014.

[10] A. Cohen, D. Levi-Hevroni, P. Fridman, D. Chapman, A. Rack, M. P. Olbinado, A. Yosef-Hai, and D. Eakins, "In-situ radiography of a split-hopkinson bar dynamically loaded materials," *Technical report for Sissa MediaLab*, vol. 14, pp. T06008–T06008, June 2019.

[11] M. P. Olbinado, X. Just, J.-L. Gelet, P. Lhuissier, M. Scheel, P. Vagovic, T. Sato, R. Graceffa, J. Schulz, A. Mancuso, J. Morse, and A. Rack, "Mhz frame rate hard x-ray phase-contrast imaging using synchrotron radiation," *Optics Express*, vol. 25, p. 13857, June 2017.

[12] A. Needleman and V. Tvergaard, "Analysis of plastic flow localization in metals.," *Applied Mechanics*, vol. 45, pp. S3–S18, Mar. 1992.

[13] A. L. Gurson, *Plastic Flow and Fracture Behavior of Ductile Materials Incorporating Void Nucleation, Growth, and Interaction*. phdthesis, Brown University - Applied Mechanics, June 1975.

[14] Z. L. Zhang, "A complete gurson model," *SINTEF materials Technology*, vol. 67, pp. 155–168, Jan. 2000.

[15] A. Needleman, "An analysis of decohesion along an imperfect interface," *International Journal of Fracture*, vol. 42, pp. 21–40, Jan. 1990.

02

Metallic structures

12

Vanishing auxetic behaviour for metal lattice structures at impact rates of strain

**G.C. Ganzenmüller[1*] | A. Roth[1*] | P. Jakkula[1]
| F. Gutmann[1] | A. Pfaff[2] | D. Eakins[3] |
D. Chapman[3] | B. Lukic[4] | A. Rack[4] |
S. Hiermaier[1,2]**

[1]Universität Freiburg, Institut für Nachhaltige Ingenieursysteme, INATECH, Gips-Schüle-Professur für Nachhaltige Ingenieursysteme, Germany

[2]Fraunhofer Ernst-Mach Institut für Kurzzeitdynamik, EMI, Freiburg, Germany

[3]University of Oxford, Department of Engineering Science, UK

[4]European Synchrotron Radiation Facility, Structure of Materials Group, beamline ID19, Grenoble, France

Correspondence
G. C. Ganzenmüller, Universität Freiburg, Emmy-Noether Str. 2, D-79110 Freiburg, Germany
Email: georg.ganzenmueller@inatech.uni-freiburg.de

This works reports experimental investigations at different velocities for the auxetic 3D anti-tetra-chiral lattice structure additively manufactured from 316L steel. Velocities range from the quasi-static regime over the Split-Hopkinson regime at 10 m/s to the gas gun regime up to 432 m/s. The dynamic compaction behaviour is visualized using high-speed optical cameras, and ultrafast X-Ray imaging for the highest velocities. We find that a homogeneous auxetic structural response can only be observed for velocities up to 10 m/s. At a velocity of 65 m/s, the homogeneous response transitions into a travelling auxetic wave front, similar to a plastic wave front in shock physics experiments. For even higher velocities, the auxetic response is replaced by a structural collapse front with zero Poisson's ratio.

---

[*]Equally contributing authors.

1 | INTRODUCTION

Auxetic materials have been investigated for many years due to their unconventional lateral contraction behaviour. As a consequence of their negative Poisson's ratio, they shrink in the lateral directions upon compression, and grow upon stretching. Historically, foams made of polymers have shown this phenomenon at low levels of mechanical performance. With the advent of the Selective-Laser-Melting additive manufacturing technology for metals, it is now possible to design such metamaterials with tailored properties, reaching high-levels of mechanical performance. Therefore, industrial applications of these materials are now within reach, and it has become important to fully understand their deformation behaviour, including damage and failure. One of the application areas where auxetic metamaterials are expected to perform better than their conventional counterparts is protection against impact. Under a concentrated compression load, auxectic materials contract and show enhanced resistance against indentation. To date, this mechanism has been mainly experimentally confirmed for quasi-static and comparatively slow loading conditions up to approximately 10 m/s. However, the intended usage scenarios encompass loading velocities which are higher by one order of magnitude. This work investigates the compaction behaviour over a wide range of compression velocities ranging from quasistatic to 432 m/s. To this end, we employ a universal testing machine, a direct-impact Hopkinson bar, a low pressure gas gun, and a high pressure gas gun. Deformations are recorded using high-speed cameras. At impact velocities > 100 m/s, ultrafast X-Ray imaging at the European Synchrotron source in Grenoble is employed. The remainder of this work is organized as follows. We describe the materials and the manufacturing method, followed by a description of the experimental methods. Subsequently, the dependence of Poisson's ratio on impact speed is analysed.

2 | MATERIALS AND METHODS

2.1 | Specimen manufacturing

We study the 3D Anti-Tetrachiral Structure (ATC) which was introduced by Hsin-Haou et al. [1]. Its design was inspired by [2]. The goal was to achieve contraction through internal rotation of the unit cells around their respective centers. The unit cell and the resulting lattice structures are shown in Fig. 1. This metamaterial exhibits transverse isotropy within the X-Y-plane, but different mechanical behaviour in the Z-direction. Therefore, in all following experiments the load is applied exclusively in Z-direction to ensure comparability between the results. Specimens were manufactured at Fraunhofer Ernst-Mach-Institute using an EOS M 400 3D printer and 316L powder also from EOS.

2.2 | Quasi-static testing

The structure is compressed at a strain rate of 10^{-3} /s using a Zwick Z100 testing machine in displacement control mode. Force was measured using a 100 kN load cell with an accuracy better than 0.1% for forces larger than 200 N. The structural deformation is recorded as monochrome images using a Basler ace 2 camera with 12 MP resolution. Images are post-processed using global Digital Image Correlation (DIC), to yield quantitative full-field displacement measures. We use the DIC code *Correli* [3].
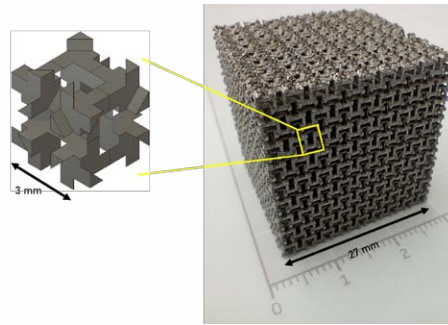
FIGURE 1 left: CAD model of the ATC unit cell. right: photograph of printed specimen with 9x9x9 unit cells and a total edge length of 27 mm.

2.3 | Testing with Hopkinson Bars

Testing at higher velocities, $\approx$ 10 m/s is done using a Direct Impact Hopkinson Bar (DIHB) with instrumented striker. The setup is detailed in [4] and we only note the key details here for brevity: The bars are 40 mm diameter 7075 aluminium. The maximum pulse duration is 0.78 ms. Force measurement is facilitated using strain gauges on input- and output bar. The strain gauge signals are amplified by a factor of 100 using a high-bandwidth amplifier (Elsys SGA-2) and digitized by a transient recorder with 14 bit resolution (Elsys TPCE). The entire setup is carefully calibrated as a system under quasi-static loading with a reference load cell, such that calibration factors are obtained which convert Wheatstone bridge voltage output to force reading. These calibration factors correct for potential strain gauge misalignment and unknown electrical resistance in the connections. However, the calibration rests on the assumption that the Young's modulus of the bars is not strain-rate sensitive. The advantage of the setup are the nearly identical stress waves propagating away from each other in the input and the output bar. This facilitates the evaluation a force equilibrium and allows to calculate an average force between the two signals, which is nearly free from oscillations. For the higher compaction velocity considered here, 65 m/s, the instrumented striker is replaced by a short striker made from Polyoxymethylene (POM) without strain gauges. This reduced mass can be accelerated to 70 m/s in the same setup. Due to the low speed of sound in POM, the pulse duration is not reduced. However, a strain gauge cannot be reliably attached to the striker, so only the force on the output bar is available for this configuration. In all cases, images are recorded using a Photron SAZ high-speed camera and post-processed using DIC.

2.4 | Gas Gun testing and X-Ray imaging

For compaction velocities in the range of 100 m/s to 432 m/s, an in-situ gas gun setup at the European Synchrotron Radiation Facility, beam line ID19 is employed [5]. The metamaterial is glued to an anvil made from Polyoxymethylene (POM) and impacted by a POM projectile. Imaging is performed by passing the Synchrontrons's X-ray radiation through the sample and onto a fast scintillator, which converts the high-energy photons to the visible spectrum. The scintillator is imaged using a split optical path and two Shimadzu HPV-X2 cameras. The cameras are interlaced in time, such that a

maximum framerate of 10 MHz can be achieved.

3 | ANALYSIS OF POISSON'S RATIO

Representative snapshots of the deformation observed in the different strain rate regimes are shown in Fig. 2. Under quasi-static compression, a uniform deformation mode is observed, where the sample contracts in an auxetic manner. The contraction is most pronounced in the center of the sample. At the boundaries of the sample, where load is applied, friction constrains the auxetic response. At around 25% nominal compressive strain, evaluated using DIC, the metamaterials reaches the densification strain, as indicated by a steep rise of the force response. Essentially the same behaviour is observed for compression at a strain rate of 300 /s, corresponding to a velocity in the direct-impact Hopkinson bar of 10 m/s. Force/displacement curves for quasi-static and 300 /s compression experiment coincide within the experimental uncertainties of approximately 5%, so no strain rate sensitivity for the is observed (data not shown in this work). Upon further increase of the strain rate to 1000 /s using the short striker configuration in the Hopkinson bar, a change of the deformation behaviour is observed. Instead of the uniform auxetic response, we now observe a localization of the auxetic response at the impact side of the sample. This localized auxetic response moves through the sample at a velocity of 160 m/s, for an impact velocity of 65 m/s. This phenomenon is similar to a plastic deformation front in shock physics experiments, which travel much slower than elastic waves. The gas gun experiments conducted at ESRF show that for an impact velocity of 432 m/s, corresponding to a strain rate of 10^4 /s, the auxetic response is completely absent. Instead, the structure exhibits cell collapse starting at the impact side of the sample, similar to a low-density foam with zero Poisson's ratio.

These qualitative observations are further analysed using DIC to compute Poisson's ratio as a function of impact velocity. For the quasi-static and Hopkinson bar experiments, this was achieved using straightforward evaluation of the gradients of the full displacement field. For the X-Ray images, a more robust approach was required due to little local contrast in the images. Here, 16 different cell positions were tracked, and Poisson's ration was evaluated from a finite difference stencil of the corresponding displacements, similar to the work of Fila *et al.* [6].

The strain rate dependency of Poisson's ratio v is shown in Fig. 3. For velocities ≤ 65 m/s, strongly auxetic behaviour with $v = -0.25 \pm 0.05$ is observed. This behaviour transitions smoothly upon increase of velocity and reaches zero Poisson's's ratio at 200 m/s and above. The observed behaviour as a function of velocity v can be approximated by a smooth logistic curve,

$$v(v) = \frac{a}{1 + \exp\left[-b(v - v_0)\right]} \tag{1}$$

with $a = -0.25$, $b = -0.03$ s/m, and $v_0 = 136$ m/s.
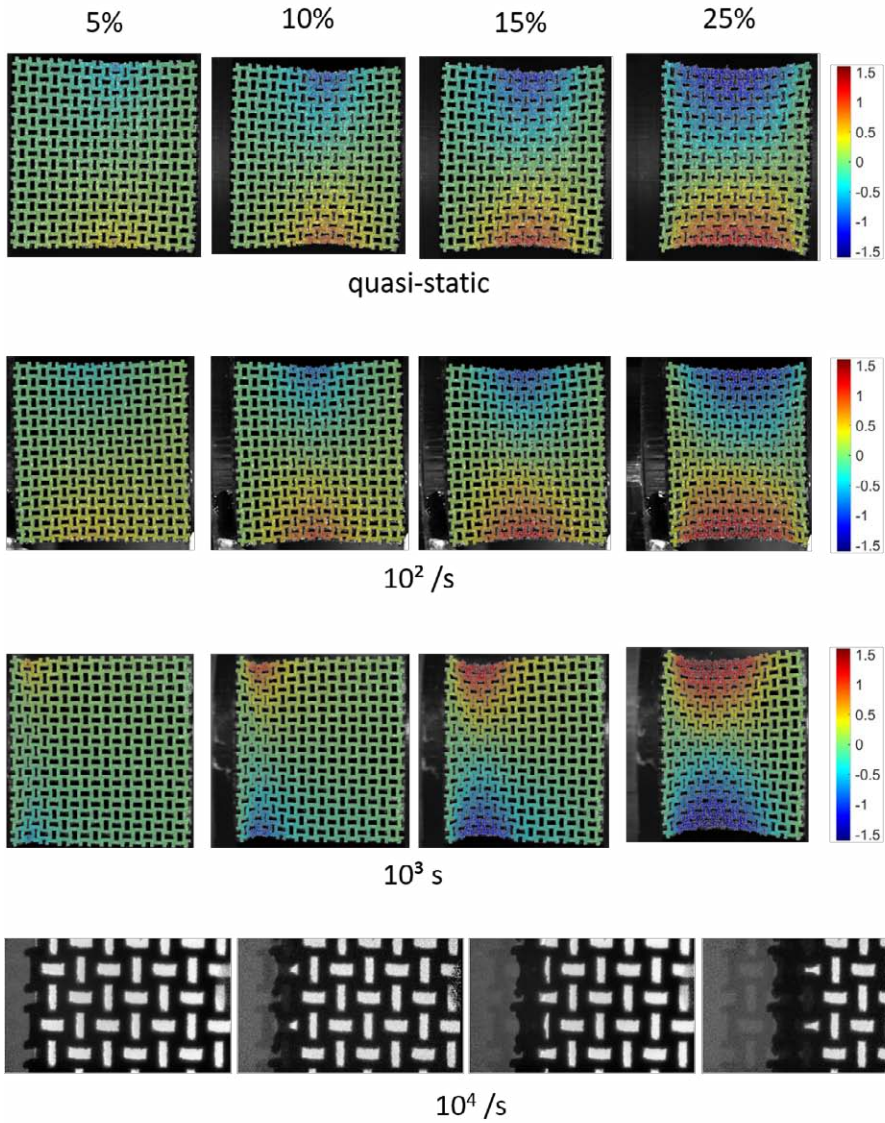
FIGURE 2 Image sequences for the different velocities tested here. Each column of images corresponds to a given nominal strain, which is noted at the top of the column. The color scale indicates the displacement in mm perpendicular to the loading direction, obtained from DIC. For the X-Ray images in the bottom row, no reliable full-field DIC analysis could be performed due to insufficient local contrast, however, it was possible to track individual regions of the images.
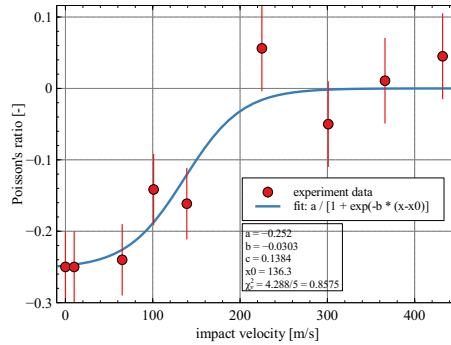
FIGURE 3   Plot of Poissons's ratio vs. impact velocity. Error bars at velocities < 100 m/s indicate the standard deviation across multiple experiments. At higher velocities, only a specimen was tested in each case, and the uncertainty was estimated using the standard deviation from the lower velocities.

4 | DISCUSSION

Auxetic behaviour of lattice materials is a structural deformation mode, not a base material property. As such, its response to dynamic loading is governed by its unit cell geometry, and timescales linked to the unit cell. This work shows for the particular choice of the anti-tetrachiral unit cell and the base material 316L steel, that auxetic behaviour can only be observed below a critical velocity of 136 m/s. This is noteworthy, as auxetic structures are often believed to be a good choice for impact protection and high-speed energy absorbers.

References

[1] Huang HH, Wong BL, Chou YC. Design and Properties of 3D-printed Chiral Auxetic Metamaterials by Reconfigurable Connections. physica status solidi (b) 2016;253(8):1557–1564.

[2] Shen J, Zhou S, Huang X, Xie YM. Simple Cubic Three-Dimensional Auxetic Metamaterials. physica status solidi (b) 2014;251(8):1515–1522.

[3] Tomičević Z, Hild F, Roux S. Mechanics-Aided Digital Image Correlation. The Journal of Strain Analysis for Engineering Design 2013 Jul;48(5):330–343.

[4] Jakkula P, Ganzenmüller GC, Beisel S, Rüthnick P, Hiermaier S. The Symmpact: A Direct-Impact Hopkinson Bar Setup Suitable for Investigating Dynamic Equilibrium in Low-Impedance Materials. Exp Mech 2021 Oct;.

[5] Lukić B, Blasone M, Duplan Y, Forquin P, Escauriza E, Rutherford M, et al. Ultra-High Speed X-ray Imaging of Dynamic Fracturing in Cementitious Materials under Impact. EPJ Web Conf 2021;250:01014.

[6] Fíla T, Koudelka P, Zlámal P, Falta J, Adorna M, Neuhäuserová M, et al. Strain Dependency of Poisson's Ratio of SLS Printed Auxetic Lattices Subjected to Quasi-Static and Dynamic Compressive Loading. Advanced Engineering Materials 2019;21(8):1900204.

$\boxed{13}$

Open Hopkinson Bar as a Method for Impact Testing of Additively Manufactured Cellular Metamaterials

Tomáš Fíla[1] | **Jan Falta[1*]** | **Petr Zlámal[1*]** |
Petr Koudelka[1*] | **Jan Šleichrt[1*]** |
Michaela Neuhäuserová[1*] | **Václav Rada[1*]** |
Ondřej Jiroušek[1*]

[1]Czech Technical University in Prague,
Faculty of Transportation Sciences, Prague,
110 00, Czech Republic

Correspondence
Tomáš Fíla, Czech Technical University in
Prague, Faculty of Transportation Sciences,
Prague, 110 00, Czech Republic
Email: fila@fd.cvut.cz

Open Hopkinson Pressure Bar (OHPB) apparatus is used, together with conventional split Hopkinson pressure bar (SHPB), for dynamic testing of additively manufactured cellular metamaterials at intermediate and high strain rates. Benefits of the OHPB testing method over standard established methods are discussed. The investigated metamaterials include various types of auxetic lattices manufactured from powdered austenitic steel by powder bed fusion technology. It is found out that the investigated type of metamaterials exhibits significant strain rate sensitivity of the stress-strain curves as well as of the apparent auxeticity. Moreover, its deformation mechanism changes with the increasing impact velocity as the buckling of the individual struts is reduced by the inertia effects.

---

[*]Equally contributing authors.

---

1 | INTRODUCTION

Currently, rapid development of modern and progressive methods for the fabrication of novel materials is taking place, while the advances in the innovative material production methods such as 3D printing, laser powder bed fusion (PBF), nanofabrication or state-of-the-art coating procedures have allowed for the onset of metamaterials. The mechanical metamaterials are described as a group of materials developed to exhibit deformation behavior that is not observed in conventional, naturally occurring, materials. Due to this fact, unfortunately, the internal structure of metamaterials is usually complex and analysis of their mechanical properties is not easy and dependent on a number of factors. Moreover, the deformation behavior exhibits mechanisms that are still not sufficiently characterized and understood. Therefore, an in-depth research aimed at the analysis of the mechanical properties and deformation behavior of metamaterials under a variety of conditions is currently ongoing, while a special attention is being paid to behavior at intermediate and high strain rates. Often, the specialized experimental techniques are developed for such purposes. The subject of this paper is the investigation of metamaterials at high strain rates using a non-standard split Hopkinson bar method. While the conventional split Hopkinson pressure bar (SHPB) is a well-established technique for the dynamic testing of materials, it can only be used straightforwardly for experiments with ductile and high-strength materials, typically solid metals. Its application on soft materials and materials with low mechanical impedance is problematic and may lead to unreliable results [1, 2]. Such type of the experiments usually requires an upgrade of the experimental apparatus and it is also necessary to employ the advanced data correction techniques to be able to properly evaluate the relevant mechanical properties [1, 3]. A number of research papers investigating lattices [4], foams [5] or honeycombs subjected to dynamic loading using a variety of split Hopkinson bars is rapidly growing. Related phenomenons including strain rate sensitivity, inertia effects [5] and change of deformation modes at high strain rates [3] are also subject of interest. Digital image correlation (DIC) represents an advanced approach for evaluation of the SHPB experiments and this technique is being increasingly employed, e.g., for analysis of impact behavior of metal foams [6]. On the other hand, the principle of SHPB has some problems limiting its application in experiments with soft and cellular materials, where high deformations, typically connected with a broad spectrum of strain rates, is necessary to be able to relevantly describe the deformation behavior of the materials. A novel technique called Open Hopkinson Pressure Bar (OHPB) has been developed to overcome some of the aforementioned problems. The principle of the OHPB technique is based on the direct impact Hopkinson bar variants [7, 8, 9] and can be used as a method for the intermediate and high strain rate testing. It was first published in 2016 by Govender and Curry [8]. In this paper, a physical representation of the OHPB is presented showing that the results measured using the OHPB method are reliable and directly comparable with the SHPB method. The technique exhibits a number of advantages and beneficial arrangements over the SHPB method, particularly in the testing of soft and low impedance cellular materials [10]. Although the method has a lot of advantages, it is not, in general, superior to the other existing split Hopkinson bar methods and has its own disadvantages. As in the other cases, the experimental technique and its performance have to be carefully adjusted to fit in the application envelope of the technique.

In this paper, an OHPB is employed for uni-axial compression of additively manufactured auxetic lattices at intermediate and high strain rates. It is found out that the investigated type of metama-

terials exhibits significant strain rate sensitivity of the stress-strain curves as well as of the apparent auxeticity. Moreover, its deformation mechanism changes with the increasing impact velocity as the buckling of the individual struts is reduced by the inertia effects.

2 | MATERIALS AND METHODS

2.1 | OHPB Principle

The principle of the OHPB method is similar to the other direct impact Hopkinson bar methods. The principle of the OHPB is compared with the established forward and reverse direct impact Hopkinson bar methods (FDIHB, RDIHB) in Fig. 1. While in the forward and reverse direct impact Hopkinson bar only the transmission bar is instrumented with a strain gauge, the OHPB is instrumented with strain gauge on both the incident and the transmission bar.
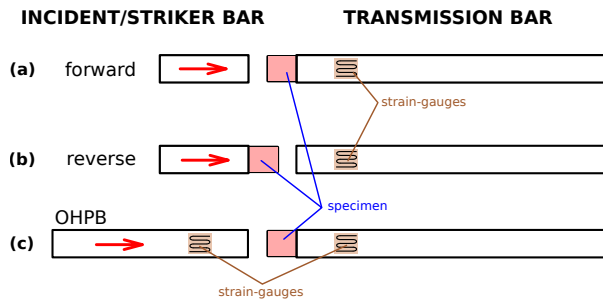
FIGURE 1   (a) forward direct impact Hopkinson bar, (b) reverse direct impact Hopkinson bar, and (c) the OHPB.

The OHPB has two bars (incident and transmission) instrumented with strain-gauges. The incident bar is put directly in the barrel of the gas-gun and thus it substitutes the striker bar used in the conventional SHPB. The specimen is located at the transmission bar. During the impact, the gas-gun is used to accelerate the incident bar that directly impacts onto the specimen. The strain waves are induced in both bars by the deformation of the specimen and propagate from the bar-to-specimen interface to the free ends of the bars. At the free ends, the pulses are reflected back as the tensile pulses that propagate again to the interface with the specimen. The standard time window of the experiment ends when the reflected waves produce superposed signals at the strain-gauges. However, as the boundary conditions of the experimental setup are well defined, a wave separation technique can be employed to prolong the time window of the experiment [11]. As the waves propagate from the interfaces with the specimen they exhibit an approximately identical amplitude and shape. The transmission pulse occurs later than the incident pulse as the strain wave has to propagate through the specimen (similarly to the SHPB). The strain-gauge signals are used to calculate the actual forces, velocities and displacements at the respected interfaces of the bars with the specimen (input and output) [8]. In the OHPB, the evaluation of the strain (or actual length of the specimen) is directly dependent on the initial impact velocity. Therefore, unlike in the standard SHPB method, it is crucial to measure the pre-impact velocity with high precision, e.g., with DIC, as this quantity directly affects

the evaluated results of the experiment. In case of the SHPB, the striker bar impact velocity serves only as a secondary parameter useful for the initial verification of the incident strain wave amplitude.

2.2 | Design of the OHPB

A modification to the OHPB apparatus originally described in [8] was proposed and assembled in our laboratory. In this configuration, the incident bar is not entirely inserted in the barrel of the gas-gun, but its forward section, carrying the strain-gauges, is always in front of the barrel [11]. The position of the bars during the impact is ensured not by the axis of the barrel, but by a linear guidance system. The maximum impact velocity of the method is constrained by the length of the linear guidance system and the incident bar. The OHPB experimental setup is shown in Fig. 2.
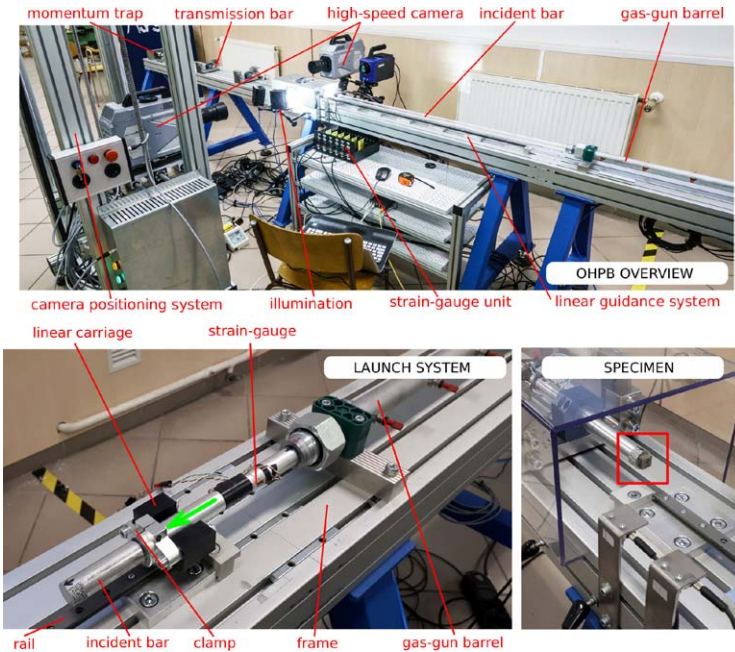
F I G U R E 2   The overview of the OHPB experimental setup.

In the presented configuration, the typical length of the incident bar ranges from 1500 mm to 1800 mm. The rear part of the incident bar is inserted in the barrel of the gas-gun while the forward part is guided by the linear rail system. The strain-gauges at the incident bar are mounted typically 200 mm from the impact face while the linear guidance system is usually placed in front of the strain-gauges. This system consists of a friction clamp, an aluminum alloy flange, a carriage (DryLin T, TW-04-12, IGUS, Germany) with a low friction polymeric liner, and a linear guide rail with a length of 1400 mm. The adjustment and calibration of the clamp tightening moment before the experiments represents an important aspect that can negatively affect the results. The system is attached to the main frame using a set of washers. At the peak air pressure of 1 MPa, the gas-gun can accelerate the incident bar made of aluminum alloy with a typical length of 1600 mm and mass of approx. 1.5 kg to the

maximum impact velocity of approx. $18 - 20\,\text{ms}^{-1}$. The significantly lighter polymethyl-methacrylate (PMMA) bar with an increased length of $1750\,\text{mm}$ can be accelerated to the maximum impact velocity of approx. $25 - 30\,\text{ms}^{-1}$. Thus, the maximum strain rate of the OHPB method overlaps with the lower range of the strain rates of our SHPB. It is possible to employ the OHPB method for testing at the strain rates ranging between the drop-weight tower test and the SHPB. The lower strain rate limit in the OHPB is constrained predominantly by the impacting mass (mass of the striker bar). As the impact energy is linearly proportional to the impacting mass and also proportional to the square of the impact velocity, the impact energy decreases dramatically with the lower impact velocities. With a reduced energy margin in the low velocity experiments, the strain rate during the impact can drop dramatically, because the specimen absorbs a significant portion of the impact energy.

2.3 | Additively manufactured auxetic lattices

Three types of additively manufactured periodic auxetic lattices were manufactured using laser PBF from powdered 316L-0407 austenitic steel: i) 2D re-entrant, ii) 3D re-entrant, iii) missing rib. The overall dimensions of the specimens were approximately $12.0 \times 12.0 \times 13.0\,\text{mm}$ with porosity ranging from $52\,\%$ (2D re-entrant) to $74\,\%$ (3D re-entrant). The cubic specimens are shown in the respected plots in Fig. 3.

3 | EXPERIMENT

During the experiments with the additively manufactured lattices, the effects of micro-inertia, strain rate sensitivity and strain rate related friction were analyzed. The specimens were investigated under both quasi-static and high strain rate uni-axial compression conditions using the OHPB as well as the SHPB, in total at four selected strain rates. At each strain rate, a set of at least five specimens was tested to evaluate reproducible results and to guarantee sufficient level of statistics. At first, the specimens were measured under quasi-static conditions and then the parameters of the high strain rate experiments were adjusted for all the lattice types to achieve similar (comparable) strain rate and maximum strain. Experiments at two lower strain rates (approx. $500\,\text{s}^{-1}$ and approx. $1000\,\text{s}^{-1}$) were conducted using the OHPB whereas the set of two higher strain rates (approx. $1500\,\text{s}^{-1}$ and approx. $3000\,\text{s}^{-1}$) was measured using the SHPB.

4 | RESULTS AND CONCLUSION

Strain rate sensitivity was investigated through analysis of the stress-strain curves. The stress-strain and strain rate-strain curves for all types of the structures are shown in Fig. 3a (2D re-entrant), Fig. 3b (3D re-entrant), and Fig. 3c (missing rib). Strain rate sensitivity was identified for all types of the lattices. It was also found out that the auxetic lattices showed less buckling effects with the increasing strain rate as the inertia effects prevented the side movements. For demonstration of this behavior, the 2D re-entrant lattice type was selected and its behavior is shown in Fig. 3d. Specific strain energy density ratio was calculated as a ratio of the strain energy density at a given strain rate and the quasi-static strain energy density (both integrated in a range of strain from 0 to 0.15). The specific strain energy density ratios of all the structures plotted against the average strain rate are shown in Fig. 3e
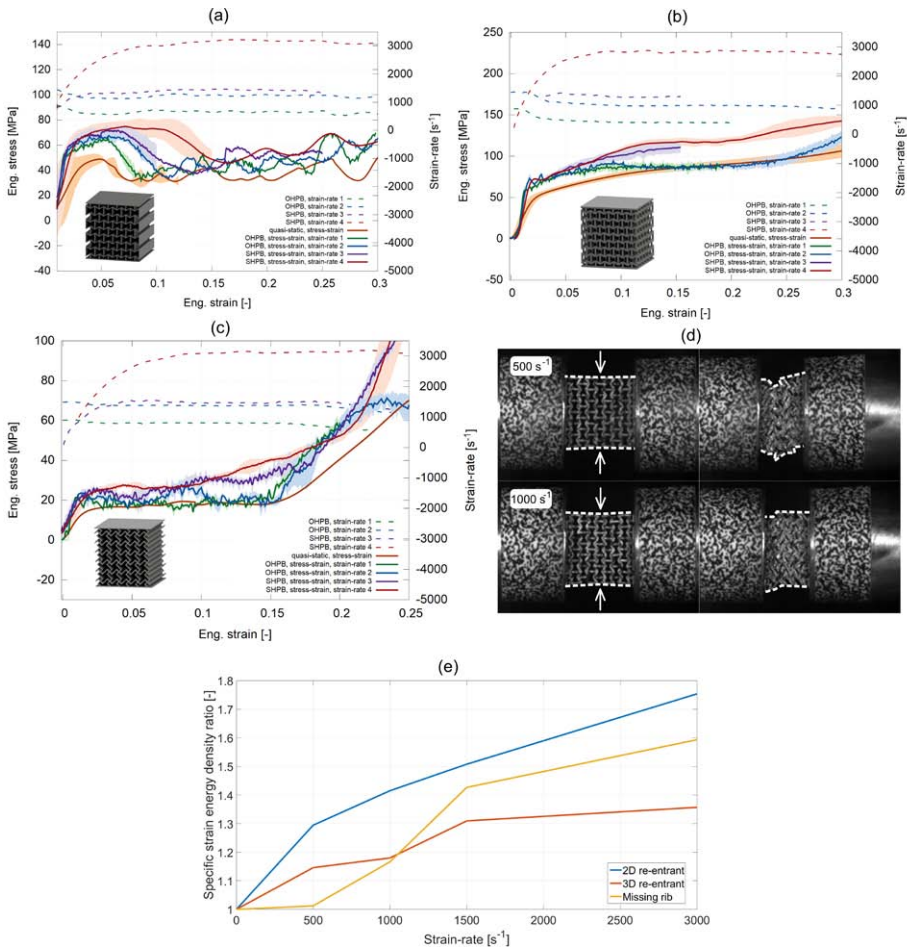
FIGURE 3   Stress-strain curves for 2D re-entrant (a), 3D re-entrant (b), and missing rib (c). Buckling effects of the 2D re-entrant at two different strain rates (d). Specific strain energy density ratio for all types of the structures (e).

and are summarized in Tab. 1. All the structures exhibited a similar trend in the strain rate sensitivity as the specific strain energy density ratio increased with the impact velocity.

TABLE 1   Specific strain energy density ratio at the given strain rates.

Type of lattice	Specific strain energy density ratio			
	$500\,\mathrm{s}^{-1}$	$1000\,\mathrm{s}^{-1}$	$1500\,\mathrm{s}^{-1}$	$3000\,\mathrm{s}^{-1}$
2D re-entrant honeycomb	1.30	1.42	1.51	1.75
3D re-entrant honeycomb	1.15	1.18	1.31	1.36
2D missing-rib	1.01	1.17	1.43	1.59

Strain rate sensitivity of three types of auxetic lattices was analyzed using the OHPB method, that represents another type of direct impact Hopkinson bar arrangement and has the instrumentation of both bars. The results were compared with the experiments conducted in the conventional SHPB at higher strain rates. The lattices exhibited significant strain rate sensitivity and inertia effects affected their deformation behavior during compression. The OHPB method was evaluated as a vital technique for direct impact testing with many benefits and possible fields of application (e.g., instrumented penetration of medium-sized panels).

References

[1] Johnson T, Sarva S, Socrate S. Comparison of low impedance split-Hopkinson pressure bar techniques in the characterization of polyurea. Experimental mechanics 2010;50(7):931–940.

[2] Chen W, Zhang B, Forrestal MJ. A split Hopkinson bar technique for low-impedance materials. Experimental Mechanics 1999;39(2):81–85.

[3] Peroni M, Solomos G, Babcsan N. Development of a Hopkinson bar apparatus for testing soft materials: application to a closed-cell aluminum foam. Materials 2016;9(1):27.

[4] Tancogne-Dejean T, Spierings AB, Mohr D. Additively-manufactured metallic micro-lattice materials for high specific energy absorption under static and dynamic loading. Acta Materialia 2016;116:14–28.

[5] Wang P, Xu S, Li Z, Yang J, Zhang C, Zheng H, et al. Experimental investigation on the strain-rate effect and inertia effect of closed-cell aluminum foam subjected to dynamic loading. Materials Science and Engineering: A 2015;620:253–261.

[6] Liu J, Saletti D, Pattofatto S, Zhao H. Impact testing of polymeric foam using Hopkinson bars and digital image analysis. Polymer testing 2014;36:101–109.

[7] Zhao H, Elnasri I, Abdennadher S. An experimental study on the behaviour under impact loading of metallic cellular materials. International Journal of Mechanical Sciences 2005;47(4-5 SPEC. ISS.):757–774.

[8] Govender RA, Curry RJ. The "Open" Hopkinson Pressure Bar: Towards Addressing Force Equilibrium in Specimens with Non-uniform Deformation. Journal of Dynamic Behavior of Materials 2016;2(1):43–49.

[9] Hiermaier S, Meenken T. Characterization of low-impedance materials at elevated strain rates. Journal of Strain Analysis for Engineering Design 2010;45(6):401–409.

[10] Jakkula P, Ganzenmüller GC, Beisel S, Rüthnick P, Hiermaier S. The Symmpact: A Direct-Impact Hopkinson Bar Setup Suitable for Investigating Dynamic Equilibrium in Low-Impedance Materials. Experimental Mechanics 2022;62(2):213–222.

[11] Fíla T, Koudelka P, Falta J, Zlámal P, Rada V, Adorna M, et al. Dynamic impact testing of cellular solids and lattice structures: Application of two-sided direct impact Hopkinson bar. International Journal of Impact Engineering 2021;148.

14

Mechanical response of Inconel TPMS under dynamic loadings

P. Jabin Echeveste[1] * | **P. Viot PhD[1]** * | **Aitzol Lamikiz Mentxaka PhD[2]** * | **L. Le Barbenchon PhD[1]** *

[1]I2M Bordeaux UMR CNRS 5295, University of Bordeaux, Arts et Metiers Institute of Technology, Bordeaux INP, INRAe, Talence, 33400, France

[2]Dept. of Mechanical Engineering , Univ. of Basque Country UPV/EHU, Bilbao, Spain

Correspondence
Louise Le Barbenchon PhD, I2M Bordeaux UMR CNRS 5295, University of Bordeaux, Arts et Metiers Institute of Technology, Bordeaux INP, INRAe, Talence, 33400, France
Email: louise.le_barbenchon@ensam.eu

For this study, three classical geometries of TPMS obtained by additive manufacturing were considered. The constitutive material is an Inconel 718 alloy and the samples have a relative density around 30%. The mechanical behaviour of these structures is studied under uniaxial compression by imposing quasi-static and dynamic loadings. Taking into account the relative density, the sheet gyroid presented higher material parameters (stiffness, Specific absorbed energy, ...) because of its more generalized plastic deformation. The plateau stress of the architectured material increased by about 56 % when increasing the strain rate from 10^{-2}/s to 10^{3}/s for the skeletal gyroid.

1 | INTRODUCTION

Architectural materials allow the development of lightweight mechanical structures by optimizing the path of forces in normal or standard use [1, 2]. These structures can be used as energy absorbers since their mechanical response is often characterized by a threshold force over a long range of deformation. It is thus important to consider their behaviour under severe loadings in the case of dynamic charge (crash, shock) inducing large deformations [3, 4] according to the geometry of the structure, the constitutive material, the manufacturing process … TPMS structures were reported to exhibit enhanced mechanical properties compared with the truss-lattices at similar densities. In dynamic, the mechanical behaviour of stainless steel architectured samples has been already broadly studied [5, 6, 7, 8] in opposition to Inconel-based TPMS while Inconel is usually used for low and high temperature applications were dynamic loadings can happen.

2 | MATERIALS AND METHODS

2.1 | Samples conception and fabrication

Triply Periodic Minimal Surface (TPMS) samples were conceived thanks to the MSLattice software [9]. Three different geometries were chosen: primitive (also know as Schwarz P structure), sheet gyroid and skeletal gyroid (fig. 1). A relative density of 30% was set on MSLattice with a unit cell of 4 mm. Two different sample size were defined. One has 5×5×5 cell and the other has 3×3×3.
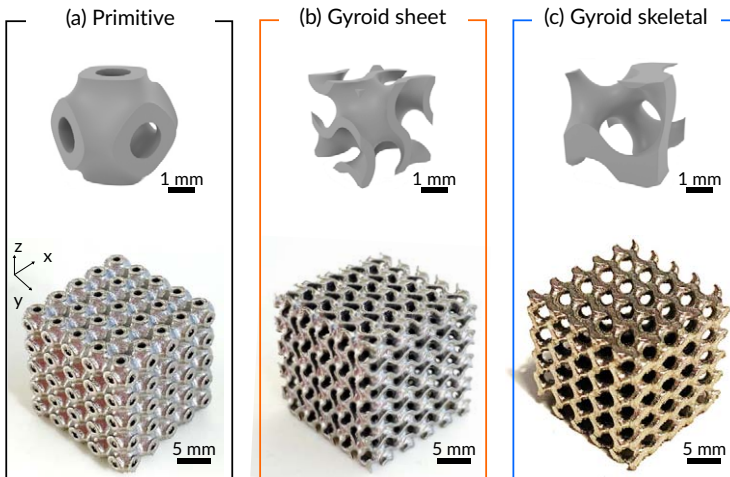
FIGURE 1 CAO of the unit cell and the resulting 5×5×5 sample. (a) Primitive. (b) Gyroid sheet. (c) Gyroid skeletal.

The samples were fabricated by additive manufacturing using the LPBF process on a Renishaw AM 500S (Bilbao, Spain). The base material an Inconel 718 alloy (ρ_{bulk} = 8190 $kg\ m^{-3}$).

The parts are manufactured in a pressure controlled chamber with a very low oxygen content which is replaced by argon. The laser has a power of 200 W, a melting point of 80 μm and a passage

speed of 2 m/s. Each layer of powders is 60 μm thick. The parts are arranged in a circular pattern and the supports between the tray and the samples are 5 mm high. For the filling of these cubes a default strategy is used. For each layer, the laser will pass twice along the contour and fill the inside with hatches (fig. 2).
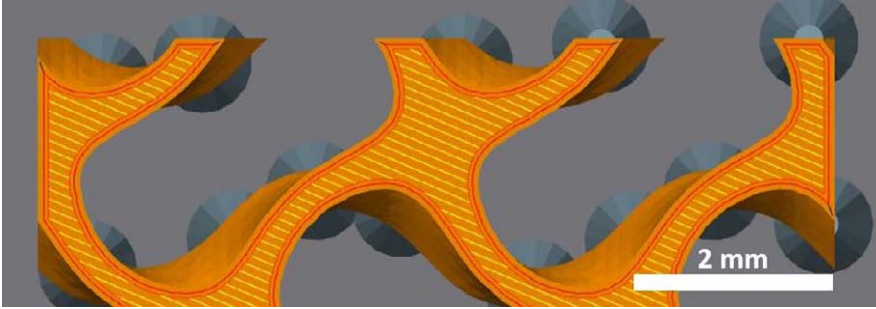
FIGURE 2   Laser path in a gyroid sheet stl cut in the slicer QuantAM.

The dimensions and mass of the resulting samples shown in fig. 1 can be found in tab. 1. Even if the CAD had the same density, it can be noticed that the resulting relative density varies depending on the geometry (tab. 1). The gyroid sheet has the highest one (0.35 ± 0.01) and the primitive has the lowest one (0.32 ± 0.01).

Geometry	Sample side length	Mass	Relative density
	(mm)	(g)	(-)
Primitive	20.3 ± 0.1	60	0.34 ± 0.01
Gyroid sheet	20.2 ± 0.2	60	0.35 ± 0.01
Gyrid skeletal	20.2 ± 0.1	60	0.32 ± 0.01

TABLE 1   Dimension and mass of the resulting TPMS Inconel cubic samples with 5×5×5 cells units obtained by additive manufacturing.

2.2 | Mechanical testing

Quasi-static compression tests were run on a Zwick Roell with a 200 kN force sensor. The displacement rate was set to 10 mm/min corresponding to a macroscopic strain rate of 8 10 ^{3} s ^{1}. A camera was used to observe the deformation modes of the different samples. The acquisition frequency was set to 1 Hz.

For dynamic loadings, steel Split Hopkinson Pressure Bars (SHPB) were used to impose a compressive loading. All the bars are made of hardened maraging steel and have a diameter of 20 mm. The input, output and stricker bar lenght are respectively $L_i n$ = 3.00 m, $L_o ut$ = 2.53 m and $L_s t$ = 0.50 m. One strain gauge is located on the input bar at 2.19 m from the specimen, while another is located on the output bar at 0.72 m from the specimen. Standard formulas for the wave transport are employed

to determine the force history at the output bar-specimen interface and the relative displacement of the specimen-bar interface [10]. A high speed camera (TMX phantom) was used to be able to capture local phenomenon.

From the force F and displacement Δh data, the nominal stress F/S_0 and the true strain $\ln(1 + \Delta h/h_0)$ have been calculated with S_0, the initial section and h_0 the initial height of the sample. The Young's modulus E has then be calculated by fitting a first degree polynom on the elastic linear part, between a 0 strain and 0.01. Another first degree polynom was fitted between a strain of 0.05 and 0.2 to capture the plateau modulus E_p. The plateau stress σ_y is defined as the matching stress of the strain where E and E_p cross.

The specific energy absorption (SEA) was calculated until a true strain of 0.3 and is defined in compression as

$$SEA = \frac{1}{\rho_{bulk}} \int_0^{0.3} \sigma(\varepsilon)d\varepsilon. \tag{1}$$

3 | RESULTS AND DISCUSSION

Fig. 3 plots the experimental stress-strain curves under quasi-static loading. The usual three stages in cellular materials can be observed. The three geometries demonstrate first a linear elastic stage followed by a stress plateau that is more or less flat depending on the geometry.
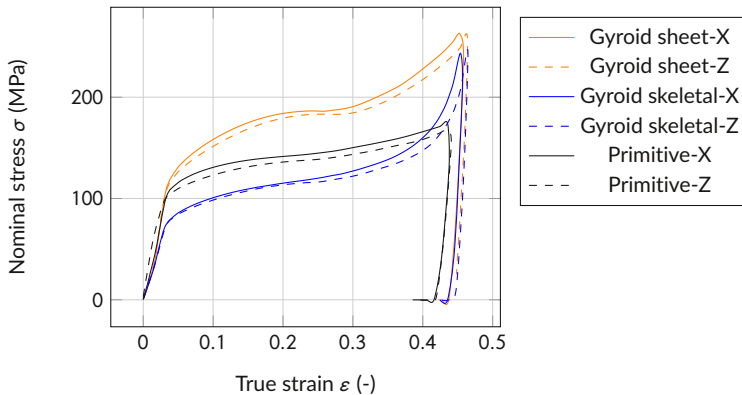
FIGURE 3   Experimental results of quasi-static compressive tests on Inconel 718 based TMPS structures.

For the skeletal gyroid geometry, the maximal displacement was enough to reach the densification stage (around 0.4) while it only starts later for the two other geometries. Macroscopically, the mechanical behaviour of the two gyroid geometries in compression seems almost isotropic (fig. 3). This observation is confirmed by the quantitative measurement of the material parameters (tab.2). For the primitive geometrie, while almost all the material parameters are isotropic, the Young's modulus is higher when the sample is loaded in the X-direction (tab. 2).

This difference in isotropy between geometries most likely comes from the specific microstructure of each geometry due to the additive manufacturing process and its interaction with the local

stress and strain fields [4]. Specific measurement of the grain orientation in the cell walls will be carried out in the future to confirm this hypothesis.

Geometry	E	σ_y	E_p	SEA
	(GPa)	(MPa)	(MPa)	(J/g)
Primitive X	4.60 ± 0.27	128.1 ± 4.2	80 ± 6	7.27 ± 0.29
Primitive Z	3.23 ± 0.05	124.2 ± 4.6	93 ± 11	7.35 ± 0.21
Gyroid sheet X	4.76 ± 0.17	161.6 ± 2.7	137 ± 7	9.67 ± 0.13
Gyroid sheet Z	4.70 ± 0.40	151.6 ± 0.5	151 ± 4	9.56 ± 0.02
Gyroid skeletal X	3.17 ± 0.11	96.2 ± 0.1	117 ± 1	5.25 ± 0.03
Gyroid skeletal Z	2.90 ± 0.56	96.8 ± 0.9	103 ± 2	5.31 ± 0.01

TABLE 2 Material parameters obtained from quasi-static loading on Inconel TPMS obtained by additive manufacturing.

The material parameters are higher for the gyroid sheet geometry. Although the relative density of this geometry is greater, it is not sufficient to explain the stiffness difference and literrature confirms that the geometry of the architecture causes this enhancement [11]. The SEA, which is a linear function of the relative density [4] is also greater for the gyroid sheet geometry (9.6 J/g against 5.3 J/g for the gyroid skeletal geometry). The primitive geometry has mechanical properties (E, σ_y and SEA) between the two gyroid geometries. One can notice the the primitive geometry display the flattest plateau phase between the three TPMS structures (tab. 2).

In quasi-static, localization bands oriented at 45° can be observed for the primitive geometry (fig. 4(a)). This type of localisation is typical of periodic architectured materials [4, 12, 13]. In this structure, plastic hinges appear while the shell like structure is compressed, forming nodes. The plastic hinges of neighboring nodes interact with each other, thereby creating a continuous zone of plastic deformation. Sheet gyroids fail in a homogenous manner and all layers display relatively uniform deformations (fig. 4(a)), however previous have already show that metallic sheet gyroid mostly display the appearance of a large number of plastic hinges in the whole structure [14]. In skeletal gyroid, large rotations appear at the junction of two unit cell as the TPMS structure is compressed. It is where most plastic deformation is concentrated while the strut intersections seem to behave like rigid nodes. Instead of deforming, the latter undergo large rigid body rotations. In short, the main parameter that seems to influence the post-yield macroscopic mechanical behaviour and the material parameters of the TPMS is the ability of the structure to develop plasticity inside.

The resulting stress/strain data obtained in the dynamic regime with the steel SHPB are noisy (fig. 5). The experimental set-up needs to be improved in order to draw conclusions on the effect of the strain-rate on the mechanical behaviour of those Inconel-based TPMS. One can yet notice that the plateau stress is enhanced by the strain-rate (fig. 5). From 96 MPa for the skeletal gyroid loaded in the X-direction in quasi-static, it goes up to about 150 MPa in dynamic. According to other studies on metallic TPMS (stainless steel), this effect is due to the enhancement of the yield stress of the base material with the strain-rate [4].

(a) Primitive

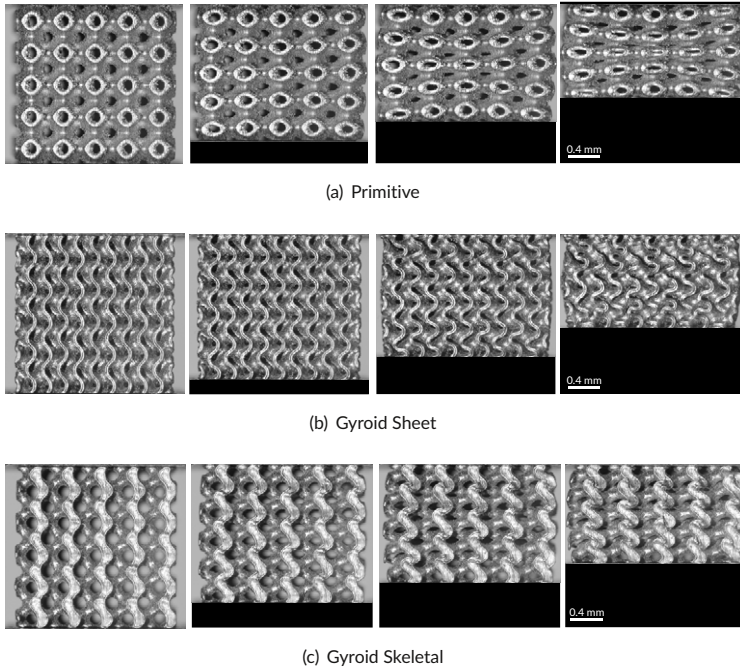(b) Gyroid Sheet

(c) Gyroid Skeletal

FIGURE 4 Pictures of the samples during a quasi-static compression along the X-axis.
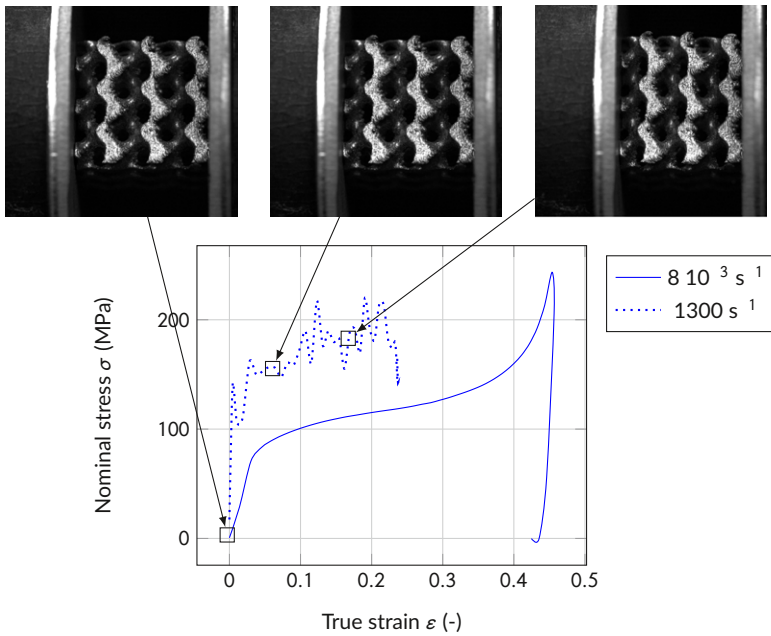
FIGURE 5 Experimental results of compressive tests on Inconel 718 Gyroid skeletal-X in dynamic and quasi-static.

4 | CONCLUSIONS & PERSPECTIVES

In this work, compression tests in quasi-static and dynamic regime have been performed on three different TPMS structures in Inconel 718 alloy obtained by additive manufacturing. The resulting samples presented some differences in the relative density (from 0.32 for the gyroid skeletal to 0.35 for the gyroid sheet). Those differencies where however not sufficient to explain the discrepencies between the material parameters of the three geometries. The local strain mechanisms and more precisely the plastic deformation is the cause of the enhanced behaviour of sheet gyroid in comparison to primitive and skeletal gyroid structures. The latest one displays the largest part on rigid body motion and is thus the one with the smalled SEA. The primitive geometry displayed an anisotric Young's modulus, greater in the X-direction in opposition to the other geometries. Inconel gyroids, both sheet and skeletal geometries, appear to be isotropic in compression. In the future, more local analysis will be pursued to confirm the origin of this anisotropy as well as dynamic loadings with SHPB to complete this study.

References

[1] Ashby MF, Bréchet YJM. Designing hybrid materials. Acta Materialia 2003;51(19):5801–5821.

[2] Brechet Y, Embury JD, Bréchet Y, Embury JD. Architectured materials: Expanding materials space. Scripta Materialia 2013;68(1):1–3. `http://dx.doi.org/10.1016/j.scriptamat.2012.07.038`.

[3] Hawreliak JA, Lind J, Maddox B, Barham M, Messner M, Barton N, et al. Dynamic Behavior of Engineered Lattice Materials. Scientific Reports 2016;6(December 2015):1–7.

[4] Tancogne-Dejean T, Spierings AB, Mohr D. Additively-manufactured metallic micro-lattice materials for high specific energy absorption under static and dynamic loading. Acta Materialia 2016;116:14–28. `http://dx.doi.org/10.1016/j.actamat.2016.05.054`.

[5] Tancogne-Dejean T, Mohr D. Stiffness and specific energy absorption of additively-manufactured metallic BCC metamaterials composed of tapered beams. International Journal of Mechanical Sciences 2018;141(February):101–116. `https://doi.org/10.1016/j.ijmecsci.2018.03.027`.

[6] Cao X, Xiao D, Li Y, Wen W, Zhao T, Chen Z, et al. Dynamic compressive behavior of a modified additively manufactured rhombic dodecahedron 316L stainless steel lattice structure. Thin-Walled Structures 2020;148(June 2019):106586. `https://doi.org/10.1016/j.tws.2019.106586`.

[7] Li X, Xiao L, Song W. Compressive behavior of selective laser melting printed Gyroid structures under dynamic loading. Additive Manufacturing 2021;46(April):102054. `https://doi.org/10.1016/j.addma.2021.102054`.

[8] Novak N, Al-Ketan O, Krstulović-Opara L, Rowshan R, Abu Al-Rub RK, Vesenjak M, et al. Quasi-static and dynamic compressive behaviour of sheet TPMS cellular structures. Composite Structures 2021;266(March):1–10.

[9] Al-Ketan O, Abu Al-Rub RK. MSLattice: A free software for generating uniform and graded lattices based on triply periodic minimal surfaces. Material Design and Processing Communications 2021;3(6):1–10.

[10] Bouix R, Viot P, Lataillade JL. Polypropylene foam behaviour under dynamic loadings: Strain rate, density and microstructure effects. International Journal of Impact Engineering 2009;36(2):329–342.

[11] Al-Ketan O, Rowshan R, Abu Al-Rub RK. Topology-mechanical property relationship of 3D printed strut, skeletal, and sheet based periodic metallic cellular materials. Additive Manufacturing 2018;19:167–183. `http://dx.doi.org/10.1016/j.addma.2017.12.006`.

[12] McKown S, Shen Y, Brookes WK, Sutcliffe CJ, Cantwell WJ, Langdon GS, et al. The quasi-static and blast loading response of lattice structures. International Journal of Impact Engineering 2008;35(8):795–810.

[13] Xiao L, Song W, Wang C, Tang H, Fan Q, Liu N, et al. Mechanical properties of open-cell rhombic do-decahedron titanium alloy lattice structure manufactured using electron beam melting under dynamic loading. International Journal of Impact Engineering 2017;100:75–89. `http://dx.doi.org/10.1016/j.ijimpeng.2016.10.006`.

[14] Zhang L, Feih S, Daynes S, Chang S, Wang MY, Wei J, et al. Energy absorption characteristics of metallic triply periodic minimal surface sheet structures under compressive loading. Additive Manufacturing 2018;23(July):505–515. `https://doi.org/10.1016/j.addma.2018.08.007`.

15

Evaluation of additively manufactured structure under dynamic condition

Matouš Uhlík[1][*] | **Antonín Prantl CSc.**[2][†]| **Martin Rund**

Daniel Melzer | **Michal Brázda** | **Ondřej Lukáš**

[1]COMTES FHT a.s., Průmyslová 995, 334 41 Dobřany, Czech Republic

[2]COMTES FHT a.s., Průmyslová 995, 334 41 Dobřany, Czech Republic

Correspondence
Matouš Uhlík
Email: matous.uhlik@comtesfht.cz

Although Additive Manufacturing is currently one of the most expanding technologies in the industrial sector, there is still limited knowledge of relation between measured material data and overall behavior of complex structures. The reliability of additively processed materials is still questioned and as a result, the knowledge of the structural performance including flow curves and local damage properties of additively manufactured parts by DED becomes increasingly important. For thin parts, which will be used without the surface machining this evaluation is even of high importance. Therefore, the mechanical performance of as-printed honeycomb structures made of 316L will be evaluated in this study and the results will be compared with results of FEM.

*Equally contributing authors

1   INTRODUCTION

It is well known, that the concept of honeycomb structures is inspired by the nature, specifically by honeybees which use these honeycomb structures as effective storage of pollen and honey. From engineering point of view, honeycomb structures are characterized as lightweight structures with high stiffness to strength ratio and high specific energy absorption, which make these structures interesting for applications in the field of automotive, aerospace, marine, defense etc. [1]

For the mentioned properties, many researchers studied the behavior of these structures under dynamic loading. Meng et al. investigated the dynamic response of the graded honeycomb structure under blast loading. [2] Wei et al. studied the effect of strain rate on stress-strain response and energy absorption density for different honeycomb cell geometry. [3] In another study, Abayazid et al. focused on cell topology optimization for oblique dynamic loading. [4] As is obvious, in the context of honeycomb structures and dynamic loading, number of different scientific research topics arises.

Benefiting from design freedom, majority of honeycomb structures are manufactured via additive manufacturing techniques. With the current expand of this technology, there is certain demand for more complex performance characterization of additively manufactured materials and structures.

In response to this demand, this particular study is presented. The aim of this study is to manufacture thin – walled honeycomb structures from austenitic stainless steel 316L via DED process and perform uniaxial tension and compression tests ranging from quasi – static strain rates to high strain rates. Specimens for tension and compression tests will be separated from thin walls and based on the results, behavior of the whole honeycomb structure under dynamic loading conditions will be predicted by finite element analysis with standard ABAQUS version 2020. Lower strain rates will be realized by servo–hydraulic machines and higher strain rates will be obtained by Drop Weight Test (DWT) machine and Split Hopkinson Pressure Bar (SHPB). Presented study builds on previous research conducted only the range of quasi-static strain rates. [5]

2   MATERIAL AND ADDITIVE MANUFACTURING PROCESS

For fabrication of honeycomb structures, Laser Powder DED system equipped with 2 kW Ytterbium fiber laser was used, namely the INSSTEK MX600. Argon gas was employed as both protective and powder acceleration medium. Process parameters are summarized in the following table:

TABLE 1   Summarization of DED process parameters

Material	Laser Power [W]	Powder Feed [g/min]	Coaxial Gas [l/min]	Powder Gas [l/min]	Shield gas [l/min]
316L	320	3.6	7	2.5	5

Laser Power output with the mean value of 320 W was automatically controlled by the actual height of the layer, using Direct Metal Tooling (DMT) mode.

As was mentioned, austenitic stainless steel 316L in the form of the commercial powder with particle size distribution 53 – 150 μm was used. To prevent undesirable diffusion effects, similar

building platform material was used. Both platform and powder chemical compositions are shown in following table:

TABLE 2   Chemical composition of powder and platform material

Material	Cr	Ni	Mo	Mn	Si	Fe
Powder	17.2	10.4	2.3	1.3	0.8	Bal.
Platform	16.2	10.5	2.1	1.1	0.4	Bal.

By application of previously described process parameters and materials, three honeycomb structures with 42 mm height, 2.7 mm wall thickness and 21 mm width were built on single platform (Fig. 1 - left). Without subsequent heat treatment or machining, specimens for uniaxial testing in tension and compression were cut off according to the schematized cutting plan (Fig. 1 - right):
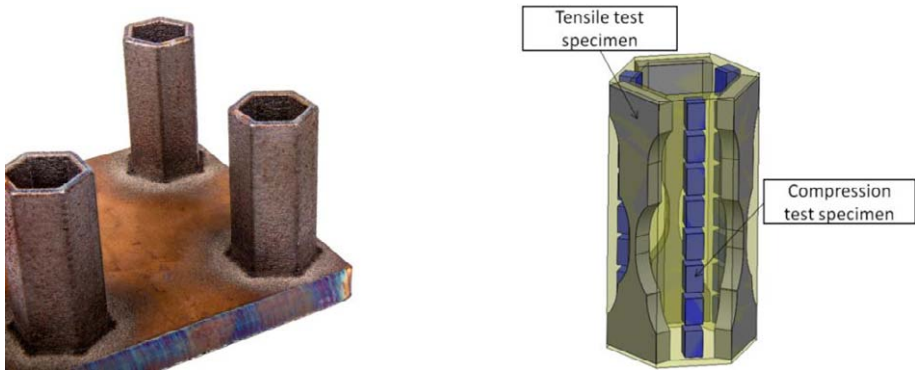
FIGURE 1   Honeycomb structures as printed (left) and the schematization of the cut off plan (right)

Specific dimensional characterization is provided for specimens determined for the tension testing (Fig. 2 – left) and compression testing (Fig. 2 – right). The geometry of the tensile test specimen has been tailored, so there is enough space for installing strain gauges in the area of elastic deformation of the specimen. In the case of dynamic tension tests, those strain gauges were allowing to obtain a force record with significantly reduced oscillations compared to the record of the load cell attached to the machine.
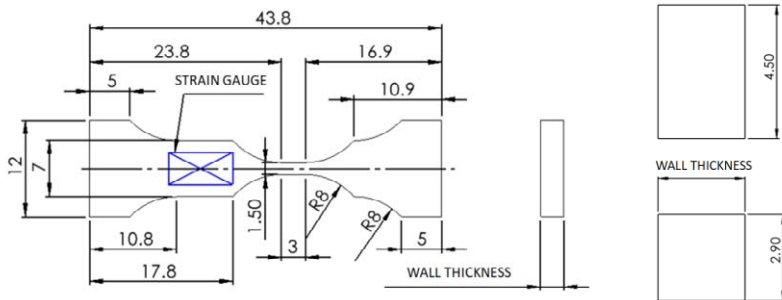
FIGURE 2   Dimensional characterization of specimens determined for tensile tests (left) and compression tests (right)

3   EXPERIMENTS AND RESULTS

With the fabricated specimens, quasi–static and moderate strain rate uniaxial testing was performed using conventional servohydraulic and electromechanical testing machines. Drop Weight Test machine was used for high strain rate tension tests (Fig. 3 – left) and conventional Split Hopkinson Pressure Bar (Fig. 3 – right) was employed for determination of the true stress – true strain response of the experimental material exposed to high strain rate compressive loading. The summary of quasi-static ad dynamic uniaxial tests is also presented in the following figure.
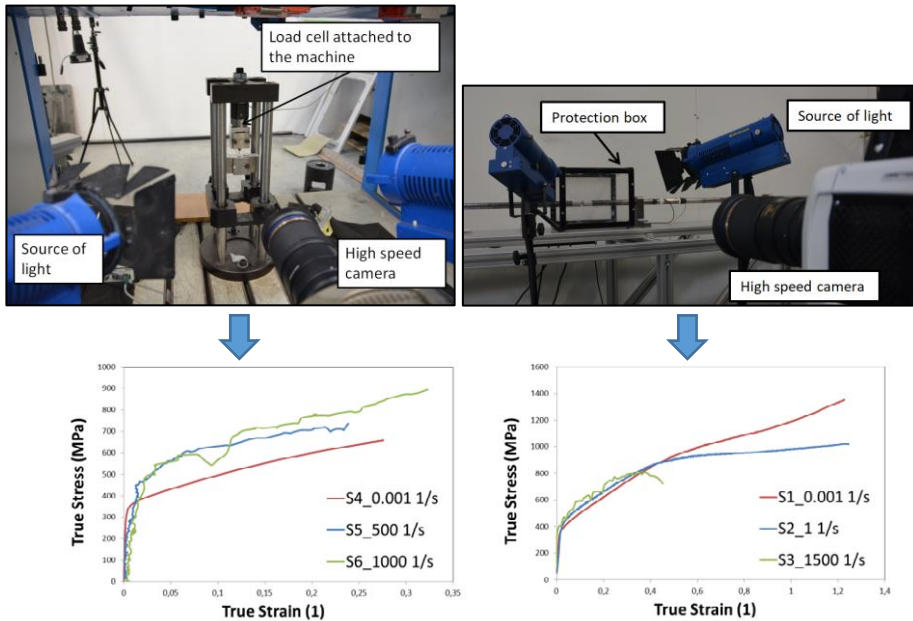
FIGURE 3   Drop Weight Test machine experimental apparatus for high strain rate tensile tests (left) and Split Hopkinson Pressure Bar for high strain rate compression tests (right)

Subsequently, the entire HC structures were deformed by the impact of a conical punch with 126° apex angle using Drop Weight Test machine (Fig. 4a). The deformation caused by the impact of the punch with different impact energies (namely 400 J, 700 J and 1500 J) was monitored by a high-speed camera. The force record was obtained by force gauge measurement placed on a falling punch. Lower impact energies (400 J and 700 J) were achieved by simple free fall of the punch (Fig. 4b), however for reaching higher impact energy (1500 J), the falling mass had to be additionally accelerated by integrated catapult system. Deformed states of structures paired with a punch impact energy labels are documented in the following figure (Fig. 4b)
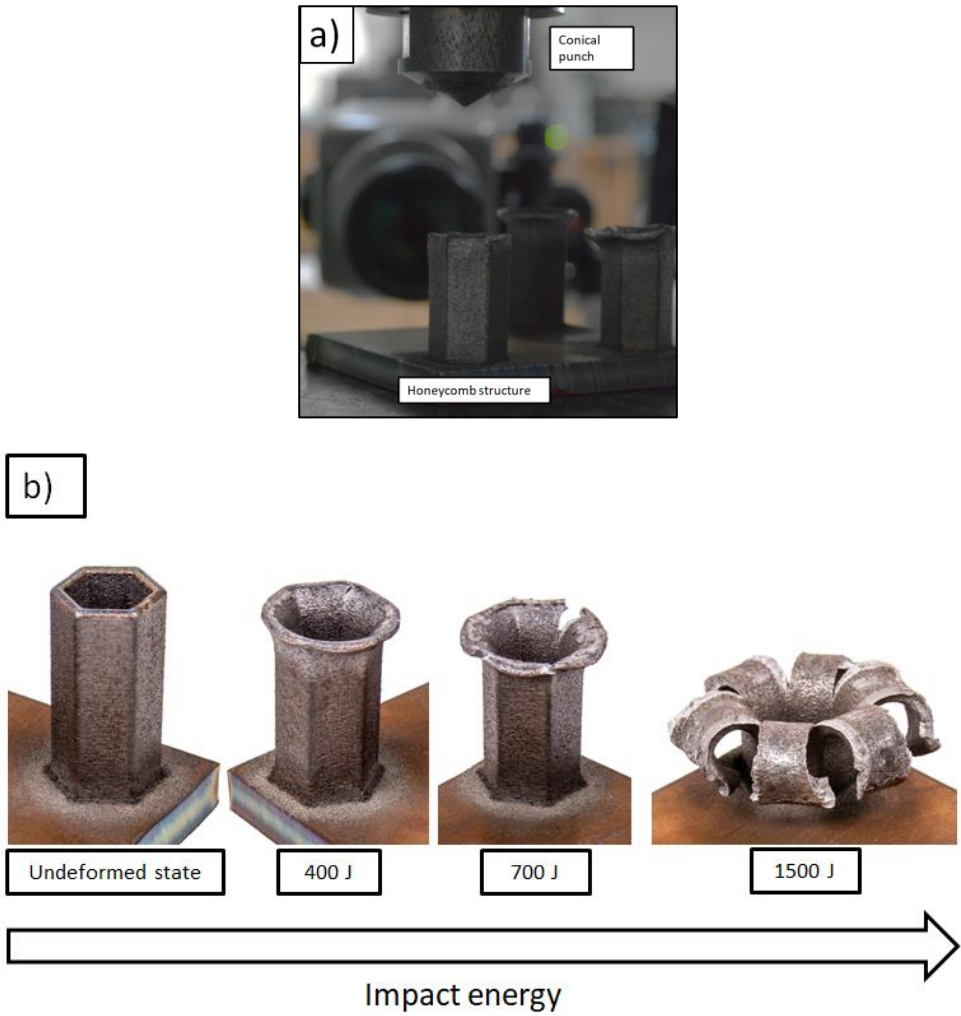
FIGURE 4 Conical punch (a), honeycomb structures deformed by different impact energies (b)

Then, FEM analysis of the deformation process based on material model calibrated experimentally on samples separated from honeycomb structure walls was performed. Conical punch was modelled as non-deformable object while the platform was modelled as object undergoing only elastic deformation. Comparison of measured and experimentally obtained force-displacement record without considering the damage model can be seen in the following table (Tab. 3):

Metallic structures

TABLE 3 Comparison of FEM analysis and experiment without considering the damage model
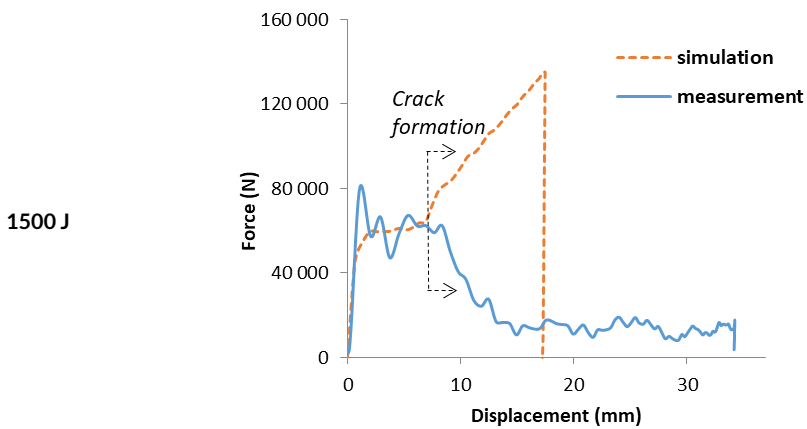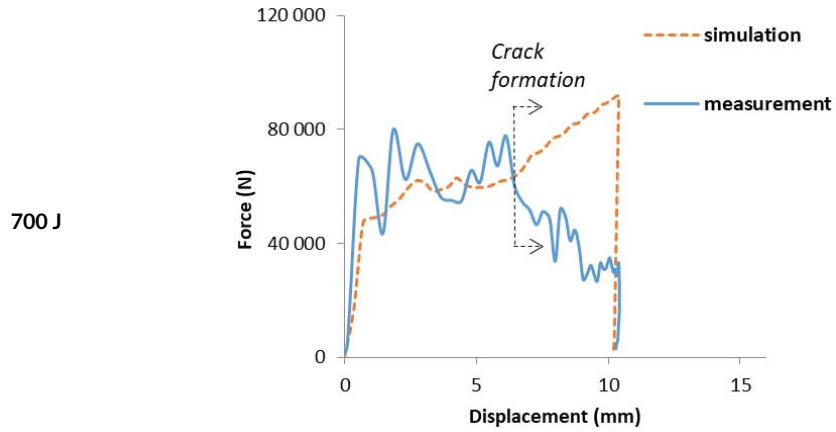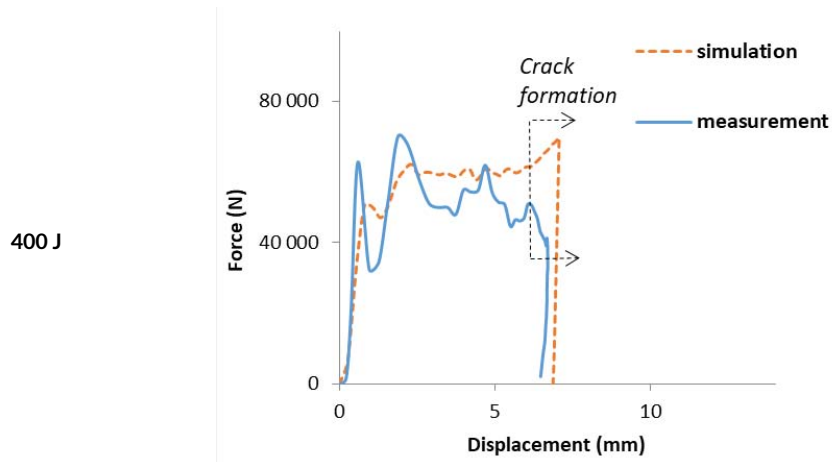
4 CONCLUSIONS

In the early stages of deformation, relatively good agreement of experimental results and results obtained by FEM analysis without considering the damage model can be seen. At the moment of crack formation, which occurs with increasing impact energy in the earlier stages of deformation, the results of the simulation and the experiment diverge. However, this moment is very well observable from the course of the force simulation – as a steep increase. At about the same time, the results of the experiment also indicate cracks formation – this is evident from the steep decrease in the force required to realize the displacement. Thus, it can be stated that a simple simulation without considering the damage model can well predict the behavioral properties of the honeycomb structure until the moment of cracking, whereas this moment can also be predicted from the simulation. Generally, the knowledge and description of the behavior of not machined 3D printed parts is gaining in importance nowadays, due to the possibility of reducing production cost spent on surface finishing.

5 REFERENCES

[1]   C. Qi, F. Jiang, and S. Yang, "Advanced honeycomb designs for improving mechanical properties: A review," *Composites Part B: Engineering*. 2021. doi: 10.1016/j.compositesb.2021.109393.

[2]   Y. Meng, Y. Lin, Y. Zhang, and X. Li, "Study on the dynamic response of combined honeycomb structure under blast loading," *Thin-Walled Struct.*, 2020, doi: 10.1016/j.tws.2020.107082.

[3]   Y. Wei *et al.*, "Topological study about failure behavior and energy absorption of honeycomb structures under various strain rates," *Def. Technol.*, 2022, doi: 10.1016/j.dt.2022.03.011.

[4]   F. F. Abayazid, D. Carpanen, and M. Ghajari, "New viscoelastic circular cell honeycombs for controlling shear and compressive responses in oblique impacts," *Int. J. Mech. Sci.*, vol. 222, p. 107262, 2022, doi: https://doi.org/10.1016/j.ijmecsci.2022.107262.

[5]   M. Urbánek *et al.*, "Prediction of Behaviour of Thin-Walled DED-Processed Structure: Experimental-Numerical Approach," *Materials (Basel).*, 2022, doi: 10.3390/ma15030806.

Energy absorption properties of the additively manufactured AlSi10Mg aluminum structures subjected to blast

M. Stanczak[1,2], T. Fras[1*†], L. Blanc[1], P. Pawlowski[3], A. Rusinek[2]

[1]Department of Protection Technologies, Security & Situational Awareness, French-German Research Institute of Saint-Louis (ISL), 68301 Saint-Louis, France

[2]Laboratory of Microstructure Studies and Mechanics of Materials, LEM3 Laboratory, Lorraine University, 57070 Metz, France

[3]Institute of Fundamental Technological Research Polish Academy of Sciences, Polish Academy of Sciences (PAS) 02-106 Warsaw, Poland

Correspondence

Teresa FRAS PhD, French-German Research Institute of Saint-Louis (ISL), 68301 Saint-Louis, France
Email: teresa.fras@isl.eu

Present address

† French-German Research Institute of Saint-Louis (ISL), 68301 Saint-Louis, France

The study discusses the role of topology of additively manufactured AlSi10Mg aluminum structures based on several exemplary cellular structures (i.e., honeycomb, auxetic, lattice, and foam). The structures are subjected to a blast induced compression. A relationship between the relative density and the deformation responses of the structures, as well as the energy absorption capacities is hereby analyzed. To investigate the influence of the manufacturing process conditions on the mechanical properties, the material behavior of the printed AlSi10Mg aluminum alloy is studied. For completeness, an analysis of the deformed microstructure is also performed. The finite element simulations conducted in LS-DYNA software are used to investigate the deformation mechanisms of the structures. The results show a good agreement with the experimental observations. The final responses indicate that by selecting the appropriate topological parameters, it is possible to affect the performance of structures significantly and thus to improve their energy absorption properties

1   INTRODUCTION

Additive manufacturing (AM), as a modern and advanced technique of structures manufacturing, may be used to produce components with complex geometrical properties. The AM methods provide freedom in designing geometry or defining density of manufactured samples. Thanks to this technique, spare parts adaptable to already existing constructions may be rapidly produced. However, the be-

havior of structures additively manufactured is complex and it still requires investigations. A particular attention should be focused on the behavior of AM structures affected by dynamic loadings, especially shock waves. This topic is investigated in details by sparse studies, e.g. [1-4].
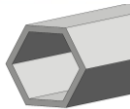
The hereby presented study concerns the experimental investigation performed by means of the Explosive Driven Shock Tube (EDST) tests. The generated shock waves affect four different AM structures consisting of 2D unit cells (honeycomb and auxetic) 3D unit cells (rhomboidal lattice and regular foam) manufactured from the aluminum AlSi10Mg alloy. Their geometry is based on the printed cubic samples without an additional post-treatment. Additionally, an analysis of the deformation and damaged processes is realized in the explicit FEM code LS-DYNA R9.0.1. The obtained results show a good agreement with the analytical calculations and the experimental observations. The results of the experimental testing and its modeling present a potential of the discussed manufacturing method in application to improved, optimized, energy-absorption structures.

2   MATERIAL AND SPECIMENS

The tested aluminum AlSi10Mg structures are additively manufactured by the Direct Metal Laser Sintering (DMLS) method applied in the EOSINT M 280 3D printer. The DMLS is based on the selective sintering of an evenly distributed powder on the build platform. The 30 μm powder layer is melted according to a bidirectional scanning strategy at an angle of 67° by a 370 W laser beam. The printing technique contributes to the formation of a fine microstructure during the solidification process and unification the macro properties [5]. The settings during manufacturing, a type of the powder, as well as the sample position in relation to the build platform or the final treatment may significantly affect the properties of the obtained product, as it is discussed in e.g. [6].

TABLE 1. Tested AM structures and their geometrical properties.

	Honeycomb	Auxetic	Lattice	Foam
Unit cell				
Area [mm²]	813.87	879,91	896,34	900,96
Height [mm]	30.01	29.98	30.06	30.01
Mass [g]	12.13	11.31	18.19	11.84
Relative Density [-]	0.173	0.151	0.250	0.164

The objective of the study is a comparison of the absorptive properties of four different geometries: honeycomb, auxetic, lattice and regular foam (**Table 1**). The honeycomb and auxetic represent the structures with 2D unit cells and lattice and foam are characterized by three-dimensional geometries. The tests were based on the 'as built' cubic samples with the edge length of 30 mm. The samples are characterized by a similar relative density equaled to 0.2 ± 0.05.

2.1 Microstructure analysis

The microstructure of the printed structures (without their post-processing) was observed using the Olympus DSX 510 optical microscope, which may achieve 13.5X optical zoom and 30X digital zoom. For the study, the samples were polished and adequately etched. The magnifications of the microstructure of the specimens as-fabricated is given in **Fig. 1**. The surfaces aligned along the building direction [XZ] and the transverse surface [XY] are schematically shown in **Fig. 1(d).**
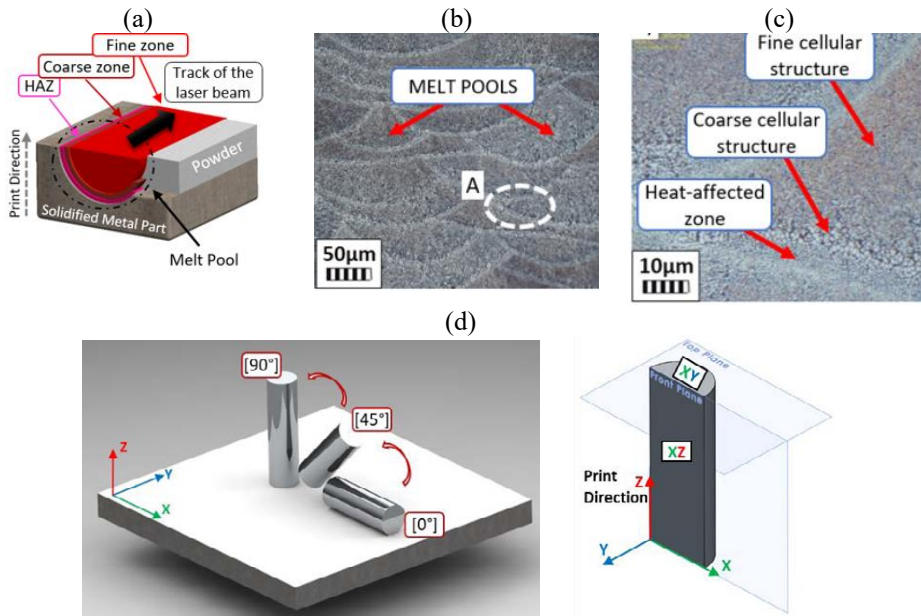
FIGURE 1. (a) The schemes of melt pool forming and (b) the optical micrographs of the AlSi10Mg as-fabricated sample, (c) enlarged area marked 'A'. (d) Orientation of the samples versus the build platform and the observed sample surfaces for the microstructural analysis

The melt pools can be related to manufacturing and the cooling process of the melted areas, [7]. As a result of differences in the cooling rate, three distinct areas are formed: a fine cellular structure, coarse cellular structure, and heat-affected zone (HAZ). The first zone was created towards the melt pool center due to a slower solidification process. The region with the coarse cellular structure is the intermediate zone between the center and the boundaries of the melt pool. The long Si particles are formed in heat-affected zones, which contact a previously solidified melt pool. The bright eutectic Al/Si phase of the micrographs is precipitated during the solidification process and included in the Al matrix of melt pools. The amount and size of other particles across the aluminum matrix can strongly influence the behavior of the manufactured samples.

2.2 Material characteristics

In order to determine the material characteristics of AlSi10Mg aluminum, the quasi-static and dynamic compression tests has been carried out. The performed tests are based on the samples printed horizontally and vertically with respect to the build platform. **Figure 2** shows the obtained results of the true stress over the plastic strain. The tests are performed at the strain rate between 0.001 /s - 3300 /s and at the temperature range of 293 K - 473 K. An adiabatic-isothermal correction of the

registered stress-strain material curves is introduced to the results at high strain rates, following the conclusions of [8].

(a)

(b)

(c)

(d)
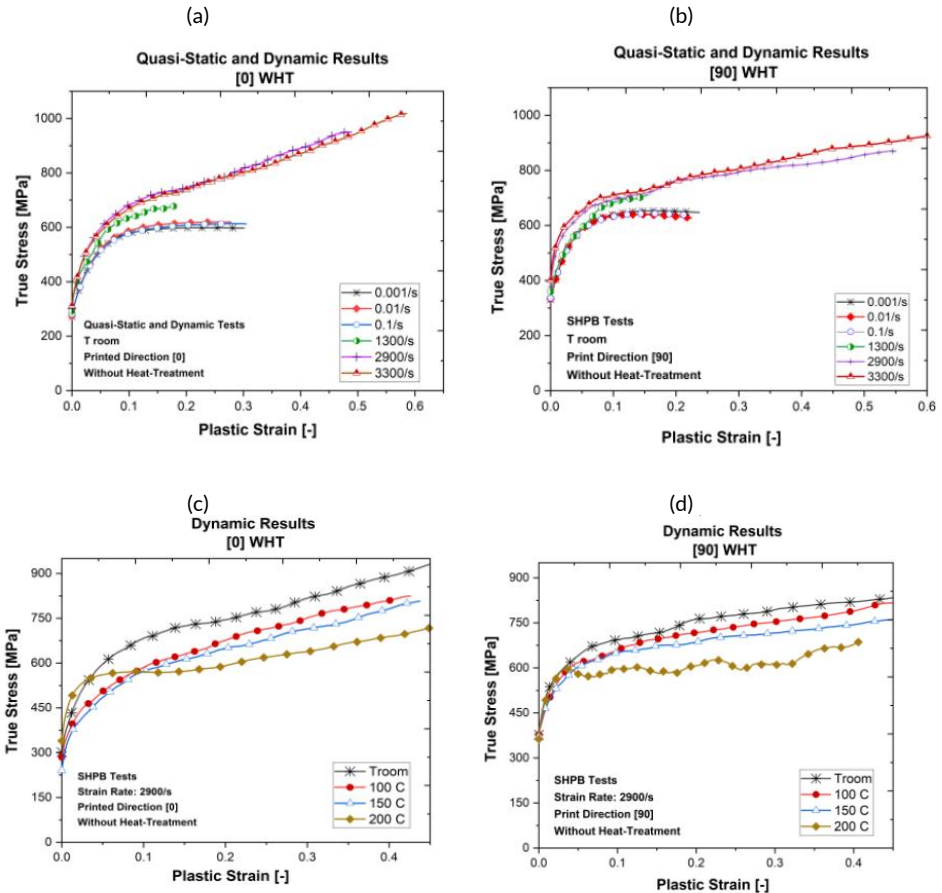
FIGURE 2. Material characterization presenting behavior of the horizontally and vertically printed samples at different strain rates (a)-(b) and at different temperatures (c)-(d). Structures without heat-treatment.

The results indicate that the print direction affect the material response. The vertically printed samples exhibit the highest values of the stress in the first deformation stage (up to the strain of 0.25). However, the horizontally printed samples exhibit highest hardening in second regime. It is observed that the AlSi10Mg aluminum is only slightly sensitive to the strain rate changes, however the temperature increase causes a stronger material softening

3   BLAST TEST RESULTS

The manufactured samples are subjected to blast loadings by means of the Explosive Driven Shock Tube (EDST) tests, [9-10]. This experimental set-up consists of the 1.75 m long shock tube, in front of which 30 g of the C-4 explosive charge is located. An explosion generates a spherical wave which travels through the tube. Due to internal reflections and the travelled distance, the blast wave forms

a planar front at the end of the tube. The movement of the front steel plate accelerated by the explosive wave causes a compression of the tested samples. During the damage process, the force transmitted to the back plate is measured by a PCE 206C piezoelectric force sensor. A high-speed camera Phantom V311 records the whole deformation process. Then, the Digital Image Correlation set-up allows to obtain the displacement of the front plate over the time.
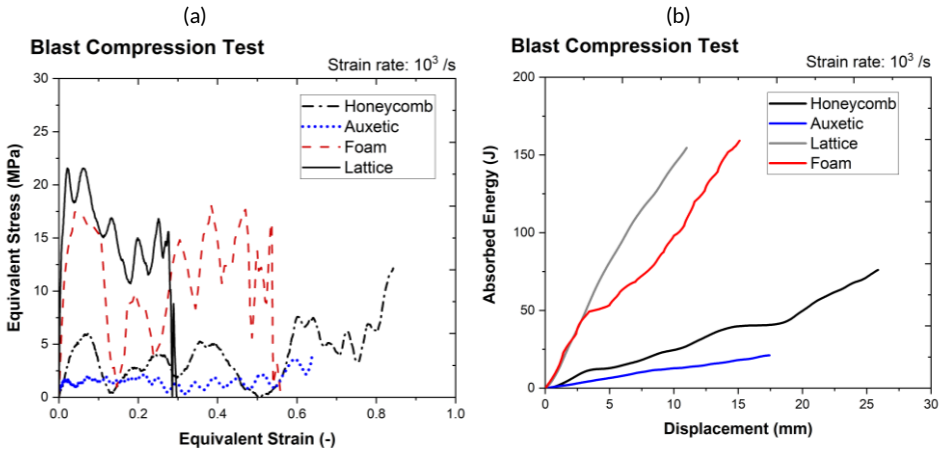
FIGURE 3. Results of the EDST blast compression tests of theAlSi10Mg additively manufactured structures: (a) stress versus strain and (b) absorbed energy versus displacement.

Typically, the response of a compressed metallic cellular structures may be described by three main phases, which is also observed for the current tests results. The elastic response of cellular structures ends with a first stress peak. This is often the maximum obtained value before the total damage of the sample. Then the deformation follows a plateau regime, in which the registered force oscillates around a certain value. In this region, the structure undergoes the plastic deformation such as bending or stretching. Finally, a sudden sharp rise in the obtained stress corresponds to a fully damaged structure.

TABLE 2. Some calculated energy-absorption properties of the AM structures in the EDST blast compression tests.

		Honey-comb	Auxetic	Lattice	Foam
Peak [MPa]	Stress	6.01	1.75	21.56	17.43
Mean [MPa]	Stress	3.52	1.44	14.18	10.39
Densification Strain [-]		0.76	0.58	0.31	0.52

The tests performed on AM samples are reported in **Fig. 3**, which shows the curves of the stress over strain and the absorbed energy over displacement are presented. While analyzing the results, it can be noticed that the main phases of the compression process are visible in the honeycomb and auxetic curves, i.e., the peak, plateau, and densification. However, the specimens with 3D geometry absorbed

all energy generated during the explosion. Therefore, the stress curves decrease to zero. Furthermore, it should be emphasized that the foam structure has collapsed later than the lattice structure in order to transfer the same amount of force. On this basis, it may be concluded that the lattice is a more efficient absorber.

Each of the curve courses is characterized by large fluctuations that can be correlated with the cell collapses and the bond breaks. The quantitative results presented in **Fig. 3(b)** and **Table 2** prove that the structures composed of 3D unit cells can increase, at least double the abortion efficiency when they are subjected to the same explosive load. In addition, it can be noticed that the auxetic structure, characterized by a negative Poisson's coefficient, obtained the lowest stress results. At the same time, the stroke efficiency is 1.4 times lower than that calculated for the honeycomb structure.
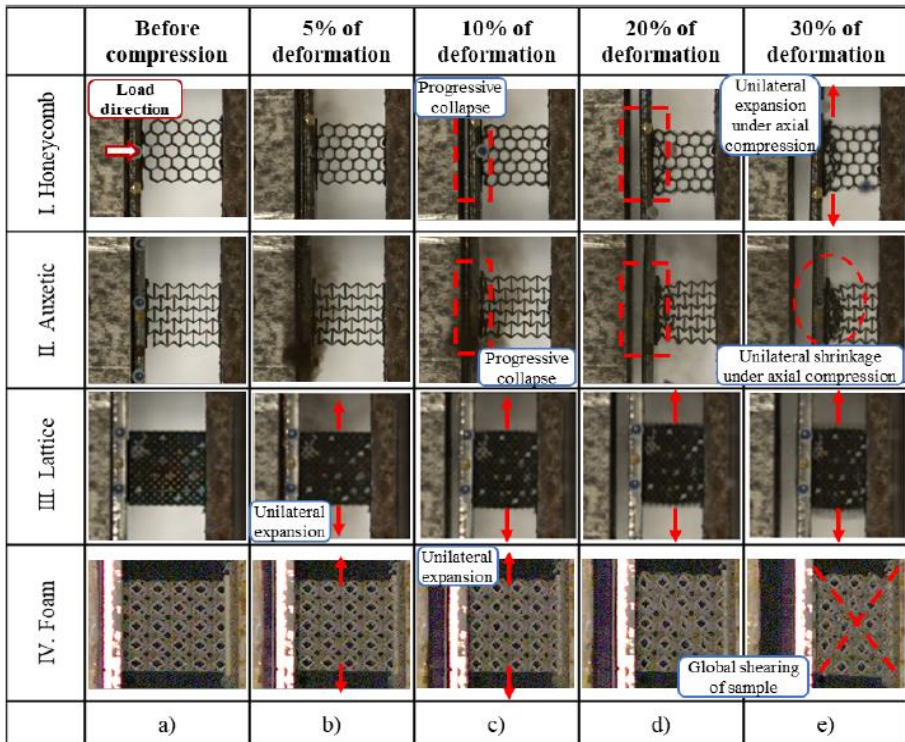
FIGURE 4. The main stages of the deformation process during the blast compression test (a-f) of the (I) honeycomb, (II) auxetic, (III) lattice and (IV) foam structure.

Figure 4 shows the deformation mechanism of the honeycomb (Fig 4-I), auxetic (Fig. 4-II), lattice (Fig. 4-III) and foam (Fig. 4-IV) subjected to the blast loading generated by means of the EDST set-up. The structures composed of a two-dimensional unit cell collapse progressively row by row. Wherein, the damage of the honeycomb is characterized by the stretching of the cells outwards. The deformation of the auxetic at the higher strain rate is stable as opposed to the quasi-static one. The synclastic curvature of the deformation indicates the dome-shape damage mode. The cells collapse towards inside the structure, which is visible in Fig. 4.3-II. The lattice and foam have a similar deformation mechanism in the initial stage of deformation, up to 10 % strain. Their collapse processes can be correlated with the absorbed energy results. Lattice is characterized by cell bending and the stretching of the whole structure during blast compression. The end of the deformation process occurs as a result of shearing the entire structure, which can be seen by analyzing the specimen after the test. In the case

of the foam structure, the shear mode of the deformation occurs after 10 % of strain, which corresponds to the brittle fracture of the cells and breaking bonds in the structure.

4 NUMERICAL MODELLING

In order to analyze the damage process in details, the explicit simulation in the LS-DYNA R9.0.1 is prepared. The experimental configuration modeled in Ls-PrePost consists of the Lagrange solid parts of the tested sample, placed between two steel plates. The contact between the components is obtained by the function *AUTOMATIC_SURFACE_TO_SURFACE (e.g. [11]). The crushing load is assigned to the nodes of the upper surface of the front plate.

The in-house obtained characteristics of the AlSi10Mg aluminum alloy are used to describe the material properties of the tested structure. To introduce the experimental curves, the *MAT_Linear_Pleasticity 024 is chosen to simulate the material behavior of structures. The *MAT_Simplified_Johnson_Cook 098 is used to describe the material behavior of the steel blocks. *Mat_098 is a simplified Johnson-Cook constitutive function which does not account for temperature effects and is decoupled from the Johnson-Cook fracture model (e.g. [12]). A maximum effective strain at failure of 0.1 is used to simulate a brittle damage. The bottom surface of the second block is fully constrained, simulating the experimental bunker wall. A more detailed description of the numerical configuration is presented in [2, 9].
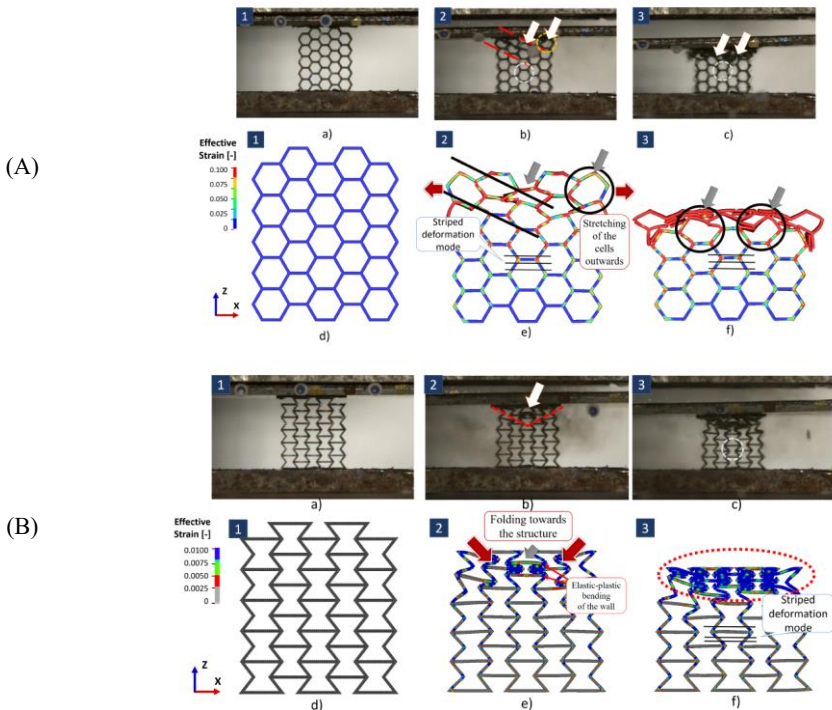
FIGURE 5. Deformation mechanism of the honeycomb (A) and auxetic (B) structures: (a)-(c) experimental images and (d)-(f) numerical representation.

The developed numerical tasks simulate the ideal conditions of the performed experimental tests when the AM structures are subjected to a blast load caused by the explosion of the 30 g of C-4

charge. Figures 5 and 6 compare the dynamic compression processes of the developed simulations with the experimental results.
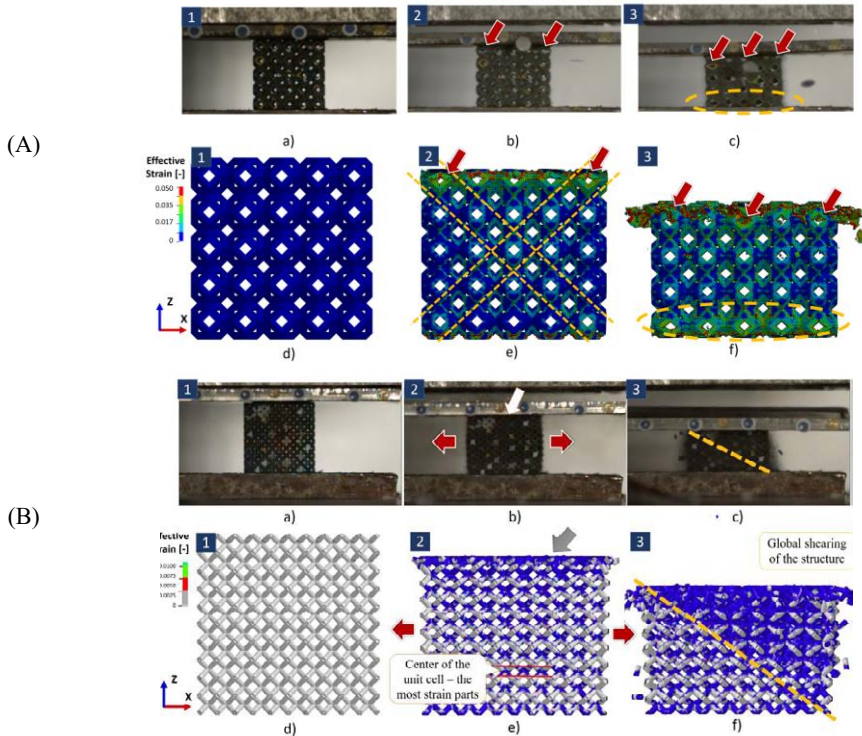
FIGURE 6. Deformation mechanism of the foam (A) and lattice (B) structures: (a)-(c) experimental images and (d)-(f) numerical representation.

The presented numerical simulations concern dynamic compression of the aluminum AM structures obtained due to the blast testing. The numerical study explains both the mechanism of the cell deformation, and further fracture of the structure. It has been proven that the selected type of contact, the material model, and the boundary conditions provide consistent results. The numerical simulations allow a deeper analysis of deformation modes, indicate the stress concentration, and show the largest deformations of each structure.

Comparing the numerical and experimental results, it may be concluded that the simulated numerically behavior of each structure is similar to the experimental response at each stage; moreover, the main deformation modes have been also numerically modeled. It has been observed that the honeycomb is characterized by the stretching of the cells outwards, and the auxetic structure by the folding of the cell towards their center. The bending of the struts is visible for the lattice structure and the foam is characterized by the deformation mechanism occurred between two corners of the cell. The numerical results prove that the structures composed of the 3D unit cell (lattice and foam) are characterized by large strains of the entire structure and exhibit the shear modes during the dynamic compression. At the same time, the deformations of the structures that consist of the 2D unit cell (honeycomb and auxetic) undergo the progressive folding of the cell rows and the band-like stress distributions.

5   CONCLUSIONS

The conducted EDST blast compression tests of the additively manufactured samples resulted in a comparison of the dynamic behavior of four geometries, i.e. honeycomb, auxetic, lattice and foam. The analysis of the blast-induce structural deformations shows that the structures composed with the 3D unit cell absorb more energy during the blast loading carried out by means of the EDST set-up. Based on the calculated energy absorption characteristics, it may be concluded that despite that these samples are characterized by a higher mass, they mitigate more efficiently an explosive load than the structures with 2D unit cells. The developed simulations analyses the deformation mechanism observed experimentally.

Additive manufacturing is a promising technology that can contribute to designing superior protective structures. The conducted investigation proved that the efficiency of mitigating explosive energy may be increased by application of the optimized AM structures, when compared to structures produced by traditional methods. The conducted research provides a good basis for an analysis and a further geometry optimization of structures applied to attenuate compressive shock waves.

REFERENCES

[1] M. Stanczak, T. Fras, L. Blanc, P. Pawlowski, A. Rusinek. EPJ Web Conf. **250**, (2021)

[2] M. Stanczak. Doctoral dissertation, Metz, l'Université de Lorraine (2022)

[3] M. Stanczak, A. Rusinek, P. Broniszewska, T. Fras, P. Pawlowski. Bull. Pol. Acad. Sci. Tech. Sci. (to be published)

[4] B. Branch, A. Ionita, B.E. Clements, D.S. Montgomery, B.J. Jensen, B. Patterson, A. Schmalzer, A. Mueller, D.M. Dattelbauma J. Appl. Phys. **121**, 135102-1-125102-9 (2017)

[5] M. Moataz, L. N. C. Attallah, Q. Chunlei, R. Noriko, W. Wei, CRC Press, Taylor & Francis **3**, 59-110 (2018)

[6] Z.H. Xionga, S.L. Liub, S.F. Lia, Y. Shic, Y.F. Yanga, R.D.K. Misrad, Mater. Sci. Eng. **156**, 148–156 (2019)

[7] F. Trevisan, F. Calignano, M. Lorusso, J. Pakkanen, A. Aversa, E. P. Ambrosio, M. Lombardi, P. Fino, D. Manfredi. Mater, **10.76** (2017)

[8] J.R. Klepaczko, A. Rusinek, J.A. Rodríguez-Martínez, R.B. Pęcherski, A. Arias, Mech. Mater. **41**, 599-621 (2009)

[9] M. Stanczak, T. Fras, L. Blanc, P. Pawlowski, A. Rusinek Met. **9**, 1350:1-24 (2019)

[10] L. Blanc, T. Schunck, D. Eckenfel. Mater., **14(14)**, 3980 (2021)

[11] T. Fras, I. Szachogluchowicz, L. Sniezek, Eur. Phys. J. **227**, 17-27 (2018)

[12] T. Fras, C.C. Roth, D. Mohr. Bull. Pol. Acad. Sci. Tech. Sci. **68(2)** (2020)

(17)

Mechanical performance of Ti6Al4V lattice metamaterials under dynamic loading

Rafael Sancho[1*] | **Irene Chichón-Romeo[1]** | **Conrado L. Garrido[2],**
Daniel Barba[2] | **Francisco Gálvez[1]**

[1]Departamento de Ciencia de Materiales, Universidad Politécnica de Madrid, C/Profesor Aranguren 3, 28040 Madrid, Spain.

[2]Departamento de Materiales y Producción Aeroespacial, Universidad Politécnica de Madrid, Plaza Cardenal Cisneros, 3, 28040 Madrid, Spain

Correspondence
rafael.sancho@upm.es
irene.chichonr@alumnos.upm.es
conrado.garrido@upm.es
daniel.barba@upm.es
f.galvez@upm.es

This work studies the compressive mechanical performance, under quasi-static (0.01s[-1]) and dynamic loading (450s[-1]), of two strut-based lattices for bone implants: the BN-type and the LN-type. The influence of relative density is also analyzed by testing lattices with four different strut diameters. Both structures show a bend-dominated deformation mechanism and a low strain-rate sensitivity for strains larger than 5% for all solid fractions. The strain rate sensitivity is mainly focused on the transition between the linear and stress-plateau region, with a stress enhancement 33% lower than the base material. With respect to the performance of the cell topology, the LN-type shows a specific behavior superior to that of the BN-type.

1. INTRODUCTION

Additively manufactured (AM) metamaterials are human-designed structures that have great potential in fields such as the aerospace, military and medicine industries due to their possibilities of light-weighting, topology optimization and multifunctionalization. For example, AM metamaterials could be used to build light and high-energy absorption add-on armors for military vehicles [1] or to design components that integrate several functionalities, such as aerospace structures that

incorporate structural, fuel management and impact protection capabilities [2] or medical implants with improved osseointegration and bone-like stiffness [3 ,4].

 These structures are usually composed of struts and nodes (lattice metamaterials), although other complex geometries such as plate-lattices or tripe periodical minimal surfaces (TPMS) are also part of this material family. The core structure of metamaterials plays an important role in mechanical performance (and in added functionality, too), but the influence of other properties of the struts, such as characteristics lengths, orientations, and microstructure, is also significant [5]. In this regard, some authors have studied and linked the influence of the core design and the strut size (porosity) on the quasi-static mechanical performance of metallic metamaterials intended for several applications [6-9]. But much less work has been done under dynamic loading and most of it is focused on metamaterials optimized for crashworthiness [10, 11], not considering other lattice configurations that are used in sectors like biomedicine. Without extending the available information under dynamic loading to different geometries and configurations, the efforts around the optimization of AM structures in order to work under wide conditions are incomplete. Therefore, in this work, the authors study, experimentally, the effect of the core structure and diameter of the struts on the mechanical performance of bio-inspired Ti6Al4V lattice metamaterials under quasi-static and dynamic loading.

2.   MATERIALS AND EXPERIMENTAL METHODS

Experimental methods

The studied specimens are two bio-inspired strut-based lattices designed for bone implants: the LN-type and the BN-type. The terms LN and BN refer to the type of function that describes the pore-size distribution. For each lattice type, four different strut diameters were considered (200, 250, 300 and 350 µm) to study the effect of the strut thickness and lattice solid fraction (s.f.) on the mechanical response. It is important to note that the present lattices have a random unit cell, which provides a more isotropic behavior compared with the periodic ones. The lattice geometries are depicted in Figure 1 and their real relative densities are collected in Table 1.

Prismatic Ti6Al4V samples, with dimensions of 17×10.5×10.5 mm approximately, were manufactured using the Selective Laser Melting (SLM) technique, in particular, employing a Renishaw AM400 machine with a modulated 200W ytterbium fibre laser. More information about the sample manufacturing, printing parameters and effect of size and orientation on Ti6Al4V can be found in [5].
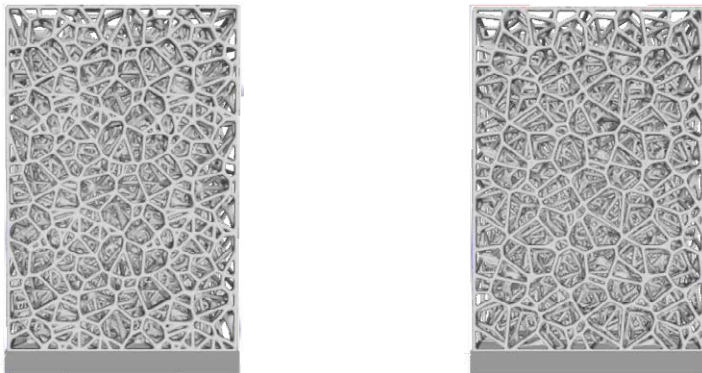
FIGURE 1 (Left) BN-type lattice and (Right) LN-type lattice with a designed strut diameter of 200 µm

TABLE 1   Real relative density (solid fraction (s.f)) for the manufactured lattices.

Lattice topology	XX-200	XX-250	XX-300	XX-350
BN (s.f)	0.42	0.49	0.56	0.60
LN (s.f)	0.52	0.59	0.61	0.68

Experimental methods

Quasi-static and dynamic compression tests were performed on the AM samples. Since the tests reported in this work belong to a preliminary study, only one experiment was conducted for each condition and lattice geometry.

Quasi-static tests were performed using a servo-hydraulic MTS universal testing machine equipped with a 100 kN load cell. The samples were deformed at a strain rate of 0.01 s^{-1}. The displacement of the compression plates was tracked using digital image correlation (DIC). On the other hand, the dynamic tests were done using a Split Hopkinson Pressure Bar system (SHPB). The samples were loaded, approximately, at an engineering strain rate of 450 s^{-1}. Figure 2 shows the schematic of the SHPB set-up used. The system comprises an input and an output bar, both made of maraging C250 steel and a projectile made of another steel, which is responsible for creating the incident compressive stress pulse in the input bar. The specimen was placed between the input and output bar and some lubricant was used to reduce the friction at the bar/specimen interface.

Using the signals from the strain gauges on the bars and applying the theory of 1D-elastic wave propagation, the force and the displacement applied to the specimen was calculated with the equations:

$$F = E_b A_b \varepsilon_t \approx E_b A_b (\varepsilon_i + \varepsilon_r) \tag{1}$$

$$\Delta l = -2c_0 \int_0^t \varepsilon_r \, dt \tag{2}$$

where E_b is the Young's modulus, A_b the cross-sectional area and c_0 the wave velocity of the bars, and ε_i, ε_r, ε_t refers to the incident, reflected and transmitted strain pulses measured on the bars. In the experiments of the present work, a Phantom VE0710 high-speed camera was used to record the failure of the sample during testing at 110000 fps and 256×176 pixels resolution.
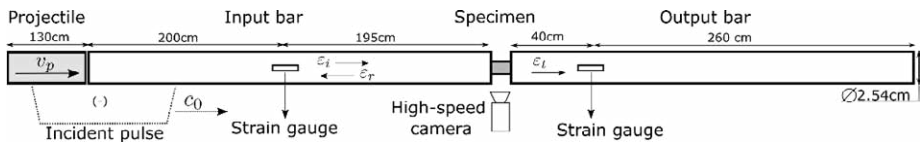
FIGURE 2 Schematic of the SHPB set-up employed in this work.

3. RESULTS AND DISCUSSION

Figure 3 depicts the experimental engineering stress-strain curves of the lattices. It is important to note that the unloading line in the high strain rate curves (solid lines) is related with the unloading part of the incident pulse and not with the load-bearing capacity of the samples. The shape of the stress-strain curves presents two main regions: 1) the linear elastic part at the beginning of the curve and 2) a quite constant-stress region that is related with the collapse mechanisms of the lattices:

yielding, buckling and crushing.   At first sight, both lattice structures show a low strain-rate dependency through deformation for all solid fractions. The stress enhancement seems to be focused on the transition between the linear and stress-plateau region, or in other words, the bell-shape peak at the beginning of the collapse region. This region corresponds to where yielding localization takes place and where the strain-rate sensitivity of the base material become more important. On the other hand, it seems that inertial effects are not important in the present case.

Figure 4 (left) shows a comparison between the Johnson-Cook strain-rate sensitivity parameter for the present lattices and such parameter for the Ti6Al4V alloy with different microstructures [12]; being the β-annealing (BA) the one with a microstructure similar to the AM alloy, a α-lamellar structure with β-phase at lath boundaries [5]. On average, the JC strain rate sensitivity parameter is 33% lower than the base material.

The evolution of the maximum yield stress in the 0-0.05 strain range as a function of the relative density is plotted in Figure 4 (right). Depending on the exponent of the power-law that fits the experimental dots, the deformation of the lattice can be stretch dominated (equal to 1) or bend dominated (greater than 1). As indicated in the graph, both lattices present bending dominated mechanism in terms of yielding. For both structures, the loading rate has little impact on the power-law exponent.

Finally, when comparing the inelastic performance of both structures, it can be seen that the LN-type lattice is preferred (higher specific properties). The explanation can be found by analyzing the deformation sequence of each lattice (see Figures 5, 6). In the LN-type lattice, the deformation and failure consolidates along one plane while in the BN-type lattice, several parallel planes accommodate the failure and deformation. It seems clear that accommodating most of the deformation in a single plane translates into a more efficient densification of the collapse region.
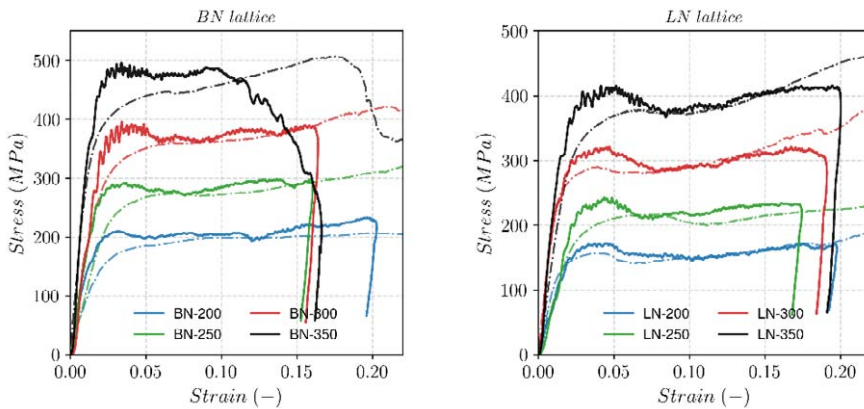
FIGURE 3 Experimental engineering stress-strain curves comparing the quasi-static (dashed line) vs the dynamic (solid line) performance. Each color corresponds to a lattice with a different strut-diameter (different solid fraction).
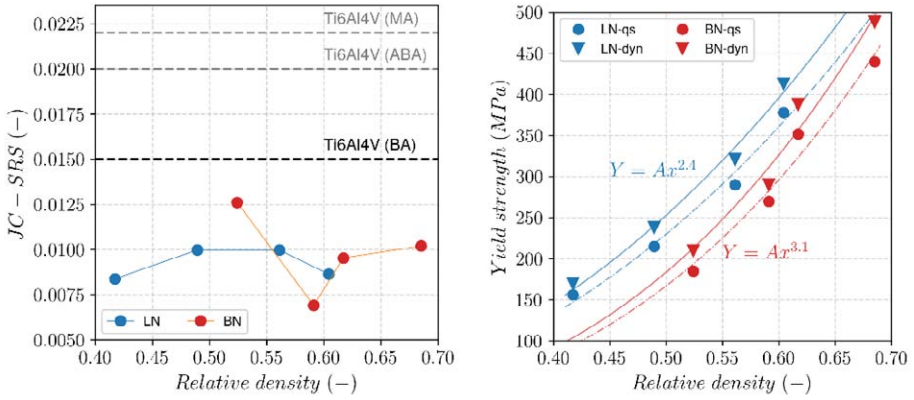
FIGURE 4 (Left) Johnson-Cook strain-rate-sensitivity parameter (*C* in the traditional equation) as a function of the relative density for the two lattices. The horizontal dashed lines indicate the JC-SRS parameter for Ti6Al4V with different microstructure: mill-annealing(MA), α+β annealing (ABA) and β annealing (BA) [12]¡**Error! No se encuentra el origen de la referencia.**. β annealing presents a similar microstructure to additive manufactured Ti6Al4V. (Right) Relationship between the yield strength* and relative density for the LN- and BN –type of lattices under quasi-static and dynamic loading. *Yield strength defined as the maximum yield stress up to 0.05 strain.
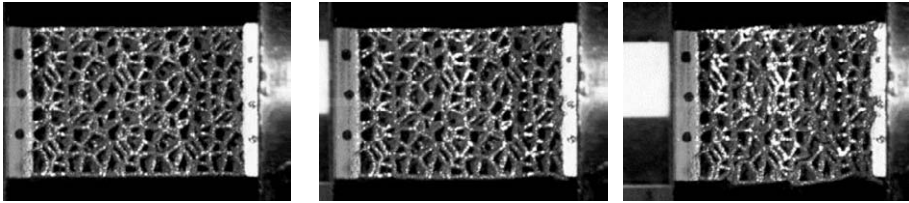
FIGURE 5 (Lattice BN-200) Deformation sequence during high strain-rate loading at strain laves of 1) 0.025, 2) 0.055 and 3) 0.20
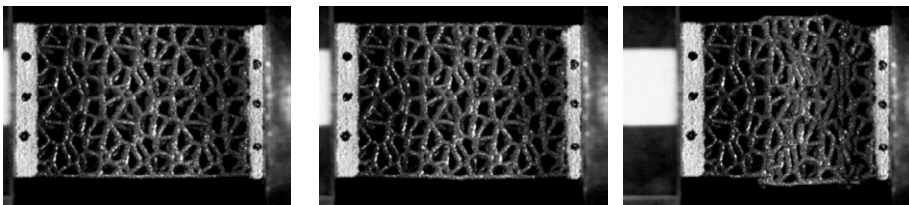
FIGURE 6 (Lattice LN-200) Deformation sequence during high strain-rate loading at strain laves of 1) 0.035, 2) 0.06 and 3) 0.19

4. CONCLUSIONS

In this work, the compressive performance of two bio-inspired strut-based lattices, BN- and LN-type, under quasi-static and dynamic loading has been studied. The influence of the solid fraction of the lattices has been considered too. The following conclusions can be drawn:

- Both lattices show a low strain-rate sensitivity. The strain rate sensitivity is more significant at the beginning of the plateau-stress region and is 33% lower than the base material.
- For the studied lattices, the solid fraction, between 40 – 70%, does not have an important influence on the strain-rate sensitivity and it is similar in both cases.
- The inelastic performance of the LN-type is more efficient when comparing with the BN-type. In both cases, the deformation is bend-dominated. The LN-type lattice tends to accommodate all the prescribed deformation along a single failure region while the BN-type fails along several planes.

Acknowledgements

References

[1] Han SC, Kang DS, Kang K. Two nature-mimicking auxetic materials with potential for high energy absorption. Materials Today 26 (2019): 30-39.

[2] Ferro CG, Varetti S, De Pasquale G, Maggiore P. Lattice structured impact absorber with embedded anti-icing system for aircraft wings fabricated with additive SLM process. Materials Today Communications 15 (2018): 185-189.

[3] Alabort E, Barba D, Reed R C. Design of metallic bone by additive manufacturing. Scripta Materialia 164 (2019): 110-114.

[4] Barba D, Alabort E, Reed R C. Synthetic bone: Design by additive manufacturing. Acta biomaterialia 97 (2019): 637-656.

[5] Barba D, Alabort C, Tang YT, Viscasillas MJ, Reed RC, Alabort E. On the size and orientation effect in additive manufactured Ti-6Al-4V. Materials & Design 186 (2020): 108235.

[6] Yan C, Hao L, Hussein A, Young P. Ti–6Al–4V triply periodic minimal surface structures for bone implants fabricated via selective laser melting. Journal of the mechanical behavior of biomedical materials 51 (2015): 61-73.

[7] Zhang XY, Fang G, Leeflang S, Zadpoor AA, Zhou J. Topological design, permeability and mechanical behavior of additively manufactured functionally graded porous metallic biomaterials. Acta Biomaterialia 84 (2019): 437-452.

[8] Lozanovski B, Leary M, Tran P, Shidid D, Qian M, Choong P, Brandt M. Computational modelling of strut defects in SLM manufactured lattice structures. Materials & Design 171 (2019): 107671.

[9] Chen X, Ji Q, Wei J, Tan H, Yu J, et al. Light-weight shell-lattice metamaterials for mechanical shock absorption. International Journal of Mechanical Sciences 169 (2020): 105288

[10] Tancogne-Dejean T, Li X, Diamantopoulou M et al. High Strain Rate Response of Additively-Manufactured Plate-Lattices: Experiments and Modeling. J. dynamic behavior mater. 5, 361–375 (2019).

[11] Harris JA, McShane GJ. Impact response of metallic stacked origami cellular materials. International Journal of Impact Engineering 147 (2021): 103730.

[12] Perosanz S, Viscasillas M, Piris NM, Hokka M, Barba D. On the effect of the microstructure on the dynamic behaviour of Ti-6Al-4V. EPJ Web of Conferences. Vol. 250. EDP Sciences, 2021

18

Plastic and fracture behavior of SLM made stainless steel 316L with application to crushing of shell-lattices

X. Li | C.C. Roth | T. Tancogne-Dejean | D. Mohr

Department of Mechanical and Process Engineering, ETH Zurich, Switzerland

Correspondence

C.C. Roth, Department of Mechanical and Process Engineering, ETH Zurich, Switzerland
Email: ccroth@ethz.ch

Stainless steel 316L made through Selective Laser Melting (SLM), a powder bed fusion process to additively manufacture material, is investigated in a combined experimental and numerical campaign. Material characterization experiments covering a range of stress states are carried out at strain rates between 10e-3/s and 10e3/s on uniaxial tension, shear, notched tension and dihedral mini-Nakazima specimens. The constituent behavior of the material is described by a Hill'48 quadratic plasticity model with a non-associated flow rule, a combined Swift-Voce hardening and a Johnson-Cook type of strain rate and temperature law. A stress state dependent Hosford-Coulomb fracture initiation model is used to model the fracture response. To further validate the identified material model in a structural application, elastically-isotropic (smooth) shell lattice are compressed at low and high strain rates and in different orientations and compared with numerical simulations.

*Equally contributing authors
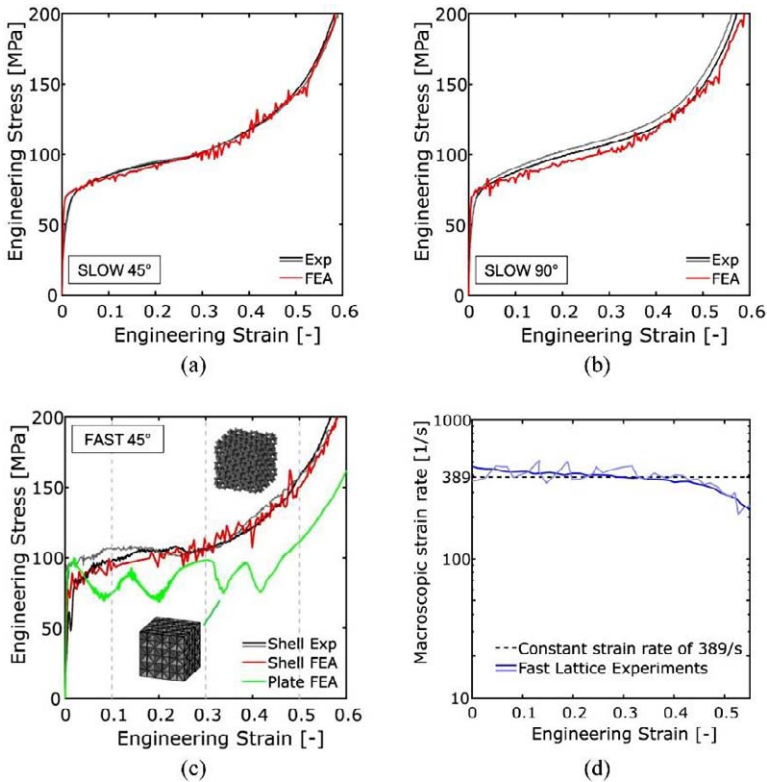
FIGURE 1 Comparison of the engineering stress-strain curves from the experiments (black and grey solid lines) and numerical simulations of smooth shell lattices (red solid lines) for different build directions and loading speeds: (a) slow 45°, (b) slow 90° and (c) fast 45°. The green solid line denotes the results from a numerical simulation on a plate lattice with same number of unit cells (3 × 3 × 3) and relative density of 25%. (d) Evolution of macroscopic strain rate as a function of engineering strain for high-speed compression tests on shell lattice. Observe the rather constant strain rate before densification strain of 50%. Adapted from [1]

REFERENCES

[1]   X. Li, C.C. Roth, T. Tancogne-Dejean, D. Mohr, Rate- and temperature-dependent plasticity of additively manufactured stainless steel 316L: Characterization, modeling and application to crushing of shell-lattices, Int. J. Impact Eng. 145 (2020) 103671. https://doi.org/10.1016/j.ijimpeng.2020.103671.

19

Modelling and optimisation of triply periodic minimal surfaces lattices subjected to high strain-rate compression

Rafael Santiago PhD[1][*] | Alia Ruzanna Aziz PhD[1] | Henrique Ramos[1] | Sara AlMahri[1] | Omar Banabila[1] | Haleimah Alabdouli[1] | Dong-Wook Lee PhD[1] | Zhongwei Guan PhD[1] |

[1]Advanced Materials Research Centre, Technology Innovation Institute, Abu Dhabi, United Arab Emirates

Correspondence

Rafael Santiago PhD, Advanced Materials Research Centre, Technology Innovation Institute, Abu Dhabi, United Arab Emirates
Email: rafael.santiago@tii.ae

Lattices based on Triply Periodic Minimal Surfaces (TPMS) are promising for aerospace, biomedical and defence applications, requiring high energy absorption with reduced structural weight. Thus, the current work focuses on modelling and optimising various TPMS lattices under impact loading conditions. Here, previously validated numerical models were used to propose a functionally graded TPMS lattice topology, which pointed to a specific energy absorption superior to a non-graded counterpart. Finally, equivalent graded and non-graded topologies were manufactured and tested in a Direct Impact Hopkinson Bar device, confirming the improvement proposed. The present study is applicable for predicting and improving the response of complex architectures of TPMS lattices subjected to impact loadings.

1   INTRODUCTION

The advancement in the development of lattice structures with customised behaviour has led to a growing number of multidisciplinary applications for lightweight impact energy absorbing structures [1-4]. A number of researchers [1, 5-8] have discovered that the mechanical properties of a lattice structure can be optimised by infinite combinations of the material, architecture and relative density. Amongst various lattice structures, the triply periodic minimal surfaces (TPMS) geometries emerge as versatile architectures suitable for most additive manufacturing (AM) techniques.

TPMS structures are shell-based lattices which are mathematically defined with an open cell and self-structured design [4-5, 9-14]. Zhao et al. [13] investigated the compressive mechanical response of a series of Gyroid and Primitive TPMS topologies, both experimentally and numerically. In their study,

*Equally contributing authors

although the numerical model could predict the overall response and failure mode, the simulation resulted in an error of between 10 and 30%. In another study, Wang et al. [14] carried out quasi-static compression tests on cylindrical shells constructed by gyroid TPMS lattices. The authors developed an explicit finite element model based on shell elements and bi-linear material models and reported a good approximation with the experimental data. The mechanical response of TPMS structures made of 316L stainless steel subjected to quasi-static and high strain rates have been experimentally tested and numerically modelled by Li et al. [15]. The plasticity model with strain-rate and temperature-dependent showed a good agreement with the measured results.

This study focuses on numerical simulation of Diamond topologies with different relative densities under static and dynamic loadings. Finite element (FE) simulations were then validated and used to propose graded Diamond architectures with superior impact performance. Finally, samples of functionally graded lattices were manufactured and experimentally tested to evaluate the results pointed by the models.

2   MATERIALS AND METHODS

Functionally graded (FG) lattices were designed with the aim of enhancing the specific energy absorption (SEA) and residual deformation after impact (DAI) of the Diamond (D) lattice. In particular, a total of three gradients were studied, which are given by

Linearly Graded 1 (LG1):
$$\rho = 0.20 + 0.0125z, \tag{1}$$

Quadratic Graded 3 (QG3):
$$\rho = 0.10 + 0.075z - 0.0047z^2, \tag{2}$$

Quadratic Graded 4 (QG4):
$$\rho = 0.20 + 0.0375z - 0.00235z^2, \tag{3}$$

where ρ is associated to the relative density and z is the vertical position determined from the base of the TPMS. In the current study, all of the graded lattices present the same overall relative density of $\bar{\rho} = 30\%$, and a non-graded topology is deemed as the baseline (BL) structures. **FIGURE 1** illustrates the relative density distribution across the height of the lattice structures.

Three-dimensional explicit finite element simulations were performed using the ABAQUS/Explicit software package. The 16mm x 16mm x 16mm cube lattices were modelled with the surface thicknesses were defined based on the relative density. The CAD files for these lattices were imported into Abaqus as a standard tessellation language (.stl) format. In Abaqus software, the meshes were then generated for the lattice models by defining the modified quadratic tetrahedral elements (C3D10M) combined with hourglass control [16].
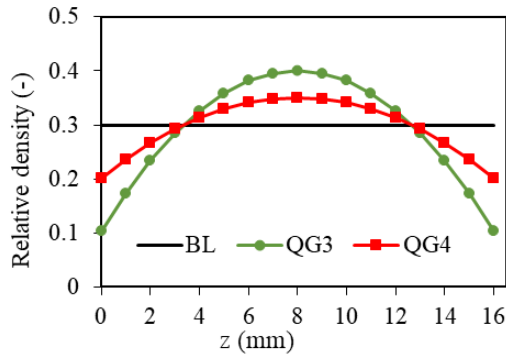
FIGURE 1: Relative densities distribution of the functionally graded lattices against the baseline structures.

The dynamic experiments were simulated by modelling the TPMS lattices between two rigid platens using surface-to-surface contact capability in Abaqus for all of the possible interactions, as shown in **FIGURE 2**. The upper rigid platen was allowed to translate only along the z-direction, while the bottom platen was held as fully fixed. The impact mass and velocity were specified at the upper rigid platen, based upon the direct impact Hopkinson bar (DIHB) test conditions outlined by AlMahri et al. [2].
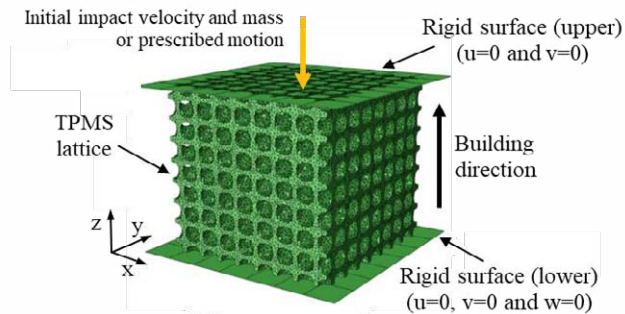
FIGURE 2: Boundary conditions applied for the FE lattice simulation.

In an effort to assess the FE results, the mechanical properties and deformation mode were investigated for functionally graded TPMS structures fabricated from 316L stainless steel by selective laser melting technique from gas-atomised powder. Prior to extracting the specimens from a build platform, a 2-hour post-heat treatment cycle of 600 °C in a vacuum furnace was applied.

Tests were undertaken on the lattices in a direct impact Hopkinson bar (DIHB) device as schematically given in **FIGURE 3**. Here, the stainless steel bar and the striker had dimensions of 19 mm in diameter and 2 m lenght. A compressed air reservoir attached to a high-speed discharge valve was used to accelerate a 0.559 kg striker towards the specimen placed on the transmitted bar. Directly after the impact, the transmitted bar signal was detected by a strain gauge that was fixed away from the specimen bar interface. The output signals were conditioned by a high-frequency strain amplifier followed by data logging using Picoscope at 1M samples/sec. A high-speed camera (Photron Fastcam Nova S16) operating at a rate of 50,000 fps was used to record the morphology under dynamic loading. The video data is post-processed with image tracking via PFA software to extract the strain history and striker velocity.
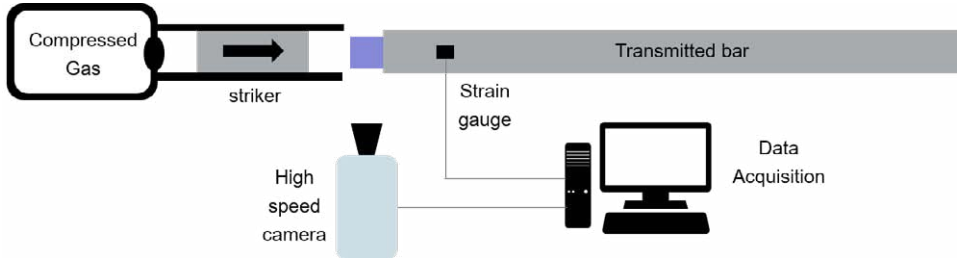
FIGURE 3: Schematic on the Direct impact Hopkinson bar (DIHB) experimental setup.

3   RESULTS

3.1   Numerical Prediction

The comparison of the mechanical behaviour between the BL and graded topologies after impact is summarised in Figure 4. It is clear that the lattices have deformed distinctively due to the grading of the structures. It is interesting to note that the BL failed by shear-band formation, whereas most of the graded lattices deformed by layer-based, typically initiated at the section with the lowest relative density.
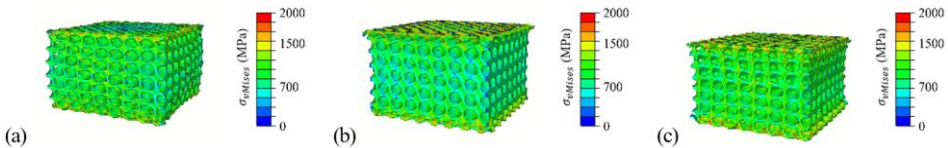
FIGURE 4: The deformation of (a) BL, graded Diamond TPMS (b) QG3 and (c) QG4 at $\varepsilon = 0.30$ of impact loading.

The DAI and SEA for strain up to 0.50 for the BL and graded topologies are given in Table 1. For both QG3 and QG4 with negative curvature quadratic functionally graded lattices, an improvement in SEA and DAI was observed. The SEA for the QG3 and QG4 are higher than the BL, with an enhancement of approximately 10.5 % and 31.0 %, respectively. Accordingly, lower residual deformation after impact was recorded with a reduction of 6.6 % and 8.2 %, respectively.

TABLE 1: Details of the specific energy absorption and residual deformation after impact for the BL and the functionally graded structures.

Topology	SEA[1] (J/g)		DAI (mm/mm)	
BL	27.79	-	0.56	-
QG3	36.39	(+31.0%)	0.52	(-8.2%)
QG4	30.70	(+10.5%)	0.53	(-6.6%)

[1]: up to ε=0.50.

3.2   Experimental Verification

The BL, QG3 and QG4 lattices were manufactured, resulting in an overall relative density of 36% for all the topologies. Although the same topologies used in Section 3.1 was considered for manufacturing, limitations of the equipment used resulted in slightly higher relative densities.
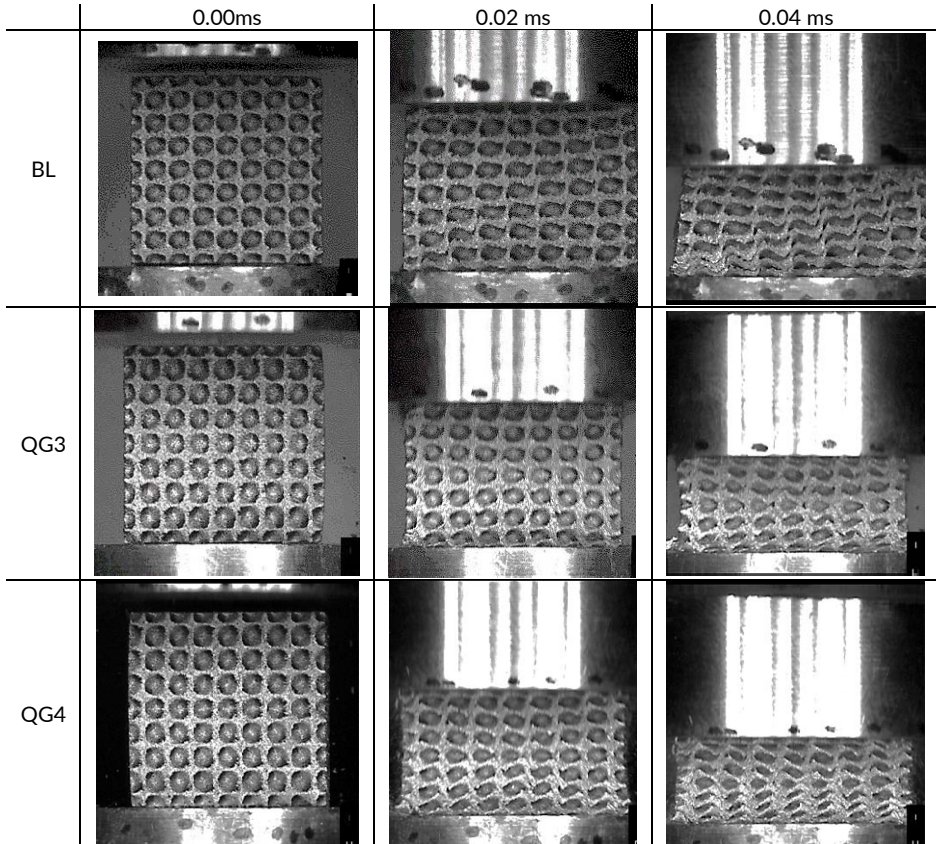
FIGURE 4: Evolution of the lattices TPMS deformation mode during the impact.

The topologies were tested under impact in a DIHB device, with the deformation evolution summarised in **FIGURE 4**. It was noted that the deformation mode changed from a shear-band formation in BL to a progressive layer buckling in QG3, caused by the lower relative density lattice layer in the impacted and opposite cube faces. In addition, the QG4 topology exhibited a mixed deformation mode, with the shear band in its central part and progressive layer buckling in the impacted and opposite faces. The FE modelling in Section 3.1 predicted the change in the deformation mode, as observed experimentally.
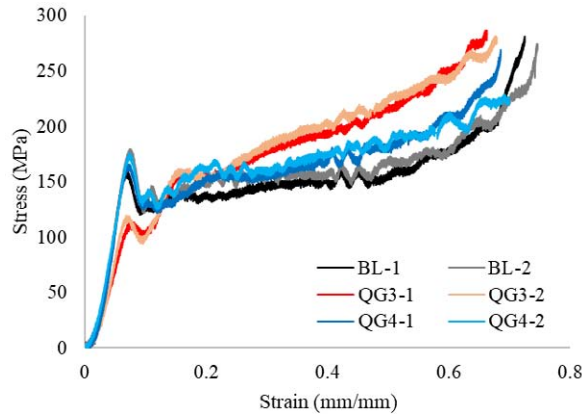
FIGURE 5: Strain-stress responses of BL-*n*, QG3-*n* and QG4-*n* topologies during impact, being *n* the specimen identification number.

Figure 6 compares the compressive strain-stress of the topologies during impact, showing the differences between the three topologies responses. The BL exhibited an almost flat stress plateau until the densification, and the graded topologies presented a crescent strain-stress response. Besides this, it was noted that the QG3 strain-stress slope is higher than the QG4 lattices. The observed strain-stress responses agree with the FE simulations.

TABLE 2: Summary of experimental results for the BL, QG3 and QG4 topologies.

Topology	SEA (J/g)		DAI (mm/mm)	
BL	28.55	-	0.73	-
QG3	33.81	(+18.4%)	0.67	(-5.0%)
QG4	30.68	(+7.5%)	0.68	(-8.0%)

As summarised in Table 2, the SEA increased by 18.4% and 7.5% for QG3 and QG4, respectively, compared to BL; meanwhile, the DAI subsequently reduced 5.0% and 8.0%. In general terms, the FE predicted the SEA increasing and the decreasing of DAI; however, the SEA was overestimated, probably due to a higher relative density resulting in the samples tested.

4   CONCLUSIONS

This study showed that using functionally graded topologies can improve the impact performance of TPMS lattices, resulting in structures with superior impact energy absorption and lower deformation after impact for the same overall relative density. An appropriate graded topology depends on the boundary conditions, which can be defined using finite element modelling.

5   REFERENCES

[1]   L.J. Gibson, M.F. Ashby, Cellular Solids, Cambridge University Press, 1997.

[2]   S. AlMahri, R. Santiago, D. Lee, H. Ramos, H. Alabdouli, M. Alteneiji, Z. Guan, W. Cantwell, M. Alves, Evaluation of the Dynamic Response of Triply Periodic Minimal Surfaces Subjected to High Strain-Rate Compression, Addit. Manuf. (2021) 102220.

[3]   G. Del Guercio, M. Galati, A. Saboori, P. Fino, L. Iuliano, Microstructure and Mechanical Performance of Ti–6Al–4V Lattice Structures Manufactured via Electron Beam Melting (EBM): A Review, Acta Metall. Sin. (English Lett. 33 (2020) 183–203.

[4]   N. Novak, O. Al-Ketan, L. Krstulović-Opara, R. Rowshan, R.K. Abu Al-Rub, M. Vesenjak, Z. Ren, Quasi-static and dynamic compressive behaviour of sheet TPMS cellular structures, Compos. Struct. 266 (2021) 1–10.

[5]   R.K. Abu Al-Rub, D.-W. Lee, K.A. Khan, A.N. Palazotto, Effective Anisotropic Elastic and Plastic Yield Properties of Periodic Foams Derived from Triply Periodic Schoen's I-WP Minimal Surface, J. Eng. Mech. 146 (2020) 04020030.

[6]   I. Maskery, N.T. Aboulkhair, A.O. Aremu, C.J. Tuck, I.A. Ashcroft, Compressive failure modes and energy absorption in additively manufactured double gyroid lattices, Addit. Manuf. 16 (2017) 24–29.

[7]   R. Mines, Applications for Additively Manufactured Metallic Microlattice Structures: Core Materials in Beams and Panels, Energy Absorbers (Static and Impact), SpringerBriefs Appl. Sci. Technol. (2019) 75–95.

[8]   M. Smith, W.J. Cantwell, Z. Guan, Impact and Blast Response of Lattice Materials, in: Dyn. Lattice Mater., John Wiley & Sons, Ltd, Chichester, UK, 2017: pp. 155–178.

[9]   S. Altamimi, D.-W. Lee, I. Barsoum, R. Rowshan, I.M. Jasiuk, R.K. Abu Al-Rub, On Stiffness, Strength, Anisotropy, and Buckling of 30 Strut-Based Lattices with Cubic Crystal Structures, Adv. Eng. Mater. (2022) 2101379.

[10]   S. V. Balabanov, A.I. Makogon, M.M. Sychov, M. V. Gravit, M.K. Kurakin, Mechanical properties of 3D printed cellular structures with topology of triply periodic minimal surfaces, Mater. Today Proc. 30 (2019) 439–442.

[11]   K. Krishnan, D.-W. Lee, M. Al Teneji, R.K. Abu Al-Rub, Effective stiffness, strength, buckling and anisotropy of foams based on nine unique triple periodic minimal surfaces, Int. J. Solids Struct. 238 (2022) 111418.

[12]   S. Ma, Q. Tang, X. Han, Q. Feng, J. Song, R. Setchi, Y. Liu, Y. Liu, A. Goulas, D.S. Engstrøm, Y.Y. Tse, N. Zhen, Manufacturability, Mechanical Properties, Mass-Transport Properties and Biocompatibility of Triply Periodic Minimal Surface (TPMS) Porous Scaffolds Fabricated by Selective Laser Melting, Mater. Des. 195 (2020).

[13]   M. Zhao, D.Z. Zhang, F. Liu, Z. Li, Z. Ma, Z. Ren, Mechanical and energy absorption characteristics of additively manufactured functionally graded sheet lattice structures with minimal surfaces, Int. J. Mech. Sci. 167 (2020).

[14]   Y. Wang, X. Ren, Z. Chen, Y. Jiang, X. Cao, S. Fang, T. Zhao, Y. Li, D. Fang, Numerical and experimental studies on compressive behavior of Gyroid lattice cylindrical shells, Mater. Des. 186 (2020) 108340.

[15]   X. Li, C.C. Roth, T. Tancogne-Dejean, D. Mohr, Rate- and temperature-dependent plasticity of additively manufactured stainless steel 316L: Characterisation, modeling and application to crushing of shell-lattices, Int. J. Impact Eng. 145 (2020) 103671.

[16]   M. Smith, ABAQUS User's Manual, Version 6.14, Dassault Systèmes Simulia Corp, United States, 2014.

20

316L architected materials made by LMD-P and SLM: a comparative study of manufacturing and compressive behavior

C.Buros[1] | P.Viot[2] | J.Lartigau[1]

[1] Univ. Bordeaux, ESTIA INSTITUTE OF TECHNOLOGY, F-64210 Bidart, France

[2] Arts et Métiers, I2M, F-33405 Talence, France

Correspondence

C.Buros, Univ. Bordeaux, ESTIA INSTITUTE OF TECHNOLOGY, F-64210 Bidart, France
camille.buros@estia.fr

The behavior of architected materials depends on the bulk material and its porous structure. Mechanical properties of parts produced by additive manufacturing highly depends on the parameters of the process. This work focuses on the behavior of metallic architected structures under compressive loading, considering both the 3D printing strategy and morphology of the architecture. Tri-hexagonal structures in 316L steel are fabricated by LMD-P and SLM and tested under quasi-static compressive loading. The structure of the bulk material is also studied through microscopic observations. This paper presents the experimental set-up and the corresponding characteristics obtained.

1   INTRODUCTION

Cellular materials are defined by Gibson & Ashby (1997) as a set of cells with solid faces and/or beams assembled in such a way that they fill the space. Architected materials represent a new class of cellular materials achieving new structural and functional properties, pushing the limits of Ashby's maps. Architected materials are defined either as the combination of two or more materials, or a material and space, assembled in such a way that they possess characteristics not achievable with the material alone [1]. Several examples of architected materials exist: fibrous and particulate composites, periodic (or lattice) structures, sandwich structures, etc [1]. The materials studied in this study are periodic structures. These materials are composed of regular cells repeated along different orientations in space [2]. Due to their low mass and their periodic structure, these materials possess several advantages. They are particularly interesting to optimize the microstructure according to a

desired final application. These materials are, for example, regularly used for lightweight applications. Due to their ability to absorb energy during an impact, architectural structures are widely used for applications involving the protection of goods and people. An effective protection is guaranteed when the energy absorbed is maximized for a minimized impact force. Architectural materials can undergo large deformations for moderate stress [2]. The emergence of additive manufacturing (AM) technologies permits designing and manufacturing new geometries for these materials.

In this work, the architecture generated during the fabrication enables the absorption of shock energy. Hence there is a particular interest in optimizing the architecture that can be finely reproduced by AM, unlike a conventional cellular material [3]. However, the microstructure and mechanical behavior of metallic parts made by AM depend on many parameters in order to obtain, from the numerical geometry, a real structure with expected properties. In this study, periodic architected structures are fabricated by LMD-P and SLM. The material used is an austenitic stainless steel 316L, also named X2CrNiMo17-12-2. This work presents first results about the influence of the processing parameters on both microstructure and mechanical behavior at different strain rates.

2   MANUFACTURING OF PARTS

Two metal additive manufacturing technologies are considered in this study: laser metal deposition with powder (LMD-P) and selective laser melting (SLM). For this first phase of the study, the fabricated structures present a tri-hexagonal periodic structure of different dimensions and geometries.

2.1   Laser Melting Deposition – Powder (LMD-P)

LMD-P technology is classified as a direct energy deposition (DED) technology [4]. During the manufacture of parts, metallic powder – in this study 316L steel - is sprayed through a nozzle, deposited, and fused by a laser beam onto a surface, called the substrate. When the melt pool cools down, the metal solidifies to create part layers. Various materials can be manufactured through this process with high flexibility regarding the part dimensions and faster manufacturing time than SLM process. However, post-processing steps are usually required to obtain a correct surface flatness [5].

The machine used in this study is a BeAM MAGIC 800 machine that has a fiber laser head (maximum power 2kW) mounted on a 3-axis system. The nozzle used in the fabrication of the tri-hexagonal structures has an output diameter of 1.2 mm.

Cubes of 25 x 25 x 30 mm (Figure 1a), cylinders of 25 mm diameter and 30 mm height (Figure 1b) and blocks of 85x85x15 mm (Figure 1c) are fabricated on steel substrates of dimensions 50 x 50 x 5 mm and 150 x 150 x 5 mm.
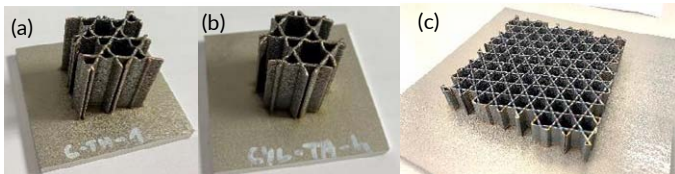
Figure 1 : Tri-hexagonal structures manufactured by LMD-P : (a) cube, (b) cylinder, (c) block

To realize the tri-hexagonal pattern, single beads were deposited. Experiments were carried out to study the influence of scanning speed V (mm/min) and of the distance when the laser is off during a trajectory intersection - which we will call laser off distance - noted d (mm). First-order parameters (laser power, scanning speed and powder feed rate) plus layer height Δz (mm) are determined following previous experiments with the machine. One set of parameters was identified as reference from

performed experiments. The input parameters used for each sample fabrication are presented in Table 1.

Table 1 : Input parameters used for manufacturing tri-hexagonal structures

Input parameters	Values
Laser power P	200 W
Layer height Δz	0.15 mm
Powder feed rate F	13 % (2.8 – 3.0 g/min)
Scanning speed S	1000 mm/min
Laser distance off d	0 mm

2.2   Selective Laser Melting (SLM)

Selective Laser Melting (SLM) is an additive manufacturing technology based on a powder bed and a thermal energy source. During the manufacture of parts after a layer of metal powder is deposited on a support and fused by a laser beam according to the desired geometry. After the first layer is solidified a second layer of powder is deposited and melted. The SLM process allows the manufacturing of complex geometries with a high dimensional accuracy. However, the size of the parts produced is limited by the dimensions of the powder bed [6].

The machine used in this study is a SLM 280HL (SLM Solutions) equipped with a fiber laser with a beam diameter of 80 μm and wavelength of 1070 μm. Cubes of 25 x 25 x 30 mm^3 and cylinders of 25 mm diameter and 30 mm height are fabricated (Figure 2). The input parameters used were determined from previous experiments with the machine.

Figure 2 : Tri-hexagonal structures manufactured by SLM

3   STRUCTURE

The morphology and microstructure of parts made by additive manufacturing processes depend strongly on the cooling rate and thermal gradients in the melt [5, 6]. Austenitic stainless steels, such as 316L steel, exhibit a microstructure composed of highly heterogeneous patterns distributed over several scales [8, 9, 10].

3.1   Material and methods

To observe the microstructure of the structures fabricated by LMD-P and SLM, the samples were cut along the direction of fabrication to observe the stacking of the layers. The surfaces were polished with sandpapers of different grain sizes: P120, P400, P800, P1200, P2400 and P4000, then diamond solutions of 3 μm and 1 μm were used. For etching, the samples are placed in a solution composed of - HCl - H2O in the same quantity for twenty seconds. The microstructure is observed with a digital microscope OLYMPUS PMG3. The images are analyzed with the software ToupView.

3.2 Results

The observed structures show several overlapping melt baths with an elliptical deposition shape. This microstructural feature is typical of additive manufacturing processes and is a consequence of the Gaussian distribution of laser energy [11].

For the structures fabricated by LMD-P, various grain morphologies are observed within the microstructure: columnar grains and equiaxed grains. Columnar grains are represented by an elongated shape that grows in the direction of a maximum thermal gradient. In Figure 4, the growth direction of the columnar dendrites is perpendicular to the curved edges of the melt pool and converges towards the center. On the contrary, in the central zone of the melt pool, equiaxed dendrites are observed (Figure 3). This phenomenon is the consequence of a change in the heat transfer mode. In a 316L steel, several microstructural features are observed. In the central zone of the melt, where the metal in liquid form solidifies slightly later, convective heat transfer dominates. On the contrary, at the edges of the melt, conductive heat transfer is the dominant transfer mode [11].
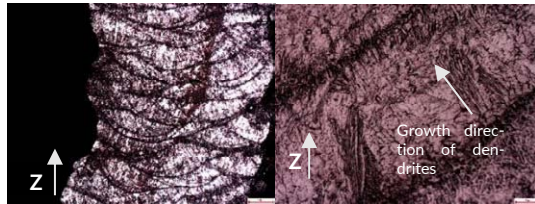
Figure 3 : Micrographs of 316L tri-hexagonal structures made by LMD-P

4 MECHANICAL BEHAVIOUR

4.1 Material and methods

To analyze the macroscopic compression behavior of architectural structures, uniaxial quasi-static compression tests are first performed on a ZWICK Roell machine with a capacity of 250 kN. Before performing dynamic tests, it is important to observe and measure the phenomenon involved under simpler experimental conditions and observe the macroscopic response of the material at low strain rates [12]. The performed tests are conducted at speeds of 10 mm/min and 500 mm/min for both additive manufacturing technologies. A crosshead displacement of 10 mm is imposed on LMD-P structures, and a crosshead displacement of 15 mm is informed for SLM structures. Images of the deformation phase are captured by a CANON EOS 50D camera at an image capture rate of 1 and 3 Hz at 10 mm/min and 3 Hz at 500 mm/min. Thermal images are captured by a FLYR SC 7000 camera at a frequency of 150 Hz during the tests at 500 mm/min.

4.2 Results

Mean, forces-displacement curves and the applied compressive testing parameters are presented in Figure 4.

In this work, tri-hexagonal structures undergo compressive strengths between 85 kN and 113 kN for structures made by LMD-P and between 100 kN and 107 kN for those made by SLM without reaching failure for both processes. The classical behavior of a cellular material under compressive loading is found during the loading phase - for both FA processes - a linear elastic region, characterized by a linear slope, is observed, followed by a plastic plateau characterized by a waviness, and then a densification region characterized by the collapse of cells into the structure [1]. With the images captured during the test, the deformation of the structure for various displacements imposed by the machine crosshead is observed in Figure 5.
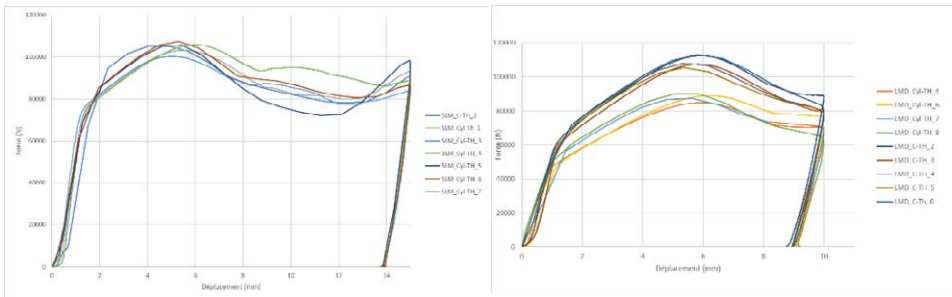
Geometry	Process	Test reference	Speed test mm/min	Average test time s	Maximum displacement mm	Maximum force N
Tri_hexagonal cube	SLM	C1	500	2,5	15,0	105940
Tri_hexagonal cube	SLM	C2	500	2,3	15,0	105313
Tri_hexagonal cube	SLM	C3	10		10,0	
Tri-hexagonal cylinder	SLM	R1	10	54,9	15,0	103192
Tri-hexagonal cylinder	SLM	R2	10	49,6	15,0	107997
Tri-hexagonal cylinder	SLM	R3	10	49,6	15,0	100185
Tri-hexagonal cylinder	SLM	R4	10	49,6	15,0	105842
Tri-hexagonal cylinder	SLM	R5	500	2,1	15,0	105723
Tri-hexagonal cylinder	SLM	R6	500	2,6	15,0	107399
Tri-hexagonal cylinder	SLM	R7	500	2,4	15,0	99730,6

Geometry	Process	Test reference	Speed test mm/min	Average test time s	Maximum displacement mm	Maximum force N
Tri-hexagonal cylinder	LMD-P	CYL-TH-1	10	5,9	7,0	86987,5
Tri-hexagonal cylinder	LMD-P	CYL-TH-4	10	33,7	10,0	84833,8
Tri-hexagonal cylinder	LMD-P	CYL-TH-5	10	33,0	10,0	72918,3
Tri-hexagonal cylinder	LMD-P	CYL-TH-6	10	33,7	10,0	88876,7
Tri-hexagonal cylinder	LMD-P	CYL-TH-7	500	1,6	10,0	87276,6
Tri-hexagonal cylinder	LMD-P	CYL-TH-8	500	1,5	10,0	90003,7
Tri_hexagonal cube	LMD-P	C-TH-2	10	34,5	10,0	112490
Tri_hexagonal cube	LMD-P	C-TH-3	10	33,9	10,0	107443
Tri_hexagonal cube	LMD-P	C-TH-4	500	1,4	10,0	108013
Tri_hexagonal cube	LMD-P	C-TH-5	500	1,4	10,0	105404
Tri_hexagonal cube	LMD-P	C-TH-6	500	1,3	10,0	113015

Figure 4 : 316L tri-hexagonal structures compressive behavior (a) manufactured by SLM, (b) manufactured by LMD-P, (c) obtained mechanical results

The phenomenon of buckling, characterized by the undulation on the compression curve, is visible in Figure 5. The structure shows an elasto-plastic behavior - as defined by Gibson & Ashby (1997) - meaning, the collapse of the cells is due to the plastic buckling of the walls. In this case, the material is permanently damaged. The observed buckling induces local plasticity and is indicative of the quality of the part, which has few porosities in the microstructure that could have initiated cracking. The local temperature is quantified by the thermal camera during the tests at 500 mm/min and reaches a maximum temperature of 100°C. Compared to foams (stochastic materials), architected materials possess higher strength. Indeed, during deformation, the walls of the foams twist while those composing the architected materials stretch and compress [1, 3]. Architected materials behave similarly to open cell foams, making them particularly suitable for energy absorption applications.
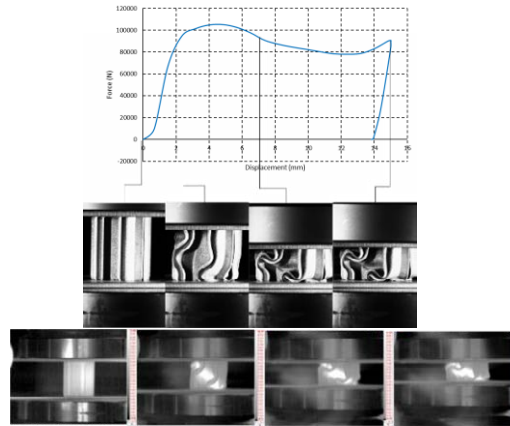
Figure 5 : Compressive behavior of an architected tri-hexagonal structure made by SLM at 500 mm/min

5   CONCLUSIONS AND PERSPECTIVES

The rapid breakthrough in additive manufacturing processes has led to the emergence of new complex design hardly achievable with subtractive processes. Hence, intentionally designed porous materials, as architected structures, have quickly spread out in various industrial and research sectors. With these types of materials, a mechanical behavior can be targeting through the precise control of the microarchitecture, making them good candidates for energy absorption applications. However, the microstructure and mechanical performance of architected materials are affected by the numerous input parameters applied during their fabrication, as well as process-induced defects. The mechanical behavior of architected structures is profoundly dependent of the intrinsic characteristics of the material: the density of the bulk material, the pattern of the structure, the microstructure and the modes of mechanical solicitation. In this work, the compressive behavior of LMD-P and SLM 316L architected materials, through quasi-static compression tests were investigated. The typical behavior of cellular materials in compression was highlighted.

To represent problematics of impact absorption, further investigations will be performed through dynamic testing under high-strain rate. Moreover, given the high forces underwent by tri-hexagonal structures without reaching failure, a manufacturing investigation study to introduce defects into the microstructure (particularly porosity) will be led with the aim of dissipating more energy for reduced applied forces. In comparison with the structures made without apparent defects, this investigation should also save manufacturing time.

6   ACKNOWLEDGMENTS

7   REFERENCES

[1] Gibson, L. & Ashby, M., 1997. Cellular solids Structures and properties. 2e éd. s.l.:Cambridge University Press.

[2] Benedetti, M. et al. (2021) 'Architected cellular materials: A review on their mechanical properties towards fatigue-tolerant design and fabrication', Materials Science and Engineering R: Reports. Elsevier Ltd. doi:10.1016/j.mser.2021.100606.

[3] Ashby, M. (2013) 'Designing architectured materials', Scripta Materialia, 68(1), pp. 4–7. doi:10.1016/j.scriptamat.2012.04.033.

[4] ASTM 2021, American Society for Testing and Materials, "Additive manufacturing - General principles - Fundamentals and vocabulary (ISO/ASTM 52900:2021)," 2021.

[5] Addispace (2017) Diagnosis and study of opportunities of metallic additive manufacturing on sudoe aerospatial sector. Available at: www.addispace.eu.

[6] Costa, L. & Vilar, R., 2009. Laser powder deposition. Rapid Prototyp., 15(4), pp. 264-279.

[7] Liverani, E. et al. (2017) 'Effect of selective laser melting (SLM) process parameters on microstructure and mechanical properties of 316L austenitic stainless steel', Journal of Materials Processing Technology, 249, pp. 255–263. doi:10.1016/j.jmatprotec.2017.05.042.

[8] Barkia, B. et al. (2020) 'On the origin of the high tensile strength and ductility of additively manufactured 316L stainless steel: Multiscale investigation', Journal of Materials Science and Technology, 41, pp. 209–218. doi:10.1016/j.jmst.2019.09.017.

[9] Godec, M. et al. (2020) 'Quantitative multiscale correlative microstructure analysis of additive manufacturing of stainless steel 316L processed by selective laser melting', Materials Characterization, 160(December 2019). doi:10.1016/j.matchar.2019.110074.

[10] Ma, M. et al. (2013) 'Control of shape and performance for direct laser fabrication of precision large-scale metal parts with 316L Stainless Steel', Optics and Laser Technology, 45(1), pp. 209–216. doi:10.1016/j.optlastec.2012.07.002.

[11] Saboori, A. et al. (2020) 'Microstructure and mechanical properties of AISI 316L produced by directed energy deposition-based additive manufacturing: A review', Applied Sciences (Switzerland). MDPI AG. doi:10.3390/app10093310.

21

Impact-dynamic behaviour of Ti6Al4V metal lattice structures

Patricia Verleysen PhD[1*] | Luca Corallo MD[1*] | Antonio Cutolo PhD[2*] | Brecht Van Hooreweder PhD [2*]

[1]Materials Science and Technology, Ghent University, Gent, 9052, Belgium

[2]Research group Additive Manufacturing, Mechanical Engineering Department, KU Leuven, Leuven, 3001 Belgium

Correspondence
Patricia Verleysen PhD, Materials Science and Technology-DyMaLab, Ghent University, Gent, 9052, Belgium
Email: Patricia.Verleysen@UGent.be

In present contribution, results of a study into the impact-dynamic behaviour of Ti6Al4V metal lattice structures are presented. Samples with a rhombic dodecahedron lattice structure and three different relative densities are considered. The high strain rate tests are performed using split Hopkinson pressure bar and direct Hopkinson pressure bar setups. The digital image correlation technique is used to monitor the macroscopic strain fields in the samples. Additionally, for the static tests, strain data on the unit cell level could be obtained. The tests show a significant improvement of the strength with increasing strain rate. However, the increase in strength occurs at the expense of deformation capacity.

1   INTRODUCTION

ASTM International describes additive manufacturing (AM) as the revolutionary process of creating three-dimensional objects by the successive addition of material – whether plastic, metal, ceramic, composite, or something else [1]. This contrasts with traditional manufacturing, which cuts, drills, and grinds away unwanted excess material from a solid piece of material.

The main advantage of AM is that the production process is able to produce components with a very complex shape. Often even shapes that are impossible to make with traditional techniques. Additionally, using AM techniques allows to put material only where it is needed from a structural or usage

*Equally contributing authors

point of view. This not only makes it possible to significantly reduce the use of materials, but also to create components that are extremely light.

Laser powder bed fusion (LPBF) is an additive manufacturing technique for metals which has seen an increasing use in different fields, especially due to its ability to produce complex geometries. Extensive research into LPBF has led to a more thorough understanding of the process, including the process parameters. The related improvement of the quality of LPBF components has led to a more general acceptance of the technique for applications such as medical implants, aerospace and aviation parts, and automotive components [2]. Crucial for aerospace and automotive applications is the development of strong, but lightweight, functional components to achieve lower fuel consumption and a reduced environmental impact [3]. In addition, safety of crew and passengers is of utmost importance, making the implementation of lightweight energy-absorbing structures a key aspect in aircraft and vehicle design [4]. Linking these requirements to the new opportunities offered by LPBF, complex lightweight lattice structures stand out to play a key role in the future of automotive, aviation and aerospace applications.

Advances in LPBF have allowed the production of lattice structures (LS), also known as scaffolds, with complex unit cells having dimensions down to the micrometer scale [5]. Related with the small dimensions, the concept of meta-materials is introduced, in which the lattice is considered as a structure when its small-scale properties are considered, but behaves like a material with homogenized properties at the large macroscale. The mechanical behaviour of these types of structures can be tuned by varying the cell topology and geometry, and the material. Due to the many degrees of freedom of both the lattice structure and the material, it is possible to make LS with unique combinations of properties. Since these materials are inherently lightweight, they are especially attractive to the automotive and aeronautical sectors [6]. For applications where energy needs to be absorbed, strength and deformation capacity are important. In addition, since it is usually a matter of absorbing energy during impact, both must be ensured at high deformation rates.

In order to extend the knowledge and understanding of the impact behaviour of AM LS materials, present contribution presents results of an experimental study on the mechanical behaviour of these materials. Ti6Al4V scaffold materials with a rhombic dodecahedron lattice structure and three different nominal relative densities were manufactured by LPBF. To cover a range of strain rates from 0.01/s to well-above 1000/s, purpose-designed material samples were tested in compression using three different test facilities. Static and high speed imaging combined with digital image correlation (DIC) was used to obtain detailed information on the deformation at the lattice and macroscale.

2   MATERIALS AND EXPERIMENTAL TECHNIQUES

2.1   Materials

The material studied is a Ti6Al4V with a rhombic dodecahedron lattice structure, see Figure 1, produced by LPBF. The unit cell has a size of 2mm. For production three nominal relative densities, i.e., 20%, 30% and 40%, were aimed at. However, measurements showed that slightly higher relative densities of 25%, 36% and 46%, respectively, were obtained.
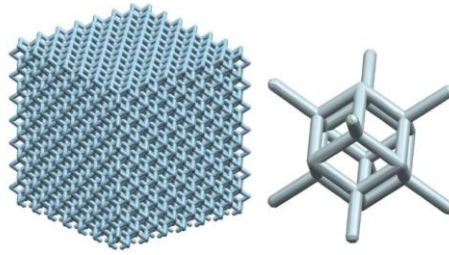
FIGURE 1   Rhombic dodecahedron lattice structure (left), rhombic dodecahedron unit cell (right).

2.2   Experimental setups and measurement techniques

Three experimental setups were used for the compression tests: a conventional setup for the quasi-static tests, a split Hopkinson bar facility for the medium strain rate tests and a direct impact setup for the highest strain rates. For all tests, the same sample geometry and dimensions were used, i.e., blocks with a square base of 10mm by 10mm and a height of 15mm. In all setups, identical boundary conditions were imposed. The same hardened steel plates were used to protect the setup components in contact with the sample. Between the sample and the hardened plates, 0.3mm thick Teflon sheet was applied to reduce friction.

The static tests were performed using an Instron conventional test bench. In total, 7 samples were tested at a strain rate of 0.015/s. Camera imaging during preliminary tests showed that the samples had a strong tendency to also displace perpendicular to the compression direction. Therefore, an alignment tool was designed to ensure that a pure axial deformation was imposed to the samples. Deformation of the sample was recorded using two 5Mpxl F–504B Allied Vision Stingray cameras. Each camera was positioned on a different side of the sample: a side on which a very fine speckle pattern was applied and a side that was painted white. Images of the deforming speckled side were used to obtain strain fields at the cell level. Images of the white side for global strain measurements. Indeed, preliminary experiments showed that the irregular texture of the sample surface allowed macroscopic DIC processing without the need for speckles. Several high-intensity light sources were used to illuminate the irregular sample surfaces. Additionally, also speckles were applied on the hardened plates in contact with the sample to calculate their relative displacement using DIC. This allowed to obtain an accurate value for the average compression strain in the sample.

For the dynamic tests, a conventional split Hopkinson pressure bar (SHPB) test facility was used for the material samples with the lowest density. For the higher density samples, the strain rate imposed to the samples in the SHPB tests was too low to reach a sufficiently high sample deformation. Therefore, also a direct impact Hopkinson pressure bar (DHPB) setup was used for the characterization of the dynamic properties. A schematic presentation of the DHPB setup is given in Figure 2. The sample is positioned in a holder, as shown in picture 3, at the end of a 6m long aluminium bar with diameter of 25mm. The sample holder can move freely over the bar. A long, cylindrical impactor is accelerated towards the sample and imposes the fast deformation aimed at.
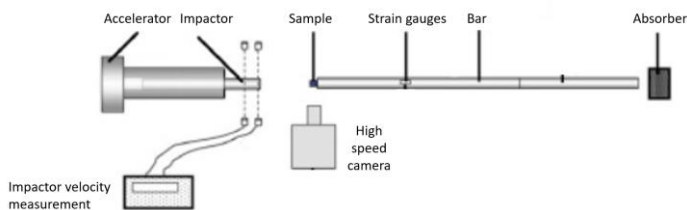
FIGURE 2   Schematic presentation of the direct impact compression setup in which the sample is positioned at the end of a bar which serves as a dynamic load cell.

As is the case in conventional split Hopkinson bar setups, measurement of the wave transmitted by the sample to the bar allows to calculate the force imposed to the sample. In all dynamic tests, Photron AX200 high speed cameras are used to obtain the sample deformation. After the tests, the recorded images were processed using the commercial MatchID software.
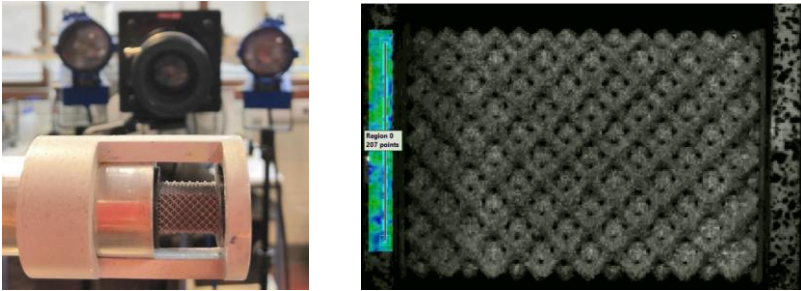
FIGURE 3   Sample positioned at the end of a bar in the direct impact setup prior to testing (left). An impactor, coming from the right, deforms the sample at a high deformation rate. Picture of the undeformed sample and speckled plates taken by a high speed camera (right).

3   RESULTS

3.1   Global and local deformation fields
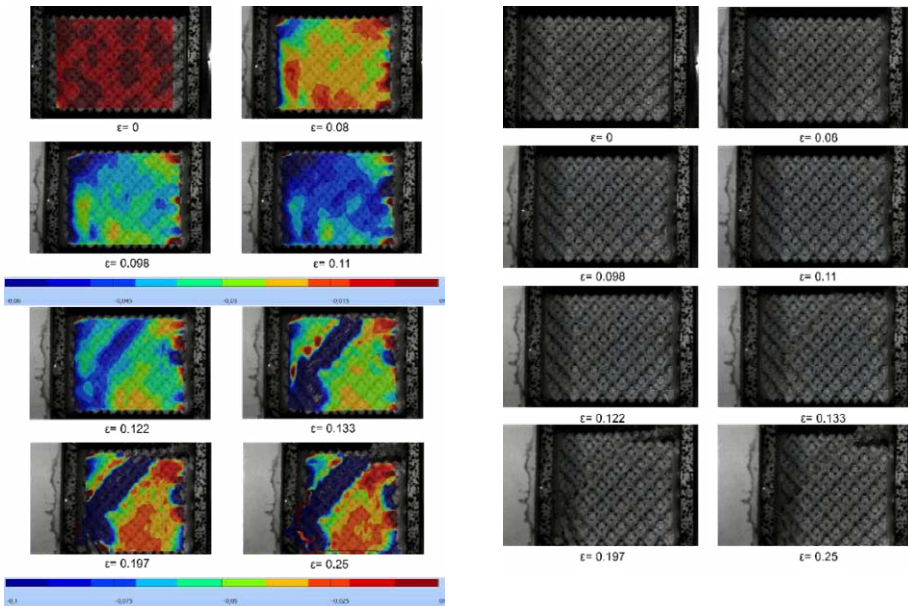
FIGURE 4   Macroscopic axial strain obtained by DIC during a direct impact experiment on a sample with relative density of 40% (right). The sample axis is oriented horizontally. During the test, an average strain rate of 605/s was reached. Original pictures taken by high speed camera (right). The indicated strain ε is the average macroscopic compression strain at the time the images were taken.

Figure 4 presents the axial strain field at different stages during a DHPB test on a 40% density sample. DIC processing parameters were selected in such a way that the macroscopic, homogenized strain is obtained. From the onset of loading, clear heterogeneities in the strain distribution are observed. From an average compression strain of 0.11, the formation of a localized shear band preceding fracture is visible. However, only at a strain level of 0.25, the final fracture occurs.

Figure 5 represents principal strain fields at the metal lattice cell level. These were obtained by DIC processing of a fine speckle pattern applied to the sample. Since a considerable, unevenly distributed out-of-plane displacement occurred at this scale, the strain values give only a qualitative indication of the real strain.
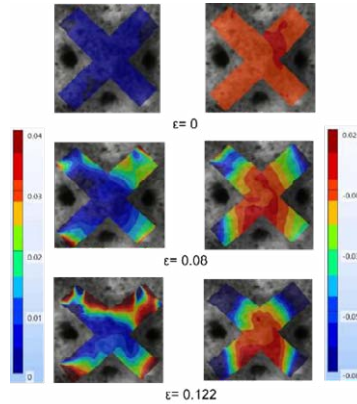
FIGURE 5   Major principal strain (left) and minor principal strain (right) at the cell level obtained by DIC. The indicated strain ε is the average macroscopic strain at the time the images were taken.

3.2   Stress-strain curves

The left graph of figure 6 presents stress-strain curves obtained for the materials with the three different densities for tests at a strain rate of 0.015/s. The right graph gives the maximum stress as a function of strain rate. The higher density samples are more sensitive to strain rate than the 20% density samples. Additionally, the strength evolves more than proportionally with the density. At a strain rate of 1/s, the peak stress reached in the 40% samples is 3.5 time higher than the one in the 20% samples.
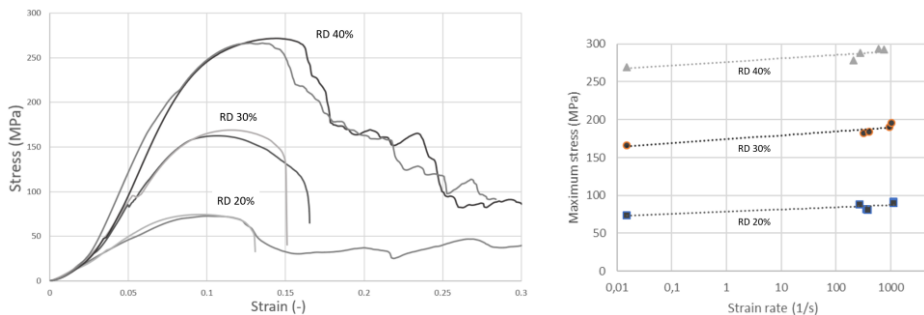
FIGURE 6   Representative static stress-strain curves obtained for the three material densities considered (left). Evolution of the maximum stress as a function of strain rate (right).

4   CONCLUSIONS

In present study results are presented of static and dynamic tests on Ti6Al4V metal lattice structures with three different densities. To cover a wide range of strain rates, going from quasi-static to dynamic rates, three different test techniques were used. All techniques heavily rely on the use of static and high speed camera imaging during testing. Analysis of the recorded images allowed optimisation of the set-ups, such as the introduction of alignment tools. The presented results also show that the additional effort associated with the use of digital image correlation (DIC) is justified. Indeed, the technique allows an accurate determination of the overall deformation imposed on the specimen, which is essential especially for the direct impact tests. Additionally, the macroscopic DIC strain fields reveal onset of the critical strain localisation prior to sample failure. DIC processing of high resolution images of deforming fine speckle patterns applied to the statically tested samples proved to be able to capture the strain distribution at the unit cell level qualitatively.

The tests show a significant improvement of the strength level with increasing strain rate. However, the increase in strength occurs at the expense of deformation capacity. Additionally, at higher strain rates, also the scatter on the failure strain increased, especially for the samples with the highest density.

5   REFERENCES

[1]   https://sn.astm.org/?q=features/5-most-important-standards-additive-manufacturing-.html. Consulted May 25, 2022.

[2]   DebRoy T, Wei H, Zuback J, Mukherjee T, Elmer J, Milewski J, Beese A, Wilson-Heid A, De A, Zhang W. Additive manufacturing of metallic components process, structure and properties. Progress in Materials Science 2018;(92)112 – 224.

[3]   Del Olmo E, Grande E, Samartin CR, Bezdenejnykh M, Torres J, Blanco N, Frovel M, Canas J. Lattice Structures For Aerospace Applications. In L. Ouwehand, editor, 12th European Conference on Spacecraft Structures, Materials and Environmental Testing. ESA Special Publication 2012; (691)6.

[4]   Heimbs S. Energy absorption in aircraft structures. In International Workshop on Hydraulic Equipment and Support Systems for Mining, 2012; 17–18. Trans Tech Publ. Ltd. Zurich, Switzerland.

[5]   Maconachie T, Leary M, Lozanovski B, Zhang X, Qian M, Faruque O, Brandt M. Slm lattice structures: Properties, performance, applications and challenges. Materials Design, 2019(183).

[6]   Aslan B and Yildiz A. Optimum design of automobile components using lattice structures for additive manufacturing. Materials Testing, 2020(62).

$$\textbf{22}$$

Dynamic behaviour of additively manufactured mathematical lattice structures: effects of topology, wall thickness and material

Govind Gour[1]*| William Garson[2]| David Townsend[1] PhD|

Fauzan Adziman[2] PhD| Antonio Pellegrino[1]*PhD

[1] Department of Engineering Science, University of Oxford, Oxford, Oxfordshire, OX1 3PJ, UK

[2] Alloyed Ltd, Unit 15, Yarnton, Kidlington OX5 1QU

Correspondence

Antonio Pellegrino PhD,
Department of Engineering Science, University of Oxford, Oxford, Oxfordshire, OX1 3PJ, UK
Email: antonio.pellegrino@eng.ox.ac.uk

Additive manufacturing (AM) is a powerful tool for designing novel parts in various industries, enabling new geometries that cannot be manufactured using traditional manufacturing techniques, to be produced. In particular periodic lattice structures enable the manufacturing of parts with improved functionality and lower weight.

In this study, selective laser melting (SLM) was used to manufacture novel lattice geometries using Ti6Al4V and AlSi10Mg alloys. Three triply periodic minimal surfaces (TPMS) geometries were investigated: Gyroid, Diamond and Primitive. The dynamic compression performance of these topologies with a range of wall thicknesses were compared for both Ti6Al4V and AlSi10Mg structures. The deformation mode of the samples is discussed and the suitability of each geometry for dynamic load bearing structures is assessed.

1   INTRODUCTION

The potential industrial uses of AM parts are wide-ranging, and various research efforts have been undertaken to ascertain the suitability of the new designs for industrial use. Reduction of system

*Equally contributing authors

weight is critical for aerospace and automotive industries [1], and AM aerospace parts have been designed to simultaneously reduce system weight while improving functionality.

Triply Periodic Minimal Surfaces (TPMS) geometries are of particular interest compared to other more traditional lattice structures because the geometries contain continous channels [2]. The continuous channels of TPMS geometries enable the possibility of using the geometries for heat sink and heat exchanger purposes, which has lead to the study of fluid flow through TPMS structures [3]. Zhang et al. [2] also showed the potential for the 3 TPMS structures mentioned above to be used in energy absorbing applications through quasi-static compression testing of the geometries. The structures have also been identified as self-supporting [4], meaning that they may be favoured for additive manufacturing due to their low requirement for additional supports in the building process. This combination of factors has led to a large number of studies being performed on the manufacturing, microstructure and quasi-static behaviour of TPMS geometries.

The aim of this work is to characterise the response of 3 triply periodic minimal surface (TPMS) geometries to high strain rate and quasi-static compressive loading. The geometries were produced by additive manufacturing, using selective laser melting (SLM) of the Ti6Al4V and AlSi10Mg alloys.

The dynamic compression performance of Gyroid, Diamond and Primitive TPMS structures with a range of wall thicknesses were compared for both Ti6Al4V and AlSi10Mg structures. The deformation mode of each geometry was discussed with reference to images recorded during experiments. Finally, the suitability of each TPMS structure for dynamic load bearing structures is discussed and recommendations for future work are made.

2   SPECIMENS DESIGN AND MANUFACTURING

The Triply Periodic Minimal Surfaces explored in this study are the Gyroid [5], the Schwarz Diamond and the Primitive [6] (Figure1). These geometries are impossible to produce by traditional manufacturing due to the curvature of the cell walls in all three dimensions.

The specimen size was determined using preliminary simulations. Gyroid and Primitive specimens were manufactured with a unit cell size of 3.5mm and 4 unit cells would be used to create a square cross-section. The Diamond specimens consisted of one unit cell with a height of 3.5mm, and a width and depth of 7mm. The nominal length of all specimens in the direction of compression was 3.5mm and the nominal cross-sectional area was 49mm^2. The Gyroid geometries were manufactured with 0.3mm, 0.4mm and 0.5mm wall thicknesses. The Diamond and Primitive geometries were manufactured with 0.4mm, 0.5mm and 0.6mm wall thicknesses. The combination of unit cell size and wall thickness was chosen for each geometry to ensure that the range of structures tested had comparable relative densities.
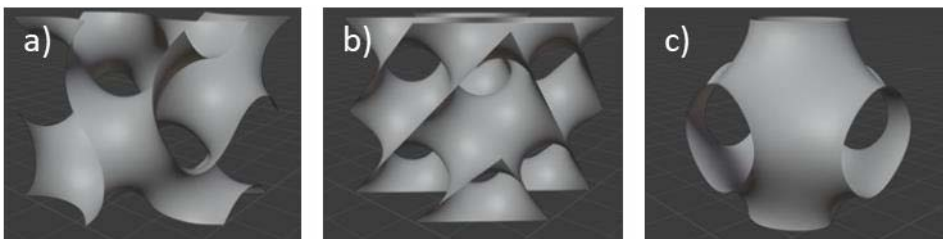
FIGURE 1   Gyroid, Diamond and Primitive geometries
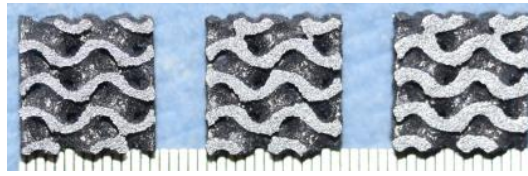
FIGURE 2   AlSi10Mg Gyroid Specimens with 0.3mm, 0.4mm and 0.5mm wall thickness

3   EXPERIMENTAL METHODS

Low strain rate compression experiments on Etnean sand were conducted using a screw-driven universal testing machine. The dynamic response of the TPMS specimens detailed above was measured by means of a series of laboratory experiments on the Split Hopkinson Pressure Bar apparatus detailed in [7,8]. The setup comprised of striker, input and output bars of length equal to 2.7 m. All bars were made of Ti-6AL-4V and had diameter equal to 16 mm.

4   RESULTS

This section present an extract of the results obtained during this study. The presented results provide an overview of the dynamic behavior of primitive TPMS structures. Comparable outcomes were obtained on the Gyroid and Diamond geometries.

Figure 3 shows the engineering stress - engineering strain curves obtained by dynamic compression of Primitive structures manufactured from Ti6Al4V. It can be seen that the peak and minimum stress values increase with increasing wall thickness, and that the densification onset strain decreases as wall thickness increases. These trends are consistent with those shown in similar experiments for the Gyroid and Diamond geometries and with those observed in the literature. The TPMS geometries tested here as these structures are 'sheet-based' rather than 'strut-based'. This means that compressive loads are supported through a combination of bending and compression in the cell walls Notably the Ti6Al4V Primitive structures demonstrate a high degree of stretch dominated behaviour, with minimum stresses measured considerably lower than the initial peak stresses.

It is noted that the reduction of forces and displacements to engineering stresses and strains represents only a way to normalize the obtained results as the results refer to the behavior of the lattice structures and not to the behavior of the inherent materials.

The analysis of the response of AlSi10Mg Primitive structures under dynamic compression shows that the shape of the curves is similar regardless of base material, suggesting that the deformation behaviour of the geometry is not significantly affected by base material chosen when compressed at high strain rates.

The comparison of the engineering characteristics for Ti6Al4V Primitive structures under compression at quasi-static and high strain rates shows that the Primitive structures exhibit a moderate strain rate dependence, with the measured peak and minimum stresses higher for the dynamic tests. In particular, it is clear that the Ti6Al4V Primitive structures reduced their load bearing capability considerably after the peak stress in quasi-static compression compared to the dynamic compression results.
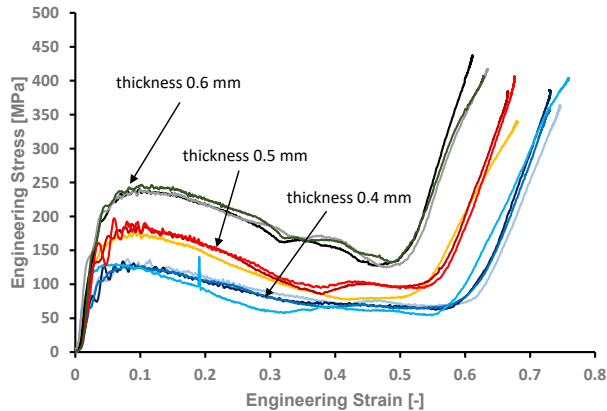
FIGURE 3   Dynamic compressive behavior of Ti6Al4V primitive structures of different thicknesses.
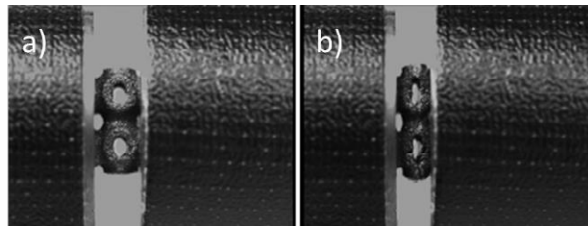
FIGURE 4   High speed camera images illustrating the deformation of primitive structures at the point of a) peak force and b) just before the onset of densification.

5   REFERENCES

[1]   Zhang, L., Gour, G., Petrinic, N., & Pellegrino, A. (2020). Rate dependent behaviour and dynamic strain localisation of three novel impact resilient titanium alloys: Experiments and modelling. Materials Science and Engineering: A, 771, 138552.

[2]   Zhang, L., Feih, S., Daynes, S., Chang, S., Wang, M. Y., Wei, J., & Lu, W. F. (2018). Energy absorption characteristics of metallic triply periodic minimal surface sheet structures under compressive loading. Additive Manufacturing, 23, 505-515.

[3]   Luo, J. W., Chen, L., Min, T., Shan, F., Kang, Q., & Tao, W. (2020). Macroscopic transport properties of Gyroid structures based on pore-scale studies: permeability, diffusivity and thermal conductivity. International Journal of Heat and Mass Transfer, 146, 118837.

[4]   Yang, L., Yan, C., Han, C., Chen, P., Yang, S., & Shi, Y. (2018). Mechanical response of a triply periodic minimal surface cellular structures manufactured by selective laser melting. International Journal of Mechanical Sciences, 148, 149-157.

[5]   Schoen, A. H. (1970). Infinite periodic minimal surfaces without self-intersections (No. C-98).

[6]   Schwarz, H. A. (1972). Gesammelte mathematische abhandlungen (Vol. 260). American Mathematical Soc..

[7]   Varley, L., Rutherford, M. E., Zhang, L., & Pellegrino, A. (2020). The mechanical response of wet volcanic sand to impact loading, effects of water content and initial compaction. Journal of Dynamic Behavior of Materials, 6(3), 358-372.

[8]   Pellegrino, A., De Cola, F., Dragnevski, K., & Petrinic, N. (2016). The dynamic response of etnean sand and the effect of its impingement on Ti-6Al-4 V alloy. Journal of Dynamic Behavior of Materials, 2(4), 438-451.

$\widehat{23}$

Split Hopkinson pressure bar experiments on additive manufactured lattice structures with different volume fractions

Sören Bieler[1][*] | Kerstin Weinberg[1]

[1]Institut für Festkörpermechanik,
University of Siegen, Paul-Bonatz-Straße
9-11, 57076 Siegen, Germany

Correspondence
Institut für Festkörpermechanik, University
of Siegen, Paul-Bonatz-Straße 9-11, 57076
Siegen, Germany
Email: soeren.bieler@uni-siegen.de

Funding information

The additive manufacturing technology allows printing of specifically designed delicate structures in outstanding resolution. For protective applications, truss-like objects are of particular interest. Here closely spaced diagonal elements form a lattice which results in a low density of the material but a high ability to absorb energy through elastic or plastic deformation. Therefore, the structural behavior of such lattices under impact loading is essential. A Split-Hopkinson pressure bar experiment realizes the impact loading conditions. We investigate the energy-absorbing material properties of the structures by varying the truss diameters in the lattices and evaluate the dissipated energy experimentally and numerically.

Abbreviations: SHPB, TB, IB

[*]Equally contributing authors.

1 | INTRODUCTION

Energy absorbing materials and structures, such as foams and or honeycomb structures, are of significant importance for many applications, cf. [1]. Lattice structures have proven to be especially useful for energy absorption, [2]. Lattice structures can be classified into two types, irregular and regular ones. Open-cell foam structures are an example of irregular formations, [4, 5], which habe a stochastic lattic-like structure. On the opposite typical regular lattice structures are characterized by periodically repeating elementary cells with a topology displyed in Fig. 1. Among the lattice structures, many different types can be found (FCC, FCCZ, BCC, BCCZ, Cuboctahdron), cf. [3]. Special features of these structures are high strength at low density, good energy absorption, and good stiffness-to-weight ratio [6, 7]. Because of the low density of the lattice structures, the amount of material required to produce them is relatively small [8]. The octet structure is very suitable for energy absorption. With the increasingly advanced development of 3D printers, it is becoming easier to produce such systems and study their properties. Lattice structures have the advantage that results are subject to minor variation due to the regular structure than is the case with foams. Therefore we investigate the energy absorption capacity for different volume fraction V_f of additive manufactured specimens.
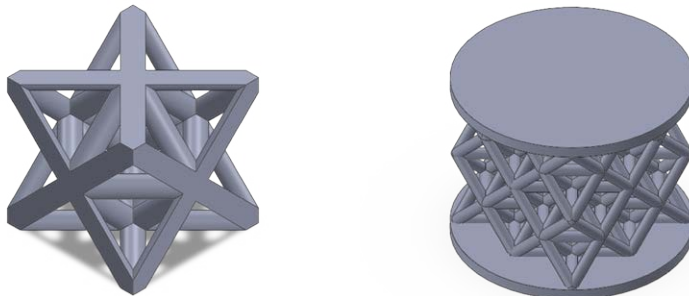
FIGURE 1   Octet unit cell (left) and the stacked cells constituting the specimen (right)

2 | SPECIMEN AND EXPERIMENTAL SETUP

The octet structure for the experiments was first created in SolidWorks CAD software. The unit cells shown in Fig. 1 were created for different strut diameters within the cell. However, the edge length of 6.5 mm per unit cell remains constant. After completing the unit cell of the octet structure, it has been duplicated and finally represents the specimen for our experiments.

2.1 | Preparation of the specimens

For better fixation to the Split Hopkinson pressure bar (SHPB) experiments, the lattice structures are provided with a cap on the top and bottom sides. The cap has a thickness of 0.5 mm and is fixed to the structure by the printing process. It is essential to consider how the dimensions of the unit cell are chosen. Since an SLA 3D printing process produces our specimens, excellent structures can be created. However, care must be taken here that the unit cell is not too dense. Otherwise, a fusion of the trusses will occur, which no longer depicts the actual structure. We chose an edge length of 6.5 mm for the unit cell and then attached it to the octet structure. DURABLE resin from the company *Formlabs* was chosen as specimen material. In contrast to rigid and brittle resins that the company also provides, DURABLE resin has much more ductile and tough properties. Thus, deformation of the specimen takes place, but not fracture. The resin is a mixture of acylated and methacrylate monomers and oligomers as well as photoinitiators, cf. [9, 10]. The SLA technology used UV lasers spots as a light source to cure the polymer resin. The specimens are printed at a resolution of 50 microns. A specimen in our research has four unit cells per layer by two layers, see Fig. 1. The different strut diameters lead to different volume fractions V_f of material. The volume fraction V_f and the surface area for an octet unit cell at various strut diameters are plotted in Fig. 2. As can be seen, the surface area decreases again from a strut diameter of more than 1.75 mm. This decreasing means that the struts "merge" with each other from this value on, and the classical octet structure is no longer present. We investigate three different specimen types with a truss diameter of 1.2 mm, 1.4 mm, and 1.6 mm for our experiments.
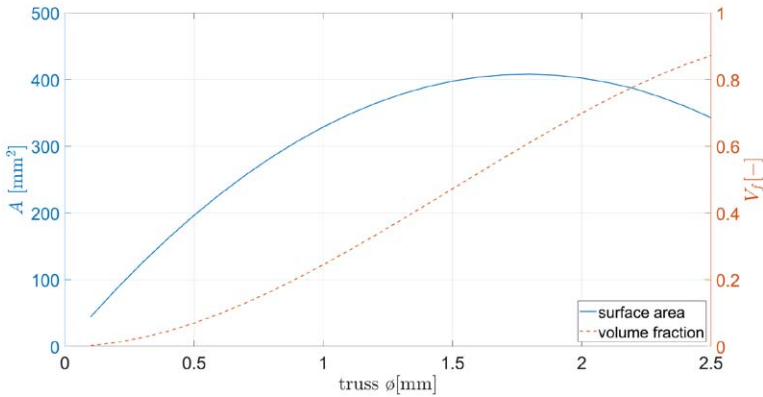
FIGURE 2   Geometric properties of the octet structure for different strut diameters by a unit cell edge length of 6.5 mm

2.2 | Split Hopkinson pressure bar

The setup of the SHPB consists of a striker accelerated gas gun and two long bars, namely the incident bar (IB) and the transmission bar (TB). The dimensions of the individual components can be taken from Table 1. A data acquisition system processes the data of the strain gauges applied to the center of the

bars. The corresponding specimen is clamped between the two bars. The striker is accelerated and hits the surface of the IB. This impact induces a compression wave into the system, traveling through the IB. At the IB and specimen interface, the one-dimensional wave splits into two parts. One part is reflected and travels through IB in the opposite direction. The transmitted part enters the specimen and then the TB. The wave signal can be measured at the strain gages and then evaluated. Due to the relatively low density of the specimen in contrast to solid cylinder specimens, the impedance mismatch is significant, resulting in a very weak signal of the strain gauge applied to the TB. Since the SHPB has a bar diameter of 20 mm, the structures created had to be adapted to make them suitable as specimens. The printability of such filigree structures is also limited. For our experiments, we vary the strut diameters of the structures between 1.2 mm and 1.6 mm.

TABLE 1   SHPB setup

	incident bar	transmission bar	striker	specimen
diameter [mm]	20	20	20	20
length [mm]	1800	1800	300	14
material	aluminum	aluminum	aluminum	DURABLE resin

3 | EXPERIMENTS

The dynamic behavior of lattice structures is of great importance for research, so publications have already been made on this subject. The authors of [11] investigated lattice sandwich structures that were abruptly loaded by a falling weight. The focus here is on shock absorption. We use the SHPB system to estimate the extent to which the deformation of the specimen absorbs the measured elastic pulses. For each specimen type, seven measurements were performed. Accordingly, 21 measurements were performed for the three specimen types. The elastic energy contained in the pulse can be determined as

$$W = \int_V w^e \, \mathrm{d}V = A \, c \, t_0 \int_0^\varepsilon \sigma(\tilde{\varepsilon}) \, \mathrm{d}\tilde{\varepsilon} \tag{1}$$

where V, A, c, t_0 are the volume, cross-sectional area, elastic wave velocity, and the loading duration of the bar material, respectively. The time duration of the pulse depends on the striker length and its propagation speed, [12]. If we assume elastic bar material ($\sigma = E\,\varepsilon$), the energy of a measured pulse can be calculated by integration. So Eq. (1) can be rewritten as

$$W = E \, A \, c \int_{t_0}^t \varepsilon \, \mathrm{d}\tilde{t} \tag{2}$$

So the energy of each pulse can thus be expressed as follows:

$$W_I = E\,A\,c \int_{t_{0_I}}^{t_I} \varepsilon_I\,\mathrm{d}\tilde{t} \qquad W_R = E\,A\,c \int_{t_{0_R}}^{t_R} \varepsilon_R\,\mathrm{d}\tilde{t} \qquad W_T = E\,A\,c \int_{t_{0_T}}^{t_T} \varepsilon_T\,\mathrm{d}\tilde{t} \quad (3)$$

A part of the compression wave results in a deformation of the specimen. This means that part
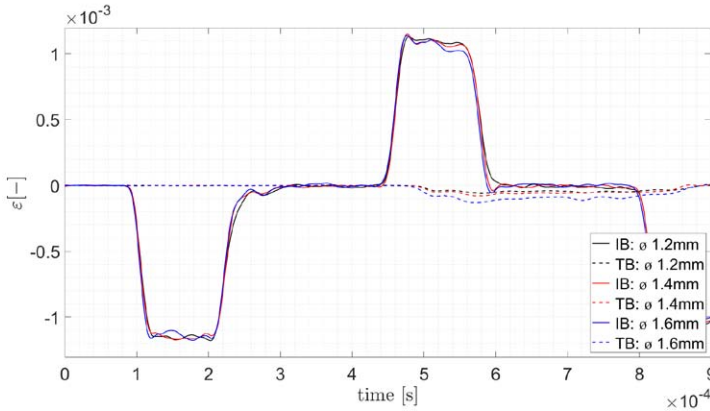
FIGURE 3 Measured pulses of an Octet specimen with a truss diameter of 1.2 mm

of the energy contained in the pulse is dissipated here by the deformation. Accordingly, there is an energy difference between the introduced pulse and the reflected and transmitted pulse sum. Using a solid cylinder as a specimen, the impedance mismatch between the bar and specimen is tiny. However, this deforms only to a limited extent due to its geometry. The cross-section area of the lattice structures is much smaller and not constant over the length of the specimen. This smaller cross-section area also depends on the strut thickness of the specimen structure. However, these structures are more likely to allow deformation. At a higher impedance mismatch, the reflected pulse turns out to be larger than the transmitted one. As shown in Fig. 3, the transmitted pulse has a much smaller amplitude than the reflected pulse, but it is longer than the reflected pulse. The SHPB test is mainly used to determine material properties such as Young's modulus under high strain rates [13]. This classical evaluation is not performed in our experiments. Our research is focused on an energy-based evaluation of the measured signal. The main aspect is the energy absorption capacity of the specimen structure. Since both pulses are included in the energy balance, it is possible to calculate how much energy was required to deform the specimen.

$$\Delta W = |W_I| - (|W_R| + |W_T|) \tag{4}$$

Table 2 shows the energy absorption of the different specimen. It can be seen that the energy absorbtion capacity of the specimen is not only dependent on the diameter of the struts, as it initially increases from a strut diameter of 1.2 mm to 1.4 mm, but then decreases again for a strut diameter of 1.6 mm.

TABLE 2   Results of energy absorption by specimen deformation

specimen	A [mm^2]	V [mm^3]	V_f [-]	$\frac{\Delta W}{W_I}$ [-]
octet (truss diameter: 1.2 mm)	364,05	91,39	0.33	0.26
octet (truss diameter: 1.4 mm)	388,93	116,82	0.43	0.30
octet (truss diameter: 1.6 mm)	403,57	142,69	0.52	0.34

4 | FINITE ELEMENT ANALYSIS

Additionally, the ABAQUS software was used to perform a finite element analysis (FEA). For this reason, we modeled the setup of the SHPB with ABAQUS itself. The specimen was imported as part from SOLIDWORKS. The specimen's structure is meshed by using C3D10 (ten-node tetrahedral) elements. This allows us to identify the maximum size of displacement or find the position of stress magnitudes. In Fig. 4 the local plastic strains are plotted. The largest deformations occur at the nodes of the struts. In the simulation, a rotation of the specimen was detected during compression. The authors already observed this phenomenon [14] for relatively thin structures. The buckling of some struts causes this rotation. This rotation behavior no longer occurs at a very high volume density, i.e., very thick strut diameters. In our experiments, this rotation occurs for all strut diameters (1.2 mm to 1.6mm).
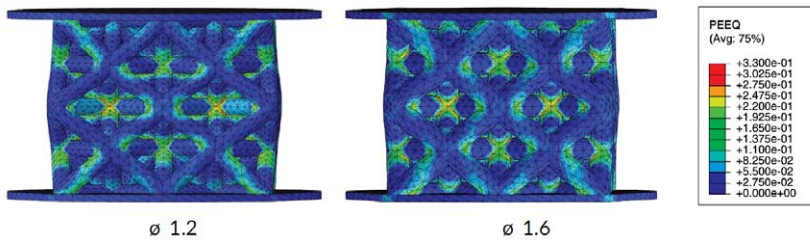
FIGURE 4   FEA of different specimen types showing the local equivalent plastic strain as contour

5 | CONCLUSION

From the measured incident, reflected, and transmitted signals, we can calculate the energy of each pulse by using Eq. (3) and (4). From the results, it can be seen that the energy absorption is highest for a strut thickness of 1.4 mm. At a very low specimen density, a higher reflected pulse is obtained. At a very high density, a better transmission into the TB of the pulse is received. It can be concluded that the absorption properties of the structure depend on the density of the unit cell respectively on the diameter of the struts. If the bar structures are thin, the specimen can be deformed well, but the impedance mismatch between the specimen and the bar also increases, resulting in a high reflected pulse. With thick beam structures, a better transmission into the TB occurs due to the specimen's

higher cross-sectional area. However, the beams are less easily deformed. Accordingly, the best absorption variant compromises structures that can be deformed relatively quickly but are not too thin. In addition, the FEA shows that elastic or plastic buckling of some beam structures causes the specimen to rotate, an effect which we wish investigating further in SHPB experiment.

References

[1] Pan C, Han Y, Lu J. Design and optimization of lattice structures: A review. Applied Sciences 2020;10(18):6374.

[2] Li X, Ghasri-Khouzani M, Bogno AA, Liu J, Henein H, Chen Z, et al. Investigation of compressive and tensile behavior of stainless steel/dissolvable aluminum bimetallic composites by finite element modeling and digital image correlation. Materials 2021;14(13):3654.

[3] Maconachie T, Leary M, Lozanovski B, Zhang X, Qian M, Faruque O, et al. SLM lattice structures: Properties, performance, applications and challenges. Materials & Design 2019;183:108137.

[4] Vesenjak M, Öchsner A, Hribersek M, Ren Z. Behaviour of cellular structures with fluid fillers under impact loading. The International Journal of Multiphysics 2007;1(1):101–122.

[5] Bogusz P, Popławski A, Stankiewicz M, Kowalski B. Experimental Research of Selected Lattice Structures Developed with 3D Printing Technology. Materials 2022;15(1):378.

[6] Dziewit P, Janiszewski J. Qualitative evaluation of the deformation process of regular cellular structures manufactured using 3D printing. Mechanik 2018;91(3):250–252.

[7] Al-Ketan O, Rowshan R, Al-Rub RKA. Topology-mechanical property relationship of 3D printed strut, skeletal, and sheet based periodic metallic cellular materials. Additive Manufacturing 2018;19:167–183.

[8] Moon SK, Tan YE, Hwang J, Yoon YJ. Application of 3D printing technology for designing lightweight unmanned aerial vehicle wing structures. International Journal of Precision Engineering and Manufacturing-Green Technology 2014;1(3):223–228.

[9] Ling C, Cernicchi A, Gilchrist MD, Cardiff P. Mechanical behaviour of additively-manufactured polymeric octet-truss lattice structures under quasi-static and dynamic compressive loading. Materials & Design 2019;162:106–118.

[10] 3D PrintingMaterials for Engineering,Manufacturing, and Product Design. https://formlabscom/materials/engineering/ 2022;.

[11] Jhou SY, Hsu CC, Yeh JC. The Dynamic Impact Response of 3D-Printed Polymeric Sandwich Structures with Lattice Cores: Numerical and Experimental Investigation. Polymers 2021;13(22):4032.

[12] Song B, Chen W. Energy for specimen deformation in a split Hopkinson pressure bar experiment. Experimental mechanics 2006;46(3):407–410.

[13] Aghayan S, Bieler S, Weinberg K. Determination of the high-strain rate elastic modulus of printing resins using two different split Hopkinson pressure bars. Mechanics of Time-Dependent Materials 2021;p. 1–13.

[14] Tancogne-Dejean T, Spierings AB, Mohr D. Additively-manufactured metallic micro-lattice materials for high specific energy absorption under static and dynamic loading. Acta Materialia 2016;116:14–28.

03

Simulation

(24)

Design of a simplified cranial substitute and Modal Analysis

Natacha Elster[1, 2*] | Johanna Boutillier[2], Nicolas Bourdet[1], Pascal Magnan[2], Pierre Naz[2], Rémy Willinger[1], Caroline Deck[1]

[1]Icube Laboratory UMR7357, Strasbourg University, Strasbourg, 67000, France

[2]Acoustic and soldier's protection group, French-German Research Institute of Saint Louis, Saint-Louis, 68000, France

Correspondence

*Natacha Elster, MD
Email: natacha.elster@etu.unistra.fr

Present address

*ICube Laboratory, Strasbourg University, 2 rue Boussingault, 67000, Strasbourg, France

Funding information

Humans exposed to high-speed loading often have Traumatic Brain Injuries. One proposed injury mechanism assumes that vibration modes of the cranium would be excited by the dynamic loading, leading to cerebral lesions. To investigate this hypothesis, a cranial substitute with a similar modal behaviour as to dry human craniums was designed.

Under the assumptions of homogeneity, isotropy and elasticity of the material, the 3D-printing building process was chosen. A spherical cap was designed using Finite Element Modelling. The substitute was then 3D-printed and subjected to an Experimental Modal Analysis to validate its behaviour in the frequency domain.

1 INTRODUCTION

Humans exposed to high-speed loading such as blast events often have Traumatic Brain Injuries [1]. Several injury mechanisms were proposed in the literature [2], and one is particularly of interest: the skull deflection. That latter assumes that the load applied when blast waves reach the human cranium induces cerebral lesions. Indeed, blast waves can be approximated by impulse signals, which can excite a large range of cranial natural frequencies associated to mode shapes. Experimental Modal Analysis (EMA) can be used to extract these cranial vibration modes in the frequency domain. In order to better understand this mechanism, a cranial substitute with a similar modal behaviour as to a dry human cranium needs to be created. In the literature, EMA was performed on 4 dry human craniums of the 50th percentile in a total of four studies [3–6]. In the range [0–5] kHz, 13 frequencies were found. Hence the goal of the present study is to design said substitute according to those frequencies. The 3D-printing building process was chosen, and therefore a few assumptions such as the homogeneity and isotropy of the material are verified. In a second step, a 3D-printed truncated sphere, embedded at its base, is dimensioned thanks to Finite Element modelling predictions.

---

*Equally contributing authors

2   MATERIALS AND METHODS

A simplified geometry of a truncated sphere was chosen for the new cranial substitute, leading to the choice of the 3D-printing building process. In this section, the comprehensive methodology adopted to design this substitute using modal analysis is presented. The diagram proposed on FIGURE 1 summarizes the several steps detailed in the following.
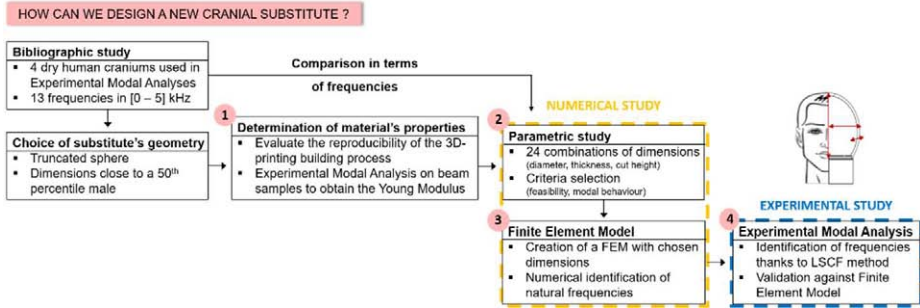
FIGURE 1. Diagram of the methodology adopted to design a cranial substitute using modal analysis.

2.1   Determination of material's properties

The 3D-printing building process is chosen for several reasons such as the cost and the feasibility of the structure. The material considered in this study is the general-purpose resin IORA black (iSQUARED²), used for the PolyJet technology. PolyJet technology jets drops of the liquid polymer resin, before curation with a UV light layer by layer. In this paper, the goal is to print a truncated sphere made from a quasi-homogeneous and isotropic material. Therefore, these assumptions as well as the reproducibility of the method need to be evaluated. A total of 20 beam-shaped samples are made: 10 beams are printed in X-direction and 10 in Y-direction of the 2D printing tray's section. Ratios of length/thickness and length/width are respectively 18 and 13. An EMA is then performed for each cantilever beam to obtain its modal parameters *i.e.,* its frequencies and mode shapes, in 21 measurement points. In a second step, the Young Modulus could be estimated from the natural frequencies of each samples by applying beam's theory.

2.2   Parametric study

The obtained Young Modulus can be used to design a 3D-printed cranial substitute. First step consists in defining the geometry of the substitute: as a first approximation, a truncated sphere with dimensions close to a 50th percentile human cranium was chosen. However, the Young Modulus of the IORA black material is different from the one of cranial bone in dynamic conditions (about 5000 MPa). It is therefore mandatory to adapt the dimensions of the substitute in order to have a close vibratory behaviour as to a dry human cranium. A parametric study is thus performed numerically by varying the external diameter, thickness and cut height of a Finite Element Model (FEM). Each combination is then evaluated in terms of feasibility and modal behaviour to find the best suitable dimensions. An example of three possibilities of cut height is presented on FIGURE 2.

FIGURE 2. Illustration of the parametric study performed on the Finite Element Model.

2.3 Finite Element Model

The numerical identification of frequencies is then completed on the FE Model thanks to LS-Dyna with an implicit solver. The model is made of 21077 hexahedral elements with 3 elements through thickness, and the constitutive law of the material is elastic isotropic.

2.4 Experimental Modal Analysis

Once the geometrical dimensions are chosen, the substitute is 3D-printed and embedded at its base by a clamp device. It is then subjected to an Experimental Modal Analysis to obtain the vibratory response of the structure [7]. FIGURE 3 presents the experimental setup used for the EMA. The first step consists in exciting the structure at several frequencies, and recording its temporal response at different measure points. The impactor of a shaker (LDS V200) is in contact with the substitute, and a chirp signal of amplitude 1V and frequency range [0-10] kHz is transmitted to the shaker for each measure. A scanning laser vibrometer (OptoMET SWIR) is used to record the temporal evolutions of the vibrations' velocity in a given measure point, with 10 repetitions per point to ensure the reproducibility of results. Two configurations of interest are chosen, each with 52 measure points divided in three measure lines. Measure lines were chosen thanks to the FEM to ensure recording a great amplitude of vibrations. FIGURE 4 presents the vertical (A) and horizontal (B) measure lines defined for both configurations.
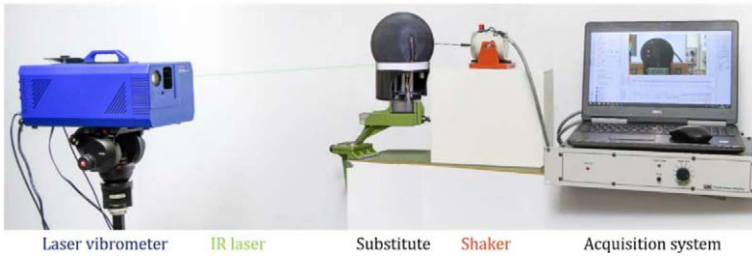
FIGURE 3. Setup used to perform an Experimental Modal Analysis on the cranial substitute.
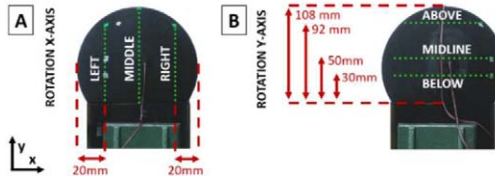
FIGURE 4. Measurement lines defined for the EMA of the substitute: (A) vertical and (B) horizontal.

The second step of an EMA is to extract the natural frequencies of the structure. For that purpose, the temporal evolutions of vibrations are computed in the frequential domain. FIGURE 5 presents a schematisation of frequential evolutions obtained for three different measure points. The amplitude peaks are associated with natural frequencies, for example there are three frequencies for the first and third measure points. To robustly identify each frequency, an identification algorithm has to be used, here a Least-Squares Complex Frequency (LSCF) algorithm in output-only conditions [8] was chosen. The method consists in defining n polynomials to describe the frequential evolutions. For each polynomial k, where $1 < k < n$, its roots are plotted directly on the frequential evolutions. Therefore, if the roots of the n different polynomials are the same, a stabilisation line is drawn, as illustrated in blue on FIGURE 5. As a result, each stabilisation line corresponds to a natural frequency of the structure.
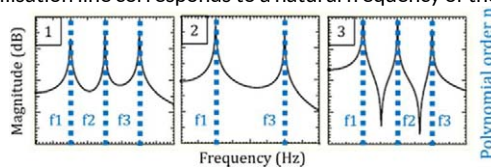
FIGURE 5. Schematisation of stabilisation diagrams obtained for three different points.

3   RESULTS

In this section are presented the properties of the studied materials, as well as the results of the Experimental Modal Analysis performed on the chosen cranial substitute and its corresponding FEM. Results are solely presented in terms of natural frequencies.

3.1   Properties of the material

First, the volumetric mass is measured from the beam-shaped samples, giving a value of 1170.8 ± 6.53 kg/m^3. In addition, results from the EMA performed on the 20 beams are gathered in TABLE 1. On the frequency range [0–10] kHz, 6 frequencies are found. Close results are obtained for X- and Y-directions as attested by the low standard deviations**Erreur ! Source du renvoi introuvable.**, supporting the isotropy hypothesis. A mean Young Modulus of 2663 ± 228 MPa could then be extracted from 20 beams x 21 measure points x 6 frequencies. Relative errors between analytical and experimental results are bounded by 0.1% and 7.5%. The homogeneity hypothesis is thus certified. On another note, a Poisson ratio of 0.38 ± 0.04 was obtained experimentally from the propagation of ultrasonic waves through 6 cylindrical samples.

Mode	Frequency (Hz)	Young modulus (MPa)	Mode	Frequency (Hz)	Young modulus (MPa)
0	103 ± 1	2666 ± 67	3	3734 ± 26	3018 ± 42
1	637 ± 4	2655 ± 32	4	5753 ± 27	2624 ± 25
2	1693 ± 21	2382 ± 61	5	8614 ± 106	2638 ± 65

TABLE 1. Mean natural frequencies of 20 beams obtained for an Experimental Modal Analysis between [0-10] kHz.

3.2   Design of a cranial substitute using Modal Analysis

The second part of the study consists in designing a cranial substitute using Modal Analysis. Thanks to a parametric study, a truncated sphere with an external diameter of 133 mm, a cut height of 108 mm, and a thickness of 5 mm is built. A numerical determination of frequencies and an Experimental Modal Analysis are then performed to establish its complete vibratory response. Obtained results are gathered in TABLE 2.

FEM	Cranial substitute (relative gaps %)	Dry skulls	Number of skulls [references]		Experimental relative gaps (%)
X	X	700	1	[6]	X
946	X	866 ± 42	3	[3,4,6]	X
X	X	1342 ± 59	3	[5,6]	X
X	X	1770 ± 20	1	[5]	X
2008	2102 ± 23 (4.69%)	1893 ± 14	1	[5]	9.94
2272	X	2484 ± 47	1	[5]	X
2976	2953 ± 26 (0.76%)	2802 ± 58	1	[5]	5.83
3475	3512 ± 52 (1.06%)	3423 ± 130	1	[5]	2.52
3636	3610 ± 36 (0.72%)	3634 ± 96	1	[5]	0.66
3844	3954 ± 66 (2.86%)	3845	1	[5]	2.76
4278	4145 ± 97 (3.11%)	4113 ± 62	1	[5]	3.86
4308	4371 ± 21 (1.46%)	4284 ± 63	1	[5]	1.99
4561	4587 ± 78 (0.56%)	4692 ± 87	1	[5]	2.88

TABLE 2. Comparison of frequencies (Hz) found on dry human craniums in the literature to those of the substitute.

Numerically, 58 vibration modes are obtained on the frequency range [0–10] kHz, whereas experimentally 52 frequencies are detected. To ensure that the detected frequencies are not spurious, and to validate the Finite Element Model, a comparison with computational vibrations modes is required. Thus,

experimental frequencies are compared individually to each computational frequency to identify the best fit. Among the 52 vibration modes detected, 34 of them are common to the Finite Element Model. The smallest experimental frequency is 2102 ± 23 Hz; while the largest is 9223 ± 28Hz. The quantification of errors show low relative gaps in the range [0.34 % - 5.71 %].

The last part of the study consists in verifying that these experimental and computational frequencies are close to the 13 frequencies found on dry human craniums in the literature. Among the 13 frequencies found on dry human craniums, 8 of them are common to the cranial substitute. Computed experimental relative errors are between 0.66 % and 9.94 %.

4   DISCUSSION

The quantification of errors computed during the comparison between experimental and numerical frequencies of the cranial substitute evidenced a good identification. Remaining discrepancies can be explained by several factors, such as the boundary conditions, the experimental uncertainties due to high frequencies noise, and of course the determination of the mechanical properties thanks to beam's theory. A parametric study performed with the Finite Element Model showed that by varying the Young Modulus of ± 10 %, a uniform shift of ± 6 % in frequencies was observed. For the Poisson ratio, a variation of ± 20 % induced largest non-uniform variations up to 20 %, as well as modes inversions.

Moreover, on the frequency range [0-5] kHz, a total of 8/13 frequencies are common between dry human skulls of the 50th percentile and experimental results obtained on the substitute. Observed discrepancies can be explained firstly by the different geometries, particularly the fact the skull is not in reality a homogeneous truncated sphere. The skull is characterized by its irregularities and crevices that influence the overall vibratory response. In addition, in the literature Experimental Modal Analyses of dry human craniums were commonly performed in free-boundary conditions; while the cranial substitute was embedded at its base. Changing boundary conditions affect the modal behaviour of a structure.

Therefore, as a perspective of this study, it would be interesting to proceed to the analysis of the substitute's mode shapes. It would be needed to perform the EMA by rotating the substitute such as the measure lines cover the entire structure and that complete mode shapes are obtained.

5   CONCLUSION

It was shown in this study that 65% of the cranial substitute frequencies were corresponding to those of the Finite Element Model. The substitute also has 8/13 common frequencies with a dry human cranium and therefore could be used as a possible experimental substitute for studying responses under high dynamic loadings such as a blast event.

6   ACKNOWLEDGEMENTS

7 REFERENCES

1. Wojcik BE, Stein CR, Bagg K, Humphrey RJ, Orosco J. Traumatic brain injury hospitalizations of U.S. army soldiers deployed to Afghanistan and Iraq. *American Journal of Preventive Medicine*, 2010; 38(1 SUPPL.): S108–S116.
2. Ouellet S, Philippens M. The multi-modal responses of a physical head model subjected to various blast exposure conditions. *Shock Waves*, 2018; 28(1): 19–36.
3. Franke. Response of the Human Skull to Mechanical Vibrations. *The Journal of the Acoustical Society of America*, 1956; 28(6).
4. Gurdjian ES, Hodgson VR, Thomas LM. Studies on mechanical impedance of the human skull: Preliminary report. *Journal of Biomechanics*, 1970; 3(3): 239–247.
5. Khalil TB, Viano DC, Smith DL. Experimental analysis of the vibrational characteristics of the human skull. *Journal of Sound and Vibration*, 1979; 63(3): 351–376.
6. Taleb L, Willinger R, Fellmann G, Kopp CM. Analyse modale de la boîte crânienne humaine in vitro. *Mécanique Industrielle et Matériaux*, 1993; 46(2): 92–95.
7. Ewins DJ. *Modal Testing: Theory, Practice and Application*. Second Edi. Research Studies Press LTD; 2001.
8. Peeters B, Van der Auweraer H. PolyMAX: A revolution in operational modal analysis. *Proceedings of the 1st International Operational Modal Analysis Conference, IOMAC 2005*, 2005(January 2005).

Simulation

25

Numerical modeling of auxetic lattices subjected to dynamic compression in SHPB

Petr Koudelka[1] | **Tomáš Fíla**[1*] |

Radim Dvořák[1*] | **Michaela Neuhäuserová**[1*] |

Jan Falta[1*] | **Jan Šleichrt**[1*] | **Petr Zlámal**[1*] |

Ondřej Jiroušek[1*]

[1]Faculty of Transportation Sciences, Czech Technical University in Prague, Prague, 110 00, Czech Republic

Correspondence
Petr Koudelka, Faculty of Transportation Sciences, Czech Technical University in Prague, Prague, 110 00, Czech Republic
Email: koudepe5@cvut.cz

We demonstrate numerical modelling of the mechanical response of auxetic structures subjected to dynamic uniaxial compressive loading in split Hopkinson pressure bar (SHPB) at the strain rates of $1500\,\mathrm{s}^{-1}$ and $3000\,\mathrm{s}^{-1}$. The stress-strain characteristics as well as compressive strain dependent Poisson's ratio of re-entrant honeycomb and missing-rib auxetic lattices are assessed in LS-DYNA simulations with explicit time integration. Numerical results are supported by SHPB experiments utilized for both calibration of finite element modeling and verification of the simulations. The studied lattices were additively manufactured by laser powder bed fusion from 316L stainless steel. The numerical aspects of the simulations together with the influence of the 3D printing quality on the reliability of the results are discussed.

*Equally contributing authors.

1 | INTRODUCTION

Structural cellular solids form a group of materials suitable for optimization efforts to increase the efficiency of structures in the absorption of deformation energy. Initially, the metal foams revolutionized design practices in vibration damping and the crash-worthiness of vehicles by a combination of typical deformation response (i.e., significant plateau region of constant stress in a wide range of compressive strain) and a high porosity. However, the limitations of the manufacturing process and, thus, imperfections of the resulting microstructure in many cases restrict their application potential which was further accentuated by recent advances in other fields of material science. Particularly the additive manufacturing methods enable to construct porous lattices with a pore-size down to a sub-millimetric scale. Here, the geometry of the lattice can be pre-determined in detail by an arbitrary modeling tool, which can be subjected to relatively simple optimization routines. This also enables development of conceptually new types of (meta)materials with unique mechanical properties highly optimized with respect to their application where one such interesting material property is the negative Poisson's ratio (NPR) of the so-called auxetic materials [1].

The paper is focused on the numerical modeling of the mechanical response of auxetic structures subjected to dynamic uniaxial compressive loading in split Hopkinson pressure bar (SHPB) [2]. The stress-strain characteristics as well as compressive strain dependent Poisson's ratio are studied numerically at strain rates of $1500\,s^{-1}$ and $3000\,s^{-1}$. Three auxetic unit-cells having uni- or biaxial auxetic characteristics are considered. The structures are developed by a periodic assembly of unit-cells in the respective spatial directions. Due to the complex deformation response of the auxetic structures, the reference data for the development of numerical simulations are obtained from the experiments with the samples of structures manufactured using 3D printing from 316L stainless steel. Dynamic loading is performed using a Split Hopkinson Pressure Bar (SHPB) apparatus, while the development of a full-scale numerical representation of the SHPB apparatus for an explicit time integration scheme in LS-DYNA was selected for finite element modeling. The numerical aspects of the simulations together with the influence of the 3D printing quality on the reliability of the results are discussed. The ability of the numerical simulations to describe the deformation response of the investigated auxetic lattices is assessed based on the numerical stress-strain curves and the graphs of the strain-dependent Poisson's ratio.

2 | MATERIALS AND METHODS

2.1 | Investigated lattices

The unit-cells with the geometry of 2D missing-rib, 2D re-entrant honeycomb, and 3D re-entrant honeycomb were used to generate periodic assemblies forming the lattices satisfying the requirements on the RVE of cellular solids as defined by Ashby et al. [3] by having 6×6 or 6×7 unit-cells in the structure depending on a specific type of lattice. Visualisation of the lattices is shown in Figure 1.

The specimens for the testing were printed with an AM 250 device (Renishaw, UK) using the SLS method by sintering powdered SS316L-0407 austenitic stainless steel at minimum achievable strut thickness of 0.2 mm. In total, 5 specimens of each type at every strain rate were tested.
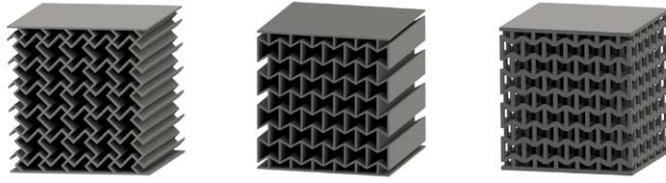
FIGURE 1   SLS printed specimens of the investigated lattices: 2D missing-rib (left), 2D re-entrant honeycomb (middle), 3D re-entrant honeycomb (right).

TABLE 1   Characteristics of the 3D printed lattices.

Type of lattice	No. of unit-cells	Dimensions [mm]	Porosity [%]
2D missing-rib	36	$14 \times 14 \times 14.8$	74.37
2D re-entrant honeycomb	42	$14.0 \times 14.0 \times 14.5$	73.43
3D re-entrant honeycomb	252	$14.0 \times 14.0 \times 14.5$	72.36

2.2 | Numerical

To be able to calibrate the numerical simulations and to compare the numerical results with the experimental data, the approach based on the development of a virtual SHPB apparatus used in the experiments was selected. For this reason, a fully three-dimensional model of the SHPB apparatus was developed in LS-DYNA. The experimental arrangement (i.e., the striker, incident, and transmission bars with the specimen placed in contact with both the incident and transmission bars) and the dimensions of the individual components was considered including the geometry of the specimens directly derived from the parametric models used for the SLS production of the samples. Any of the possible analogies for the representation of the auxetic lattices (i.e., beam analogy, solid representation with the homogenised material model, etc.) was not used due to the need to include all the potential phenomena in the simulations to have the numerical and experimental results directly comparable in terms of the stress wave propagation, the resulting overall stress-strain diagrams of the lattices, the strain-dependent Poisson's ratio, and the influence of the strain-rate on these quantities. Obviously, such an approach effectively prevented the axisymmetric formulation of the problems with the implications of the computational costs as the topology of the lattices does not allow the dimensional reduction of the problem. The arrangement of the virtual SHPB apparatus is depicted in Figure 2.

In the simulations, the initial conditions, in terms of the translational velocity of the striker bar, were imposed with the velocity value measured in the respective SHPB experiment. No body forces nor boundary conditions reflecting the slide bearings carrying the bars of the SHPB apparatus were considered. The geometry of the bars and the auxetic lattices was considered to be ideal, without imperfections in plane-parallelism, surface roughness, defects, or deviations from the geometry prescribed for the SLS testing. The mechanical results from the numerical simulations were extracted by defining the virtual strain gauges on the same location, where the measurement points were established in the SHPB experiments. At the virtual strain-gauges, the strain versus time data was acquired
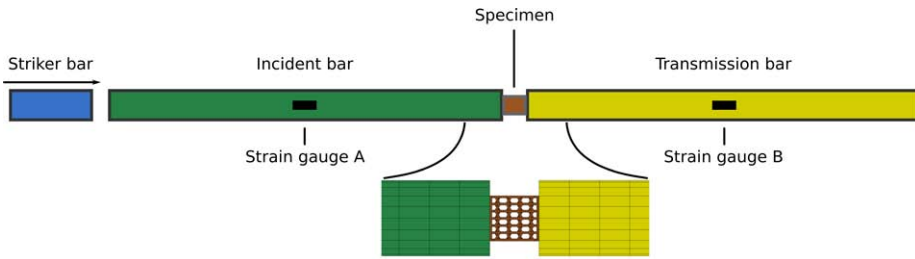
FIGURE 2   Principle of the virtual SHPB.

and used in the further post-processing using the same mathematical methods utilised for the experimental evaluation. The geometrical characteristics of the studied auxetic lattices were extracted at the locations equivalent to the full-field DIC evaluation of the high-speed camera data and from the nodal coordinates, the strain-dependent function of Poisson's ratio was established. The bars were represented by under-integrated single-point constant-stress hexahedral elements (ELFORM 1). For the auxetic lattices, 10-noded composite tetrahedral elements (ELFORM 17) were selected.

2.3 | Experimental

A modified Kolsky SHPB setup was used in the study to evaluate the response of the auxetic structures under dynamic conditions. The incident, transmission, and striker bars had the same nominal diameter of 20 mm with a solid cross-section and were made of a high-strength aluminium alloy (EN-AW-7075) to match the mechanical impedance of the specimens. The incident bar and the transmission bar had the same length of 1600 mm and were supported by eight low-friction polymer-liner slide bearings with an aluminium housing. A striker bar with a length of 500 mm was used for the generation of the incident wave. A fixed aluminium rod and a hydraulic damper were used as the absorbers of the residual kinetic energy of the experiment. For the strain wave measurement during the test, the incident and transmission bars of the SHPB setup were equipped with foil strain gauges. Three measurement points were used on the incident bar (one point in the middle of the bar and the other two points 200 mm from each of the bars' faces), while the transmission bar was equipped with one measurement point located 200 mm from the impact face of the bar. The deformation process of the samples was observed using a high-speed digital camera (FASTCAM SA-Z, Photron, Japan) with a 20 mm square CMOS sensor. As a compromise between the frame rate and the image resolution with respect to the DIC analysis, a 256×168 px image resolution at approximately 130 kfps was used in the experiments.

Two impact velocities of the striker bar were used - a lower striker impact velocity of approximately 21 m $\cdot$ s^{-1} was used to compress the specimens at a strain-rate of approximately 1500 s^{-1} while higher striker impact velocity of approximately 43 m $\cdot$ s^{-1} was used to compress the specimens at a strain-rate of approximately 3000 s^{-1}. Depending on the type of the auxetic structure, the specimens in the low-rate experiments were compressed to a maximum overall strain of approximately 25 − 30 %. The specimens in the experiments conducted at the high-rate reached a significantly higher overall strain of approximately 40 − 50 %. For the minimisation of the wave dispersion effects, cylindrical soft copper pulse-shapers were placed on the incident bar's impact face in this set of experiments.

FIGURE 3   Comparison of the numerical and experimental stress-strain curves (left) and functions of Poisson's ratio (right) of the 2D missing-rib lattice.

Depending on the type of auxetic structure and strain-rate, the diameter and the thickness of the pulse-shapers varied between $7 - 8$ mm and $0.5 - 1$ mm, respectively. The pulse-shapers were very effective in filtering out the high frequencies causing the Pochhammer-Chree oscillations and in the reduction of the ramp-in effect during the initial phase of the wave impact on the specimen. A sufficient quality of the dynamic equilibrium was reached in all the experiments at all strain-rates. Using the pulse-shaping technique, it was possible to maintain a constant strain-rate during the impact up to the densification of the auxetic structure. All the methods used for the evaluation of the stress-strain curves exhibited good convergence after the initial phase of the impact, representing a good quality dynamic equilibrium during the experiment. The strain-rate-strain curve showed constant values of the strain-rate up to the densification of the structures. Approximately 35 images of the deforming specimen during the first deformation pulse were captured using the high-speed camera and processed using the DIC technique.

3 | RESULTS AND CONCLUSION

Figures 3 - 5 depict the numerical and experimental stress-strain diagrams calculated from the dynamic loading at both strain-rates together with numerically and experimentally determined functions of Poisson's ratio and a comparison with the quasi-static results.

It can be seen that the numerical simulations capture the measured stress-strain response of the samples as well as the strain dependent Poisson's ratio with reasonable accuracy including the experimentally observed strain rate effect.

A significantly lower precision of the FEA was achieved in the case of the stress-strain response of the 2D re-entrant honeycomb structures where, at both strain rates, sufficient conformity between the numerical and experimental stress-strain curves was obtained for compressive strains up to 0.1, i.e., for the yield point and initial part of the plateau region.

For all the structures and initial conditions, lower precision of the numerical results was assessed for the strain dependent Poisson's ratio. Even though the resulting numerical curves were within the standard deviations of the experiments in many cases, the overall trends or magnitudes of the Poisson's ratio exhibited significant deviations in both missing-rib and 2D re-entrant honeycomb struc-

Simulation
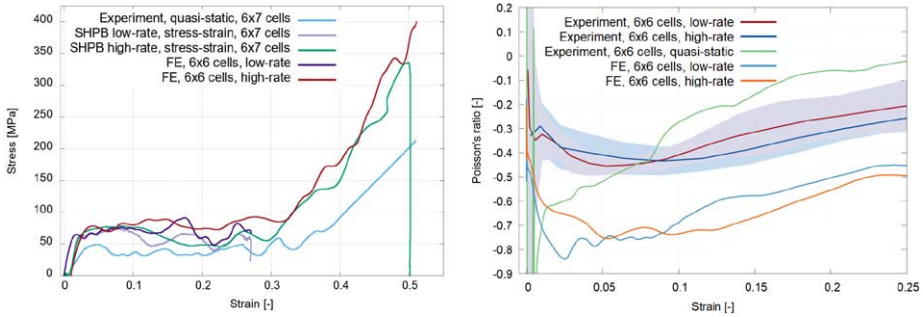
FIGURE 4   Comparison of the numerical and experimental stress-strain curves (left) and functions of Poisson's ratio (right) of the 2D re-entrant honeycomb.
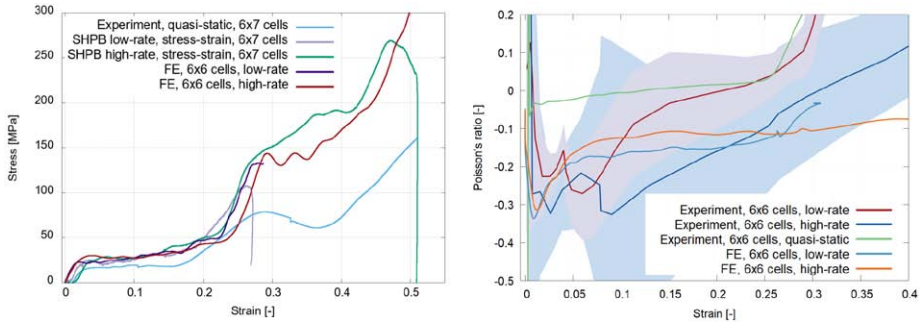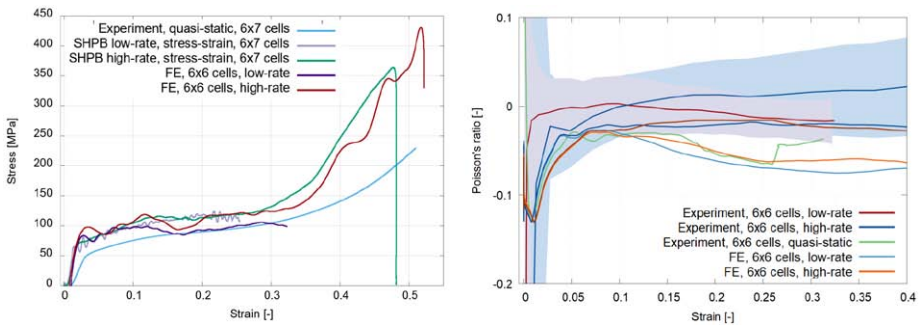

FIGURE 5   Comparison of the numerical and experimental stress-strain curves (left) and functions of Poisson's ratio (right) of the 3D re-entrant honeycomb.

tures. However, significantly higher precision was achieved for the 3D re-entrant honeycomb where orthotropy of the Poisson's ratio was identified.

Based on the computed micro-tomographical inspection of the samples, the primary source of error in precision of the FEA was attributed to the differences between the printed and prescribed geometry of the lattices which influences the deformation response of the samples in strut joints and during self-contact conditions. This factor together with the need for more complex constitutive model in the simulations outlines future direction of the research.

References

[1] Lim TC. Auxetic Materials and Structures. Springer Singapore; 2015. https://doi.org/10.1007/978-981-287-275-3.

[2] Fíla T, Koudelka P, Zlámal P, Falta J, Adorna M, Neuhäuserová M, et al. Strain Dependency of Poisson's Ratio of SLS Printed Auxetic Lattices Subjected to Quasi-Static and Dynamic Compressive Loading. Advanced Engineering Materials 2019;21(8):1900204. https://doi.org/10.1002/adem.201900204.

[3] Gibson LJ, Ashby MF. Cellular Solids. Cambridge University Press; 1997. https://doi.org/10.1017/cbo9781139878326.

26

Finite element modeling concepts for the dynamic compression response of additively manufactured lattices structures

Konstantin Kappe[1]* | **Aron Pfaff[1]** | **Martin Jäcklein[1]** | **Klaus Hoschke[1]**

[1] Fraunhofer Institute for High-Speed Dynamics, Ernst-Mach-Institut, EMI, Freiburg, Germany

Correspondence
Konstantin Kappe, Additive Design & Manufacturing, Fraunhofer Institute for High-Speed Dynamics, Freiburg, Germany
Email: Konstantin.Kappe@emi.fraunhoder.de

In this study, different modeling concepts of additively manufactured lattice structures under dynamic loading are presented. Besides the simulation with a volume discretization, a more efficient beam-based model is developed. Some difficulties in adapting current quasi-static modeling concepts for dynamic compression have been identified and modifications to overcome these problems are presented. To validate the different approaches, experimental investigations of a representative auxetic lattice structure are performed. The structures are manufactured using laser powder bed fusion. The compression behavior under the impact velocities of 5 m/s and 100 m/s is investigated and analyzed using digital image correlation. Both simulation approaches show a good agreement with experimental results. Especially, the modified beam-based simulation approach constitutes to be an effective way to model complex lattice structures with comparatively low computational costs and high accuracy under different dynamic loading conditions. Prospectively, the new modified beam-based simulation approach can be used for optimization strategies in order to further improve the energy absorbing characteristics and enable a lightweight design.

INTRODUCTION

In the last years, lightweight cellular structures like honeycombs, foams or lattices have gained notable attention. Their remarkable mechanical properties such as increased specific strength and stiffness or their energy absorbing capabilities make them attractive for many applications.[1, 2] Thus, they are increasingly applied in a wide range of technical fields, like automotive, aerospace or defense. Furthermore, the development of new manufacturing processes, like laser powder bed fusion (LPBF), enables the fabrication of filigree and complex structures with new materials and tailored material properties.[3, 4] Through the newly gained degrees of freedom, there are innumerable possibilities of cell topologies and design configurations. In particular, lattice-like structures show excellent properties. They can exhibit higher strength to weight than traditional foams [5] and are especially suitable for the absorption of impulsive energy due to their open topology, which allows enough space for plastic deformation.[6, 7] It is even possible to design cellular lattice structures with special properties, such as negative Poisson ratios,

that do not occur in conventional solids. However, due to the variety of possibilities, the design options are hard to overview and efficient simulation models are needed to study different topologies and design optimal structures under different loading conditions.

The static responses of several lattice cell topologies are investigated analytically, numerically and experimentally in several studies.[2, 8, 9] Luxner et al. uses different finite element models to predict the linear-elastic response of lattice structures. Both beam elements and continuum elements are used to predict the elastic moduli. The shortcomings of the beam-based approach are uncovered and a modified simulation approach was developed, where the stiffness in the vicinity of the vertices is increased [8]. However, for dynamic compression applications such as crash, impact or blast mitigation, the nonlinear dynamic response and the energy absorbing characteristics of cellular structures are of interest. Smith et al. use continuum elements and beam elements to predict the nonlinear structural behavior of bcc and bcc-z lattice structures under a quasi-static compression load, whereas possible solutions regarding the simplification of the beam elements are proposed by an artificial increase of the thickness of the beam elements in the vertex area.[10]

However, at varied loading rates of cellular structures, different deformation behaviors occur and other influence factors, such as inertia, are relevant. Multiple studies confirm that three categories of deformation behavior can be identified [11, 12]: (1) The quasi-static mode, where the deformation is macroscopically homogeneous, (2) the transition mode, where the deformation occurs mainly on the impact side, and (3) the shock mode, where the deformation proceeds sequentially from impact to the non-impact end and inertia effects have a significant influence. For explicit analysis, the modified beam-based model approaches for lattice structures proposed in [8] and [10] are not practical due to an increased timestep or increased mass, which influences the inertia effects.

In order to be able to model lattice structures in different dynamic application scenarios, e.g. crash or blast loads, and to enable optimization, a volume element and a computationally effective modified beam-based simulation approach are developed and compared in this study. Therefore, a complex additively manufactured auxetic lattice structure under various impact velocities is investigated. Lattice cubes are made by LPBF of the aluminum alloy Scalmalloy® and tested in experiments. Impact velocities of 5 m/s and 100 m/s are examined using drop weight and planar plate impact experiments. The response towards the different velocities is analyzed. Furthermore, the experiments are simulated and compared using the different finite element model techniques with the explicit solver LS-Dyna. Based on the experimental and numerical results, the influence of the impact velocity on the compression and energy absorbing behavior is analyzed

MATERIAL AND METHODS

Design of Lattice Structures

The single lattice unit cell and assembly of cells investigated in this work are presented in Figure 1. The lattice topology is inspired by studies from [13], where the lattice is used as a sandwich core structure under blast loading. The structure exhibits auxetic behavior constituted by a negative poisson´s ratio. The dimensions of a single cell are 12.5 x 12.5 x 10 mm³. An assembly of the unit cell is created, consisting of 4 x 4 x 5 cells. The diameter of a single strut is 1 mm, resulting in a relative density ρ_{rel} of 7.7 %.
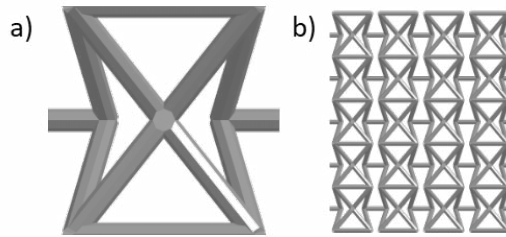
Figure 1 CAD Model of auxetic lattice structure a) unit cell and b) cell assembly

Additive Manufacturing

The auxetic lattice structures are manufactured using the LPBF process on the EOS M400 system using the aluminum-scandium-magnesium alloy powder, called Scalmalloy®. The aluminum alloy can reach a yield stress of approximately 340 MPa, which can be increased by heat-treating to approximately 530 MPa. However, this reduces the failure strain about 50 %. These values, combined with the density of 2.7 g/cm³ make Scalmalloy® a promising choice for lightweight energy absorbing structures. [14] A particular challenge is the orientation of the structures relative to the build platform. It influences, for example, the geometrical accuracy, surface quality or the material properties. The lattice structures are produced in an orientation, that the cubic cell assembly is tilted 45° around its X and Y axis. Small exposure cross sections, as is the case with the present lattice structures, cause strongly shortened laser paths in the case of a strip-shaped, undulating exposure strategy. Inertial effects cause an irregular melt pool in such laser paths and thus a reduced material quality. Furthermore, the material quality is degraded due to an inhomogeneous energy input.[15] For those reasons, a single exposure path following the contour is defined in order to increase the material quality. The following parameters are used for exposure: laser power 400 W; exposure speed 900 mm/s; laser path distance: 0.17 mm. In order to maintain high ductility and avoid failure of the lattice structures, the specimens are not heat treated after the manufacturing process.

Experimental methodology

The dynamic behavior of the additive manufactured lattice structures is investigated using both drop weight and planar plate impact experiments. The behavior at impact velocities of 5 m/s and 100 m/s is studied.

Drop weight test

The low-velocity impact tests are carried out by drop weight experiments. The cubic lattice structures are placed on a force sensor. A total impact mass of 20.4 kg, consisting of 2.8 kg for the sled and an additional weight of 17.6 kg, is used. A drop height is adjusted such that an impact velocity of 5 m/s between the impact mass and the lattice test specimen is set. To investigate the deformation behavior of the impact scenario a FASTCAM SA-X type 324K-M2 high-speed camera with a framerate of 30 kHz is used. The experimental setup is shown in Figure 2 a).
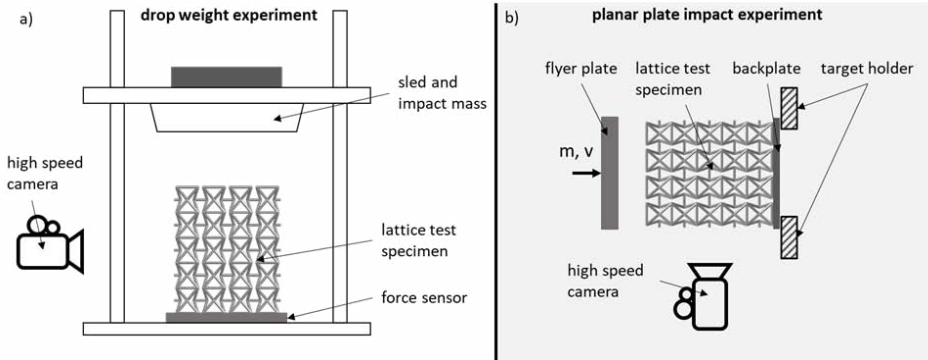
Figure 2 Experimental setup for a) drop weight experiment with 5 m/s and b) high-speed planar plate impact experiment with 100 m/s

Planar plate impact test

In the planar plate impact experiment, setup shown in Figure 2 b), the lattice cube was glued to a solid aluminum backplate with a mass of 9.675 g. The backplate was attached to the glass target holders, which immediately fails in the event of an impact. The structure is impacted by a cylindrical aluminum plate with a diameter of 70 mm, mass of 280 g and a velocity of 100 m/s. The deformation and movement of the lattice test specimen is detected by a high-speed camera with a framerate of 200 kHz. The resulting displacements and velocities of the lattice cube are evaluated by digital image correlation using GOM Correlate.

Numerical Modeling

To generate a robust, adequately accurate and time effective simulation model, both a volume- and a modified beam-based simulation model are developed. Due to the strong simplification of the beam elements, an artificial modification of the model is developed to increase the accuracy. The numerical model representative of the complex lattice structures is developed using the LS-Dyna explicit finite element code. Due to the symmetry of the lattice structures as well as the loading conditions, symmetric boundary conditions are used and only a quarter of the structure is analyzed to reduce the simulation time.

Material model

Deformation under high impulsive loading is a complex and dynamic process and requires the consideration of plastic strains and strain rate effects. Therefore, the Johnson-Cook constitutive material model is used to describe the material behavior of the lattice structures. Material characteristics of Scalmalloy® have been tested in [14] using servo-hydraulic and Split-Hopkinson testing methods. Due to the weak negative strain rate sensitivity of the material, a constitutive model based on a simplified Johnson-Cook approach is used [16]:

$$\sigma_y = \left(A + B \bar{\varepsilon}^{p^n} \right)$$

Where A, B and n are Material constants and σ_y the von Mises equivalent flow stress and $\bar{\varepsilon}^p$ the effective plastic strain. The associated parameters are shown in Table 1. Failure of the elements is not taken into account, due to the fact, that the used material has a sufficiently high failure strain as well as tensile strength and only ductile deformation occurs.

Table 1 Parameters of the Johnson-Cook material model for as-built Scalmalloy [14]

E [GPa]	A [MPa]	B [MPa]	n [-]	v [-]	ρ [g/cm³]
65	198	400	0.332	0.33	2.7

Volume element-based simulation model

Using volume elements leads to the advantage that the geometry of the lattice structure can be represented in detail. The stress distribution in the struts and the vertices can be studied in detail. For the volume-based simulation approach, tetrahedron elements with a linear interpolation function are used.[17] A contact algorithm between the struts with a static and dynamic coefficient of friction of 0.5 is utilized. However, due to the rough surface of additively manufactured components, the determination of the coefficient of friction requires further investigation. To reduce computational effort a mesh-sensitivity study of the lattice structures is performed on a single unit cell under a compression of 5 m/s. The unit cell is meshed with elements with an edge length between 0.1 mm and 0.65 mm, corresponding to an element count ranging from 630554 to 4654 elements for a single unit cell. Based on the results, an element size with the edge length of 0.25 mm is selected for further simulations.

Modified beam-based simulation model

The geometry of the auxetic lattice structure is modeled using beam elements. Beam elements are computationally effective and show in many cases accurate results. However, complex lattice structures contain many vertices, where the various struts intersect, as can be schematically seen for two struts in Figure 3. Straightforward modeling of the vertices by beam elements affects the result by two approximations [8]:

1. Overlapping domains create an increased volume and mass in the area of the vertex.
2. Possible constraints near the vertices caused by the material accumulation in these areas are not taken into account

These approximations could lead to inaccuracies in the simulation results. An increased volume and mass could result in a higher dynamic plateau stress due to effects of inertia. A neglection of the material accumulation in the vertices on the other hand can lead to a reduction of the plateau stress, due to the longer effective length of the deformed struts. To decrease the effects of this approximation, the distribution of material in the intersections should be considered in terms of the stiffness and the density. The influence on the accuracy in predicting stiffness depends on the complexity of the vertices. Thereby the number of intersecting struts, their diameter and their angle should be taken into account. With the assumption that in complex lattice structures under compression loading, the main plastic deformation occurs in the struts between the vertices, whereas the vertices itself remain undeformed, it is necessary to increase the stiffness of the beam elements inside the area of the vertices. Hence, in explicit simulation it is not practical to artificially increase the stiffness of certain elements (due to the decrease in element time step). Instead, a simple linear-elastic material is chosen for the elements. In combination with an elastic-plastic material model for the beam element outside the vertex areas, the vertices appear stiff due to the infinite strength of the linear elastic material model in progressive loading. The area for each intersecting strut is approximated using the intersection angles and the diameter of the struts. The procedure is schematically shown for two intersecting struts in Figure 3 b).
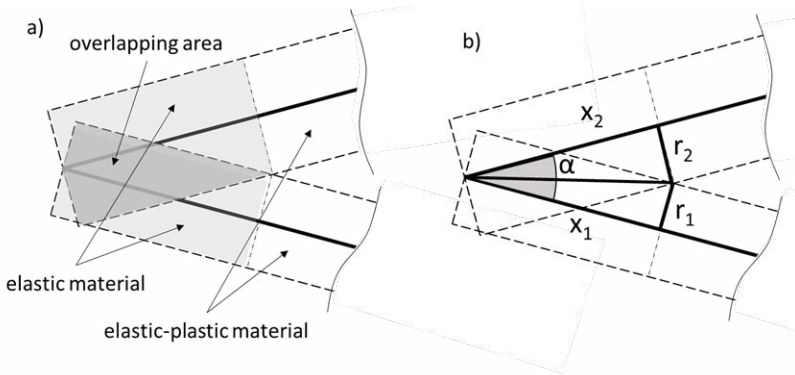
Figure 3 a) Overlapping area and different material models of beam sections for two connected struts and b) parameter for determination of vertex

To allow repeatability and adaptability, the range of overlapping vertex areas is calculated depending on the complexity of the respective vertex. Whereas the length of the artificially stiffened beam elements x_i inside the vertex area is determined by:

$$x_i = \max_{j=1\ldots n} \left(\frac{(r_i + r_j)}{2\tan(\alpha_{ij}/2)} \right)$$

Where r_i and r_j are the radii of the intersecting struts and α_{ij} the angle between them (see Figure 3 b)). When multiple struts are intersecting in a vertex, the maximum beam element length for each strut is chosen.

The relative density of the lattice structures is an important factor for dynamic loading, especially for higher strain rates.[18] However, the deviation of the mass between the manufactured samples and the beam-based simulation approach is less than 10 percent and therefore neglected in this study.

At compression of the lattice structures, the contact between the individual struts plays an important role. To take into account this effect, a beam-to-beam contact algorithm is implemented. To avoid initial penetration of the beam elements, only the elements outside the vertex areas are considered. All beam elements are modeled with Hughes-Liu beam elements as they are computationally cheap and include transverse shear strain.[19] Multiple integration points are used in the cross-section area due to high plastic deformation of the struts. A convergence study has shown that at least an element size of 1 mm between the vertices is small enough to achieve accurate results.

RESULTS AND DISCUSSION

Experiments with the auxetic lattice cubes are performed, as well as numerical simulation using the above described volume-based model approach and the modified beam-based model approach. The additively manufactured lattice cubes show a total mass of 27.8 g (ρ_{rel} of 8.2 %). This indicates a deviation from the theoretical mass of the CAD model with 26.0 g (ρ_{rel} of 7.7 %). Due to the above described overlaps of the beam elements in the vertex areas, the beam-based model has a higher mass of 30.4 g (ρ_{rel} of 9.0 %). This deviation, as it is relatively small, is neglected in the simulations. However, the accuracy of the additively manufactured lattice structures requires further investigation.

Drop Weight Experiment

The resulting transmitted forces and the corresponding deformation behavior of the drop weight experiment and simulations are shown in Figure 4. A typical compression behavior of the cellular structure can be observed in Figure 4 a), whereas the linear elastic region is followed by an almost

constant plateau force and an increase of the transmitted force due to full densification of the lattice sample. The deformation pattern of the lattice cube shows a symmetrical behavior to the center axis (see Figure 4 b)), which is typical for the homogeneous quasi-static mode.[11] Furthermore, a local cross-sectional reduction under compression is observed, which means a negative poisson's ratio and confirms the auxetic behavior of the cell topology.
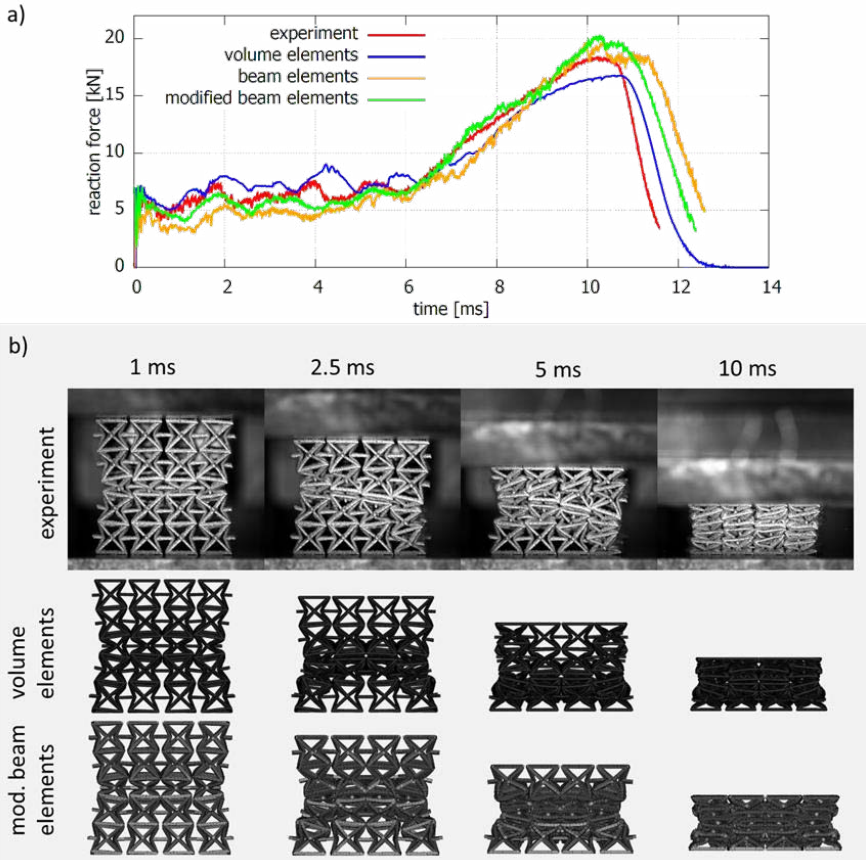
Figure 4 Comparison of a) the force time curve of the reaction forces and b) the deformation behavior at 1, 2.5, 5 and 10 ms of both simulation and experiment of the drop weight experiment with impact velocity of 5 m/s

Both the volume element-based and beam element-based simulation models show a good agreement to the experimental results. The modification of the beam-based simulation approach shows an improvement of accuracy of the simulation results, whereas a lower plateau stress is recognized with no artificial increase of the strength of the vertex elements. It can be assumed that this is due to the longer effective strut length of the lattice. In comparison the volume-based simulation model shows a slightly higher plateau force. Considering the computational effort of the simulation models, a significant reduction from 94 h 53 min for the volume-based simulation to 30 min for the modified beam-based simulation approach can be achieved. This enables an accurate and efficient numerical representation of the lattice structures and allows for design optimization.

Planar impact test

In order to validate the different simulation approaches also at higher velocities, the planar plate impact experiment is performed at a velocity of 100 m/s. To compare the deformation behavior between the experiment and the simulations accurately, this is evaluated with digital image correlation (DIC). For this, the velocity-time curves of the different cell layers, as shown in Figure 5 a) and b), are considered. The deformation pattern of the experiment and both the volume- and modified beam-based simulation are shown in Figure 5 c). The lattice cube shows a typical shock mode deformation behavior and a change to the transitional mode, since the lattice cube is crushed sequentially from the impact end and the velocity difference between the impacted and the non-impact end is constantly decreasing. At the beginning of the deformation, both simulation results show good agreement with the experiments. At the end of the deformation, there are differences between the volume and the beam-based simulation, with the volume-based simulation showing a slightly stiffer behavior. This can also be seen in the drop-weight experiment, where the plateau force is higher. The neglected negative strain rate dependency of the constitutive material could also be a reason for the overestimated strength of the lattice cube. However, there seems to be only a very small deviation and a negative strain rate dependence can lead to strong instabilities in explicit simulation [14]. Furthermore, the linear increase of the velocity of the backplate indicates a typical constant force plateau on the non-impact side.
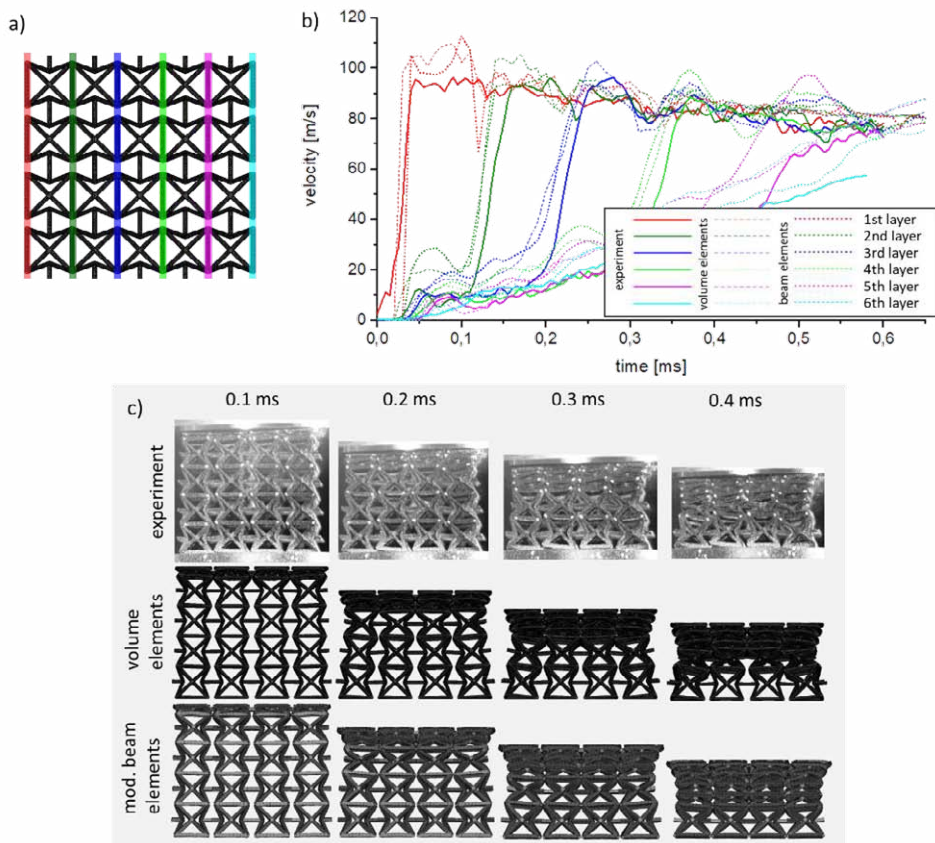

Figure 5 a) Cell layers of auxetic lattice structure, b) velocity time curve of different celular layers during planar plate impact experiment determined by DIC and c) defomation pattern of experiment, volume-based and modified beam-based simulation models

CONCLUSION

In this study, volume- and beam-based finite element modeling concepts for the nonlinear dynamic analysis of lattice structures, manufactured by LPBF additive manufacturing, are presented. The models are validated using impact experiments on a representative auxetic lattice structure with impact velocities of 5 m/s and 100 m/s. It is shown that the dynamic response under the different velocities and deformation patterns can be accurately represented by the finite element simulations. The main findings are as follows:

- Numerical investigation of filigree lattice structures with volume discretization is computationally expensive, since a large number of small elements are required which directly influence the explicit timestep. Furthermore, the creation of the simulation models causes difficulties due to the great manual effort for meshing of the structure.
- Beam elements are computationally effective, but straightforward modeling of the lattice structures with beam elements leads to inaccuracies for dynamic compression. Due to the higher effective beam length a lower strength of the lattice structures can be observed.
- A modified beam-based approach, where the beam vertices are assumed as quasi-rigid, can achieve an equivalent or even better accuracy compared to the volume-element-based approach, while reducing the computational cost significantly.

The proposed modified beam-based approach gives the possibility to model additively manufactured lattice structures with a high accuracy even at different loading rates and deformation patterns. Furthermore, it enables the possibility of an efficient automated modeling and thus allows the optimization of configurations, such as density gradients, or varied lattice topologies for energy absorbing applications. However, the modified beam-based simulation approach needs to be further validated with higher relative densities resulting in larger overlaps of the vertices, and for more complex cell topologies. Furthermore, manufacturing tolerances, for example differences in strut diameter or material properties, are not yet taken into account and their influences must be further investigated.

References

[1]   H. Altenbach und A. Öchsner, *Cellular and porous materials in structures and processes*. Wien, New York: Springer Verlag, 2010.
[2]   L. J. Gibson und M. F. Ashby, *Cellular Solids: Structures and properties - Second edition*.
[3]   M. K. Thompson *et al.*, „Design for Additive Manufacturing: Trends, opportunities, considerations, and constraints", *CIRP Annals*, Jg. 65, Nr. 2, S. 737–760, 2016, doi: 10.1016/j.cirp.2016.05.004.
[4]   A. Pfaff, M. Jäcklein, K. Hoschke und M. Wickert, „Designed Materials by Additive Manufacturing—Impact of Exposure Strategies and Parameters on Material Characteristics of AlSi10Mg Processed by Laser Beam Melting", *Metals*, Jg. 8, Nr. 7, S. 491, 2018, doi: 10.3390/met8070491.
[5]   A. S. Phani und M. I. Hussein, Hg., *Dynamics of lattice materials*. Hoboken, New Jersey: Wiley, 2017.
[6]   L. Yang, L. Sui, X. Li, Y. Dong, F. Zi und L. Wu, „Sandwich plates with gradient lattice cores subjected to air blast loadings", *Mechanics of Advanced Materials and Structures*, S. 1–12, 2019, doi: 10.1080/15376494.2019.1669092.

[7]   H. N. G. Wadley, „Multifunctional periodic cellular metals" (eng), *Philosophical transactions. Series A, Mathematical, physical, and engineering sciences*, Jg. 364, Nr. 1838, S. 31–68, 2006, doi: 10.1098/rsta.2005.1697.

[8]   M. H. Luxner, J. Stampfl und H. E. Pettermann, „Finite element modeling concepts and linear analyses of 3D regular open cell structures", *J Mater Sci*, Jg. 40, Nr. 22, S. 5859–5866, 2005, doi: 10.1007/s10853-005-5020.

[9]   K. Ushijima, W. J. Cantwell, R. A.W. Mines, S. Tsopanos und M. Smith, „An investigation into the compressive properties of stainless steel micro-lattice structures", *Jnl of Sandwich Structures & Materials*, Jg. 13, Nr. 3, S. 303–329, 2011, doi: 10.1177/1099636210380997.

[10]   M. Smith, Z. Guan und W. J. Cantwell, „Finite element modelling of the compressive response of lattice structures manufactured using the selective laser melting technique", *International Journal of Mechanical Sciences*, Jg. 67, 36–37, S. 28–41, 2013, doi: 10.1016/j.ijmecsci.2012.12.004.

[11]   Y. Sun und Q. M. Li, „Dynamic compressive behaviour of cellular materials: A review of phenomenon, mechanism and modelling", *International Journal of Impact Engineering*, Jg. 112, S. 74–115, 2018, doi: 10.1016/j.ijimpeng.2017.10.006.

[12]   Z. Zheng, J. Yu und J. Li, „Dynamic crushing of 2D cellular structures: A finite element study", *International Journal of Impact Engineering*, Jg. 32, 1-4, S. 650–664, 2005, doi: 10.1016/j.ijimpeng.2005.05.007.

[13]   G. Imbalzano, P. Tran, P. V.S. Lee, D. Gunasegaram und T. D. Ngo, „Influences of Material and Geometry in the Performance of Auxetic Composite Structure under Blast Loading", *AMM*, Jg. 846, S. 476–481, 2016, doi: 10.4028/www.scientific.net/AMM.846.476.

[14]   P. Jakkula, G. Ganzenmüller, F. Gutmann, A. Pfaff, J. Mermagen und S. Hiermaier, *Strain Rate Sensitivity of the Additive Manufacturing Material Scalmalloy®*, 2021.

[15]   M. de Angelo *et al.*, „The macroscopic behavior of pantographic sheets depends mainly on their microstructure: experimental evidence and qualitative analysis of damage in metallic specimens", *Continuum Mech. Thermodyn.*, Jg. 31, Nr. 4, S. 1181–1203, 2019, doi: 10.1007/s00161-019-00757-3.

[16]   G. R. Johnson und W. H. Cook, „A Constitutive Model And Data For Metals", 1983.

[17]   J. Bonet und A. J. Burton, „A simple average nodal pressure tetrahedral element for incompressible and nearly incompressible dynamic explicit applications", *Commun. Numer. Meth. Engng.*, Jg. 14, Nr. 5, S. 437–449, 1998.

[18]   G. M. L. Gladwell, R. Moreau, H. Zhao und N. A. Fleck, *IUTAM Symposium on Mechanical Properties of Cellular Materials*. Dordrecht: Springer Netherlands, 2009.

[19]   J. O. Hallquist, *LS-DYNA Theory Manual - March 2006.*

27

Towards Programming the Strain Rate Dependency into Mechanical Metamaterials

Sankalp Patil [1,2] | **Georg Ganzenmüller** [1,2] |
Florian Gutmann [1,2] | **Klaus Hoschke** [1] |
Stefan Hiermaier[1,2]

[1]Fraunhofer Institute for High-Speed Dynamics, Ernst-Mach-Institute, EMI, 79104 Freiburg im Breisgau, Germany

[2]Institute for Sustainable Systems Engineering, INATECH, Albert-Ludwigs Universität Freiburg, 79110 Freiburg im Breisgau, Germany

Correspondence
Sankalp Patil

Fraunhofer Institute for High-Speed Dynamics, Ernst-Mach-Institute, EMI, 79104 Freiburg im Breisgau, Germany.
Email: sankalp.patil@emi.fraunhofer.de

Institute for Sustainable Systems Engineering, INATECH, Albert-Ludwigs Universität Freiburg, 79110 Freiburg im Breisgau, Germany.
Email: sankalp.patil@inatech.uni-freiburg.de

This work presents a methodology to introduce a pronounced strain rate sensitivity into additively manufactured metallic lattice structures where the base material does not have a pronounced intrinsic strain rate sensitivity. The new design incorporates a friction mechanism that brings along its own time scale to couple with the time scale of loading. This delivers a strain rate dependent behaviour irrespective of the base material with which the cell is fabricated. To demonstrate the behaviour, the new design has been manufactured additively with FDM and L-PBF processes, and has been characterized experimentally at strain rates between $0.001\ \mathrm{s}^{-1}$ and $0.1\ \mathrm{s}^{-1}$. Furthermore, the dissipative capability, i.e., the restoration of the cell shape upon load removal is demonstrated.

Abbreviations: FDM, Fused Deposition Modeling; L-PBF, Laser Powder Bed Fusion.

1 | INTRODUCTION

This work presents a methodology to introduce a pronounced strain rate sensitivity into additively manufactured metallic lattice structures where the base material does not have a pronounced intrinsic strain rate sensitivity. Typically, the strain-rate sensitivity is observed pronouncedly for polymers. Here, the material gets brittle and stiff when loaded at a higher velocity compared to the behaviour at a lower velocity. However, many metals show similar behaviour but is less pronounced to that of the polymers. There is a need for a practical technique in the case of metallic lattice structures that induce pronounced strain rate sensitivity. To the authors' knowledge, currently no metallic lattice structure or a practical technique that induces pronounced strain rate sensitivity exists to date. This situation is in stark contrast with polymeric lattice structures where the intrinsic material property usually plays a significant role in witnessing a pronounced strain rate dependent behaviour. The viscoelastic and viscoplastic nature due to the sliding of polymeric chains past each other hold account for such a time dependent behaviour [1]. A similar mechanism is required in the case of metallic lattice structures to introduce pronounced strain rate sensitivity.

Atomic dislocations are responsible for the strain rate dependent behaviour in metals [2], similar to that of the chain arrangements in polymer. Even though the decoupling of time scale exists in both the cases, the mechanism in metals do no induce a pronounced strain rate dependency as by the mechanism in polymers. However, the aforementioned mechanisms are inherent to a material. In order to be independent of the intrinsic material properties, the designs should include mechanisms that bring along its own time scale and couples with the time scale of loading thus inducing a strain rate dependent behaviour due to the presence of a mechanism on a decoupled time scale. Friction, being dissipative and time-dependent [3] [4] can have its time scale coupled on to the velocity at which the structure will be loaded. In such a case, the sliding strain rate experienced by a smaller friction element in a structure will be much higher than that experienced by the actual structure.

The time dependent behaviour of metallic lattice structures has been characterized by many authors in order to assess the energy absorbing and dissipative capabilities [6] [7] [8]. However, the attempts made to design a strain rate dependent lattice structure or unit cell are limited or not existing in the case of metals. S. Janbaz et al. [9] have designed a strain-rate dependent mechanical metamaterial by laterally attaching two beams with different levels of strain rate dependencies, i.e. hyperelastic and visco-hyperelastic thus acting as a single beam. The direction in which the beam buckles is governed by the velocity of loading thus having a controlled response. However, the technique is introduced and illustrated with polymers.

Here, we deviate from the path of employing complicated material mixes to introduce pronounced strain rate sensitivity into metallic lattice structures. Instead, a mechanism at the mesoscale that brings in its own time scale is necessary. This work presents the design methodology of the unit cell by considering friction as a time dependent mechanism at the mesoscale and thereby investigates the time-dependent phenomena by experimental characterization. The resulting friction unit cells are manufactured additively via FDM and L-PBF processes and are experimentally characterized at various strain rates to verify the desired behaviour.

2 | UNIT CELL: PRINCIPLE OF OPERATION

The Fig. 1 shows a 2D auxetic unit cell with an added friction mechanism. It is designed with the fundamental idea of redirecting the vertical compressive load into the horizontal direction, such that the central stems are pressed against each other, creating contact pressure. Therefore the friction force is affected by the axial compression. The magnitude of the friction force can be controlled by the geometry of the curved beams. Their thickness, t and bending radii, R are the dominant parameters to achieve this task. As in Fig. 1, the unit cell design frames to be a close representation of the classical viscoelastic model. Here, the curved beams represent the spring signifying stiffness and the linear frictional struts within auxetic cell represent the dashpot signifying damping behaviour of the structure.
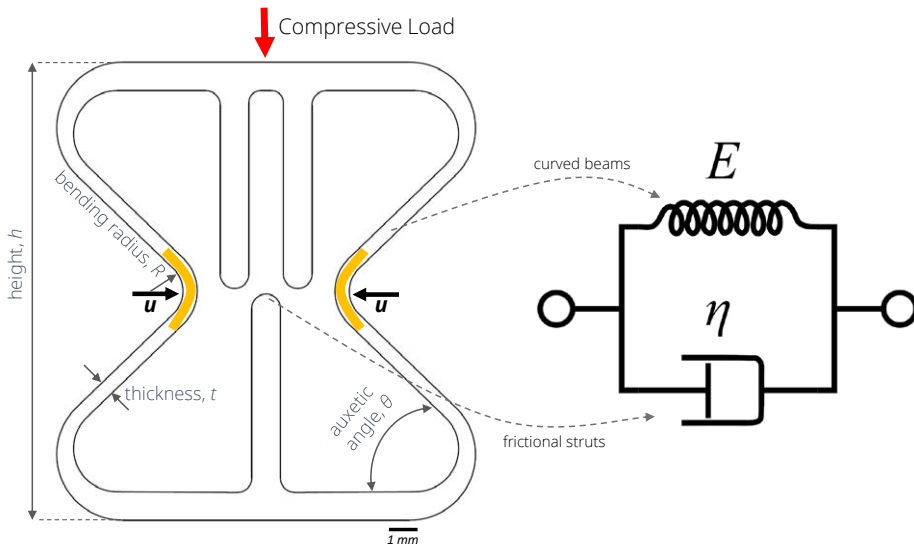
FIGURE 1 Unit cell design along with the representation of its key geometrical features. The design strategy redirects the vertical compressive load into displacement of the curved beams in horizontal direction, u. The curved beams and the linear frictional struts of the unit cell respectively represent the spring and dashpot of the classical viscoelastic model.

Furthermore, the contact pressure is distributed over a large area to decrease stress concentrations and exploit the proportional regime of coulomb friction, i.e., a constant ratio of normal force and friction force. A large frictional force can be generated without exceeding the material strength. This is because the friction force is effected by the curved beams which span the entire height of the unit cell. Thus, their length is maximized, which is advantageous as bending stresses are inversely proportional to the third power of the bending length. All these design features aid in strongly interlocking the surfaces of linear struts giving rise to large friction forces. It is noteworthy that the shear strain rate experienced by the sliding surfaces in contact will be very high when compared to that of the nominal strain rate experienced by the entire structure. This is due to the length of interlocking surfaces being in the order of only a few micrometres.

Simulation

3 | MATERIAL AND METHODS

3.1 | Material and Manufacturing

The polymeric specimens were manufactured on a Markforged X7 fused deposition modeling machine in 100 µm layers. We employed Onyx[TM] (coal-microfiber filled nylon) as the fused filament.

The metal specimens were produced on an EOS M 100 LPBF machine with a 200 W laser unit (YLR-series, CW-laser, wavelength 1070 nm) in 20 µm layers. For the production, recycled Ti6Al4V powder (EOS Titanium Ti6Al4V) sieved with a 63 µm mesh was used. An argon-based inert gas atmosphere of O_2 < 0.1 % was applied in order to avoid oxidation. The test specimens were examined in the as-built state without further surface or heat treatment.

3.2 | Experimental Setup

The polymeric and metallic friction cells were subjected to compressive loads by employing a Zwick-Roell Z100 testing system with 100 kN load cell. The accuracy class of the load cell is 1 for forces less than 200 N. The cross-head velocities of the machine were chosen to achieve nominal strain rates of 0.001 s^{-1}, 0.01 s^{-1} and 0.1 s^{-1} on the auxetic friction cells. The cyclic loading was performed by controlling the cross-head position in the universal testing machine. To this end, a speckle pattern was applied to the specimen in order to record the deformation field. The Basler ace 2 USB camera was employed to record the deformation images at the frame rate of 0.16 - 16.5 Hz. The camera can record a maximum of 255 images at any given frame rate. A total of 5 specimens each for metallic and polymeric versions were tested at each strain rate to assess the reproducibility.

4 | RESULTS

As evidenced by the force-displacement data shown in Fig. 3, the auxetic friction cell exhibits a pronounced positive strain rate sensitivity in both the cases of additively manufactured polymeric (Onyx[TM]) and metallic (Ti6Al4V) structures. The friction cells were axially loaded up to a compressive strain of 25 %, i.e., a displacement of 4 mm and at varying strain rates. As strain rate increases from 0.001 s^{-1} to 0.1 s^{-1} , the plateau force shifts up by approximately 25 % and 10 % in the case of polymeric and metallic friction cell respectively. The sudden rise in the force is due to the friction between rough surfaces, i.e., friction force due to the linear struts sliding with respect to each other. The spike in the force is significant in the case of metallic cells when compared to that of polymeric cells at all strain rates. In the case of metallic cell, the force suddenly drops after a compressive strain of approximately 17 %. This is due to the minute rupture in the curved beams of the metallic structure at this state.

Additionally, we also witness a hysteresis from the structure that is noticeable from the force-displacement curves. This means that the friction cell retracts back to its original shape upon load removal, thereby dissipating energy. The deformation fields of polymeric and metallic cell correlating the loading and load removal paths at the strain rate of 0.01 s^{-1} are depicted in the Fig. 2. It can be
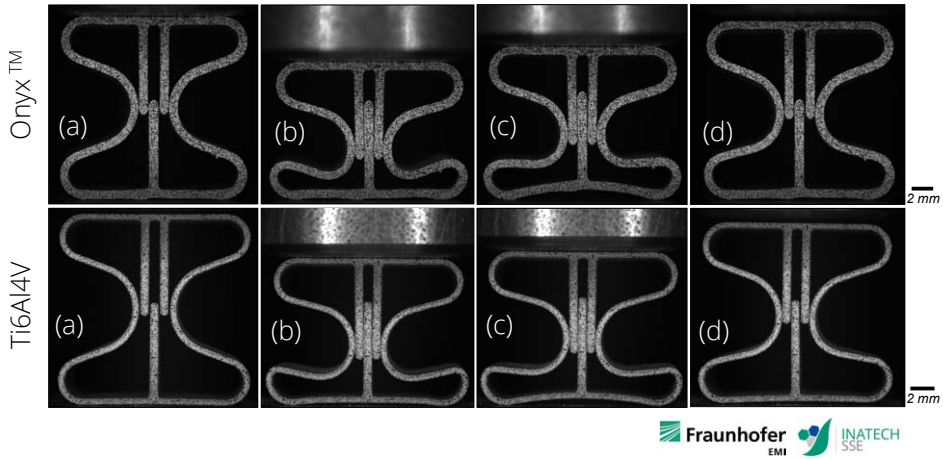
FIGURE 2 Experimental images with deformation histories of polymeric (top) and metallic (bottom) auxetic friction cell visualized with a grey scale speckle pattern. The friction cell under a compressive strain of 25 % at the nominal strain rate of 0.01 s^{-1} is depicted in the figure. The states (a) and (b) represent the deformation of the auxetic frcition cell under compressive load. Upon load removal, the cell retracts back to its mere actual shape as evident from states (c) and (d).
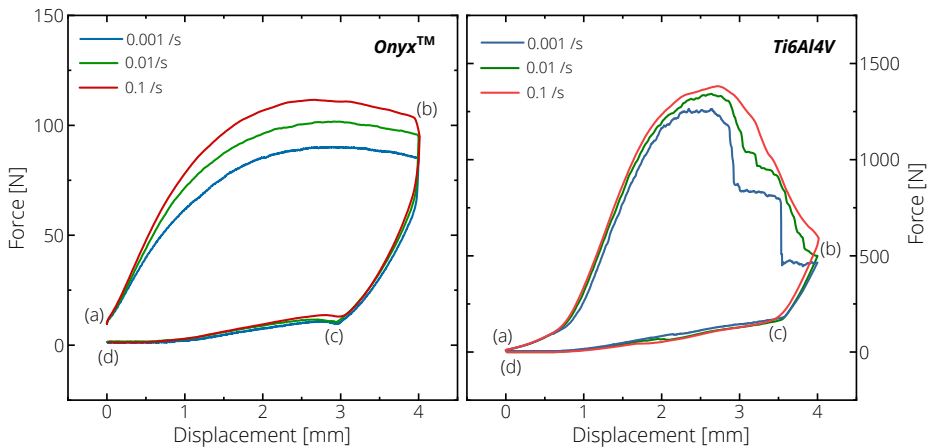
FIGURE 3 Experimental results of polymeric (left) and metallic (right) auxetic friction cell under compression at varying strain rates. These curves are averages of individual experiments. The states (a), (b), (c) and (d) represent the deformation fields shown in Fig. 2.

inferred from the initial, (a) and final, (d) states that the friction cell retracts back to its original shape irrespective of the base material. The state (b) corresponds to the compressive strain of 25 %, where the vertical compressive load is redirected into the displacement of curved beams in horizontal direction thereby affirming the contact of sliding surfaces. Qualitatively, the deformation states are similar for both metallic and polymeric cells at all tested strain rates, also evident from the force-displacement curves. The energy dissipated increases as the strain rate increases for both cases.

Simulation

5 | DISCUSSION AND CONCLUSION

We have presented a simple unit cell which is able to introduce a pronounced strain rate sensitivity into additively manufactured lattice structures, especially metallic structures where the base material does not have a pronounced intrinsic strain rate sensitivity. We have introduced friction between rough surfaces as a mechanism at the mesoscale whose time-dependent properties [3] have strongly influenced the macroscopic properties. The design of the auxetic friction cell not only introduces strain rate dependency but also the structure retracts back to its original shape upon load removal indicating excellent dissipative properties. With such a methodology, the dynamic response of the material can be controlled and structures can be tailored for specific properties.

This study has not addressed the behaviour of a lattice structure employing the auxetic friction unit cell. We leave this open for future investigation, but it is noteworthy that the behaviour would be dependent on the deformation behaviour of the neighbouring unit cells and of course the arrangement. Related works, in particular that of A. Garland et al. [10] propose a dissipative honeycomb structure wherein the elements slide against each other to induce a Coulombic friction to dissipate energy. The bending moment is strongly concentrated at the roots of the cantilever friction legs that are compliant. In order to develop a significant friction force, a thick cantilever beam would be required. Their study is focussed on the energy dissipation and the strain rate dependency of such a dissipative structure is not addressed. However, the design of the auxetic friction cell circumvents the limiting friction force by coupling the contact forces with the force resisting axial compression.

It is evident from the implementation that the strain rate dependency and the dissipative properties can be controlled by geometrical choices and be independent of the complicated material mixes. The methodology of decoupling of time scales at the mesoscale leads to the overall time dependent behaviour. Nevertheless, the parametrization of the key geometrical features of the auxetic friction cell will lead to a more controlled dynamic response and this frames to be the next steps of this work.

Acknowledgements

References

[1] Ganzenmüller GC, Patil S, Maurer M, Sauer M, Jung M, Hiermaier S. A Simple Glassy Polymer Model. Journal of Dynamic Behavior of Materials 2019 Sep;5(3):331–343.

[2] Fan H, Wang Q, El-Awady JA, Raabe D, Zaiser M. Strain rate dependency of dislocation plasticity. Nature Communications 2021 Mar;12(1):1845.

[3] Oestringer LJ, Proppe C. On the calculation of a dry friction coefficient. PAMM 2019;19(1).

[4] Hu J, Song H, Sandfeld S, Liu X, Wei Y. Multiscale study of the dynamic friction coefficient due to asperity plowing. Friction 2021 Aug;9(4):822–839.

[5] Gao ZY, Yu TX, Lu G. A study on type II structures. Part I:. International Journal of Impact Engineering 2005 Aug;31(7):895–910.

[6] Tancogne-Dejean T, Spierings AB, Mohr D. Additively-manufactured metallic micro-lattice mate-rials for high specific energy absorption under static and dynamic loading. Acta Materialia 2016 Sep;116:14–28.

[7] Fíla T, Koudelka P, Falta J, Zlámal P, Rada V, Adorna M, et al. Dynamic impact testing of cellular solids and lattice structures: Application of two-sided direct impact Hopkinson bar. International Journal of Impact Engineering 2021 Feb;148:103767.

[8] Neuhäuserová M, Fíla T, Koudelka P, Falta J, Rada V, Šleichrt J, et al. Compressive Behaviour of Addi-tively Manufactured Periodical Re-Entrant Tetrakaidecahedral Lattices at Low and High Strain-Rates. Metals 2021 Aug;11(8):1196.

[9] Janbaz S, Narooei K, Manen Tv, Zadpoor AA. Strain rate–dependent mechanical metamaterials. Sci-ence Advances 2020;.

[10] Garland AP, Adstedt KM, Casias ZJ, White BC, Mook WM, Kaehr B, et al. Coulombic friction in meta-materials to dissipate mechanical energy. Extreme Mechanics Letters 2020 Oct;40:100847.

Simulation

28

Transferable Parameter Optimisation Strategy for Dynamic Interlaminar Interfaces

Y. Song[1]* | H. Liu[1] | Z. Xu[1] | N. Petrinic[1] | M. Lißner[1,2,3]

[1] Department of Engineering Science, University of Oxford, Parks Road, Oxford, OX1 3PJ, United Kingdom

[2]DCIM (Dresden Center for Intelligent Materials), TU Dresden, Dresden 01069, Germany

[3]ILK (Institute of Lightweight and Polymer Technology), TU Dresden, Dresden 01307, Germany

Correspondence
M. Lißner
Email: maria.lissner@tu-dresden.de

Present address
Department of Engineering Science, University of Oxford, Parks Road, Oxford, OX1 3PJ, United Kingdom

A wide range of industrial applications are subjected to extreme conditions such as dynamic loadings found in e.g., bird strikes on aero engines and car collisions. The structures are not only required to withstand those dynamic loading conditions but also need to be light in weight. Many of the additive manufacturing techniques nowadays revolve around adhesion of layers of materials, which creates weakness in the interface between layers. Therefore, it is important to be able to simulate the interface behaviours for more demanding applications of 3D printed components. In current projects, a semi-automatic parameter calibration strategy was established based on a previously published cohesive model, as a prove of concept. A layer cohesion model for 3D printed components can then be easily generated by calibrating the existing cohesive model against appropriate experimental results.

---

*Equally contributing authors

1   INTRODUCTION

Additive Manufacturing (AM) or 3D printing technologies have been progressing drastically over the past decade thanks to the RepRap project and its opensource approach. The AM technologies previously are mainly used by engineers to iterate engineering designs rapidly, which coins the term, rapid-prototyping. However, as further research is being conducted, the existing techniques are constantly improving, while new forming techniques are also being developed such as volumetric 3D printing. The state-of-the-art AM technologies are increasingly being used for production of functional or load-bearing engineering parts, thanks to the constantly expending material catalog and increasing in-print speed and volume [1].

The most popular 3D printing techniques are based on layering materials on top of each other, i.e. Fused Deposition Modeling (FDM), Stereolithography (SLA), Masked Stereolithography (MSLA) and Selective Laser Sintering (SLS). That causes the printed material to possess the layered microstructure, which induces anisotropic material properties which may fail along the layer interfaces [2], especially in the case of FDM and SLS. In order to fully utilise Finite Element Analysis (FEA) packages when designing with 3D printed components for extreme use cases (e.g. high strain-rates), a calibrated dynamic material model will be crucial for accurately representing the interface's mechanical performance. Many researchers have contributed to the material models for various 3D printed metamaterials [3-5] . However, there is a lack of literature on the layer interface model where failure is most likely to occur.

In this paper, we present a semi-automatic and time efficient dynamic cohesive model optimisation strategy, based on a readily available adhesive bond material card (UMAT) and corresponding experimental results. The calibrated UMAT is then compared with the original manually calibrated UMAT in terms of accuracy. With proven success of the proposed strategy, it can be translated to 3D printed materials and their numerical representation for dynamic loading scenarios.

2   FINITE ELEMENT MODEL FORMULATION

2.1   Specimen Specifications

The UMAT calibration strategy is developed based on our previous works on Titanium-Titanium adhesive bond [6]. For simplicity, only the Mode I loading case is presented in this paper. As shown in **Figure 1** below, the FE model is constructed in a way that replicates the gauge section of the test specimens. The gauge section of the Mode I specimen consists of a butt-joint of 4mm thick endcaps, manufactured from Ti-6Al-4V alloy (refer to "Ti" in the following sections). The end-caps were bonded together with a rubber toughened epoxy film adhesive of thickness 0.3mm using a proprietary bonding fixture. The bonding surfaces were treated to provide optimal adhesion.

Figure 1b shows the FE model in LS-Dyna, constructed from two disk geometries of 4mm thickness and 10mm diameter (green and red region), with a 0.3mm cohesive layer (blue region) in between. The element size was set to 0.3mm in the loading direction so that the bond line consists of a single layer of cohesive elements. The MAT_ELASTIC_001 material card was chosen for the Ti end-caps with property inputs: Young's Modulus, $E = 2 \times 10^5 \ MPa$; Poisson's Ratio, $v = 0.34$; Density, $\rho = 4.43 \times 10^{-6} \ kg/mm^3$. A custom UMAT was used for the cohesive element layer. For detailed description of the UMAT, please refer to the previous work by M. Lißner et al. [6].
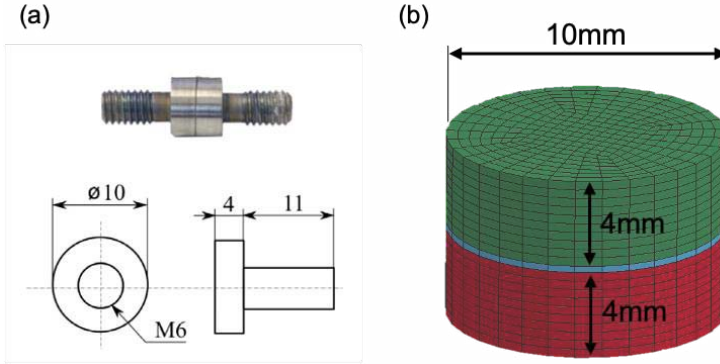
FIGURE 1 (a) Mode I test specimen dimensions and, (b) Corresponding FE model of the gauge section in LS-Dyna.

2.2   Boundary Conditions

The experiments were carried out in 3 levels of strain rates: quasi-static (QS), medium-rate (MR) and high-rate (HR). The QS and MR experiments were conducted using high-stiffness screw-driven servo-electric and servo-hydraulic testing machines respectively. The HR experiments were per-formed on a Split Hopkinson Tension Bar (SHTB) [6]. The displacement rates for QS, MR and HR were $v = 0.05mm/s$, $v = 10mm/s$ and $v = 3000mm/s$ respectively. Therefore, the same displace-ment rates were applied to the FE model through the nodes on the top surface, with displacement constraints applied to the nodes on the bottom surface in all directions, as illustrated in **Figure 2** below.
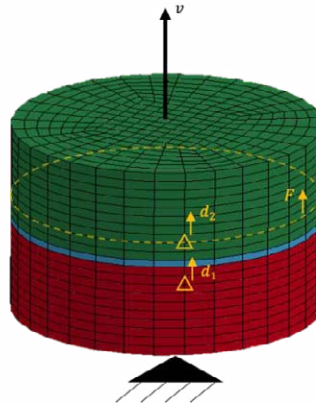
FIGURE 2   Illustration of the FE model boundary conditions, with history output nodes for displacement (yellow triangles) and planner reaction force (yellow dash line).

During the experiments, the bond line separation displacement was measured by tracking two points on both sides of the bond line using Digital Image Correlation (DIC). The QS and MR tests follow a setup explain in [6] which allows the direct measurement of the cohesive response, the traction separation law (TSL). This setup follows the SHB theory in which a long rod with a strain gauge attached is used. The obtained force is a combination of loading cell and strain gauge meas-ured force which acts on the specimen. The force in the HR experiments is obtained using the strain gauges on the loading bars. To ensure comparability between the FE model and the experiments,

the bond line separation displacement, d, was extracted by calculating the difference in displacement between two probing nodes, $d = d_2 - d_1$, marked by yellow triangles in **Figure 2**. The resulting force was extracted by enabling SECFORCE keyword on the cross-section plane marked by yellow dash line in **Figure 2**.

3 PARAMETER OPTIMISATION STRATEGY

Previously the UMAT subroutine was calibrated using the manual approach, where parameters were initially determined from the mechanical properties extrapolated from the experimental traction-separation curves, then finetuned within the range of uncertainties through numerous iterations. Due to the key features of the traction-separation curves having multiple contributors, each may also have effect on the others, the manual optimisation process required extensive human input in terms of trial-and-error and some level of intuitions. Such approach imposed unnecessary biases towards the final parameter set. Although a decent agreement with the experimental results was reached, there was a lack of confidence in the level of optimisation achieved from an incomplete exploration of the design domain.

To improve upon the previous method, a parameter identification workflow was employed within the LS-Opt engine, as illustrated by the schematic in **Figure 3** below. In such workflow, a quadratic polynomial metamodel was selected; design domain sampling points were automatically selected for each iteration using the "D-Optimal" point selection algorithm; number of sampling points was kept at default which will automatically adapt to the problem according to the number of active variables in the "Setup" block; the error measurement algorithm was set to "MSE", which stands for Mean Square Error between reference experimental curve and the predicted curve. Hence, the objective of the LS-Opt engine was to minimize the aforementioned "error".
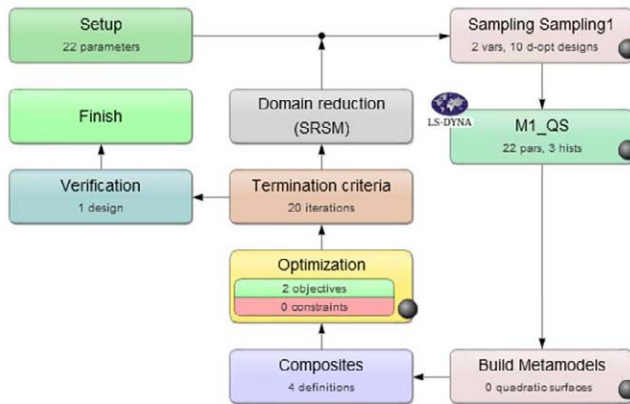
FIGURE 3 Schematic of the parameter identification workflow in LS-Opt.

To further reduce dimensionality of the metamodel hence computational time, we divided the procedure into 3 stages, each with only a subset of the parameters being optimised. The stages were determined according to distinct and independent features of the traction-separation curves, as shown in **Figure 4**. Stage I and Stage II covers the elastic region and the energy release region of the QS traction-separation response respectively; the rate dependency was then calibrated against the full response curve in MR and HR cases in Stage III. Each stage has a certain number of governing

parameters (marked in **Table 1**), so only these parameters were optimised while keeping other parameters at an estimated value. After each stage, the governing parameters will be fixed at the calibrated value before moving onto the next stage. Note that both Mode I (with subscript "_N") and Mode II (with subscript "_S") governing parameters were being optimised in the workflow to account for potential interactions between them.
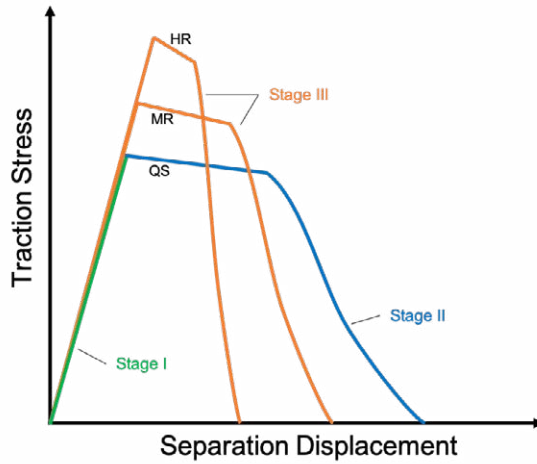
FIGURE 4 Example of traction-separation curves with illustration of the optimisation stages.

TABLE 1 Corresponding active parameters in the material card for each stage; green: elastic region; blue: plastic-softening region; orange: rate dependency

Card 1							
Variable	mid	ro	mt	lmc	nhv	iortho	ibulk	ig
Type	1	1.2e-9	48	25	23	0	26	4

Card 2							
Variable	ivect	ifail	itherm	ihyper	ieos	lmca	unused	unused
Type	1	1	0	0	0	0		

Card 3	1	2	3	4	5	6	7	8
Variable	density	intfail	E (MPa)	G (MPa)	t_a (mm)	t_a0 (mm)	damp	edot_ref
Type	0	4	2000	220	0.3	0.038	0.0	0.1

Card 4	9	10	11	12	13	14	15	16
Variable	T_0N	T_refN	G_0N	G_refN	p_N	P_refN	T_0S	T_refS
Type	1.9	38.0	0.23	3.0	-0.01	0.65	1.8	36.0

Card 5	17	18	19	20	21	22	23	24
Variable	G_0S	G_refS	p_S	P_refS	f_v0	f_vref	y_N	y_S
Type	0.25	9.0	-0.03	0.8	0.02	0.54	1.0	0.85

4   RESULTS & DISCUSSION

In this section, we compare the results of manual parameter optimisation method to that of the proposed automatic optimisation method. The optimised parameter sets were used to generate the FE simulated response curves in all three loading rates, which were then overlayed on top of the experimental response curves.

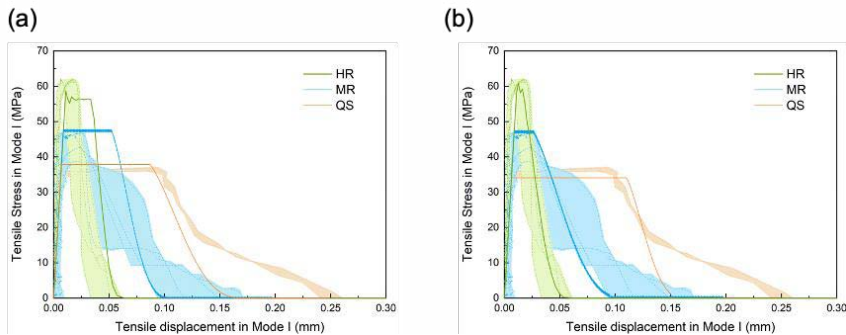**FIGURE 5**   Mode I experimental responses (shaded regions) in QS, MR and HR loading cases compared with simulated responses (solid lines) with (a) manually optimised parameter set and (b) automatically optimised parameter set.

As shown in **Figure 5a**, the elastic region had a good agreement between experimental and simulation results. However, in the QS case, there is a slight over prediction of plateau stress and significant under prediction of total dissipated energy due to faster softening. Also, in both MR and HR cases, the predicted plateau is wider. Such characteristics indicate suboptimal parameters governing the dissipated energy and its rate dependency. **Figure 5b** shows the prediction from optimised parameter set using the proposed method, where a visible improvement can be observed in terms of energy dissipation and rate dependency, especially the width of the plateau region in MR and HR cases. Quantitatively, a minimum of 11.6% increase in accuracy (reduce in MSE) was recorded, with MR case having the most improvement in accuracy of 42.7%. These indicated that the proposed optimisation method was able to suggest more appropriate parameter values for the dynamic cohesive zone model, especially for the energy dissipation and rate dependency governing parameters. On the other hand, the predicted QS response curve in **Figure 5b** still shows a visible deviation from the experimental curve, which implies either a limitation in the cohesive zone model or some unexplained mechanism occurring around 0.14mm displacement. Such anomaly could potentially act as an indication or motivation for further investigations.

TABLE 2   Comparison between Mean Square Errors (MSE) using manually calibrated and automatically calibrated parameter sets, under different loading rates.

Loading Rate	Manual Calibration MSE	Automatic Calibration MSE	% Improvement
QS	48.51	42.86	11.6
MR	104.88	60.06	42.7
HR	32.05	25.92	19.1

5   CONCLUSION

In this study, an automatic parameter optimisation method for cohesive zone model was proposed. A trial was conducted on a previously established cohesive zone model which was originally calibrated against experimental results manually. The results from the new method were then compared to the previous results and some key conclusions are listed below:

- The manual calibration process, although with some level of physical implications, still shows potential for improvements.
- The proposed method was able to achieve a minimum of 11.6% improvement over the previous method in terms of predicted traction-separation responses, with highest improvement in MR loading case of 42.7%.
- The proposed method can expose limitations in either model formulations or experimental understandings of a material system.

Finally, given the generality of such method, this cohesive zone model can easily be transferred to fit the application of interlayer cohesive failure of 3D printed materials by changing the solid element material properties and optimising against appropriate experimental data. However, this is beyond the scope of the current study and left for future works.

6   REFERENCES

[1] Ngo TD, Kashani A, Imbalzano G, Nguyen KTQ, Hui D. Additive manufacturing (3D printing): A review of materials, methods, applications and challenges. Composites Part B: Engineering 2018;143:172-96.

[2] Song Y, Li Y, Song W, Yee K, Lee K-, Tagarielli VL. Measurements of the mechanical response of unidirectional 3D-printed PLA. Mater Des 2017;123:154-64.

[3] Zou R, Xia Y, Liu S, Hu P, Hou W, Hu Q et al. Isotropic and anisotropic elasticity and yielding of 3D printed material. Composites Part B: Engineering 2016;99:506-13.

[4] Kucewicz M, Baranowski P, Małachowski J, Popławski A, Płatek P. Modelling, and characterization of 3D printed cellular structures. Mater Des 2018;142:177-89.

[5] Somireddy M, Czekanski A, Singh CV. Development of constitutive material model of 3D printed structure via FDM. Materials Today Communications 2018;15:143-52.

[6] Lißner M, Alabort E, Cui H, Rito R, Blackman BRK, Petrinic N. Experimental characterisation and numerical modelling of the influence of bondline thickness, loading rate, and deformation mode on the response of ductile adhesive interfaces. J Mech Phys Solids 2019;130:349-69.

04

Polymers

29

Shockwave localization in additively-manufactured polymer structures

Dana M. Dattelbaum PhD[1][*] | **Lindsey Kuettner[1], Brian Patterson[1], Rachel Huber[1], Axinte Ionita[1], Zhehui Wang[1], Christopher Campbell[2], Tali Natan[1], and Brianna MacNider[3][†]**

[1]Los Alamos National Laboratory, Los Alamos, NM 87545 USA

[2]Texas A&M University, College Station, TX 77843 USA

[3]University of California San Diego, La Jolla, CA 92093 USA

Correspondence

Dana M. Dattelbaum PhD, Dynamic Experiments, Los Alamos National Laboratory, Los Alamos, NM, 87545, USA
Email: danadat@lanl.gov

Present address

†LGRF Fellow to Los Alamos National Laboratory, Los Alamos, NM, 87545, USA

Additive manufacturing (AM) has created a new paradigm in control of structure-property relationships for a wide variety of material classes and applications. Here, we describe investigations of the response of polymer AM structures under high strain rate, shockwave loading conditions for applications in shock wave dissipation, focusing, and wavefront manipulation. Shock wave experiments are performed using a single stage light gas-gun synchronized to the X-ray bunch sequence of the Advanced Photon Source, allowing for up to 8 frames of in situ X-ray phase contrast imaging during a single shock event. We have examined the shockwave coupling to several types of polymer AM structures. The experiments have been analyzed using several types of image analysis techniques to better understand localization and deformation behaviors.

1   INTRODUCTION

Additive manufacturing (AM) techniques have enabled topological tailoring of polymeric structures at the micrometer scale, producing new classes of materials with exquisite control of structure-property relationships.[1-18] For polymer-based structures, AM offers control structure across decades in scale. At the nanometer scale, there is control of network chemistry, crosslinking and crystallinity, filler particles and polymer-filler interactions through AM feedstock materials and fillers.

---

*Equally contributing authors

At the micrometer-scale, individual polymer ligaments can be varied in both scale and geometry around connection or node points. And at the millimeter scale, layer symmetries can be tailored to affect deformation or compaction mechanisms, and to alter wave propagation through the structures. As a result of this unprecedented control, polymer-based AM structures have been used to achieve material properties simply not possible in stochastic structures. These have included tailored thermal transport, high mechanical strength-to-density ratios, and controlled acoustic transmission.[8-18]

1.1 Additively-manufactured (AM) polymer structures

In this work, we describe features of shockwave localization in several different types of interface-dominated AM polymer structures, Table 1. Shockwave coupling, localization, and deformation phenomena were measured in situ using dynamic x-ray phase contrast imaging at the Dynamic Compression Sector (DCS), Sector 35, Advanced Photon Source, Argonne, IL, (APS). In each of the structures, the void dimensions (Table 1), and void spacing are 10's-100's mm, ensuring wave interactions are set up within the structures on shock propagation timescales. Further, we apply and evaluate various approaches of image analysis to better understand deformation fields arising from the shockwave interactions within the void structures.

TABLE 1   Description of polymer AM structures, print feedstock, and void morphologies and dimensions investigated in this work.

AM topology	Feedstock	Void morphology and dimensions
3rd-order fractal Menger	2PP-acrylate	Cubic, $l = 63, 180, 560$ μm
2nd-order fractal Menger	2PP-acrylate	Cubic, $l = 180, 560$ μm
2nd-order cylindrical	2PP-acrylate	Cylindrical, $\phi = 170, 550$ μm
Squirt-flow	2PP-acrylate	Elliptical, $x = 47$ μm, $y = 174$ μm

1.1.1. Prior work

Polymeric foams have traditionally been used extensively as structural supports, as well as impact and blast mitigation. There are few examples of the application of additive manufacturing to optimization of shockwave propagation through control of wave interactions at the micrometer-to-centimeter length scales.[1,2-7] Towards that end, we previously demonstrated control of shockwave propagation in different lattice symmetry,[2,3] fractal,[4] and diode[5] AM polymer structures.[6] The features of shock wave coupling to AM topologies are strongly related to its topology and layer symmetry, polymer properties at high strain rates, and the physical spacing of structural elements, such as ligaments & voids. Wave dynamics can be modified from one in which there is a high degree of localization – *e.g.* jet formation – to one in which compaction of the layers occurs to form a shaped wavefront. These observations were only possible using high brilliance X-rays from the Advanced Photon Source (APS) coupled to plate impact drivers at the Dynamic Compression Sector (DCS).
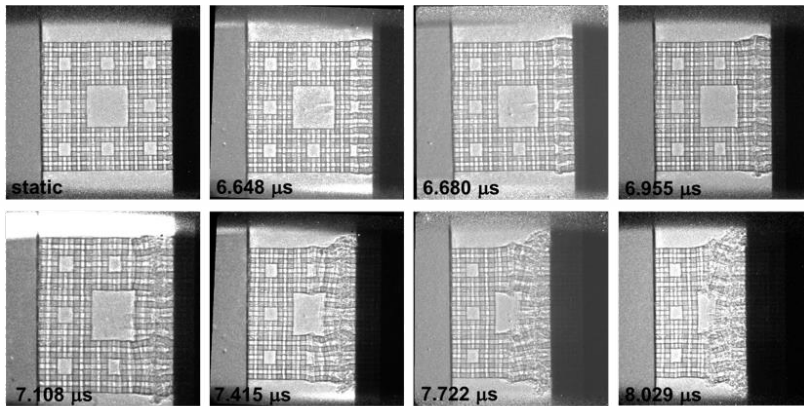
FIGURE 1 Pre-shock (static) and 7 dynamic frames from x-ray phase contrast imaging of a 3rd-order Menger structure during shockwave loading following projectile impact at 331 m/s (Shot 19-2-017). The frames are timed to the 24-bunch mode of the Advanced Photon Source. In the phase contrast images, the shock travels from the baseplate (right side, no transmission) into the structure, resulting in substantial lateral displacement and dissipation of the shock. (D. M. Dattelbaum *et al. AIP Adv.* **10**, 075016 (2020).

Of note, we previously demonstrated unprecedented shockwave dissipation could be achieved in fractal-based AM structures which introduce free surfaces, or interfaces, within a critical spacing (or timescale $t \sim L/2c_l$) that is determined by shock strength, and rarefaction (fan) or release wavespeeds; *e.g.* the material's sound velocity (c_l) at pressure.[4] The dissipative effect is similar to localization phenomena related to "hot spots" in the shock initiation of explosives, but instead of energy localization leading to reactive burn, rarefaction interactions and material deformation can lead rarefaction interactions and reduction of the shock front. An example is shown in Fig 1 in which a 3rd-order fractal Menger structure (L = 0.126 mm) is shock loaded following plate impact at ~318 m/s. As the shock traverses the first few layers, rarefaction waves from free surfaces of the cubic voids interact, resulting in significant lateral deformation and buckling.[6] The kinetic energy imparted to the structure from the impact event is partitioned into elastic and viscoplastic energy, with viscoplastic energy increasing with time/distance (in this experiment leading to a temperature rise DT = +170 K). This prior work was aimed at defining guiding principles for the topological optimization of shock mitigating materials such that optimization of mechanical strength and shock or blast wave dissipation could be achieved.

1.1.2. Image analysis

Image analysis has been sparsely applied to quantify shockwave localization in AM structures; much of which has been inferred from simulation. Here, we introduce several methods of velocity field analysis for the X-ray images, or "X-ray velocimetry" enabled by dynamic phase contrast imaging. Two of the critical steps of X-ray velocimetry are similar to optical velocimetry, namely, feature recognition or object identification from individual movie frames to another, and feature matching or object tracking from one frame to another. Even though X-ray velocimetry is not widely practiced in the literature, we have used existing algorithms for optical imaging and velocimetry for the X-ray data. Several challenges in X-ray velocimetry are recognized: a) Low signal-to-noise ratio in the raw data limited by the X-ray source intensity and camera hardware; b) Shockwave or impact on the porous structure can modify the features significantly and frequently destroy the features completely from one movie frame to another; *i.e.*, many features are not recognizable after the impact or the shockwave front; so manual tuning of the existing algorithms is necessary for X-ray velocimetry

to improve the reliability of the velocity estimation; c) It is difficult to obtain the 2D velocity uniformly across the images because of the limited number of features; d) There is limit amount of information on 'ground-truths' to validate the algorithms; *i.e.*, except for some estimates of the shock velocity based on the bulk material properties; and e) The velocity field is intrinsically 3D, while the X-ray image only captures the projected information.

2 EXPERIMENTAL

2.1 Materials

Macro-3D printing using photolithography was used to fabricate polymer AM structures using a Nanophotonics NanoProfessional GT. This system can fabricate structures with resolutions approaching 100 nm over 100 x 100 mm samples. The printing is achieved via 2-photon polymerization of positive-tone photoresists, in this case a proprietary acrylate polymer. The structures were characterized using X-ray computed tomography with a Carl Zeiss Microscopy Inc, Xradia 520 Versa instrument, using the 4X objective, and 1.5 s exposure time over 3001 images (60 keV, 5 W source, 2.7 μm pixel size). Four different AM polymer structures are presented here. They include 3rd- and 2nd-order fractal Menger[19] structures (Fig. 2a and 2b), a cylindrical analog – 2nd-order cylindrical (Fig. 2c), and a squirt-flow architecture[20] (Fig. 2d). The Menger structures, M_n are made up of 20^n smaller cubes, each with side length of $(1/3)^n$. The squirt flow structures were inspired by Ref. 20, but modified for shock-wave shaping based on our guiding principles.
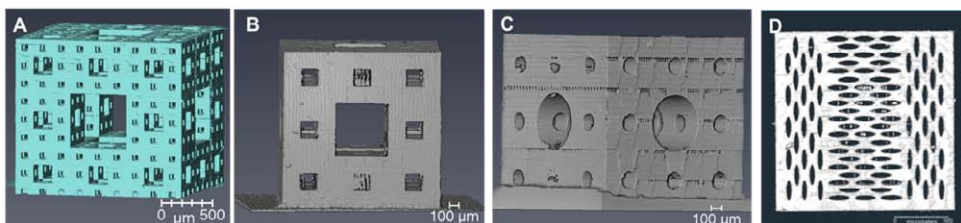

FIGURE 2 Various 3D X-ray CT renderings of additively-manufactured polymer structures subjected to shock wave compression. The structures are a) 3rd-order fractal Menger, b) 2nd-order fractal Menger, c) 2nd-order cylindrical, and d) squirt-flow architectures.

2.2 Dynamic X-ray phase contrast imaging experiments

The experimental configuration for dynamic X-ray phase contrast imaging at the DCS has been described in detail previously.[1-7,21-24] Briefly, X-ray bunches ("pink" beam, E = 25.0 ± 0.9 keV, l = 0.05 nm) are aligned normal to the impact (shock) direction in an experimental target mounted to the end of the 12.7 mm diameter gun barrel of a single stage light gas gun. Impact is timed to the 24-bunch mode of the APS (Dt = 153.4 ns), with eight images detected using an X-ray-to-optical light scintillator and recorded using four intensified CCDs (Roper Scientific). In addition, three photonic Doppler velocimetry[25] probes were used to record projectile velocity, shockwave breakout time in the material, and transmitted wave at the rear sample/window interface.

2.3 Image analysis

Two different approaches to image analysis of shocked AM structures were pursued: ground-truth and particle image velocimetry (PIV). Since the relative displacement of various material features in the target can be estimated via inspection, a manual "human-in-the-loop" method was devised to

generate a ground truth result which consisted of a user interface written in MATLAB which stream-lined manual identification of matching points on the target between two adjacent frames. Once all visible pairs of matching points had been identified and a displacement had been calculated for each, velocimetry could be performed simply by interpolating these displacements onto a regular grid of sample points. Ground truth generated using this method was determined to be sufficiently accurate for validation, since a successful velocimetry result from conventional algorithms should agree with the displacement of visible features evident via manual inspection.

One of the most common techniques for automatic analysis of 2D sequential images is particle ima-ging velocimetry (PIV) via cross-correlation, which has been implemented in MATLAB under the name PIVlab by Ref. 26. Cross-correlation PIV relies upon frequency-space comparison between portions of subsequent frames. The algorithm scans through the second frame with a small rectan-gular portion of the first frame, attempting to maximize the average correlation coefficient (calcula-ted by multiplying together the Fourier transform of the patch and the Fourier transform of an equally-sized patch of the second image, then taking the inverse Fourier transform). A sequential method of patch comparison is built on top of this Fourier-space correlation, successively refining the optimized result until a stopping criterion is reached, after which a velocimetry result is reported for that portion of the image.

3   RESULTS AND DISCUSSION

3.1   Plate impact experiments

Dynamic, single bunch X-ray phase contrast imaging (PCI)[2-7,21-24] has allowed for in situ measurement of shockwave coupling to stochastic and AM polymer structures with spatial (few micrometer) and temporal resolutions (<100 nanoseconds) that were not possible previously. In prior work, we found that regular lattice layer symmetry structures fabricated using direct ink write (DIW) methods result in localization and material extrusion (jetting) in the case of a simple cubic layer symmetry, and cre-ation of a sinusoidal front in a face-centered tetragonal symmetry.[2,3] In these experiments, the feed-stock material, polydimethylsiloxane, retains its ductility even at high strain rates, giving rise to the jetting phenomena as the material is compressed and extrudes between ligaments. Here, we present the results of dynamic PCI experiments on four different AM structures.

3.1.1. 3rd- and 2nd-order fractal Menger
Cubic void structures in the 3rd- and 2nd-order fractal Menger structures are spaced at L = 0.126 and 0.36 mm, respectively. At an input condition resulting from plate impact at ~300 m/s, $P \sim 0.7$ GPa, $U_s \sim 1.99$ km/s,[6] the sound velocity on the principal isentrope is $c_l \sim 2.30$ mm/ms. At this input condition, the timescale for rarefaction interactions is commensurate with shockwave propagation, and dissipation occurs within the first 30 (3rd-order) to <180 (2nd-order) ns.[6] Inspection of Figures 1 and 3 reveal the general shock localization mechanisms in the fractal structures. Figure 3 shows the static (top right) and seven (left-to-right, top row, then bottom row) dynamic frames from X-ray phase contrast imaging of a 2nd-order Menger structure during shockwave loading following projec-tile impact at 318 m/s (Shot 20-2-081). There is greater magnitude to the focusing of the shock wave in the first layer of voids in the cell (at right) leading to material ejection into the central void (image center, Frames 4-6) compared to the 3rd-order structure shown in Figure 1.

FIGURE 3 Pre-shock (static) and 7 dynamic frames from X-ray phase contrast imaging of a 2nd-order Menger structure during shockwave loading following projectile impact at 317 m/s (Shot 20-2-081). There is greater focusing of the shock wave by the first layer of voids in the cell (at right) leading to material ejection into the central void (image center, Frames 4-6) compare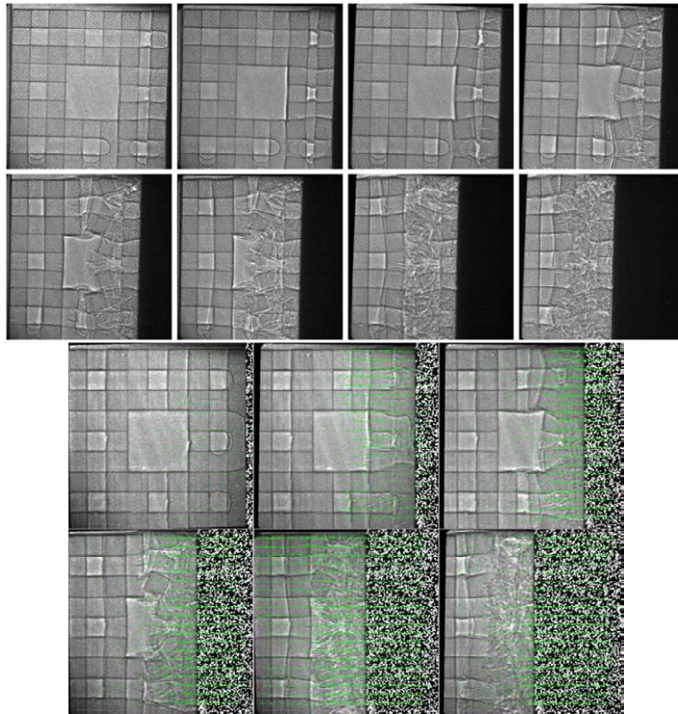d to the 3rd-order structure shown in Figure 1. (bottom) PIVlab X-ray velocimetry analysis of the PCI images of the shocked Menger structure shows increasing lateral deformation of the solid matrix with time.

3.1.2. 2nd-order cylindrical

A 2nd-order cylindrical void-analog of the Menger structures was studied to compare the dynamic void collapse and compaction response with cylindrical rods vs. cubic voids. Figure 4 shows a series of dynamic X-ray phase contrast images from a target impacted at 316 m/s (Shot 20-2-083). Here, the void collapse is similar to collapse observed in related spherical and rod-like voids, with the downstream wall collapsing into the void. This is best seen on Frames 5, 6 and 7. From inspection of the dynamic PCI images, one can observe the initial collapse of the first layer of cylindrical voids, including a "wrap-around" effect on the material flow around the voids. This leads to less lateral material displacement compared to the cubic voids in the Menger structures.

TABLE 2   Summary of plate impact experiments diagnosed by dynamic X-ray phase contrast imaging at the DCS. The impact velocity, u_0, in m/s, X-ray bunches recorded in image frames, and general observations on deformation mechanisms of several shocked AM topologies are given.

Shot #	Topology	u_0 (m/s)	Image frames (X-ray bunches)	Deformation mechanism
19-2-017	3rd-order Menger	331	0, 1, 2, 3, 4, 6, 8, 11	Layer buckling and rubblization within first void layer
20-2-081	2nd-order Menger	317	1, 2, 3, 5, 7, 9, 12, 15	Deformation localization at first layer and material ejection
20-2-083	2nd-order Cylindrical	316	1, 2, 3, 5, 7, 9, 12, 15	Void collapse with less lateral displacement vs. cubic voids

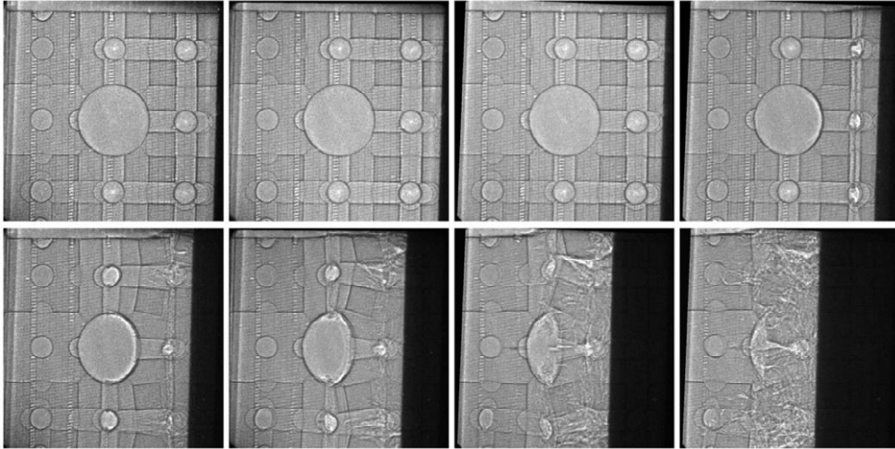| 21-2-121	Squirt-Flow	416	0, 1, 2, 3, 4, 5, 7, 9	Preferential closure of elliptical voids with long axis normal to shock direction

FIGURE 4 X-ray phase contrast images from a 2nd-order cylindrical void structure impacted at 316 m/s (shot 20-2-083). Frames 1-4 (bunches 1, 2, 3, 5) are in the top row, left-to-right. Frames 5-8 (bunches 7, 9, 12, 15) are in the bottom row.   Here, the void collapse and material extrusion occur with less lateral motion, as the downstream wall is collapsed into the void.

3.1.3. Squirt-flow

Squirt-flow structures have been previously proposed for energy dissipation by Cohen *et. al.*[20] Here, we modified the squirt-flow structure to have elliptical channels oriented with their long axis parallel and perpendicular to the shock propagation direction. Dynamic X-ray phase contrast images for shot 21-2-121 are shown in Fig. 5. While all of the voids in the 1.7×1.7 mm field-of-view (FOV) are shock loaded at the baseplate/sample interface simultaneously, collapse of the elliptical features occurs promptly for voids oriented perpendicular (long-axis) to the shock direction, giving rise to wave shaping of the front. In fact, the oppositely-oriented voids on the top and bottom of the FOV become rotated due to this flow field, and many do not appear to fully collapse. It is expected that this effect is due to weakening of the axial stress in these regions from dissipation of the shock in the central region.
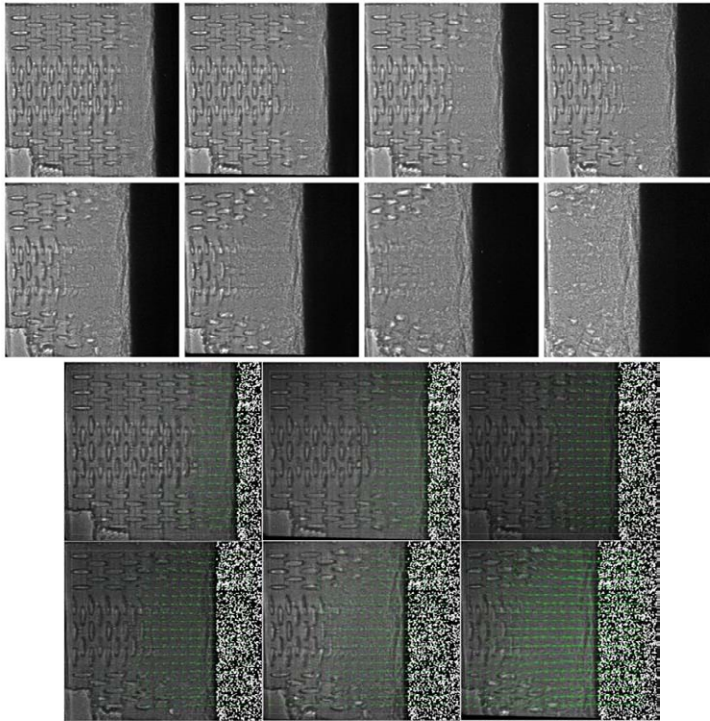
FIGURE 5 (Top) Eight dynamic frames from X-ray phase contrast imaging of a squirt-flow structure during shockwave loading following projectile impact at 416 m/s (Shot 20-2-121). Here, the shock collapses the elliptical voids, with collapse occurring preferentially in the center of the material where the ellipses are oriented with the long axis perpendicular to the front. This leads to faster wave propagation through the middle of the target. (bottom) PIVlab velocimetry results of the first six frames. The X-ray velocimetry analysis shows the angular motion outside the central set of elliptical voids.

3.2   Image analysis

In order to increase the robustness of this ground truth method, a unique speckle pattern was printed on the impactor (visible on the right side the frames in Figure 6a and Figure 4), shifted to align with the impactor's edge. This eases velocimetry analysis, since it is known with high confidence that the impactor is a rigid body and should therefore correspond with a unidirectional constant velocity field. Figure 6a gives an example of the ground truth approach applied to one of the dynamic frames in 20-2-081. Ground truth generated using this method was determined to be sufficiently accurate for validation, since a successful velocimetry result from conventional algorithms should agree with the displacement of visible features evident via manual inspection.

The results of the ground truth velocimetry of shot 20-2-081 are given in Fig. 6b-c. By definition, the velocimetry via this ground truth method is successful in tracking clearly-visible moving features of the target. In regions where no discernible feature is present in subsequent frames, interpolation onto a regularly-spaced grid is used to estimate the velocity field within these gaps. Once the impactor moves into the field of view, a prominent shoulder in the velocity field becomes visible near the corresponding edge of the plot. One major feature of interest is the secondary smaller shoulder in velocity (visible in the third frame of Figure 3) which precedes the impactor by several hundred

micrometer. This second shoulder or front is shown in Figure 6b, stacked corresponding to inter-frame time, and in 3D in Figure 6c. The front moves out in front of the baseplate with time, as expected, but is not a discontinuous shock front, but rather a wide band of velocities.
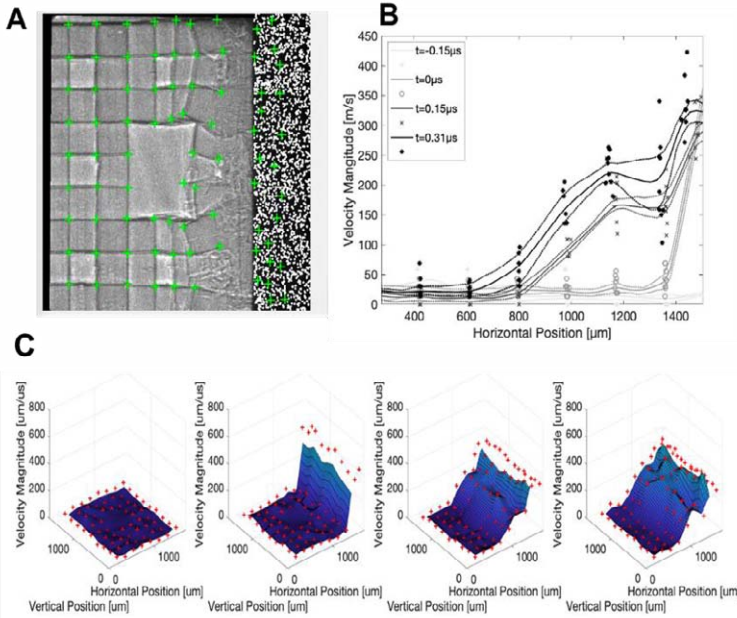

FIGURE 6 a) Single frame analysis from shot 20-2-081 using the ground truth approach. Here, the 4th frame is shown, in which shock localization led to "cell" rotation and material extrusion lateral to the shock direction. b) Corner velocity as a function of horizontal position stacked by frame shows a broad velocity disturbance with a maximum of ~250 m/s moving into the structure. The velocity increase is not discontinuous (shock-like), but is spread over nearly 0.5 mm.

Building off of the cross-correlation PIV results for second-order Menger sponge target, we used the same velocimetry method to analyze shock compression of the squirt-flow structure, shot 21-2-121. Figure 5 (bottom) shows the PIVlab results of the dynamic PCI frames in shot 21-2-121 (impact velocity = 416 m/s). In this structure, the central voids with long-axis perpendicular to the front preferentially collapse, and the PIVlab analysis shows the divergence of the shock flow with rotation of the oppositely-oriented voids at top and bottom. Though quantitative analysis via comparison to a ground truth was not performed on this experiment (the aforementioned ground truth method was less successful on these irregular non-rectangular features), in general cross-correlation PIV worked better for the squirt-flow target than for the Menger target, indicated by a reduced sensitivity to noise and pre-processing parameters. This improvement appeared to be caused by the nature of target destruction during the event: destruction of the squirt-flow structure was marked by smooth deformation of the material, while that of the Menger sponge target exhibited more fracturing behavior and motion of smaller rigid fragments. Note that this smooth deformation behavior closely resembles more common applications of cross-correlation PIV (such as analyzing fluid flow with seed particles), where discontinuities in the velocity field are less common. The Fourier-space comparison on which this method relies will typically fail near regions of the image with high spatial gradients in the velocity field, since successive iterations of comparison with different patch sizes will likely lead to drastically different velocity results for those regions.

4   CONCLUSIONS

Additive manufacturing has enabled the heirarchical assembly of structures at the mesoscale not possible using traditional techniques. We have measured the dynamic response of several AM polymer structures with high spatiotemporal (single bunch) X-ray phase contrast imaging at the Advanced Photon Source, directly imaging and quantifying deformation fields in the shock-loaded structures. As with our earlier studies, features (in this case, voids) must be spaced within a volume that allows for the shockwave (and release waves) to couple on relevant timescales to affect the shock-driven flow. Here, we have examined 2nd- and 3rd-order fractal Menger structures, a cylindrical Menger-analog, and a squirt-flow architecture. Overall, there is greater material displacement in the 2nd-order Menger structure compared to the 3rd-order Menger structure, due to the stronger shock at the 2nd layer of voids - *e.g.* the shock is not as dissipated in the first layer - which is consistent with our prior finite element simulations. Replacement of the cubic voids with cylindrical rod-shaped voids results in void collapse reminiscent of shock-driven bubble collapse and a "wrap-around" effect in the flow such that there is less displaced material outside of the void. Lastly, a squirt-flow structure exhibited smooth deformation of the material, and preferential void compression along the center axis, which resulted in a shaped wavefront and faster wavespeed in the center.

The rich experimental dataset offers insights into AM material deformation under shock loading, and we describe new "X-ray velocimetry" approaches based on image analysis to quantitatively measure deformation fields. Semi-manual velocity field analysis is necessary to generate a ground truth for automated algorithm validation and overcome the difficulties associated with feature destruction in a shockwave and impact environment. We have also described automatic velocity field retrieval using PIVLab, which is commonly applied to particle flows. Other velocimetry algorithms may be used for future work. Due to the unique challenges in dynamic material experiments and X-ray imaging, a combination of algorithm improvement and better experimental data generation through imaging hardware improvements and introduction of contrast agent would be key ingredients towards routine applications of X-ray velocimetry for AM material qualification, dynamic material modeling, and better understanding of dynamic material responses to shockwaves and impact.

While the results we described here are sufficiently interesting, it seems critical to develop automated feature recognition algorithms through better understanding of how the features are created or destroyed, especially for AM structures. Further improvement of the phase contrast imaging resolution and contrast improvement will also be helpful. We conclude that a combination of algorithm improvement and better experimental data would pave the way towards routine X-ray velocimetry for AM material and other dynamic X-ray phase contrast imaging applications.[4.]

5   REFERENCES

[1]   J. A. Hawreliak, J. Lind, B. Maddox, M. Barham, M. Messner, N. Barton, B. J. Jensen, and M. Kumar, Sci. Rep. 6, 28094 (2016).

[2]   B. Branch, A. Ionita, B. E. Clements, D. S. Montgomery, B. J. Jensen, B. Patterson, A. Schmalzer, A. Mueller, and D. M. Dattelbauma, "Controlling shockwave dynamics using architecture in periodic porous materials." *J. Appl. Phys*. **121**, 135102 (2017).

[3]   B. Branch, A. Ionita, B. M. Patterson, A. Schmalzer, B. Clements, A. Mueller, D. M. Dattelbaum, B. J. Jensen, and D. M. Dattelbaum, Polymer **160**, 325–327 (2019).

[4]   D. M. Dattelbaum, A. Ionita, B. M. Patterson3, B. A. Branch and L. Kuettner, *AIP Advances* **10**, 075016 (2020).

[5]   J. E. Spowart *et al.*, in Society of Experimental Mechanics Annual Proceedings, 2019.

[6]   D. M. Dattelbaum, B. Branch, A. Ionita, B. M. Patterson, L. Kuettner, and M. Herman, "Shockwave interactions with additively-manufactured polymer structures," AIP Conf. Proc. (in press) (2020).

[7]   J. Lind *et al.*, J. Mater. Res. **34**(1), 2–19 (2019).

[8]   B. I. Popa *et al.*, Phys. Rev. B **88**(2), 024303 (2013)

[9]   P. M. Reis, J. Appl. Mech. **82**(11), 111001 (2015).

[10]   T. A. Schaedler, A. J. Jacobsen, and W. B. Carter, Science **341**(6151), 1181–1182 (2013).

[11]   T. A. Schaedler, A. J. Jacobsen, A. Torrents, A. E. Sorensen, J. Lian, J. R. Greer, L. Valdevit, and W. B. Carter, Science **334**(6058), 962–965 (2011).

[12]   J. Shim, C. Perdigou, E. R. Chen, K. Bertoldi, and P. M. Reis, Proc. Natl. Acad. Sci. U. S. A. **109**(16), 5978–5983 (2012).

[13]   S. Singamaneni, K. Bertoldi, S. Chang, J.-H. Jang, S. L. Young, E. L. Thomas, M. C. Boyce, and V. V. Tsukruk, Adv. Funct. Mater. **19**(9), 1426–1436 (2009).

[14]   A. Torrents, T. A. Schaedler, A. J. Jacobsen, W. B. Carter, and L. Valdevit, Acta Mater. **60**(8), 3511–3523 (2012)

[15]   P. Wang *et al.*, Phys. Rev. Lett. **113**, 014301 (2014).

[16]   M. Wegener, Science **342**(6161), 939–940 (2013).

[17]   F. Xin and T. Lu, Sci. Rep. **6**, 27432 (2016).

[18]   E. B. Duoss, T. H. Weisgraber, K. Hearon, C. Zhu, W. Small, T. R. Metz, J. J. Vericella, H. D. Barth, J. D. Kuntz, R. S. Maxwell, C. M. Spadaccini, and T. S. Wilson, Adv. Funct. Mater. 24, 4905 (2014)

[19]   K. Menger, in *Classics on Fractals, Studies in Nonlinearity*, edited by G. A. Edgar (Westview Press, 2004).

[20]   T. Cohen, P. Kurzeja, K. Bertoldi, J. Mech. Phys. Solids, 109, 22-33 (2017).

[21]   B. J. Jensen, S. N. Luo, D. E. Hooks, K. Fezzaa, K. J. Ramos, J. D. Yeager, K. Kwiatkowski, T. Shimada, and D. M. Dattelbaum, AIP Adv. 2, 012170 (2012).

[22]   B. J. Jensen, C. T. Owens, K. J. Ramos, J. D. Yeager, R. A. Saavedra, A. J. Iverson, S. N. Luo, K. Fezzaa, and D. E. Hooks, Rev. Sci. Instrum. 84, 013904 (2013).

[23]   B. J. Jensen, K. J. Ramos, A. J. Iverson, J. Bernier, C. A. Carlson, J. D. Yeager, K. Fezzaa, and D. E. Hooks, in 18th Aps-Sccm and 24th Airapt, edited by W. Buttler, M. Furlanetto, and W. Evans (Iop Publishing Ltd., Bristol, 2014), Vol. 500, pp. 1–19.

[24] S. N. Luo, B. J. Jensen, D. E. Hooks, K. Fezzaa, K. J. Ramos, J. D. Yeager, K. Kwiatkowski, and T. Shimada, Rev. Sci. Instrum. 83, 073903 (2012).

[25] O. T. Strand, D. R. Goosman, C. Martinez, T. L. Whitworth, and W. W. Kuhlow, Rev. Sci. Instrum. **77**, 083108 (2006).

[26] Thielicke, William, and René Sonntag (2021). "Particle Image Velocimetry for MATLAB: Accuracy and Enhanced Algorithms in PIVlab." Journal of Open Research Software, vol. 9, Ubiquity Press, Ltd., doi:10.5334/jors.334.

Polymers

30

On the strain-rate dependent design of 3D printed mouthguards

M. Lißner[1,2,3] | **D. Townsend**[1] | **N. Petrinic**[1] |
J. Bergmann[1]

[1]Department of Engineering Science, University of Oxford, Oxford, OX1 3PJ, United Kingdom

[2]DCIM (Dresden Center for Intelligent Materials), TU Dresden, Dresden, 01069, Germany

[3]ILK (Institute of Lightweight Engineering and Polymer Technology, TU Dresden, Dresden, 01307, Germany

Correspondence
Maria Lißner
Email: maria.lissner@tu-dresden.de

The 3D printing technology enables the development of sports protective equipment with enhanced functionalities. Nevertheless, it is crucially important to understand the mechanical performance of 3D printed structures in representative loading environments in which the equipment is used. Therefore, this project aims at contributing to a reliable prediction of the mechanical performance of 3D printed mouthguards using a combined experimental-numerical approach. A calibrated material model based on experimental observations is used to numerically analyse the mechanical performance of 3D printed mouthguards under impact. A numerical setup is established representing the experimental methodology. The investigation showed that the strain-rate dependent calibrated material model is able to represent experimentally obtained results of solid 3D printed mouthguards. Furthermore, mouthguards with different air cell cavities are successfully numerically investigated and assessed.

1 | INTRODUCTION

Although sports and physical activity have a variety of health benefits [1], certain sports can lead to an increased risk of concussions and orofacial injuries [2]. For example, in contact sports such as boxing and rugby or hardball sports such as field hockey, impacts to the orofacial area can affect the health of participants. In addition, it is difficult to completely prevent potentially debilitating head injuries such as sports-related concussions, e.g., ICB (intracranial hemorrhage) and TBI (traumatic brain injury), through the use of protective sports equipment. One of the reasons for this could be that the equipment is not able to proactively inform the athlete about their health management. Another reason could be that the mechanical performance of the material used is not fully understood for the environment in which the sports equipment is utilized or the equipment is not tested and evaluated in representative environments.

New technologies such as additive manufacturing (also referred to as 3D printing) are believed to enable elaborate designs of sports equipment that can accommodate wearable sensor technologies (e.g., GPS, heart rate monitoring systems). These are being considered to monitor the health of athletes during competitions [3, 4]. The sensor location is critical for accurate measurements, whilst at the same time the sports equipment must be able to withstand sport-specific conditions. 3D printing enables precise printing of cavities that could house the wearable technologies, while contributing to resource-efficient manufacturing by minimizing excess material. Although new technologies offer the opportunity to improve existing sports protection devices, a fundamental understanding of the mechanical performance of the 3D printed material system is necessary in order to withstand the impact scenarios while safely accommodating the sensor technologies.

Some investigations exist in which suitable 3D printable materials are tested at different strain-rates covering a wide range of impact speeds and energies observed in the different sports [5]. The experimental observations provide the fundamentals for numerical modelling techniques capable to represent real-world scenarios. In [5] strain-rate dependent experiments using 3D printed coupon specimens were used to calibrate existing material models. While specimens with different air cell geometries were used to successfully verify the material model's ability to predict the experimental findings. This ability is important for the numerical design of 3D printed mouthguards.

Although, further investigation is necessary, an initial attempt is made to establish a combined experimental-numerical framework able to design 3D printed mouthguards with different air cell geometries. This is believed to support the design of sophisticated mouthguards aiming to enhance the level of protection offered against e.g. concussions of athletes.

2 | NUMERICAL METHOD

The considered material is based on the investigation carried out by Saunders et al. [5]. The 3D printable material is a TPC (Thermoplastic copolyester) highly flexible and with excellent energy returns. These characteristics are beneficial for sport protective equipment since they should be designed so that repeatable hits are possible without compromising their structural health as well as the athletes health and comfort.

The material model used in this work for further verification on the structural level, is investigated

and calibrated by Lißner et al. [6]. They initially verified the obtained model parameters using coupon specimens with different air cell geometries.

For the design framework this work considers the newly established experimental setup by Goldberg et al. [7] which enables the testing of mouthguards at much higher impact energies than previous literature has reported. Replicating the entire setup in the numerical workspace allows the accurate design of 3D printed mouthguards before experiments are carried out for verification. The creation of a so-called digital twin enables an accurate design framework by minimising the amounts of experiments and the related material usage. Nevertheless, it is important to highlight that this is only possible with accurate, representable material models.

2.1 | Numerical setup

The numerical analysis is performed using the ABAQUS/Explicit finite element commercial solver. The numerical setup follows the experimental setup reported in [7]. The mouthguard is placed on a fixture resembling the jaw. The hockey ball is placed closely on top of the mouthguard but not in contact. Figure 1 shows the numerical setup based on the experimental developed one. The CAD drawings of each part were used in the simulation to ensure the accurate replication of the experiments in the numerical model.
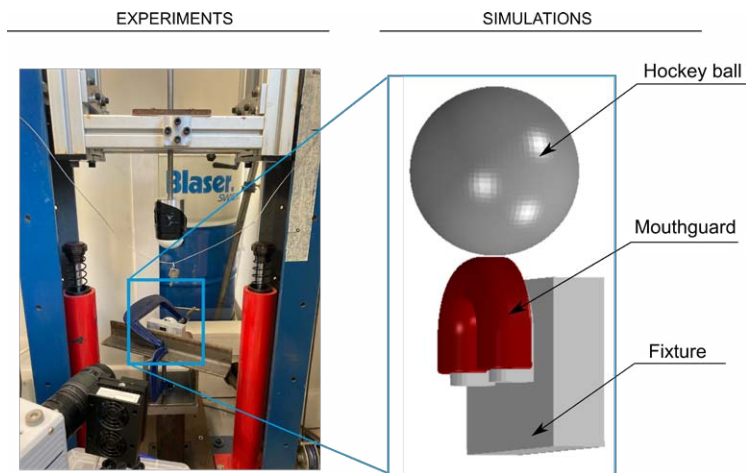
FIGURE 1   Graphical illustration of the numerical setup used to carry out the simulations based on the experimental description.

2.2 | Material and mesh definition

The fixture on which the mouthguard sits is made from aluminium alloy and is modelled as a rigid body due to its high stiffness compared to the one of the mouthguard material.

The hollow hockey ball is modelled following the dimensions of balls used in field hockey which have a diameter of 73 mm and a wall thickness of 10 mm [8]. Eight-node hexahedral elements were

TABLE 1   Material model definitions for the hockey ball [8] and the mouthguard [6] according to studies reported in the literature.

Hockey ball					
Reduced polynomial strain energy potential					
Density [t/mm^3]	C10	C20	D1	D2	
2.0 e-8	3.87	11.46	0	0	
Mouthguard					
Neo Hooke model		Strain hardening power law			
C	D	A	n	M	sratio
2.1636	0	0.4245	0.9964	-0.5	0.9

used together with a mesh size of 2 mm. The constitutive behaviour is described by a hyperelastic material model using a reduced polynomial strain energy potential based on experimental results found in the literature [8]. The parameters are found in Table 1.

The mouthguard follows the same geometrical dimensions as tested in the experiments due to the same CAD model being used for the 3D print. The material used is equivalent to the one reported in [5], while the considered material model definition follows the one studied in [6]. That means, the mouthguard's constitutive behaviour is represented by a hyperelastic and strain rate dependent material model available in ABAQUS/Explicit. Similarly to the work in [6], the mouthguard is modelled using six-node tetrahedral elements with a mesh size of 1 mm. The used parameters for describing the material behaviour are summarised in Table 1.

For the numerical design of mouthguards with air cells of different geometries, preliminary structures are modelled using the same mouthguard dimensions with the same air cell geometries reported in [5]. To start, the air cells are located on the front side of the mouthguard with a wall thickness of 1 mm.

2.3 | Boundary conditions

According to the experiments, the fixture is restricted to move in all directions. The mouthguard sits on the fixture using tie constraints so as to replicate the experiments. Although, the experiments were drop tower tests from which the ball was dropped from a specific hight, the simulation starts the analysis when the ball is close in contact with the mouthguard to reduce computational time. In order to represent the experiments, the following considerations were used: First, the internal cavity of the ball was filled with air using the fluid cavity definition in ABAQUS. Second, the whole model was defined with a gravitational load. Third, a predefined field included the velocity of the hockey ball at this stage, as measured in the experiments, which is equivalent to 4000 mm/s. This corresponds to an impact energy of 20 J, which is the load under investigation in this work. The contact between the hockey ball and the mouthguard is defined with a frictional coefficient of 0.2.

For assessing the accuracy of the whole model strategy, direct experimental outputs in the form of displacement histories are used. The displacement history of the mouthguard follows the same approach as in the experiments – a node on the mouthguard is used to extract this information.
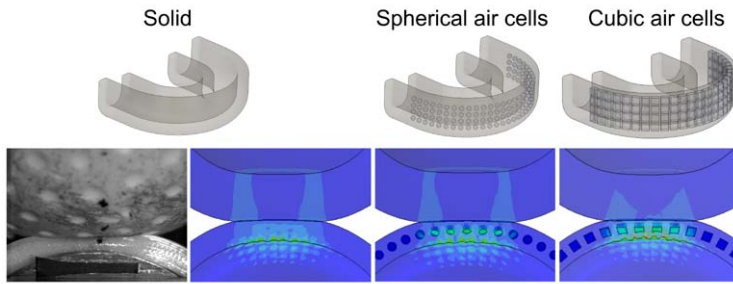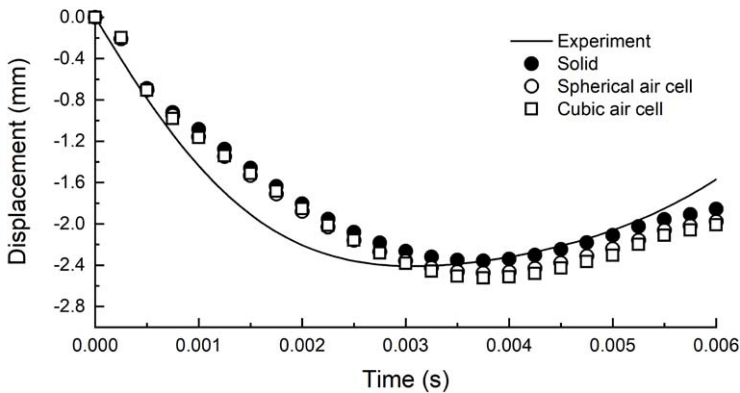
FIGURE 2   Displacement history comparison of mouthguard experiment and mouthguard simulations with solid, spherical and cubical air cell structures.

3 | RESULTS AND DISCUSSION

The results of the simulation of the solid mouthguard experiment using a 3D printed material and the material model calibrated using solid coupon specimens show good agreement with the experimental observations as shown in Figure 2. The difference of the initial slope may be due to the selected Neo Hooke strain energy potential. It is believed further investigation is necessary to identify the most suitable material model for the material to improve the numerical prediction of the experiments. Nevertheless, this investigation provides a good starting point in the numerical design of 3D printed mouthguards with different air cell geometries capable to host wearable devices such as sensors.

Simulations of the mouthguards with air cell cavities demonstrate overall a similar mechanical response when compared to the solid mouthguards. This is already a good indication that air cells can be incorporated without compromising the structural integrity. Nevertheless, it is important to highlight that the air cell location is necessary to be investigated further since in case of frontal hits wearable devices sitting in that locations might be most likely to be broken due to the maximum load occurring there.

4 | CONCLUSIONS

In this work, a combined experimental-numerical design framework is demonstrated aiming at contributing to the development of sport protective equipment such as mouthguards with enhanced functionalities. The following conclusions can be drawn:

- Numerical simulations of droptower solid mouthguard experiments were successfully performed. They result in a good representation of the experimental observations.
- The successful experimental representation in the numerical model verifies the calibrated material model based on strain rate dependent experiments.
- The numerical design analysis of 3D printed mouthguards with different air cell cavities demonstrate the importance of air cell cavity location in which wearable devices can sit. This is to minimise the risk of damaging the devices after non-severe hits and therefore, risking the loss of important data.
- The investigation presented in this work demonstrates a good starting point in the design process of 3D printed mouthguards. Yet, further studies are believed to be necessary to fully comprehend the materials deformation on a structural level as well as to identify the strategic locations of air cells hosting wearable devices.

Acknowledgements

References

[1] Warburton DER, Nicol CW, Bredin SSD. Health benefits of physical activity: The evidence. Canadian Medical Association Journal 2006;174(6):801 – 809.

[2] Knapik JJ, Marshall SW, Lee RB, Darakjy SS, Jones SB, Mitchener TA, et al. Mouthguards in sport activities: History, physical properties and injury prevention efectiveness. Sports Medicine 2007;37(2):117–44.

[3] Daneshvar DH, Baugh CM, Nowinski CJ, McKee AC, Stern RA, Cantu RC. Helmets and Mouth Guards: The Role of Personal Equipment in Preventing Sport-Related Concussions. Clinics in Sports Medicine 2011;30(1):145–163.

[4] Higgins M, Halstead PD, Snyder-Mackler BD L. Measurement of impact acceleration: Mouthpiece accelerometer versus helmet accelerometer. Journal of Atheletic Training 2007;42(1):5–10.

[5] Saunders J, Lißner M, Townsend D, Petrinic N, Bergmann J. Impact behaviour of 3D printed cellular structures for mouthguard applications. Scientific Reports 2022;12(1):4020.

[6] Lißner M, Thomson D, Petrinic N, Bergmann J. Strain Rate Dependent Constitutive Modelling of 3D Printed Polymers. EPJ Web of conferences 2021;250(1):02029.

[7] Goldberg T, Lißner M, Townsend D, Petrinic N, Bergmann J. A Novel Method for the Mechanical Testing of Sports Mouthguards. Applied Sciences 2021;12(1):3449.

[8] Ranga D, Cornish J, Strangwood M. The Role of Materials and Construction on Hockey Ball Performance. Engineering of SPort 7 2008;.

Polymers

31

Dynamic behaviour of additively manufactured PA12 subjected to combined tension – torsion loading

Yuan Xu[1][†] | **Gustavo Quino[2]** | **Karthik Ram Ramakrishnan[2]** | **Antonio Pellegrino[1]**

[1]Department of Engineering Science, University of Oxford, Oxford, OX1 3PJ, UK

[2]Bristol Composites Institute, University of Bristol, Bristol, BS8 1TL, UK

Correspondence
Yuan Xu, Department of Engineering Science, University of Oxford, Oxford, OX1 3PJ, UK
Email: yuan.xu@eng.ox.ac.uk

Present address
[†]Department of Engineering Science, University of Oxford, Oxford, OX1 3PJ, UK

Selective Laser Sintering (SLS) is a type of additive manufacturing (AM) method that possesses many advantages such as high printing resolution and capability of producing complex geometries without additional support. Among the most common materials used in AM, polyamide 12 (PA12) has drawn increasing attention. The existing studies on the mechanical characterisation of SLS PA12 are however limited to single loading scenarios of tension, compression, or shear, despite the engineering fact that structures are commonly subjected to multiaxial loads. In this study, combined tension-torsion Hopkinson bar experiments are conducted to unravel the dynamic multiaxial behaviour of SLS PA12 and its pressure dependency. A novel thin-walled tube geometry is proposed to produce appropriate deformation and failure of the specimen at both tensile and torsional loading conditions. The high-speed deformation of specimens is measured via digital image correlation (DIC). The multiaxial failure of SLS PA12 is presented covering a range of stress states from pure shear, combined shear-tension, and plain strain tension.

INTRODUCTION

Recently, additive manufacturing (AM) technologies have been progressively shifted from visual prototypes to end-use parts that are increasingly employed in aerospace, defense, and automotive sectors where high rate of deformation dominates the behaviour of the structures [1]. A broad set of standard mechanical characterisation tests such as tension, compression, flexion, shear and fracture are conducted on AM samples [2-4]. Yet, very little is known about the dynamic behaviour of AM parts under impact loading conditions, not to mention any complexity of varied loads.

Polyamide 12 (PA12) is by far, due to a combination of strength, rigidity, and chemical resistance, the most widely used polymer in Selective Laser Sintering (SLS), one of the most promising AM techniques [5]. It is therefore imperative to investigate the mechanical properties of SLS manufactured PA12 under conditions of high-rate deformation. The objective of this study is to explore an experimental approach to reveal the dynamic behaviour of additive manufacturing polyamides subjected to varied multiaxial loads at high strain rates, from which the stress locus at high-rate loading can be populated.

MATERIALS AND MANUFACTURING

Additive Manufacturing Method

The EOS Formiga P110 (EOS GmbH Electro Optical Systems, Krailling, Germany) was used for the selected laser sintering (SLS) of the samples from commercial polyamide powder PA2200 supplied by EOS. A 30W CO_2 laser was used for layer-by-layer sintering of the powders. The parameters used for the SLS printing are provided in Table 1.

TABLE 1   Process parameters used for SLS.

Parameters	Values
Particle diameter	D50 = 58 μm
Powder ratio	50/50
Powder bed temperature	170°C
Frame temperature	150°C
Layer thickness	100 μm
Energy density	3.36 J/cm²
Laser beam diameter	250 - 400 μm
Cooling time	> 12 h

The additively manufactured parts are, due to the layer-by-layer production, to some extent direction dependent. The commercial data from the manufacturer show that PA12 products manufactured using SLS technology have, within test standard ISO 527-1/-2, an isotropic tensile modulus of 1700 MPa and isotropic tensile strength of 50 MPa. The strain at break is 20% (manufactured in X- and Y-direction) and 10% (in Z-direction).

Specimen Design

The specimens employed in all the high-rate experiments, including tension, torsion, and combined tension-torsion, are designed as thin-walled cylinders (Fig. 1). The gauge section has wall thickness of 0.5 mm, internal diameter of 16.65 mm, and gauge length of 2 mm. Both ends of the specimen

are shaped with an octagonal slot and external threads to enable the transmission of both torque and axial load throughout the specimen. Fillets with a radius of 2 mm join the gauge section with both ends. Note that the fillet applies to both the inner wall and the outer wall of the specimen, resulting in a dog-bone shape at the axisymmetric cross section. All the samples under investigation were manufactured in the Y-direction.
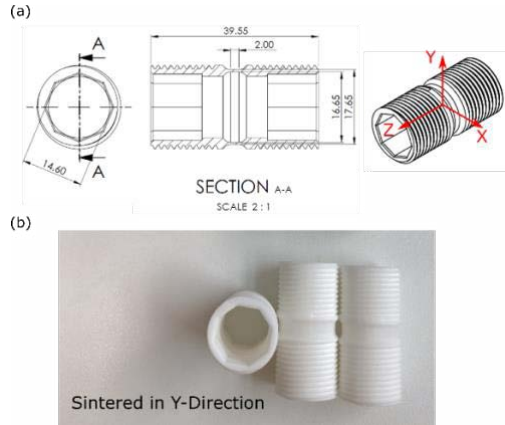

FIGURE 1   Geometry and dimensions of the tubular specimen.

The mechanical symmetry benefited from the axisymmetric dog-bone however brings difficulty in measurement. Coordinate measuring machine WENZEL is utilised to inspect the inner wall of the sample. An inner diameter of approximately 16.50 mm is measured, as shown in Fig. 2. The reduced dimension from the designated value might be attributed to the shrinkage after sintering.
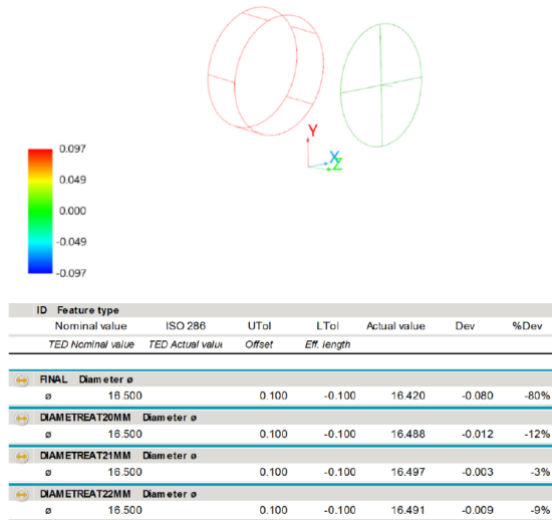

ID	Feature type						
	Nominal value	ISO 286	UTol	LTol	Actual value	Dev	%Dev
	TED Nominal value	TED Actual value	Offset	Eff. length			
	FINAL Diameter ø						
	ø 16.500		0.100	-0.100	16.420	-0.080	-80%
	DIAMETREAT20MM Diameter ø						
	ø 16.500		0.100	-0.100	16.488	-0.012	-12%
	DIAMETREAT21MM Diameter ø						
	ø 16.500		0.100	-0.100	16.497	-0.003	-3%
	DIAMETREAT22MM Diameter ø						
	ø 16.500		0.100	-0.100	16.491	-0.009	-9%

FIGURE 2   Measurement of the inner diameter using a coordinate measuring machine.

EXPERIMENTAL METHOD

Experiments were conducted using a combined tension-torsion Hopkinson bar (TTHB) system that was designed and developed at the Impact and Shock Mechanics Laboratory, University of Oxford.

The TTHB apparatus, as shown schematically in Fig. 3, essentially consists of an incident bar, a transmitted bar, with the specimen sandwiched in between, a rapid release clamp station, a torsion and tension loading station, and a data acquisition system. More information on the working principle of the TTHB, as well as signal interpretation in a typical TTHB experiment, can be found in [6-7]. In this study, two Photron SA-5 cameras were synchronised to record the high-speed deformation of the specimen, from which the high-rate strain variance was calculated via digital image correlation (DIC) techniques. The high-speed cameras were triggered by the incident wave signal recorded by the strain gauge on the incident bar, while the transmitted waves recorded from the transmitted bar were processed to derive the load history on the sample.
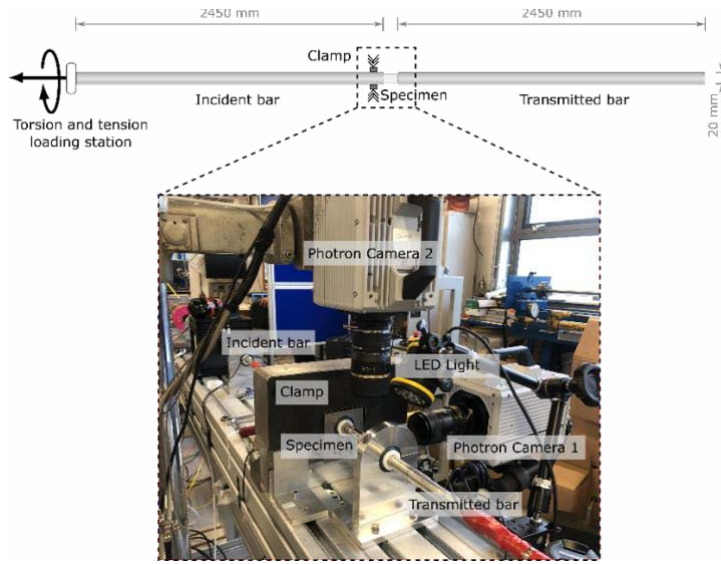

FIGURE 3   Schematic of the split Hopkinson tension-torsion bar (TTHB) and the test setup.

RESULTS AND DISCUSSION

Experiments presented in this study are summarised in Table 2, categorised according to the type of tests by tension, combined tension-torsion, and torsion.

TABLE 2   Summary of TTHB experiments.

Type of test	Ultimate stress (MPa)		Strain Rate (s⁻¹)		Elongation at break (%)	
	Tension	Shear	Tension	Shear	Tension	Shear
Tension	54.9		119		3.4	
Combined tension-torsion	37.6	24.9	136	331	4.2	9.0
	38.0	27.6	287	747	8.3	18.8
Torsion		42.3		3645		91.4
		40.9		2388		129.0

The mechanical response of PA12 subjected to high-rate tensile load is presented in Fig. 4. History of the engineering strain measured from the two cameras demonstrate consistent deformation at different locations along the circumference of the specimen. Constant strain rate loading was

achieved, as shown by the linear slope of the strain history till the fracture of the specimen. The behaviour at the beginning of loading was not successfully measured due to the stress wave interference. The spike at around 50 microseconds might be attributed to some initial slack in the mechanical connection between the specimen and the Hopkinson bars. The ultimate stress is measured 54.9 MPa, slightly higher than the commercial tensile strength 50 MPa tested at quasi-static conditions. The elongation at break 3.4% is significantly lower than the provided strain 20%.
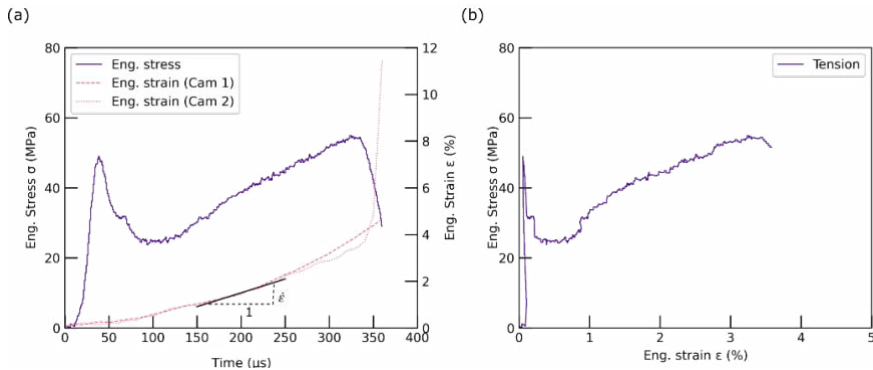

FIGURE 4   Tension loading test: (a) histories of engineering stress and strain; (b) engineering stress-strain curve.

The mechanical response of PA12 subjected to high-rate torsional load is presented in Fig. 5. Again, consistent deformation at different locations along the circumference was observed till the fracture of the specimen at approximately 130 %. Constant strain rate can be measured from the linear slope of the strain history. A classical viscoplastic deformation behaviour is shown from the engineering shear stress-strain curve.
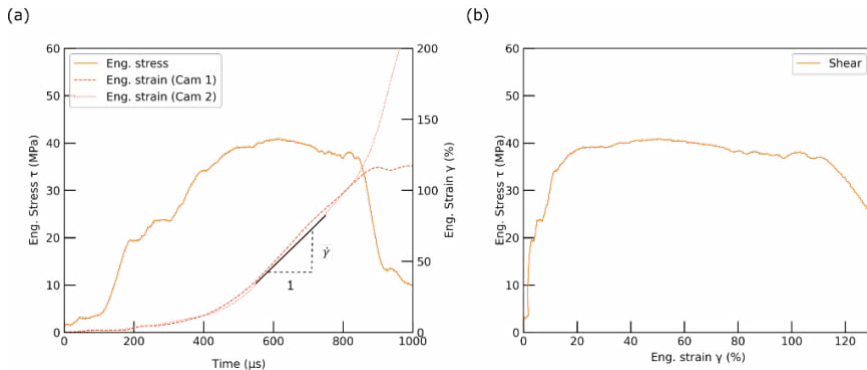

FIGURE 5   Torsion loading test: (a) histories of engineering stress and strain; (b) engineering stress-strain curve.

The mechanical response of PA12 subjected to a combined tension-torsion load at high rate is presented in Fig. 6. Consistency of the deformation was observed in shear (Fig. 6b), whereas the tensile deformation displayed considerate discrepancy (Fig. 6a), plausibly due to the concurrent effect of the combined loading. Furthermore, the ultimate strength in tension and shear was compromised compared to the single loading scenarios (Fig. 4 and Fig. 5). The tensile fracture strain increased slightly while the shear counterpart reduced significantly. The initial behaviour in tension is treated invalid because of the oscillation and thus removed from further interpretation.
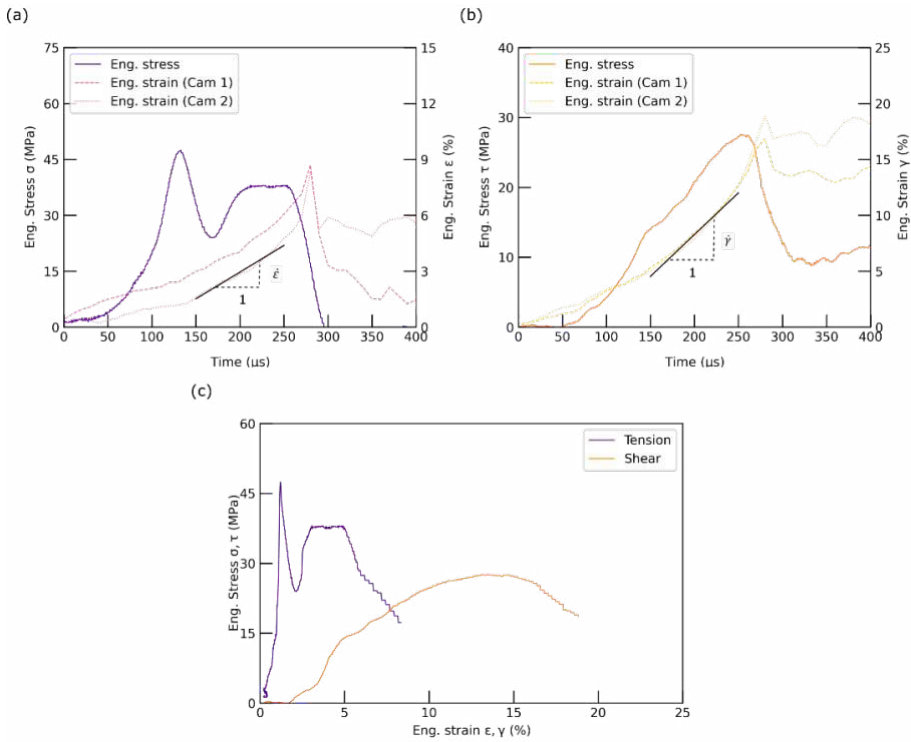
FIGURE 6   Combined tension-torsion test: (a) histories of engineering stress and strain in tension; (b) histories of engineering stress and strain in shear; (c) engineering stress-strain curves in tension and shear.

The ultimate stresses of PA12 measured under varied stress states are subsequently plotted in a normal stress versus shear stress space to depict the multiaxial failure locus at a strain rate on the order of 10^2-10^3 s^{-1} (Fig. 7). Future experiments would cover a wider range of combinations of the tension and torsion loads. This will allow for populating the stress locus of PA12 under arbitrary impact or shock loading, which contributes to optimal design of engineering structures using additively manufactured PA12 parts. The work presented also offers an experimental tool to assess the predicative ability of the existing plasticity models of PA12 or developing new models.
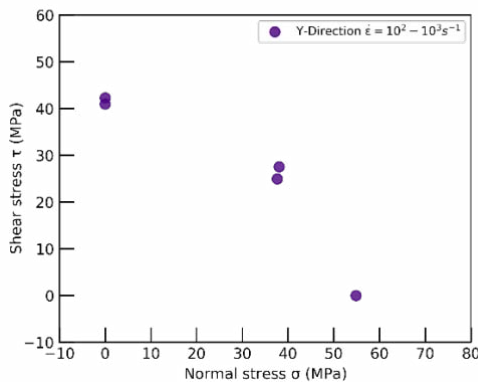

FIGURE 7   Multiaxial failure locus at high rates of deformation.

CONCLUSIONS

The dynamic multiaxial behaviour of PA12, additively manufactured using selective laser sintering method, is assessed using a novel split Hopkinson tension-torsion bar system. The deformation and failure are presented under various loading conditions involving tension, torsion, and combined tension-torsion. A thin-walled tubular geometry was employed to allow for valid deformation of the specimens in different loading cases. A classical viscoplastic deformation behaviour was obtained from the engineering shear stress-strain responses. The ultimate strength measured from multiaxial loading reduced when compared with the single loading behaviour. The multiaxial failure locus was depicted from the direct experimental measurements. The present study focuses on the PA12 sintered in Y-direction. Future work will include the behaviours of PA12 parts produced in Z-direction to evaluate the anisotropy of the properties and the AM techniques.

References

[1] Brighenti R, Cosma MP, Marsavina L, Spagnoli A, Terzano M. Laser-based additively manufactured polymers: a review on processes and mechanical models. J Mater Sci 2021;56:961–98.

[2] Dizon JRC, Espera AH, Chen Q, Advincula RC. Mechanical characterization of 3D-printed polymers. Addit Manuf 2018;20:44–67.

[3] Schneider J, Kumar S. Multiscale characterization and constitutive parameters identification of polyamide (PA12) processed via selective laser sintering. Polym Test 2020;86:106357.

[4] Cano AJ, Salazar A, Rodríguez J. Effect of temperature on the fracture behavior of polyamide 12 and glass-filled polyamide 12 processed by selective laser sintering. Eng Fract Mech 2018;203:66–80.

[5] Crespo M, Gómez-del Río MT, Rodríguez J. Failure of SLS polyamide 12 notched samples at high loading rates. Theor Appl Fract Mech 2017;92:233–9.

[6] Xu Y, Farbaniec L, Siviour C, Eakins D, Pellegrino A. The development of split Hopkinson tension-torsion bar for the understanding of complex stress states at high rate. In: Lamberson L., Mates S., Eliasson V. (eds) Dynamic Behavior of Materials, Volume 1. Conference Proceedings of the Society for Experimental Mechanics Series. Springer, Cham. 2021, p. 89-93.

[7] Zhou J, Xu Y, Aceves M, Farbaniec L, Patsias S, Macdougall D, Reed J, Petrinic N, Eakins DE, Siviour C, Pellegrino A. The mechanical response of commercially pure copper under multiaxial loading at low and high strain rates. Int J Mech Sci 2022;224:107340.

Polymers

32

Dynamic compression behaviour of TPMS structures enabled via Additive Manufacturing

Utzeri M. [1]*,† | **Scapin M.[2]** | **Sasso M.[1]** | **Peroni L.[2]**

[1]DIISM, Università Politecnica delle Marche, Via Brecce Bianche, 60131 Ancona, Italy

[2]Department of Mechanical and Aerospace Engineering, Politecnico di Torino, Corso Duca degli Abruzzi 24, Turin, 10129, Italy

Correspondence
Mattia Utzeri, DIISM, Università Politecnica delle Marche, Via Brecce Bianche, 60131 Ancona, Italy
Email: m.utzeri@pm.univpm.it

Present address
†DIISM, Università Politecnica delle Marche, Via Brecce Bianche, 60131 Ancona, Italy

Cellular materials are receiving great attention for their excellent mechanical properties. They should be applied in energy absorbers or in structural components having optimized mass distribution. In this paper, 3D periodic lattice structures, TPMS (triply periodic minimal surface) were analyzed. Gyroid and Diamond structures were considered with different densities. Two kinds of Additive Manufacturing technologies and materials were investigated: Fused Filament Fabrication (FFF) of nylon reinforced by short carbon fibers, and Masked Stereolithography (MSLA) of photo-reactive liquid resin. Compression tests under quasi-static and dynamic loading conditions were performed and the results compared in terms of specific energy absorption.

1   INTRODUCTION

Lattice structures, as cellular materials, received great attention in the last two decades for their benefits, such as high strength-to-weight ratio, heat exchange, load bearing, excellent energy absorption, and minimizing material requirements [1,2]. In general, a lattice structure is an architecture formed by an array of spatially arranged unit cells with edges and faces. Additive Manufacturing (AM) offers the

---

*Equally contributing authors

potential to realize metamaterials with unprecedented specific energy absorption and crashworthiness capabilities, which could be exploited in different engineering fields thanks to the possibility of fabricating geometries in almost all types of shapes [3-5].

Among these architected materials, Triply Periodic Minimal Surface (TPMS) structures exhibit structural and functional properties that could meet requirements for cutting-edge applications in the aerospace, automotive and biomedical sectors [6,7]. Several materials can be employed in the manufacture of these structures, including metals, polymers, ceramics, composites, etc.

In this work, the energy absorption efficiency was evaluated for 3D periodic lattice structures. In order to investigate how the structure density relates to mechanical properties, four relative densities were considered. This study also wants to highlight how the cellular material shape and the manufacturing technology affect the mechanical properties of the entire structure [8]. Thus, the samples were printed with two kinds of Additive Manufacturing technologies and materials. The first technology is the Fused Filament Fabrication (FFF), which can print high-strength thermoplastic materials, in this study is Carbon-PA. However, the FFF deposition strategy is well-known for the presence of defect that plays a big role in the sample quality. The counterpart of FFF is the MSLA technology which is based on thermoset materials. The 3D-printed parts with this technology have lower strength than the ones printed by FFF. However, the presence of defects is quite lower inside those parts. All these peculiarities based on the AM technology gave different compressive properties to the 3D printed TPMS structures. The experimental tests were performed in compression at different strain-rate, from quasi-static to dynamic loading conditions. In the end, all results were compared to each other.

2   SPECIMENS PREPARATION

Two Additive Manufacturing technologies were used to prepare the samples. Fused Filament Fabrication (FFF) technique was adopted for samples made of PA reinforced by short carbon fibers; Masked Stereolithography (MSLA) technique was adopted for samples made of photo-reactive liquid resin. The raw resin is a commercial high-quality resin named Premium Tough, Liqcreate product. The resin has crystal-clear transparency and a peculiar mechanical property as high toughness and large strain to failure.
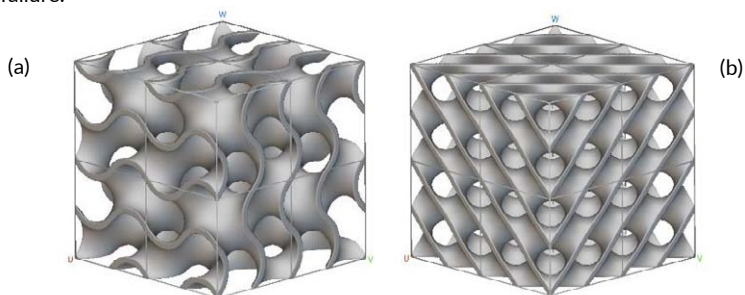

FIGURE 1   Gyroid (a) and Diamond (b) scaffolds of unit cells.

The TPMS structures were designed by means of Topology software. The nTopology software can generate a wide range of architectured and cellular materials. Among them, the Gyroid and Diamond structures were chosen. The generated shapes were exported as STL format files and then imported to the slicing softwares. The process parameters were defined inside the slicing software based on extensively testing in the laboratory; they ensure the best choice in strength, printability, and size accurancy. No 3D printed supports need be provided.

In order to measure the effective structures mechanical properties, the cubic volume of 30 mm side was filled with 8 unit cells [9]. This arrangement 2x2x2 guarantees a great compromise in terms of

maximum size can be tested and boundary condition effects on the unit cell behaviour. The scaffolds of unit cells are reported in Figure 1. The wall thickness was changed in order to manage the density: for each structure, four different wall thicknesses were considered achieving relative density equal to 15%, 20%, 25% and 30%.
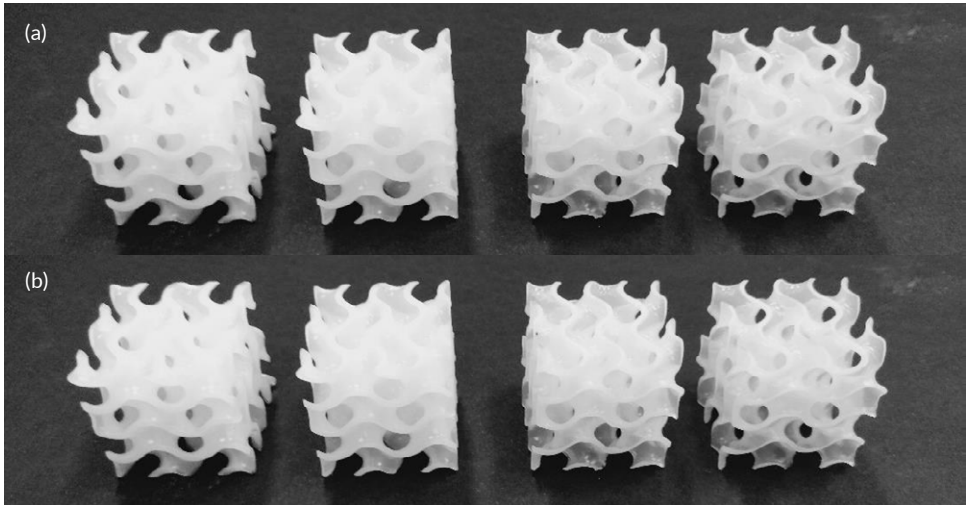

FIGURE 2 3D printed Gyroid (a) and Diamond (b) with different relative densities; The specimen relative density runs to 30% (left sample) to 15% (right sample).
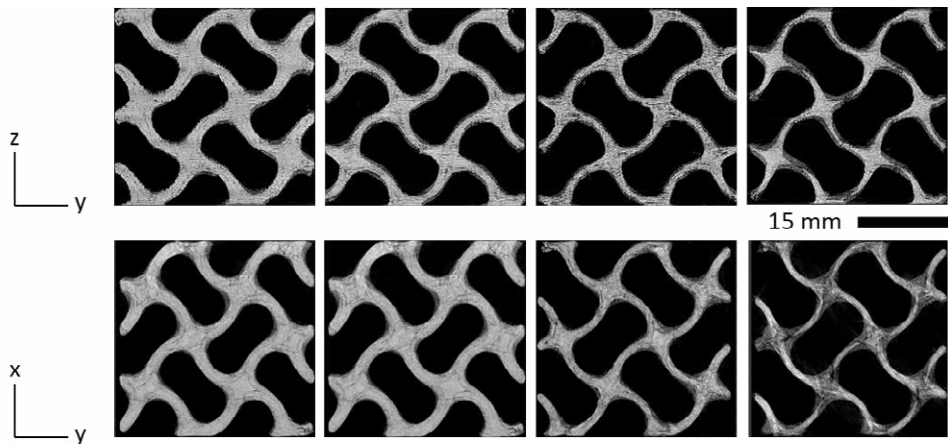

FIGURE 3   X-ray CT images (resolution of 75 μm/pixel) for carbon PA samples: x-y is the printing plane, z is the growth direction; The specimen relative density runs to 30% (left sample) to 15% (right sample).

Once the printing is complete, the structures printed by MSLA undergo one post-treatement to obtain the ultimate mechanical properties. The post-treatment consists of a post-curing for 0.5 hours. Then, the printed parts were put in oven at temperature of 60°C and flashed by ultraviolet light source with wavelength 395-405 nm. The multiple parts location inside the oven influences the postcuring grade of the component and thus the mechanical properties. So, to avoid that phenomenon all printed part was post-cured alone in the UV oven for the same amount of time. This post-treatment provides an high curing grade of the components and thus, ensures a quite stable mechanical properties; succes-sive exposition can be considered negligible. The 3D printed sample manufactured by MSLA are

showed on Figure 2. At the end, X-ray CT scans were conducted on printed samples to investigate the presence and distribution of voids (see Figure 3).

3   EXPERIMENTAL TESTS AND RESULTS

Quasi-static and medium strain-rate compression tests were performed by an electrodynamic testing machine (Electroforce3500 - TA Instruments), available at DYNLab laboratory at Politecnico di Torino. The tests were conducted at a nominal strain-rate of 10^{-3} and 3×10^1 s^{-1}. The medium strain-rate tests were recorded with a high speed camera (Photron AX50). Thanks to the high epoxy resin toughness, the TPMS structures can be compressed without reaching explosive failure [10]. Both TPMS structures show the common linear stage after the yielding point. This post-yielding behaviour can be similar to a plateau when the relative density is low. When the relative density increases, the post-yielding slope becomes more and more relevant. Both TPMS structures show a specific strain where a first failure occurs during the plastic region. After these points, the stresses drop down without reaching zero and the densification phase begins. This kind of stress-strain curve is preferable when high specific absorption energy (SEA) is required on industrial applications.
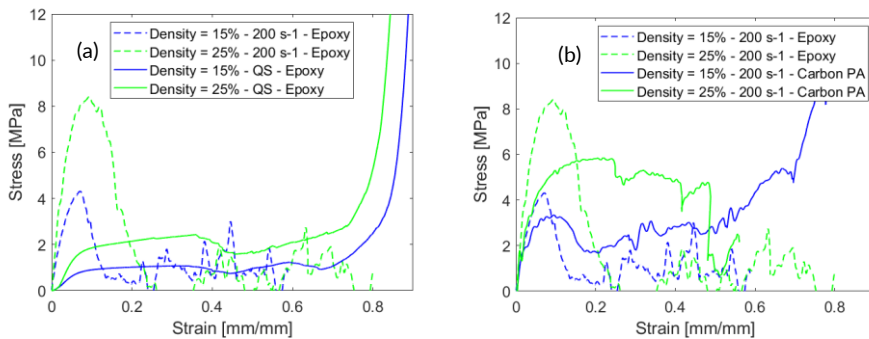

FIGURE 4   Experimental results: (a) Quasi-static and Dynamic compression properties of the structures printed by MSLA technology; (b) Dynamic compression properties of the structures printed by MSLA and FFF technology

Dynamic tests were performed by a Split Hopkinson bar, available at the lab of Polytechnic University of Marche, which is a direct tension-compression Hopkinson bar made of three aligned bars, named pre-stresses (3m), input (7.5m) and output bar (4m). Each test was recorded by a Photron® SA4 at 100 kfps. The experimental results showed a dependence of the engineering stress-strain curves on the relative density. In addition, both materials are very sensitive to strain-rate variations, significantly increasing its resistance under dynamic conditions. As shown in Figure 4.a, the yielding point of the Gyroid structure with 15% and 25% relative density reaches about four times the yielding point under quasi-static loading. However, the strain rate sensibility leads to brittle behaviour of the epoxy resin thus the TPMS structures are no longer able to withstand higher deformations. However, the Carbon-PA does not become brittle as the epoxy resin under dynamic loading, as shown in Figure 4.b. The Gyroid structures made by Carbon-PA are able to withstand high deformation and absorb energy during the impact. Indeed, they show a relevant plastic phase after the yielding point. Moreover, the TPMS structure made by MSLA shows a relevant fragmentation during the compression phase as shown by Figure 5 where the deformed Gyroid structures is visualized before the loading and at strain 10%.
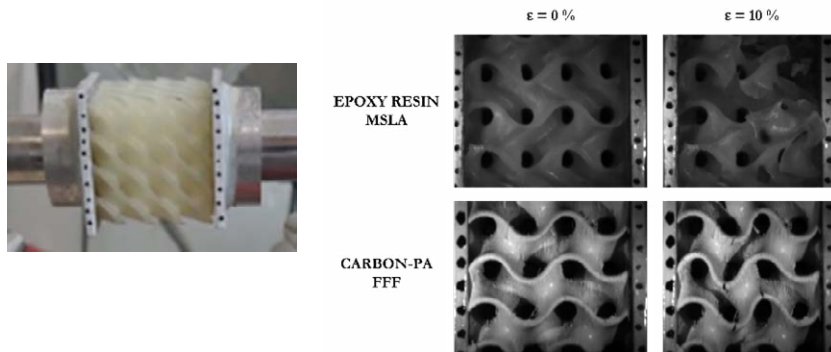
FIGURE 5   Image of the specimen mounted on the Hopkinson bar setup; Deformed shape of 25% relative density Gyroid at strain about 10%, made by MSLA

4   REFERENCES

[1] Dong, Z. & Zhao, X. (2021). Application of TPMS structure in bone regeneration, Engineered Regeneration, Volume 2, doi: 10.1016/j.engreg.2021.09.004.

[2] Sharma, D. & Hiremath, S.S. (2021). Additively manufactured mechanical metamaterials based on triply periodic minimal surfaces: Performance, challenges, and application, Mechanics of Advanced Materials and Structures, doi: 10.1080/15376494.2021.1948151

[3] Wang, H., Tan, D., Liu, Z., Yin, H. & Wen, G. (2022). On crashworthiness of novel porous structure based on composite TPMS structures, Engineering Structures, Volume 252, 113640, doi: 10.1016/j.engstruct.2021.113640.

[4] Yin, H., Tan, D., Wen, G., Tian, W. & Wu, Q. (2021). Crashworthiness analysis and optimization design of TPMS-filled structure, International Journal of Crashworthiness, doi: 10.1080/13588265.2021.1959171

[5] Sengsri, P., Fu, H. & Kaewunruen, S. (2022). Mechanical Properties and Energy-Absorption Capability of a 3D-Printed TPMS Sandwich Lattice Model for Meta-Functional Composite Bridge Bearing Applications. Journal of Composites Science; 6(3):71, doi: 10.3390/jcs6030071

[6] Nazir, A., Abate, K.M., Kumar, A. & Jeng, J.Y. (2019). A state-of-the-art review on types, design, optimization, and additive manufacturing of cellular structures, Int. J. Adv. Manuf. Technol. 104 3489–3510, doi: 10.1007/s00170-019-04085-3.

[7] Nagesha, B.K., Dhinakaran, V., Varsha Shree, M., Manoj Kumar, K.P., Chalawadi, D. & Sathish, T. (2020). Review on characterization and impacts of the lattice structure in additive manufacturing, Mater. Today Proc. 21, doi: 10.1016/j.matpr.2019.08.158

[8] Novak, N., Al-Ketan, O., Krstulović-Opara, L., Rowshan, R., Abu Al-Rub, R.K., Vesenjak, M. & Ren, Z. (2021). Quasi-static and dynamic compressive behaviour of sheet TPMS cellular structures, Composite Structures, Volume 266, 113801, doi:10.1016/j.compstruct.2021.113801.

[9] Santiago, R., Almahri, S., Lee, D.W., Alabdouli, H., Banabila, O., Ramos, O., Alteneiji, M., Guan, Z. & Alves, A. (2018). Mechanical characterization and numerical modeling of TPMS lattice structures subjected to impact loading, doi: 10.1051/epjconf/202125002005

[10] Mancini, E., Utzeri, M., Farotti, E., & Sasso, M. (2021). Model Calibration of 3D Printed Lattice Structures. Paper presented at ESAFORM 2021. 24th International Conference on Material Forming, Liège, Belgique. doi: 10.25518/esaform21.4154

33

Experimental characterization of 3D printed nylon-carbon at different strain-rates

Peroni L.[*] | **Scapin M.** | **Ciardiello R.** | **Tridello A.** | **Morena A.**[†]

Department of Mechanical and Aerospace Engineering, Politecnico di Torino, Corso Duca degli Abruzzi 24, Turin, 10129, Italy

Correspondence

Peroni Lorenzo, Department of Mechanical and Aerospace Engineering, Politecnico di Torino, Corso Duca degli Abruzzi 24, Turin, 10129, Italy
Email: lorenzo.peroni@polito.it

Present address

†Department of Mechanical and Aerospace Engineering, Politecnico di Torino, Corso Duca degli Abruzzi 24, Turin, 10129, Italy

Three-dimensional printing technology using fused deposition modeling processes is becoming more and more widespread thanks to the improvements in the mechanical properties of materials with the addition of short fibers into the polymeric filaments. Nowadays, it is possible to create components with mechanical properties such that they can be used under high loads. The prediction of the mechanical response of printed components is crucial in the design phase and requires the mechanical characterization of the material under various loading conditions depending on the applications. In the present work, the strain-rate sensitivity of nylon reinforced with short Carbon fibers has been investigated by tensile tests on fulfilled dog-bone specimens.

1 INTRODUCTION

Three-dimensional printing technology using fused deposition modeling (FDM) processes is continuously developing and evolving mainly thanks to the increased availability of materials and the improvements in their mechanical properties. FDM is one of the most used additive manufacturing

---

[*]Equally contributing authors

techniques for printing polymers. The current technologies are ripe for the transition from purely aesthetic and/or functional prototypes to structural components suitable to support high loads.

In additive manufacturing, polymers are used in a variety of forms, and in recent years particular attention has been dedicated to the development of filled polymers [1] with the aim to improves the characteristic and performances, depending on fiber matrix interactions and void formation. Commonly used fillers are carbon fibers and nanotubes, nanoparticles, and various synthetic fibers. In addition to the material itself and to the presence of reinforcing phase, the final strength of the printed parts is influenced by numerous printing parameters and their combinations, such as the morphology of the internal structure, the thickness of the walls, the height of the layers, the infill orientation, the printing speed, the temperature and diameter of the nozzle, the base plate temperature, and the build orientation. In particular, the last one is strictly correlated to the quality of the bonding between adjacent layers which can be responsible for a strong degradation of the mechanical strength especially in the direction of growth.

Often, the validation phase is performed directly with field tests on printed components. On the other hand, numerical FE-based tool could be adopted, but this make mandatory the mechanical characterization of the material and the modelling of the behavior with appropriate material models.

2   SPECIMEN PREPARATION AND EXPERIMENTAL TESTS

This study investigated the mechanical strength of nylon-carbon varying the strain-rate. The presence of the nylon matrix reinforced by short fibers (approximately 20% by weight) makes the material extremely attractive because of the resultant combination of properties: noticeable tensile strength and stiffness, high levels of impact strength, good thermal stability, and high levels of resistance to chemical agents. A summary of the datasheet properties as declared by the manufacturer is reported in Table 1. In the following, x and y are the two directions on the printing plane, and z is the growth direction, as schematically reported in Figure 1.

In general, although the filament is initially isotropic and homogeneous, it can be assumed that the printed components with FDM show an anisotropic behavior. In bulk printed components, when the angle between the stacked layers (Figure 1) is changed from one layer to the next one, the properties in the printing plane can be considered as isotropic while weaker properties results to be in the growth direction, as reported in Table 1. In addition, when polymeric materials are used, it is expected that the mechanical behavior could immediately be strongly nonlinear and then assume the connotation of plastic (or rather, irreversible) behavior [2]. Plasticity is not related to the motion of the dislocations, but to the evolution of the arrangement of the polymeric chains. The last, but not least, aspect to be considered is that with this printing technique, it is not possible to eliminate intrinsic porosity due to the presence of voids between adjacent layers. The presence of voids depends on several parameters and in turn strongly affects the mechanical strength of the printed components. This also happens in fully filled portions, in which the component is obtained by stratifying the layers: the deposition of the (molten) filament produces a texture like that which is typical for a fabric, and there is an apparent density reduction of the material. This is one of the reasons the printed structures exhibit less strength than expected, even at 100% infill. Because the printed structure is intrinsically porous, the measured mechanical properties (on a 100% infill specimen) are evaluated on the measured cross-section, hence they are averaged. The area reduction is globally perceived as a stiffness reduction, and consequently, there is a perceived reduction in elastic properties, as well as an under-estimation of mechanical strength. This highlights the need to perform mechanical tests on printed specimens in several loading conditions, depending on the applications: the properties could be different from those of the filament [3].
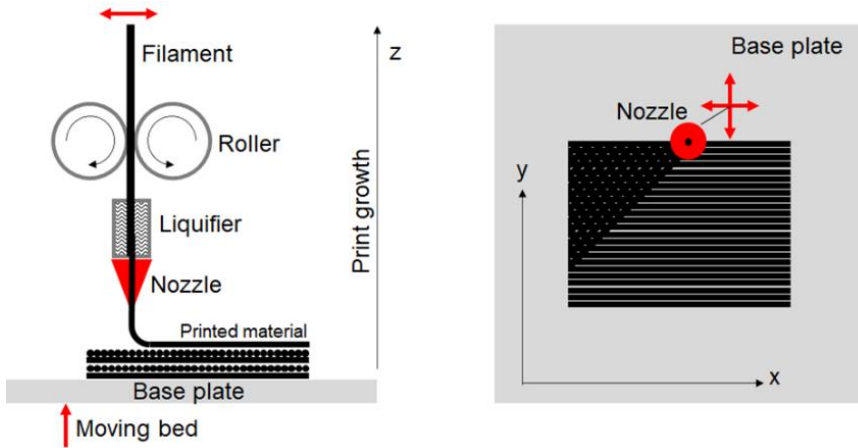
FIGURE 1   FDM printing scheme: The filament is extruded through the heated nozzle, which moves in the *x-y* plane, while the hot base plate moves in the *z* direction.

TABLE 1   Summary of the datasheet properties for Carbon-Nylon, as declared by the manufacturer, FiberForce.

Property (Units)	Direction	
	xz	*xy*
Tensile strength (MPa)	12.64	66.3
Elastic modulus (MPa)	1513	2758
Elongation at break (%)	2.0	6.7
Energy at break (J)	0.64	12.2
Density (g/cm³)	1.00	
Melting point (°C)	180	

Note: Tensile tests performed on specimens printed on Ultimaker 2+ with Olsson Ruby nozzle, nozzle temperature of 260 °C, head bed temperature of 70 °C, print speed of 40 mm/s, infill per-centage of 100%, and infill orientation of 45°.

In the present work, the mechanical characterization was performed by performing tensile tests on flat dog bone specimens (gage section of 5 × 5 mm and gage length of 10 mm) at different strain-rate covering the range between 10^{-2} and 10^{2} s^{-1}. The specimens were printed on an Ultimaker S5 with a print speed of 40 mm/s, an infill percentage of 100%, and a raster angle of ±45°.

The influence of the build orientation was investigated by printing specimens at different orientation between the longitudinal axis of the specimens and the printing growth direction, as reported in Figure 2. Angles of 0, 15, 30, 45, 60, 75 and 90° were considered. This allowed also the investigation of anisotropy of the resultant behavior. These tests were chosen to calibrate an anisotropic strain-rate dependent elasto-plastic material model based on the Hill48 yield criteria. The experimental

results could also be used to model the failure of the material which is strictly related to the load orientation with respect to the printing growth direction.
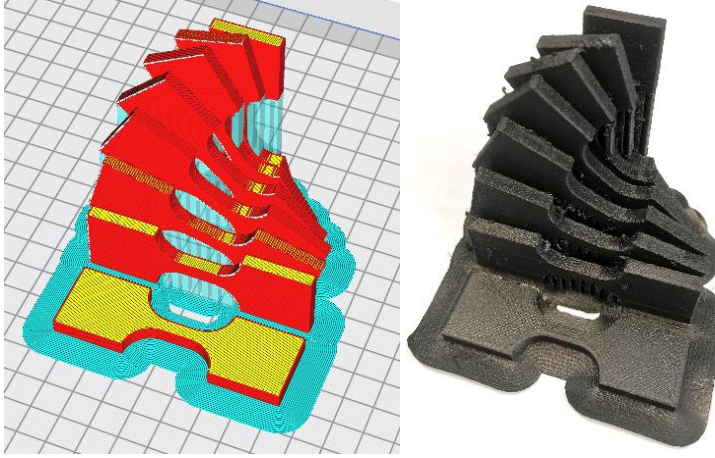

FIGURE 2   Tensile specimens printed with an Ultimaker S5 at 100% infill, at various orientations between the longitudinal axis of the specimens and the printing direction.

FIGURE 3   Setup used for the tensile tests at 10^2 s^{-1} of strain-rate.

The quasi-static and low strain-rate tests were conducted on a standard electro-mechanical testing machine, Zwick Z05, at a nominal strain-rate of 10^{-2} and 1 s^{-1}. Medium-high strain-rate tests were performed on a fast electro-mechanical testing machine (TA Instrument, see Figure 3) at a nominal strain-rate of 10^2 s-1. Each test was video recorded to directly evaluate the specimen deformation by digital image analysis.

As expected for polymers, the investigated material is sensitive to the strain-rate: the strength increases with strain-rate, whereas the ductility decreases with it. By increasing the strain-rates the molecular movement of the polymer chains are limited and consequently the overall material behavior is more rigid and brittle. The material strength appears to be critically influenced by the build

orientation. When the layer is built parallel to the load direction there is a higher volume fraction of filaments in line with the load, contributing to the largest improvement. As the layers begin to deviate from the primary load direction, delamination occurs at the weaker interfaces.

3 REFERENCES

[1] Calignano F., Lorusso M., Roppolo I., Minetola P., Investigation of the Mechanical Properties of a Carbon Fibre-Reinforced Nylon Filament for 3D Printing, Machines, 8(3), 52, https://doi.org/10.3390/machines8030052 (2020)

[2] Cicala, G.; Giordano, D.; Tosto, C.; Filippone, G.; Recca, A.; Blanco, I., Polylactide (PLA) Filaments a Biobased Solution for Additive Manufacturing: Correlating Rheology and Thermomechanical Properties with Printing Quality. Materials, 11, 1191 https://doi.org/10.3390/ma11071191 (2018)

[3] Shanmugam V., Johnson Rajendran D. J., Babu K., Rajendran S., Veerasimman A., Marimuthu U., Singh S., Das O., Neisiany R.E., Hedenqvist M.S., Berto F., Ramakrishna S., The mechanical testing and performance analysis of polymer-fibre composites prepared through the additive manufacturing. Polymer Testing 93 – 106925 https://doi.org/10.1016/j.polymertesting.2020.106925 (2021)

34

Influence of curing conditions on the dynamic behavior of SLA-printed specimens

Mohammad Reza Khosravani[1*] | **Tamara Reinicke[1]**

[1]Department of Mechanical Engineering, Chair of Product Development, University of Siegen, 57068 Siegen, Germany

Correspondence
Mohammad Reza Khosravani, Department of Mechanical Engineering, Chair of Product Development, University of Siegen, 57068 Siegen, Germany
Email:
mohammadreza.khosravani@uni-siegen.de

After 3D printing of an SLA part, the polymerization reaction may not yet be completed and printed parts cannot not perform as expected. In this context, exposing the printed parts to heat and light as a post-processing is a necessity which improves the mechanical behavior of the final parts. In the present study, we have investigated effects of curing conditions on the dynamic behavior of 3D-printed components produced by Stereolithography (SLA) technique. To this aim, Formlabs' resin has been used to print cylindrical specimens. Later, two different curing conditions were considered and applied as post-processing for SLA-printed specimens. We have conducted a series of test via split Hopkinson pressure bar to determine behavior of parts under a high loading regime. The obtained results indicate effect of curing conditions on the mechanical behavior of SLA-printed parts.

Abbreviations: AM, additive manufacturing; SLA, stereolithography; SHPB, split Hopkinson pressure bar.

1 | INTRODUCTION

Additive manufacturing (AM) has been developing rapidly and has attracted considerable attention in recent decades. AM, also known as three-dimensional (3D) printing has several advantages compared with traditional technologies. For instance, 3D printing cannot only reduce procedures and shorten the processing cycle, but can also form any shape structure without molds [1]. AM was introduced as a rapid prototyping method that can be used for different materials. As the name indicates, AM refers to adding raw materials during manufacturing, which includes various assembly and rapid prototyping processes. According to the American Society for Testing Materials (ASTM) and the International Organization for Standardization (ISO), AM is defined as the "process of joining materials to make objects from 3D model data, usually layer upon layer" [2]. Currently, 3D printing techniques are being significantly used in different applications, such as aerospace [3], electronics [4], automotive [5], dentistry [6], food industry [7], and construction [8]. In different 3D printing processes, various materials can be used owing to their wide range of chemical and mechanical properties. For instance, polylactic acid (PLA), nylon, acrylonitrile butadiene styrene (ABS), polycarbonate, and polyvinyl alcohol (PVA) have been utilized in different 3D printing processes [9–14]. This multimaterial printing can be considered as a basic pillar for the development of future technologies. The industrial applications of 3D printing have proved that the list of materials employed in this technique increases continually.

Although AM was introduced for fabrication of prototypes, this technology has been recently used for production of functional end-use products. Consequently, performance and the mechanical strength of 3D-printed parts have become of significant importance. In this context, different investigations have been conducted to study mechanical behavior, fracture, and structural integrity of additively manufactured parts [15–17]. For instance, in [18] fracture behavior of 3D-printed ABS parts is investigated. To this aim, single edge notch bending specimens with different sizes and various relative orientations are examined. Experimental tests demonstrated that the 3D-printed parts exhibit considerable anisotropy in their fracture behavior, which would not occur in the monolithic counterpart. Due to microlayering and macrolayering, considerable quasi-brittleness is also induced in the fracture behavior, and the degree of quasi-brittleness is also anisotropic. Recently, we investigated fracture of 3D-printed continuous glass fiber reinforced composites [19]. In this respect, nylon and glass fibers were used as matrix and reinforcing materials, respectively. We used fused filament fabrication process to print semi-circular bending composite specimens. Later, all specimens were subjected to three-point bending tests and their mechanical behavior was determined. Based on the experimental results, we have calculated fracture toughness in the composite specimens. The obtained results confirmed that the lowest fracture toughness belongs to unreinforced specimens. The experimental findings confirmed the crucial role of fiber reinforcement in structural integrity of 3D-printed composites.

Stereolithography (SLA) is one of the earliest additive manufacturing processes to be which is based on printing using special photocurable resin [20]. During the printing process, the precursor material is stored in liquid phase and heated in a tank located in the printing area laying above the set of lenses and mirrors. The resin is crosslinked under ultraviolet (UV) light exposure, called photopolymerization. SLA is now shifting from rapid prototyping to rapid manufacturing, but is facing challenges in parts performance and printing speed, among others. Therefore, several studies are performed to shed the lights on different aspects in this field [21–23]. For instance, The effects of

build orientation on the tensile strength of SLA-manufactured parts were investigated in [24]. The researchers used statistical design of experiments approach to determine impact of specific build orientation parameters on the mechanical strength of SLA-fabricated components. Later, in [25] an Al-based quasicrystalline alloys were used to develop a new UV-curable resin reinforced by metal particles. 3D-printed composite specimens showed improved mechanical properties (e.g., hardness) compared to the unfilled resin. Li et al. [26], synthesized core-shell nanoparticles for SLA printing, which showed improved mechanical properties in static tensile behavior and were assessed as similar to ABS material. At the same time, uniaxial tensile tests were conducted on standard SLA-printed parts to obtain their elastic modulus and ultimate tensile strength in order to develop the constitutive material model.

In the present study, we investigate effects of different curing conditions on the dynamic behavior of SLA-printed parts. To this aim, cylindrical specimens printed and two different curing conditions were considered and applied as post-processing. Later, all specimens were subjected to the dynamic loading using split Hopkinson pressure bar (SHPB). In order to ease the comprehension of the readers, the structure of this article is briefly described here. In Section 2, specimens preparation, experimental tests, and obtained results are presented and discussed. Finally, a conclusion has been furnished in Section 3.

2 | EXPERIMENTAL PROCEDURE

As the first step of specimen preparation, all the samples are first drawn in a CAD platform and then saved as '.stl' format. The specimens were printed using Formlabs Form 2 SLA printer. The slicing software was set to the highest printing quality, thus 0.025 mm layer height was selected. The specimens dimensions were 20 mm in height and in diameter. After printing, the supports structures were removed and the specimens were cleaned using an isopropanol bath. Here, beside UV exposure, two different conditions are considered for curing process: (a) exposure to air, and (b) submerging in distilled water. Both processes were performed at 20 °C, and 30 min for each curing condition.

After curing process, specimens were subjected to the dynamic test via SHPB. Fig. 1 shows a 3D-printed specimens under test conditions. In each group, five specimens were examined.

FIGURE 1   A cylindrical 3D-printed specimen between incident and transmission bar.

The utilized Hopkinson bar has aluminum incident and transmission bars with length of 1800 mm and a diameter of 20 mm. A steel striker with a diameter of 20 mm and a length of 100 mm was used. The striker is accelerated by an air gun, impacts the incident bar and generates a compressive stress pulse traveling in the incident bar. To measure the incoming, reflected and transmitted pulses strain gauges are placed in the middle of the incident and transmission bars. All the data are acquired by the HBM GEN7t system with the maximum sampling rate of one mega samples per second. The impact velocity of the striker determines the amplitude of the incident wave. The strain rate, strain and stress are calculated from the recorded strain history using the following equations:

$$\frac{\partial \varepsilon}{\partial t}(t) = -\frac{2c_0 \, \varepsilon_R(t)}{l_s} \tag{1}$$

$$\varepsilon(t) = -\frac{2c_0}{l_s} \int_0^t \varepsilon_R(t)\mathrm{d}t \tag{2}$$

$$\sigma(t) = \frac{E \, A_b}{A_s} \, \varepsilon_T(t) \tag{3}$$

where σ and ρ denote the stress and strain as function of time, E is the elastic modulus of the bars; and A_b and A_s are the cross-sectional area of the bar and the specimen, respectively. The indices R and T refer to the reflected and transmitted waves, respectively. Finally, l_s and c_0 denote the specimen length and wave speed in the bar, respectively. In experimental test via Hopkinson bar, there are two fundamental assumptions that must be verified to ensure the validity of the experimental results. The first assumption is that the stress wave propagates in both bars without dispersion [27]. This assumption is necessary so that the one-dimensional wave propagation theory can be applied to describe the transmission of the stress wave in the bars. The second assumption presumes an instantaneous equilibrium of forces in the loaded specimen and states that the reaction force on the specimen-transmission bar interface is the same as the incoming force on the specimen-incident bar interface. This assumption corresponds to an axially uniform state of deformation within the specimen [28]. On this basis, which is often described as the stress equilibrium condition, the relations (1)-(3) were deduced. Here, experiments were performed at strain rate of 30 s^{-1}. A long striker provides a long loading impulse, which makes it easier to realize the dynamic stress equilibrium. Fig. 2 shows distribution of wave signals in incident and transmission bars and strain-rate over time.
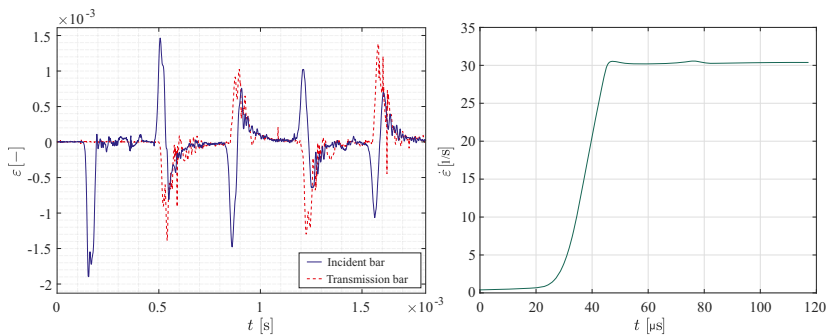

FIGURE 2   Incident and transmitted waves in the test via SHPB, and strain-rate over time.

Based on the obtained results from test via SHPB, stress-strain relationship is determined. Fig. 3 illustrates stress-strain curves of specimens cured under different conditions and strain over time. The tests performed with the use of the SHPB confirmed that the curing conditions influence the mechanical behavior of 3D-printed SLA parts. This effect is clearly visible in stress-strain curves of specimens cured at different conditions.
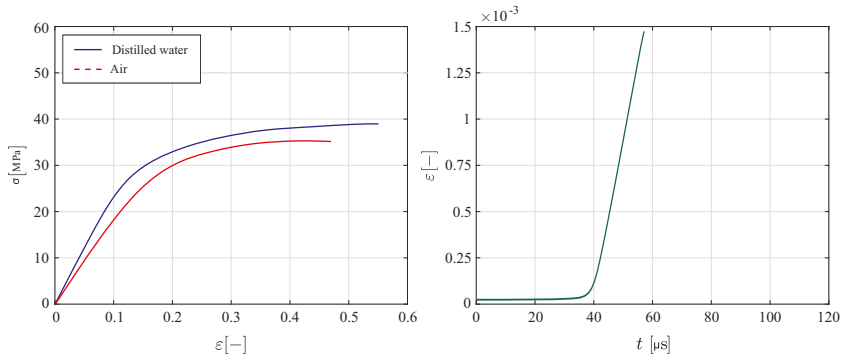

FIGURE 3   Stress-strain curves of examined specimens and strain over time.

The experimental results indicate that the highest stress value belongs to the specimen which experienced submerging in distilled water for 30 min. In this context, the curing process carried out on 3D-printed SLA parts has the main role. The presented results can be used in the design of structures and next computational modeling. The investigations on the dynamic behavior of 3D-printed SLA parts would be beneficial in the impact constructions and energy absorption applications.

3 | CONCLUSION

In contrast to traditional manufacturing processes, 3D printing is able to create more complex geometries and multicompositions. SLA as one of the 3D printing techniques is a liquid resin photo-curing process wherein liquid resin is placed in a reservoir, and a positionally programmed laser is scanned over the resin surface to initiate photopolymerization. After 3D printing process of an SLA part, the polymerization reaction may not yet be completed and printed components have not reached to their final material properties. Therefore, the 3D-printed parts cannot not perform as expected. In this context, exposing the printed parts to heat and light as a post-processing is a necessity which improves the mechanical behavior of the final parts. In the present study, we investigated effects of the curing conditions on the dynamic behavior of 3D-printed SLA parts. To this aim, cylindrical specimens were printed and beside UV exposure the samples experienced different curing processes: (a) exposure to air, (b) submerging in distilled water, both at 20 °C for 30 min. Later, all specimens were subjected to the dynamic load using SHPB. The examined specimens showed differences in the mechanical response in accordance with the curing conditions. The obtained results indicate that strength of specimens increased if test coupons experienced submerging in distilled water for 30 min. In fact, this group of specimen achieved the highest stress value. The outcome of this study can be utilized for future design and next fabrication of 3D-printed SLA parts.

References

[1]   Chen L, Liang S, Liu Y, Zhang L. Additive manufacturing of metallic lattice structures: Unconstrained design, accurate fabrication, fascinated performances, and challenges. Materials Science and Engineering: R: Reports 2021;146:100648.

[2]   ISO/ASTM52900 - 15 Standard terminology for additive manufacturing - General Principles - Terminology. West Conshohocken, USA: American Society for Testing Materials; 2015.

[3]   Kong L, Ambrosi A, Nasir M, Guan J, Pumera M. Self-propelled 3D-printed aircraft carrier of light-powered smart micromachines for large-volume nitroaromatic explosives removal. Advanced Functional Materials 2019;29:1–9.

[4]   Khosravani MR, Reinicke T. 3D-printed sensors: Current progress and future challenges. Sensors and Actuators A: Physical 2020;305:111916.

[5]   Juechter V, Franke M, Stichc A, Körner C, Singer R. Additive manufacturing of Ti-45Al-4Nb-C by selective electron beam melting for au-tomotive applications. Additive Manufacturing 2018;22:118–126.

[6]   Alsheghri A, Alageel O, Mezour M, Sun B, Yue S, Tamimi F, et al. Bio-inspired and optimized interlocking features for strengthening metal/polymer interfaces in additively manufactured prostheses. Acta Biomaterialia 2018;80:425–434.

[7]   Demei K, Zhang M, Phuhongsung P, Mujumdar A. 3D food printing: Controlling characteristics and improving technological effect during food processing. Food Research International 2022;156:111120.

[8]   Khan M, Sanchez F, Zhou H. 3-D printing of concrete: Beyond horizons. Cement and Concrete Research 2020;133:106070.

[9]   Khosravani MR, Schüürmann J, Berto F, Reinicke T. On the post processing of 3D-printed ABS parts. Polymers 2020;13:1–13.

[10] Miller A, Safranski D, Smith K, Sycks D, Guldberg R, Gall K. Fatigue of injection molded and 3D printed polycarbonate urethane in solution. Polymer 2017;108:121–134.

[11] Kim H, Yang G, Choi C, Cho Y, Kim G. Gelatin/PVA scaffolds fabricated using a 3D-printing process employed with a low-temperature plate for hard tissue regeneration: fabrication and characterizations. International Journal of Biological Macromolecules 2018;120:119–127.

[12] Nonanto R, Mei L, Bonse B, Chinaglia E, Morales A. Nanocomposites of PLA containing ZnO nanofibers made by solvent cast 3D printing: Production and characterization. European Polymer Journal 2019;114:271–278.

[13] Zolfagharian A, Khosravani MR, Kaynak A. Fracture resistance analysis of 3D-printed polymers. Polymers 2020;12:1–18.

[14] Ng N, Haq R, Marwah O, Ho F, Adzila S. Optimization of polyvinyl alcohol (PVA) support parameters for fused deposition modeling (FDM) by using design of experiments (DOE). Materials Today: Proceedings 2022;57:1226–1234.

[15] Chen Z, Xu J, Liu B, Zhang Y, Wu J. Structural integrity analysis of transmission structure in flapping wing micro aerial vehicle via 3D printing. Engineering Failure Analysis 2019;96:18–30.

[16] Marinopoulos T, Li S, Silberschmidt V. Structural integrity of 3D-printed prosthetic sockets: An experimental study for pae-diatric above-knee applications. Materials Today: Proceedings 2022;37:139–144.

[17] Khosravani MR, Bozic Z, Zolfagharian A, Reinicke T. Failure analysis of 3D-printed PLA components: Impact of manufacturing defects and thermal ageing. Engineering Failure Analysis 2022;136:106214.

[18] Nurizada A, Kirane K. Induced anisotropy in the fracturing behavior of 3D printed parts analyzed by the size effect method. Engineering Fracture Mechanics 2020;239:107304.

[19] Khosravani MR, Frohn-Sörensen P, Reuter J, Engel B, Reinicke T. Fracture studies of 3D-printed continuous glass fiber reinforced composites. Theoretical and Applied Fracture Mechanics 2022;119:103317.

[20] Manapat JZ, Chen Q, Ye P, Advincula RC. 3D printing of polymer nanocomposites via stereolithography. Macromolecular Materials and Engineering 2017;302:1600553.

[21] Weng Z, Zhou Y, Lin W, Senthil T, Wu L. Structure-property relationship of nano enhanced stereolithography resin for desktop SLA 3D printer. Composites: Part A 2016;88:234–242.

[22] Xu X, Martinez P, Madla C, Joubert F, Goyanes A, Basit A, et al. Stereolithography (SLA) 3D printing of an antihypertensive polyprintlet: Case study of an unexpected photopolymer-drug reaction. Additive Manufacturing 2020;33:101071.

[23] Hopkins M, Gunbay S, Hayes C, Mortiz V, Fuenmayor E, Lyons J, et al. Stereolithography (SLA) utilised to print injection mould tooling in order to evaluate thermal and mechanical properties of commercial polypropylene. Procedia Manufacturing 2021;55:205–212.

[24] Quintana R, Choi J, Puebla K, Wicker R. Eects of build orientation on tensile strength for stereolithography-manufactured ASTM D-638 type I specimens. The International Journal of Advanced Manufacturing Technology 2010;46:201–215.

[25] Sakly A, Kenzari S, Bonin D, Corbel S, Fournee V. A novel quasicrystal-resin composite for stereolithography. Materials and Design 2015;56:280–285.

[26] Li Y, Peng S, Miao J, Zheng L, Zhong J, Wu L, et al. Isotropic stereolithography resin toughened by core-shell particles. Chemical Engineering Journal 2020;394:124873.

[27] Gray GT. Classic split-Hopkinson pressure bar testing. Mechanical testing and evaluation, Metals handbook. Am Soc Met 2000;8:462–476.

[28] Wu X, Gorham D. Stress equilibrium in the split Hopkinson pressure bar test. Journal de Physique IV 1997;7:91–96.

DYMAT

Conference Proceedings

DYMAT 2022
26th Technical Meeting
Freiburg, Germany

Additive manufacturing of parts that are used in situations where crashworthiness is important has increased significantly over the recent years.

These conference proceedings focus on topics relevant to the dynamic behaviour of additively manufactured parts:

▸ metal, ceramic, and polymer manufacturing processes

▸ material models for the underlying base materials

▸ resultant behaviour of meta-materials or structures

▸ experimental techniques required to investigate such materials

▸ simulation approaches required to predict behaviour and interpret experiment findings